2021

Model and learning-based strategies for intensity diffraction tomography

BOSTON UNIVERSITY

COLLEGE OF ENGINEERING

Dissertation

MODEL AND LEARNING-BASED STRATEGIES FOR INTENSITY DIFFRACTION TOMOGRAPHY

by

ALEX MATLOCK

B.S., University of California Irvine, 2014
M.S., Boston University, 2021

Submitted in partial fulfillment of the

requirements for the degree of

Doctor of Philosophy

2021

Approved by

First Reader

Lei Tian, Ph.D.
Assistant Professor of Electrical and Computer Engineering
Assistant Professor of Biomedical Engineering

Second Reader

M. Selim Ünlü, Ph.D.
Professor of Electrical and Computer Engineering
Professor of Materials Science and Engineering
Professor of Biomedical Engineering
Professor of Physics

Third Reader

Jerome C. Mertz, Ph.D.
Professor of Biomedical Engineering
Professor of Electrical and Computer Engineering
Professor of Physics

Fourth Reader

Ji-Xin Cheng, Ph.D.
Moustakas Chair Professor in Optoelectronics and Photonics
Professor of Electrical and Computer Engineering
Professor of Biomedical Engineering
Professor of Materials Science and Engineering
Professor of Chemistry
Professor of Physics

All you really need to know for the moment is that the universe is a lot more complicated than you might think, even if you start from a position of thinking it's pretty damn complicated in the first place.

Douglas Adams, *The Hitchhiker's Guide to the Galaxy*

Acknowledgments

Finanical support for this thesis is gratefully acknowledged from the National Science Foundation (1840990,1846784) and the National Institute of Health (R01CA224911, R01NS108464, R21EY029412).

First, I would like to express my deepest thanks to my primary advisor, Professor Lei Tian, for his guidance and mentorship during my PhD career. Coming from a different research field in diffuse optics, Lei's advice, project ideas, and feedback was vital in melding me into a successful researcher in computational imaging. It was an absolute pleasure to be among Lei's first Ph.D. students, grow as a researcher with his lab, and help shape it into the research powerhouse that it is today.

I would also like to express my greatest appreciation to my second advisor, Professor Selim Ünlü. Selim was critical in guiding the early stages of my research career, providing both seasoned advice on how to be successful throughout my Ph.D. and designing my first research project in collaboration with Lei. I would not be where I am without his mentorship.

I am very grateful to Professor Ji-Xin Cheng and Professor Jerome Mertz for serving on my committee and providing feedback regarding my research. I would like to thank the Marseille University's Professors Anne Sentenac and Patrick Chaumet for their vital assistance on the modeling theory and simulations for my first publication. I would also like to thank my undergraduate research advisor, Director Bruce Tromberg at the National Institute of Biomedical Imaging and Bioengineering, for giving me the initial opportunity to pursue academic research and help me find my interest in biophotonics. I also would be remiss if I did not mention my other undergraduate mentors, Professor Thomas O'Sullivan (Notre Dame University), Dr. Albert Cerussi (Apple Inc.), and Professor Darren Roblyer (Boston University) for their valuable advice and aid when we worked together at the Beckman Laser Institute at the

University of California, Irvine.

None of this work would have been possible without my fellow lab members in both the Tian and Ünlü labs. My colleague in Lei's first group of Ph.D. students, Waleed Tahir, has provided immeasurable help and advice in both academic and social settings and has been a genuine friend throughout my Ph.D. experience. Yujia Xue, Yunzhe Li, Joe Greene, Shiyi Cheng, Jiabei Zhu, Hao Wang, and all the members of the Tian lab have also been vital in providing help and feedback on this research. I would also like to thank Celalettin Yurdakul, Fulya Kanik, Allison Marn, Negin Zaraee, Matt Geib, Elisa Chiodi, Iris Celebi, and the other members of the Ünlü lab for help, research insight, and community during my Ph.D.. I would like to thank Jian Zhao from Professor Ji-Xin Cheng's lab for all of his help in our collaborative research and his friendship. The visiting scholars, Jiaji Li from the Nanjing University of Science and Technology and Benedict Diederich from Jena University, also deserve my thanks for their research help and friendship. I would like to thank all of the undergraduate researchers I have mentored for their help on various aspects of the work presented here: David Kirk, Napassorn Lerdsudwichai, Joy Muthami, and Yousuf Baker.

Finally, I cannot have done any of this research and reached this point in my career without the love and support of my family, extended family, and friends. Thank you to my mom, Charlotte Matlock, and my dad, Peter Matlock, for raising me and showing me how to be a good human being that is curious and questioning of their surroundings. Thank you to my stepmom, janet Matlock, for helping talk me through my hardships and being there when I needed it. Thank you to my sister, Susan Brewer, and my brother, Robert Matlock-Williams, for always being there to support me and not complaining when I shamelessly copied your hobbies and activities growing up. Without seeing and trying to do all the amazing things you've both

done, I never would have found my own passions and pushed myself to get where I am today. Thank you to my siblings' spouses, Evan Brewer and Sami Matlock-Williams, for being amazing and supportive people for both me and my kin. Thank you to all of my extended family: Dave and Ann ludwig, Mike and Nancy Lucow, Sarah and Paul Matlock, Erich Ludwig and Ali Ross, Omar and Karen Kariuki, and everyone else in my family that have been there for me. Thank you to my best friend from high school, Oscar Garibay, for reminding me on our yearly road trips and adventures that I am more than just my research and that being spontaneous and chaotic is good for the soul. Thank you to all my other friends Michael, Travis, Jamie, all the other Alex's that I know, Kim, Dani and Taylor, Cristian, Annie, Celia, Victor, Kris, and everyone else I missed for helping me through all the steps of this endeavor. Most importantly, thank you to my partner Alejandro Lopez. You have been a constant source of love and support throughout my Ph.D. and dealt with my anxieties, need for perfection, long working hours, idiosyncrasies, and my rants with grace and aplomb. You remind me daily that there are more important things in life than work and keep me from losing my humanity to research. I am excited to see what the future holds for us, and I hope that I do not drive you too crazy.

And of course, thank you to my coffee maker for giving me the chemical funding required to get through this degree.

MODEL AND LEARNING-BASED STRATEGIES FOR INTENSITY DIFFRACTION TOMOGRAPHY

ALEX MATLOCK

Boston University, College of Engineering, 2021

Major Professors: Lei Tian, Ph.D.
Assistant Professor of Electrical and Computer Engineering
Assistant Professor of Biomedical Engineering

M. Selim Ünlü, Ph.D.
Professor of Electrical and Computer Engineering
Professor of Materials Science and Engineering
Professor of Biomedical Engineering
Professor of Physics

ABSTRACT

Intensity Diffraction Tomography (IDT) is a recently developed quantitative phase imaging tool with significant potential for biological imaging applications. This modality captures intensity images from a scattering sample under diverse illumination and reconstructs the object's volumetric permittivity contrast using linear inverse scattering models. IDT requires no through-focus sample scans or exogenous contrast agents for 3D object recovery and can be easily implemented with a standard microscope equipped with an off-the-shelf LED array. These factors make IDT ideal for biological research applications where easily implementable setups providing native sample morphological information are highly desirable. Given this modality's recent development, IDT suffers from a number of limitations preventing its

widespread adoption: 1) large measurement datasets with long acquisition times limiting its temporal resolution, 2) model-based constraints preventing the evaluation of multiple-scattering samples, and 3) low axial resolution preventing the recovery of fine axial structures such as organelles and other subcellular structures. These factors limit IDT to primarily thin, static objects, and its unknown accuracy and sensitivity metrics cast doubt on the technology's quantitative recovery of morphological features.

This thesis addresses the limitations of IDT through advancements provided from model and learning-based strategies. The model-based advancements guide new computational illumination strategies for high volume-rate imaging as well as investigate new imaging geometries, while the learning-based enhancements to IDT present an efficient method for recovering multiple-scattering biological specimens. These advancements place IDT in the optimal position of being an easily implementable, computationally efficient phase imaging modality recovering high-resolution volumes of complex, living biological samples in their native state.

We first discuss two illumination strategies for high-speed IDT. The first strategy develops a multiplexed illumination framework based on IDT's linear model enabling hardware-limited 4Hz volume-rate imaging of living biological samples. This implementation is hardware-agnostic, allowing for fast IDT to be added to any existing setup containing programmable illumination hardware. While sacrificing some reconstruction quality, this multiplexed approach recovers high-resolution features in live cell cultures, worms, and embryos highlighting IDT's potential across numerous ranges of biological imaging.

Following this illumination scheme, we discuss a hardware-based solution for live sample imaging using ring-geometry LED arrays. Inspired from the linear model, this hardware modification optimally captures the object's information in each LED

illumination allowing for high-quality object volumes to be reconstructed from as few as eight intensity images. This small image requirement allows IDT to achieve camera-limited 10Hz volume rate imaging of live biological samples without motion artifacts. We show the capabilities of this annular illumination IDT setup on live worm samples. This low-cost solution for IDT's speed shows huge implications for enabling any biological imaging lab to easily study the form and function of biological samples of interest in their native state.

Next, we present a learning-based approach to expand IDT to recovering multiple-scattering samples. IDT's linear model provides efficient computation of an object's 3D volume but fails to recover quantitative information in the presence of highly scattering samples. We introduce a lightweight neural network architecture, trained only on simulated natural image-based objects, that corrects the linear model estimates and improves the recovery of both weakly and strongly scattering samples. This implementation maintains the computational efficiency of IDT while expanding its reconstruction capabilities allowing for more generic imaging of biological samples.

Finally, we discuss an investigation of the IDT modality for reflection mode imaging. IDT traditionally captures only low axial resolution information because it cannot capture the backscattered fields from the object that contain rich information regarding the fine details of the object's axial structures. Here, we investigated whether a reflection-mode IDT implementation was possible for recovering high axial resolution structures from this backscattered light. We develop the model, imaging setup, and rigorously evaluate the reflection case in simulation and experiment to show the possibility for reflection IDT. While this imaging geometry ultimately requires a more complex model for 3D imaging, we show the technique provides enhanced sensitivity to the object's structures in a complementary fashion to transmission-based IDT.

Contents

List of Figures

List of Abbreviations

2D	.....	Two-Dimensional
3D	.....	Three-Dimensional
aIDT	.....	annular Intensity Diffraction Tomography
C. elegans	.....	Caenorhabditis elegans
CI	.....	Computational Imaging
CMOS	.....	Complementary Metal-Oxide-Semiconductor
CT	.....	Computed Tomography
DDA	.....	Discrete Dipole Approximation
DL	.....	Deep Learning
DMD	.....	Digital Micromirror Device
DOF	.....	Depth-of-Field
DPC	.....	Differential Phase Contrast
DPM	.....	Diffraction Phase Microscopy
ECE	.....	Electrical and Computer Engineering
ETL	.....	Eletrically Tunable Lens
FOV	.....	Field-of-View
FWHM	.....	Full-Width Half Maximum
GT	.....	Ground Truth
HeLa	.....	Henrietta Lacks Cells
IDT	.....	Intensity Diffraction Tomography
LED	.....	Light-Emitting Diode
LGE	.....	Lucky Goldstar Electronics
LReLU	.....	Leaky Rectified Linear Unit
MAE	.....	Mean Absolute Error
mIDT	.....	Multiplexed Intensity Diffraction Tomography
MIP	.....	Maximum Intensity Projection
MO	.....	Microscopy Objective
MRI	.....	Magnetic Resonance Imaging
MSE	.....	Mean-Squared Error
NA	.....	Numerical Aperture

nMSE	.....	Normalized Mean-Squared Error
OBM	.....	Oblique Back-Illumination Microscopy
ODT	.....	Optical Diffraction Tomography
PCC	.....	Pearson's Correlation Coefficient
PC-ODT	.....	Partial Coherence Optical Diffraction Tomography
PhC	.....	Phase Contrast
PSF	.....	Point Spread Function
QPI	.....	Quantitative Phase Imaging
ReLU	.....	Rectified Linear Unit
RI	.....	Refractive Index
SBR	.....	Signal-to-Background Ratio
sCMOS	.....	Scientific Complementary Metal-Oxide-Semiconductor
SNR	.....	Signal-to-Noise Ratio
SSNP	.....	Split-Step Non-Paraxial Model
SVD	.....	Singular Value Decomposition
TF	.....	Transfer Function
TIE	.....	Transport-of-Intensity Equation
VMSE	.....	Volumetric Mean-Squared Error

Chapter 1

Introduction

Our understanding of the universe is defined by our tools of observation. From evolution, humans have developed an impressive embedded array of sensors for interpreting our surroundings. These sensors, coupled with the computing capabilities of our brains, transform the photons, pressure waves, molecular interactions, and forces we interact with into neural impulses we use to survive, investigate, and understand the world around us. These built-in tools, however, have vastly limited sensitivity and range when compared to the complex, multi-scale structure of nature. Objects ranging from black holes to bacteria subcellular structures are invisible or unresolvable given our default toolset. Only through scientific and engineering exploits have we developed the theory, models, and technology to transform the information from these unobservable domains into information interpretable with our senses. These advances have revolutionized our daily lives as well as understanding of our universe while providing the motivation to develop new technologies capturing other, previously hidden information.

One research field providing such advancements is that of computational imaging (CI). Loosely, CI couples imaging hardware and computational software to recover previously unavailable information from images of an object of interest. Traditional CI techniques require a few key elements to recover this underlying object informa-

tion: 1) An imaging system encoding this information, 2) a model describing the the information encoding process, and 3) an algorithm inverting this model to decode the dataset and recover the object. Due to the various designs an imaging setup may take and encoding strategies that can be used, the models and inversion process are often tailored to the specific CI task. This variability can be seen in many modalities ranging from medical imaging with Computed Tomography (CT) [13, 14] or deblurring fluorescence microscopy images in 3D [15] to single-snapshot 3D photography with light field cameras [16].

While the fields within CI are highly varied, one rising imaging method holding significant promise is that of quantitative phase imaging (QPI) in optical microscopy. In this technique, the structural information of an object of interest is recovered based on the delays an illuminating field experiences as it passes through the sample. Due to the sample's density fluctuations and non-uniform 3D distribution compared to its surrounding medium, the incident light will incur temporal delays through dense materials and experience longer path lengths from becoming scattered by the object. These delays can be weak with minimal scattering or generate strong scattering behaviors drastically perturbing the illumination. Because light is too fast to observe directly without expensive technology [17], QPI methods instead recover the delays in the field's *phase* compared to an unperturbed reference field. This phase is generally defined as

$$\phi = \frac{2\pi}{\lambda}\Delta n H, \tag{1.1}$$

where λ is the illuminating wavelength of light passing through the sample, H is the sample thickness, and Δn defines the refractive index (RI) contrast between the object and the surrounding medium resulting from the object's different density. There are two primary difficulties in QPI in relating this phase to the object's underlying parameters: 1) the phase information is carried in the imaginary element of the field

and is typically lost in standard microscopes when recording the field's intensity, and 2) the separation of the object's thickness and RI is difficult when recording only the phase. To solve these limitation, QPI methods utilize specialized imaging setups encoding phase information into the acquired image as well as novel models enabling 3D object reconstruction separating the object's RI and thickness [18, 19, 20]. The development of these 3D QPI techniques holds significant promise in biology, as phase-based imaging relies only on the intrinsic structural properties of the sample without needing exogenous contrast agents. This poses a significant advantage over absorption and fluorescent-based imaging modalities in biology that must perturb the sample with dyes or fluorescing particles to evaluate the specimen. As such, QPI is well-suited for evaluating specimens in their native, unperturbed state which is vital for understanding biological processes. While not one of the most utilized imaging techniques in biological research, QPI has already shown significant potential in stem cell research [21], immuno-oncology [22], and cytopathology [23]. Here, we focus on 3D QPI techniques for biological imaging applications.

The most widely used setup for 3D QPI is currently Optical Diffraction Tomography (ODT) [18]. This interferometer-based technique utilizes a two-arm design to separately provide an unperturbed reference field and the scattered field from the sample at the image plane to generate an interferogram allowing for direct recovery of the object's phase [18]. In conventional ODT, the object is recovered in 3D from multiple interferograms at different illumination angles with linear scattering models separating the object thickness from its RI [24, 25, 18]. More recently, ODT's hardware and reconstruction algorithms have seen significant improvements expanding its utility and enabling its commercialization. Specifically, ODT has obtained significant speed developments through the use of digital micromirror devices (DMDs) [26] and annular illumination [27], resolution enhancements [27, 28], and reconstruction improvements

through iterative [29] and learning-based reconstruction methods [30, 31]. These advancements have expanded ODT into numerous biological research fields [32, 33, 34] and helped it achieve commercial success [35, 36].

While ODT and other interferometer-based 3D QPI modalities are the most widely used, a number of limitations exist to such methods. One of the main limits to this technology is its use of laser-based illumination for evaluating the sample. Lasers exhibit high spatial coherence and long temporal coherence lengths that provide high-quality interference fringes from which the object's phase can be retrieved with high sensitivity. Unwanted interference will also be generated in the form of speckle, however, from all surfaces of the imaging setup exhibiting rough features below the size of the imaging wavelength that will add noise to the measurement. This limits the measurement sensitivity and can cause unwanted artifacts to be generated in the reconstruction. Furthermore, any path length mismatches in a two-arm interferometer design can introduce phase offsets and incorrect phase measurements. If multiple phase-sensitive measurements are required to be taken sequentially for a single phase reconstruction, there may be strict requirements on the mechanical stability of the system. These factors can be prohibitive for biological labs seeking to develop in-house ODT setups, due to the significant calibration required to achieve reliable 3D QPI. Commercial versions of ODT setups minimize these factors by providing pre-calibrated, specialized ODT setups ready for 3D QPI, albeit at a premium cost.

To avoid these limitations and increase widespread adoption of 3D QPI, significant work has investigated 3D QPI in standard transmission optical microscopes with simple and inexpensive hardware modifications. Intensity-only 3D QPI techniques sacrifice the direct phase measurement capabilities of interferometric setups for simplified optical hardware that provides 3D QPI using a phase encoding mechanism and additional computational post-processing. Many phase encoding mechanisms

have been implemented, relying on sample scanning or rotation [1, 37, 7, 4], illumination engineering [8, 9, 38, 6, 4, 5], pupil engineering [39, 40], diffraction gratings [20], or other phase diversity techniques. In addition, a number of these modalities have implemented advanced scattering models enabling high-quality reconstructions using iterative inverse scattering algorithms [41, 31, 42, 43]. These models require greater computational complexity and longer processing times but significantly advance the object's 3D reconstruction quality.

In this thesis, we focus on one of the many intensity-only 3D QPI techniques known as intensity diffraction tomography (IDT). This imaging modality blends commercial optical hardware with simple, easily implementable computational algorithms to provide easily adoptable 3D QPI for biological imaging applications. We illustrate this technique's simplicity compared to existing intensity-based tomographic QPI setups with computationally efficient algorithms by first reviewing other imaging setups, models, benefits and drawbacks for phase imaging. This review is contained in Chapter 2. In Chapter 3, we review the first IDT setup developed by Ling et al. [8] with a review of the optical hardware, derivation of the forward model, and discussion on the reconstruction algorithm used for tomographic object recovery. Chapters 4-7 detail the advancements to this QPI modality with specific foci on: 1) two computational illumination strategies for high volume-rate imaging of living biological samples, 2) complex, multiple-scattering sample recovery through simulator-trained deep learning, and 3) recovery of high axial resolution objects using reflection-mode IDT.

Chapter 2

Intensity-only 3D Quantitative Phase Imaging

The wealth of intensity-only 3D QPI systems developed and in use require a phase encoding strategy to incorporate phase into their acquired intensity images. As previously mentioned, these encoding methods generally require modifying the imaging setup and/or acquisition process through scanning or rotation [1, 37, 7, 4], new illumination designs [8, 9, 38, 6, 4, 5], pupil modifications or diffraction gratings on the detection path [39, 40, 20], or any other number of techniques. With each of these methods, the forward model and inverse problem modeling the imaging process and reconstruction can vary significantly. Despite this variation, the underlying physics for these methods stems from the same basic principles. Understanding these underlying assumptions is critical to understanding the various encoding strategies and models used in 3D QPI.

Here, we first review the derivation of the underlying physics defining light scattering for 3D QPI from Maxwell's equations and discuss the significance of the assumptions made in the derivation. Following this, we review existing intensity-only 3D QPI systems and discuss their models, capabilities, and limitations. For this process, we broadly separate these modalities based on their hardware implementations into two

categories: 1) Scanning intensity tomography and 2) scanless intensity tomography. We discuss different implementations and their model variants in each section before discussing the implementation of the IDT imaging modality in Chapter 2.

2.1 Helmholtz equation from first principles

The basis of all 3D QPI systems is to relate the object's refractive index (RI), denoted at $\Delta n(\boldsymbol{r})$, where $\boldsymbol{r}$ defines 3D spatial coordinates, to the scattered field measured from the object given some incident illumination of known design. This relation requires understanding the object's interaction with an incident electric field, which can be derived from Maxwell's equations [44]

$$\nabla \times \boldsymbol{H}(\boldsymbol{r},t) - \frac{1}{c}\frac{\partial \boldsymbol{D}}{\partial t} = \frac{4\pi}{c}\boldsymbol{J}(\boldsymbol{r},t), \tag{2.1}$$

$$\nabla \times \boldsymbol{E}(\boldsymbol{r},t) + \frac{1}{c}\frac{\partial \boldsymbol{B}(\boldsymbol{r},t)}{\partial t} = 0, \tag{2.2}$$

$$\nabla \cdot \boldsymbol{D}(\boldsymbol{r},t) = 4\pi\rho, \tag{2.3}$$

$$\nabla \cdot \boldsymbol{B}(\boldsymbol{r},t) = 0, \tag{2.4}$$

where ∇ is the 3D gradient operator, $\boldsymbol{H}(\boldsymbol{r},t)$ is the magnetic field vector, $\boldsymbol{E}(\boldsymbol{r},t)$ is the electric field vector, $\boldsymbol{D}(\boldsymbol{r},t)$ is the electric displacement field vector, $\boldsymbol{B}(\boldsymbol{r},t)$ is the magnetic induction vector, ρ is the medium's charge density, and c is the speed of light. Equation (2.1) and (2.2) describe the generation of magnetic and electric fields from temporally fluctuating electric and magnetic sources, respectively, while Eq. (2.3) and (2.4) describe the electric and magnetic field behavior within a confined volume, respectively. These equations are general for describing electromagnetic field behavior in classical physics and are too complex for use in imaging without assumptions. For the case of QPI, the following assumptions are made regarding the volume in which the object exists:

1. The imaging medium acts as a dielectric and chargeless
2. The imaging medium is nonmagnetic
3. The imaging medium behaves isotropically
4. The medium's RI varies slowly compared with the illumination wavelength

The first and second assumptions require that the volume and object being evaluated generates no electric or magnetic source itself, which is typically valid for biological samples in air or aqueous media. The last two assumptions effectively require the medium to behave uniformly regardless of incident field direction without highly varying structures creating nonlinear field behavior. These assumptions result can be represented partially in a set of constituent relations

$$\boldsymbol{J}(\boldsymbol{r},t) = 0, \tag{2.5}$$

$$\boldsymbol{D}(\boldsymbol{r},t) = n^2(\boldsymbol{r})\boldsymbol{E}(\boldsymbol{r},t), \tag{2.6}$$

$$\rho = 0, \tag{2.7}$$

where $n^2(\boldsymbol{r})$ denotes the medium's permittivity which is the square of the volume's RI under non-magnetic imaging conditions. Under these assumptions, we may substitute Eq. (2.5)-(2.7) into Eq. (2.1)-(2.4) and solve via substitutions to obtain the Helmholtz equation

$$\nabla^2\boldsymbol{E}(\boldsymbol{r}) + k^2 n^2(\boldsymbol{r})\boldsymbol{E}(\boldsymbol{r}) = 0, \tag{2.8}$$

where $k = 2\pi/\lambda$ is the wavenumber for illumination wavelength λ. We note here that an additional assumption that the field is time-harmonic has been applied meaning the field's temporal frequency is constant and has been omitted for clarity. Generally, a further assumption is made that the field is scalar instead of a vector which allows

further simplification to

$$\nabla^2 U(\boldsymbol{r}) + k^2 n^2(\boldsymbol{r}) U(\boldsymbol{r}) = 0, \tag{2.9}$$

where U denotes the scalar electric field. For many 3D QPI models, a variant of Eq. (2.9) is also used with the form

$$\nabla^2 U(\boldsymbol{r}) + k^2 U(\boldsymbol{r}) = -4\pi V(\boldsymbol{r}) U(\boldsymbol{r}), \tag{2.10}$$

where

$$V(\boldsymbol{r}) = \frac{k^2}{4\pi}[n(\boldsymbol{r})^2 - n_0^2], \tag{2.11}$$

defines the *scattering potential* of the object's RI $n(\boldsymbol{r})$ relative to the surrounding uniform imaging medium's RI n_0. As discussed in more detail below, this form is used in the Born and Rytov scattering models as it helps provide linear solutions relating the observed field to the object's RI and structure.

The terms in Eq. (2.9) and (2.10) define that any changes to the field gradient through the volume should match the field changes due to the volume's varying RI. This relation describes the condition of elastic scattering, where the object of interest only changes the field behavior without adding or removing the field's energy through photon emission or absorption. These conditions adequately describes the case for biological samples, as structures such as cells and tissues are generally transparent with minimal absorbing features in the visible spectrum. Since biological substances have varied density compared to their aqueous surroundings, they will predominantly generate elastic scattering and minimally absorb incident light.

While the Helmholtz equation is fundamental in most 3D QPI models, the solution to this equation can vary highly between setups. This variation is partially due to the different phase encoding strategies used for different QPI setups, as the information recovered by the system enables different solutions to be found for describing the field

and relation to the object. In the following sections, we describe existing 3D QPI systems and models in more detail to provide understanding of these techniques to contrast with IDT.

2.2 Scanning Intensity Tomography

We first discuss the range of 3D QPI techniques utilizing mechanical scanning and defocused imaging techniques for encoding phase into intensity. These methods record defocused image pairs [37, 1, 2, 45, 3] or through-focus stacks [7, 4, 5, 46, 47, 6] with or without sample rotation to record the object's phase information and impose a linear inverse scattering model for object phase recovery. Scanning-based approaches are appealing as they can be implemented using only the scanning knob of a commercial transmission microscope, although modern systems often incorporate mechanical scanning technology [6] or electrically-tunable lenses (ETL) for high-speed acquisition [47, 46]. Here, we separate the approaches into 1) transport of intensity (TIE) tomography using differential measurements between defocused intensity image pairs and 2) through-focus scanning tomography using intensity images stacks acquired throughout the object for 3D QPI.

2.2.1 Transport of Intensity (TIE) tomography

Differential scanning tomography methods recover phase based on the Transport of Intensity (TIE) physical models and its variants [48, 49, 37, 1, 2, 50]. Originally for 2D phase retrieval, TIE recovers an object's phase using an approximated intensity gradient between pairs of intensity images acquired at defocused image planes(Fig. 2·1(a) [48]. TIE assumes the incident field $U(\boldsymbol{r}_\perp, z) = \sqrt{I(\boldsymbol{r}_\perp, z)}e^{j\phi(\boldsymbol{r}_\perp, z)}$ with amplitude $\sqrt{I(\boldsymbol{r}_\perp, z)}$ and phase $\phi(\boldsymbol{r}_\perp, z)$ follows the paraxial approximation with slowly-varying phase. Using the real part of the scalar Helmholtz equation from

Eq. (2.9), the phase can be solved for with these assumptions to [48, 49]

$$k\frac{\partial I(\boldsymbol{r},z)}{\partial z} = -\nabla\cdot(I(\boldsymbol{r},z)\nabla\phi(\boldsymbol{r},z), \tag{2.12}$$

where I is the measured intensity, and $\boldsymbol{r}$ and z denote the lateral and axial coordinates, respectively. With measurements of the intensity and the intensity gradient in the axial direction, the phase can be recovered for the object at a given axial plane by solving this function deterministically using a Green's function approach and two Poisson equations [48]. Measuring the intensity is trivial, and the intensity gradient can be estimated based on the difference of defocused intensity image pairs

$$\frac{\partial I(\boldsymbol{r},z)}{\partial z} \approx \frac{I(\boldsymbol{r},z_2)-I(\boldsymbol{r},z_1)}{z_2-z_1}, \tag{2.13}$$

where z_1, z_2 denote the defocus positions at which intensity images are acquired. This estimation assumes linear intensity gradient behavior requiring paraxial imaging conditions and small axial separation distances. The separation cannot be arbitrarily small, however, as the decreasing gradient signal with axial separation will eventually be lost to the measurement noise [51]. Many developments have surpassed these limitations for TIE using multiple image measurements and alternative filter designs [51, 52, 53], which we refer the reader to existing reviews on TIE for further information [54]. Being developed for 2D phase retrieval, this native implementation of TIE must be coupled with a 3D model for tomography in order to do 3D reconstructions.

2.2.2 TIE tomography with inverse radon transform

The simplest TIE 3D QPI approach uses diffraction-based TIE [2] to recover the 2D complex-field at each projection angle and geometric optics principles to implement 3D tomography from those projections. This sample rotation-based approach ac-

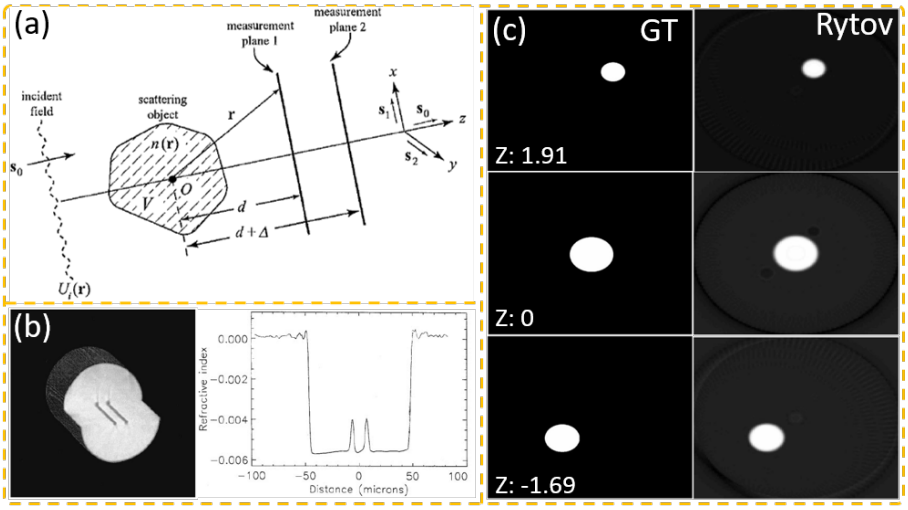

Figure 2·1: Overview figure on TIE Tomography. (a) Illustration showing that 2D projections of the object are acquired through the rotated sample with two defocused intensity measurements separated by a distance Δz acquired from each angle [1]. (b) TIE tomography RI reconstructions of a dual-core optical fiber using the inverse radon transform with a cross-section RI profile [2]. The results show adequate RI recovery with minor streaking artifacts for the fiber cores. (c)Simulated ground truth and first Rytov-based volumetric reconstructions of a simulated 3D object under noiseless conditions using TIET [3]. Results show minimal reconstruction artifacts after accounting for diffraction with the first Rytov approximation-based model.

quires intensity image pairs over a π rotation range from the sample-of-interest and recovers the object's complex amplitude using conventional TIE. An example imaging geometry for this approach can be seen in Fig. 2·1(a) with full experimental setups visible in [2]. Here, the recovered object information from each TIE reconstruction is evaluated as a projection or accumulation of the sample's volumetric complex RI information at a given viewing angle

$$u(\boldsymbol{r}|\theta) = \sqrt{I_0(\boldsymbol{r})}e^{-k\int n_{\mathrm{im}}(\boldsymbol{r},z)dz + jk\int n_{\mathrm{re}}(\boldsymbol{r},z)dz} \tag{2.14}$$

where $I_0(\boldsymbol{r})$ denotes the illuminating field intensity, $n_{\mathrm{re}}(\boldsymbol{r},z)$,$n_{\mathrm{im}}(\boldsymbol{r},z)$ are the complex RI relating to phase and absorption, respectively, and θ denotes the illumination or

viewing angle. Because each complex amplitude accumulates the phase and absorption information of the entire object volume along a given θ, the geometric optics-based filtered backprojection can be used to estimate the full 3D RI volume [2].

An example reconstruction using this hybrid TIE tomography approach is shown in Fig. 2·1(b) on a dual core optical fiber. The fiber was immersed in olive oil with baseline RI $n_0 = 1.46$ while the core and cladding exhibited small RI values of $n_{core} = 1.455$ and $n_{cladding} = 1.453$, respectively. Fig. 2·1(b) visualizes the fiber's volumetric reconstruction with a line profile showing quantitative RI contrast recovery. The results show closely match the expected RI value differences between the immersion oil and fiber RI values indicating the success of this hybrid TIE tomography approach on relatively simple manufactured objects.

Despite adequately reconstructing optical fibers, the use of geometric optics-based recovery for 3D QPI with TIE accepts greater error in the reconstruction from not accounting for diffraction in 3D. As discussed by Gbur et al. [37], ray-based projection for tomographic reconstruction is valid only in the small wavelength limit $k \gg 2\pi/\sigma$ where the smallest object feature size σ is significantly larger than the wavelength such that diffraction effects can be ignored. This condition is typically valid at X-ray wavelengths but not for optical imaging where sample features exist at or below the imaging wavelength. The model works well in Fig. 2·1(b) because the smallest fiber feature is the core at 2μm, which is roughly four times larger than the imaging wavelength of 632nm. For evaluating complex biological structures, diffraction-based 3D models must be utilized for TIE tomography methods.

2.2.3 TIE tomography with Rytov approximation

Full diffraction-based TIE tomography provides a hybrid model using TIE with the first order Rytov approximation [37, 1, 3, 45]. Briefly, this approximation assumes the field is linear in phase such that the phase delays introduced from the sample to

an incident field will sum as

$$U(\boldsymbol{r}) = e^{\psi_0(\boldsymbol{r})+\psi_s(\boldsymbol{r})}, \tag{2.15}$$

$$\psi(\boldsymbol{r}) = \ln(A(\boldsymbol{r})) + \phi(\boldsymbol{r}), \tag{2.16}$$

with the subscripts 0 and s denoting the incident and scattered field's complex phases $\psi(\boldsymbol{r})$ and $A(\boldsymbol{r})$, $\phi(\boldsymbol{r})$ denoting amplitude and phase from each field term, respectively. Applying this field definition to Eq. (2.10) and solving for the unknown object's scattered phase $\phi_s(\boldsymbol{r})$ obtains a variant of the inhomogeneous Helmholtz equation relating the object's scattering potential and phase [44]

$$\nabla^2\phi_s(\boldsymbol{r}) + k^2\phi_s(\boldsymbol{r})U_0(\boldsymbol{r}) = -4\pi V(\boldsymbol{r})U_0(\boldsymbol{r}), \tag{2.17}$$

with $U_0(\boldsymbol{r}) = e^{\psi_0(\boldsymbol{r})}$ denoting the incident field. This inhomogeneous equation is solved via the free-space Green's function $G(\boldsymbol{r})$ to provide [44]

$$\psi_s(\boldsymbol{r}) = U_0^{-1}(\boldsymbol{r}) \int_{\Gamma} V(\boldsymbol{r}')U_0(\boldsymbol{r}')G(\boldsymbol{r}-\boldsymbol{r}')d^3\boldsymbol{r}', \tag{2.18}$$

with Γ denoting the 3D object volume. The Green's function solves the inhomogeneous Helmholtz equation assuming the object is a delta point source within the volume. Here, the convolution with the Green's function and the scattering potential effectively treats the object as a 3D collection of point sources scattering the incident field. This approximation has been shown to be robust to evaluating weak contrast, large-volume objects [55] and is often used as a stand-alone technique for 3D QPI in ODT where direct phase measurements are possible [18].

For intensity-based imaging where phase is indirectly accessible, this model is difficult to utilize without additional modifications. To understand this, we first expand Eq. (2.18) with the Weyl expansion definition of the Green's function [44, 37,

1] and evaluate the logarithm of the field intensity in the Fourier plane

$$\hat{D}(\boldsymbol{\nu}|z) = j\frac{(2\pi)^2}{\eta(\boldsymbol{\nu})}\big[\hat{V}(\boldsymbol{\nu},\eta(\boldsymbol{\nu})-k)e^{jz(\eta(\boldsymbol{\nu})-k)} - \hat{V}^*(-\boldsymbol{\nu},\eta(\boldsymbol{\nu})-k)e^{-jz(\eta(\boldsymbol{\nu})-k)}\big]. \quad (2.19)$$

Here, $D = \log(I)$ is the data function for the intensity measurement, $\hat{\cdot}$ denotes the Fourier transform, $*$ denotes the complex conjugate, $\boldsymbol{\nu}$ is the lateral spatial frequency coordinates, $\eta(\boldsymbol{\nu}) = \sqrt{\lambda^{-2} - |\boldsymbol{\nu}|^2}$ is the real axial spatial frequency components neglecting evanescent fields, and z denotes the defocus plane.

The resulting data function highlights the need for adding TIE for recovering the object's 3D information. For a single intensity measurement, the object's complex RI information is mixed and unseparable with its conjugate described by the well-known twin image problem [1]. With two defocus intensity image pairs, these terms become separable using the intensity gradient following TIE [1, 37]. For this process, the gradient between data functions at positions d, $d+\Delta$ is estimated

$$\hat{D}_\Delta(\boldsymbol{\nu}|d) = \frac{\hat{D}(\boldsymbol{\nu}|d) - \hat{D}(\boldsymbol{\nu}|d+\Delta)e^{j\Delta(\eta(\boldsymbol{\nu})-k)}}{\Delta} \quad (2.20)$$

which obtains the form after simplification and cancellation of the twin image corruption

$$\hat{D}_\Delta(\boldsymbol{\nu}|d) = \frac{j(2\pi)^2}{\eta(\boldsymbol{\nu})\Delta}e^{jd(\eta(\boldsymbol{\nu})-k)}[1 - e^{j2\Delta(\eta(\boldsymbol{\nu})-k)}]\hat{O}(\boldsymbol{\nu},\eta(\boldsymbol{\nu})-k), \quad (2.21)$$

enabling 3D object recovery through a linear inversion of Eq. (2.21) over all viewing angles. Of key importance in this result is the choice of Δ with respect to the exponential term $2\Delta(\eta(\boldsymbol{\nu})-k)$. This result generates spatial frequency-dependent singularities preventing full object recovery unless the lateral spacial frequencies satisfy $\boldsymbol{\nu}^2 \leq 2\pi k/\Delta$ assuming $\boldsymbol{\nu}^2 \ll k^2$. This inequality necessitates precise choices of the intensity measurement positions and adds another constraint over 2D TIE's limitations for this scanning tomography approach to provide adequate 3D QPI.

Simulated object reconstruction results using the Rytov approach are shown in

Fig. 2·1(c) reprinted from [3]. These results show cylindrical simulated objects at three axial planes being reconstructed under noiseless conditions after acquiring images over a full 2π angular range with $\Delta = 4$ for a $d = 100$ separation for Eq. (2.21). The object radii have size of 1, 1.5, ans 1.2 and are illuminated with wavelength $\lambda = 2 \times 10^{-4}$ with arbitrary units, indicating the small wavelength limit is still valid in this example. As in the filtered backprojection case, the objects are substantially larger than the wavelength and the reconstructions provide high-quality recovery of the underlying object. While not evaluating complex objects, this simulated result shows the reconstruction capabilities of this Rytov-based technique. This approach has been expanded further to provide 3D QPI with spherical wave illumination [3], commercially available LED arrays without sample rotation [56], and with full complex RI recovery [45].

While Rytov-based TIE tomography improves upon the filtered backprojection method, the adoption of this approach has been limited for 3D QPI. This approach typically utilizes object rotation for object reconstruction which can necessitate larger datasets and specialized imaging setups for experimental applications. This limitation has made this scanning tomography approach adopted with greater success in X-ray computed tomography where the imaging geometry is common. Instead, a majority of intensity scanning tomography methods bypass the differential phase recovery of defocus plane measurements following TIE to employ through-focus object scanning coupled with 3D transfer functions derived from first Born or Rytov-based linear scattering models for high-quality reconstructions [7, 4, 6, 47].

2.3 Through-focus scanning tomography

In tandem with TIE tomography, through-focus scanning tomography methods have arisen for providing high-quality 3D QPI. This approach uses 3D Transfer Functions

(TFs) derived from the first Born or first Rytov approximations and through-focus intensity image scans to reconstruct an object volume. The key factor for this approach is the development of model-based TFs that relate the object's physical properties to the acquired intensity images. The intensity forward model for these methods have the generalized form

$$\hat{I}(\boldsymbol{\nu}) \propto H_{\mathrm{re}}(\boldsymbol{\nu})\hat{V}_{\mathrm{re}}(\boldsymbol{\nu}) + H_{\mathrm{im}}(\boldsymbol{\nu})\hat{V}_{\mathrm{im}}(\boldsymbol{\nu}), \tag{2.22}$$

where H_{re}, H_{im} are the real and imaginary transfer functions relating the object's real and imaginary permittivity or RI contrast ($\hat{V}_{\mathrm{re}}$, $\hat{V}_{\mathrm{im}}$) to the measured intensity spectra. These transfer functions were originally developed using the first Born approximation under the paraxial regime [57] but have been extended to non-paraxial imaging [58], partial and low coherence conditions [47, 4, 7], and numerous other cases. With these TFs, the object reconstruction process can be obtained efficiently using Tikhonov Regularization [59]

$$\min_{\hat{V}_{\mathrm{re}},\hat{V}_{\mathrm{im}}} \sum_{l} ||\hat{I}_l - (H_{\mathrm{re}}\hat{V}_{\mathrm{re}} + H_{\mathrm{im}}\hat{V}_{\mathrm{im}})||_2^2 + \alpha||\hat{V}_{\mathrm{re}}||_2^2 + \beta||\hat{V}_{\mathrm{im}}||_2^2. \tag{2.23}$$

Here, α, β are manually chosen weights controlling the energy-minimizing prior applying regularization to the reconstruction and l indexes the intensity images. This optimization problem is convex allowing for efficient, non-iterative object reconstruction and can be simplified to recover only the phase or absorption depending on the desired result. Solving this convex optimization is often done with deconvolution

$$V \propto \frac{H^*\hat{I}}{|H|^2 + \tau}, \tag{2.24}$$

where τ denotes the manually chosen weight regularization. For simultaneous phase and absorption recovery, a more complex form is also used as discussed later in this work [8]. Given the generic structure of the forward and inverse problem for intensity

tomography under weak scattering conditions, the critical components separating different through-focus implementations results from the TF derivation. We review these derivations now.

2.3.1 First Born approximation for weakly scattering samples

The first Born approximation follows similar form to the Rytov approximation discussed in Section 2.2.3. Rather than assuming linear phase accumulation in the total field, the Born approximation assumes the total field consists of a linear summation of the incident and scattered light

$$U_{tot}(\boldsymbol{r}) = U_0(\boldsymbol{r}) + U_s(\boldsymbol{r}), \tag{2.25}$$

where the subscripts follow the incident and scattered field definitions previously defined. To solve for the total field, this assumed field is substituted into Eq. (2.10) and evaluated directly. Solving for the incident field's contribution to the total field results in the straightforward solution of the homogeneous form of Eq. (2.10), while the Green's function can be utilized to solve for the scattered field contribution [44]. Combined, we obtain a relation between the incident field and object's scattering potential V

$$U(\boldsymbol{r}|\boldsymbol{\nu}_l) = U_0(\boldsymbol{r}|\boldsymbol{\nu}_l) + \int_{\Gamma} U(\boldsymbol{r}|\boldsymbol{\nu}_l) V(\boldsymbol{r}') G(\boldsymbol{r} - \boldsymbol{r}') d^3\boldsymbol{r}', \tag{2.26}$$

where $\boldsymbol{\nu}_l$ denotes the incident field's transverse spatial frequencies, Γ is the object volume, and G defines the free-space 3D Green's function also used in section 2.2.3. We formalize the incident field's illumination to be $U_0(\boldsymbol{r}, z|\boldsymbol{\nu}_l) = Ae^{j2\pi(\boldsymbol{\nu}_l \cdot \boldsymbol{r} + \eta(\boldsymbol{\nu}_l) z)}$, where $A = \sqrt{S(\boldsymbol{\nu}_l)}$ denotes the amplitude with S geometrically constraining the source size in the Fourier plane and $\eta(\boldsymbol{\nu}_l) = \sqrt{\lambda^{-2} - |\boldsymbol{\nu}_l|^2}$ is the illumination's axial spatial frequency.

This field definition accounts for all scattering from the object due to its recursive definition, and rigorously solving (2.26) requires an iterative, computationally intensive process [43]. To provide computational efficiency over rigor, the weak scattering approximation is often taken such that $|U_s(\boldsymbol{r})| \ll |U_0(\boldsymbol{r})|$ allowing for higher order scattering behaviors to be ignored

$$U(\boldsymbol{r}|\boldsymbol{\nu}_l) = U_0(\boldsymbol{r}|\boldsymbol{\nu}_l) + \int_\Gamma U_0(\boldsymbol{r}|\boldsymbol{\nu}_l) V(\boldsymbol{r}') G(\boldsymbol{r} - \boldsymbol{r}') d^3\boldsymbol{r}'. \tag{2.27}$$

This assumption is known as the first Born approximation in that only the first-order scattering term from the Born series expansion of the total field is considered [44]. When this approximation is valid, the scattered field from the sample behaves linearly with the object's physical parameters. With an extension of this linearity to the measured intensity image in LED array microscopy, a linear forward model with an easily implementable inverse model can be applied for efficient object recovery.

To develop this linear forward model, the relation of this field to the intensity spectra must be understood to generate a forward model following Eq. (2.22). In an acquired intensity image, the total field in Eq. (2.27) is convolved with a microscope's point spread function (PSF) $p(\boldsymbol{r}_\perp)$ filtering the lateral spatial freuqencies, all fields from the 3D volume are projected to a 2D image plane, and the square modulus of the field is taken

$$I(\boldsymbol{r}_\perp|\boldsymbol{\nu_l}) = |U(\boldsymbol{r}|\boldsymbol{\nu}_l) * p(\boldsymbol{r})|^2, \tag{2.28}$$

where $*$ denotes the convolution operator and $\perp$ denotes the lateral spatial coordinates. When transformed to the Fourier plane, the intensity spectra captures four separate interference terms between the incident field, the scattered field, and their

complex conjugates. Generally, these terms follow the form

$$\hat{I}_{0,0} \propto \hat{U}_0(\boldsymbol{\nu})P(\boldsymbol{\nu}) * \hat{U}_0^*(\boldsymbol{\nu})P^*(\boldsymbol{\nu}) \tag{2.29a}$$

$$\hat{I}_{0,s} \propto \hat{U}_0(\boldsymbol{\nu})P(\boldsymbol{\nu}) * \hat{U}_s^*(\boldsymbol{\nu})P^*(\boldsymbol{\nu}) \tag{2.29b}$$

$$\hat{I}_{0,s}^* \propto \hat{U}_0^*(\boldsymbol{\nu})P * (\boldsymbol{\nu}) * \hat{U}_s(\boldsymbol{\nu})P(\boldsymbol{\nu}) \tag{2.29c}$$

$$\hat{I}_{s,s} \propto \hat{U}_s^*(\boldsymbol{\nu})P^*(\boldsymbol{\nu}) * \hat{U}_s(\boldsymbol{\nu})P(\boldsymbol{\nu}), \tag{2.29d}$$

corresponding to the the self-interfered incident field ($\hat{I}_{0,0}$), the cross-interference between the incident and scattered field with its conjugate ($\hat{I}_{0,s}, \hat{I}_{0,s}^*$), and the self-interfered scattered field ($\hat{I}_{s,s}$). We denote the system's PSF in the Fourier space with the pupil function $P(\boldsymbol{\nu})$.

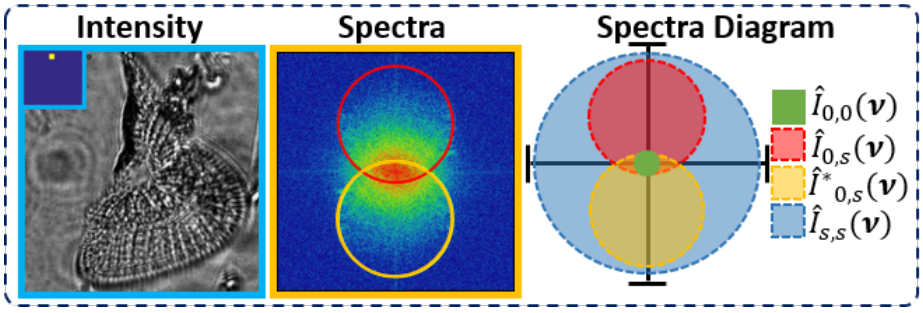

Figure 2·2: Example Intensity image, intensity spectra, and diagram of spectral contributions for an image acquired under oblique plane-wave illumination. The spectral contributions exhibit geometric constraints due to the pupil function filtering the scattered field and the incident illumination angle.

Intuitive understanding for these terms can be obtained from evaluating their behavior under plane wave incident illumination from an arbitrary illumination angle shown in Fig.2·2. The self-interfered incident field contribution $\hat{I}_{0,0}$ provides a constant background to the image and occupies the origin of the Fourier space (Fig. 2·2). This signal is typically removed through a background-subtraction process. The cross-interference terms $\hat{I}_{0,s}$ and $\hat{I}_{0,s}^*$ appear as shifted circles in the Fourier plane (Fig. 2·2).

These circles arise from the low-pass filtering of $P(\boldsymbol{\nu})$, and the circle translation in the Fourier plane depends on the field's illumination angle following synthetic aperture principles [8]. Finally, the $\hat{I}_{s,s}$ term occupies a bandwidth of 2NA and contributes spectral content behaving nonlinearly with the object's scattering potential. Under weak scattering conditions such as those assumed with the first Born approximation, this term is considered negligibly weak and is ignored or considered to be a source of noise in the reconstruction.

The remaining cross-interference terms provide the linearity required between the object's parameters to be recovered and the intensity image. These spectral contributions are used to develop H_{re} and H_{im} in Eq. (2.22) and have varied forms depending upon the imaging setup and phase encoding strategy. These variations are discussed in greater detail below.

2.3.2 Through-focus scanning tomography under partial coherence

With an understanding of the first Born model and general structure of the forward models using it for intensity-only 3D QPI, we first evaluate through-focus scanning tomography methods using this model. Through-focus scanning tomography implementations often use partial or low spatial coherence illumination for high-quality 3D QPI [4, 5]. As shown in Fig. 2·2, the use of oblique plane wave illumination for an intensity image translates the system's pupil function in the Fourier space and enhances the recovered object bandwidth following synthetic aperture principles. With low coherence from a distributed source, these translations sum to an incoherent pupil function capturing two-fold resolution improvements with greater depth sectioning over coherent microscopy [60, 57]. For this result, the key modification for the TF results from the incorporation of a source function in the illumination definition. We discuss the paraxial TF derivation here and refer the reader elsewhere [58]

for the non-paraxial case.

The assumption of partial coherence evaluates the illumination source under Köhler illumination where each point source illumination in the microscope's back-focal plane generates a mutually incoherent plane wave illumination on the sample. The resulting intensity image under a distributed, low coherence source illumination can then be modeled as an integration of the coherent TFs from each plane wave illumination. With the addition of a source function $S(\boldsymbol{\nu}_l)$ accounting for an arbitrary source geometry and a 3D Fourier transform, the intensity under partial coherence from Eq. (7.11) can be evaluated as

$$\begin{aligned}\hat{I}(\boldsymbol{\nu},\eta|\boldsymbol{\nu}_l) =& \hat{I}_0(\boldsymbol{\nu},\eta(\boldsymbol{\nu})|\boldsymbol{\nu}_l) \\ &+ \iint S(\boldsymbol{\nu}_l)\Big[P(-\boldsymbol{\nu}_l)P(\boldsymbol{\nu}+\boldsymbol{\nu}_l)\hat{G}^*(\boldsymbol{\nu}+\boldsymbol{\nu}_l,\eta(\boldsymbol{\nu})+\eta(\boldsymbol{\nu}_l))\hat{V}^*(-\boldsymbol{\nu},-\eta) \\ &+ P^*(-\boldsymbol{\nu}_l)P(\boldsymbol{\nu}-\boldsymbol{\nu}_l)\hat{G}(\boldsymbol{\nu}-\boldsymbol{\nu}_l,\eta(\boldsymbol{\nu})-\eta(\boldsymbol{\nu}_l))\hat{V}(\boldsymbol{\nu},\eta)\Big]d^2\boldsymbol{\nu}_l \end{aligned} \tag{2.30}$$

where $\hat{I}_0 = \iint S(\boldsymbol{\nu}_l)|P(-\boldsymbol{\nu}_l)|^2 d^2\boldsymbol{\nu}_l \cdot \delta(\boldsymbol{\nu},\eta)$ is the incident field intensity at the Fourier space origin. We neglect the nonlinear scattering term here following the weak scattering approximation. By assuming a complex scattering potential for the object, this spectra can be separated to provide 3D transfer functions for recovering the object's real and imaginary RI

$$\begin{aligned}H_{\mathrm{re}}(\boldsymbol{\nu},\eta(\boldsymbol{\nu})|\boldsymbol{\nu}_l) = j\iint S(\boldsymbol{\nu}_l)\Big[&P^*(-\boldsymbol{\nu}_l)P(\boldsymbol{\nu}-\boldsymbol{\nu}_l)\hat{G}(\boldsymbol{\nu}-\boldsymbol{\nu}_l,\eta(\boldsymbol{\nu})-\eta(\boldsymbol{\nu}_l)) \\ &-P(-\boldsymbol{\nu}_l)P(\boldsymbol{\nu}+\boldsymbol{\nu}_l)\hat{G}^*(\boldsymbol{\nu}+\boldsymbol{\nu}_l,\eta(\boldsymbol{\nu})+\eta(\boldsymbol{\nu}_l))\Big]d^2\boldsymbol{\nu}_l\end{aligned} \tag{2.31}$$

$$\begin{aligned}H_{\mathrm{im}}(\boldsymbol{\nu},\eta(\boldsymbol{\nu})|\boldsymbol{\nu}_l) = \iint S(\boldsymbol{\nu}_l)\Big[&P^*(-\boldsymbol{\nu}_l)P(\boldsymbol{\nu}-\boldsymbol{\nu}_l)\hat{G}(\boldsymbol{\nu}-\boldsymbol{\nu}_l,\eta(\boldsymbol{\nu})-\eta(\boldsymbol{\nu}_1)) \\ &+P(-\boldsymbol{\nu}_l)P(\boldsymbol{\nu}+\boldsymbol{\nu}_l)\hat{G}^*(\boldsymbol{\nu}+\boldsymbol{\nu}_l,\eta(\boldsymbol{\nu})+\eta(\boldsymbol{\nu}_l))\Big]d^2\boldsymbol{\nu}_l\end{aligned} \tag{2.32}$$

where H_{re} and H_{im} denote the real and imaginary TFs and the intensity image incorporates an integration over all illuminations at spatial frequencies $\boldsymbol{\nu}_l$.

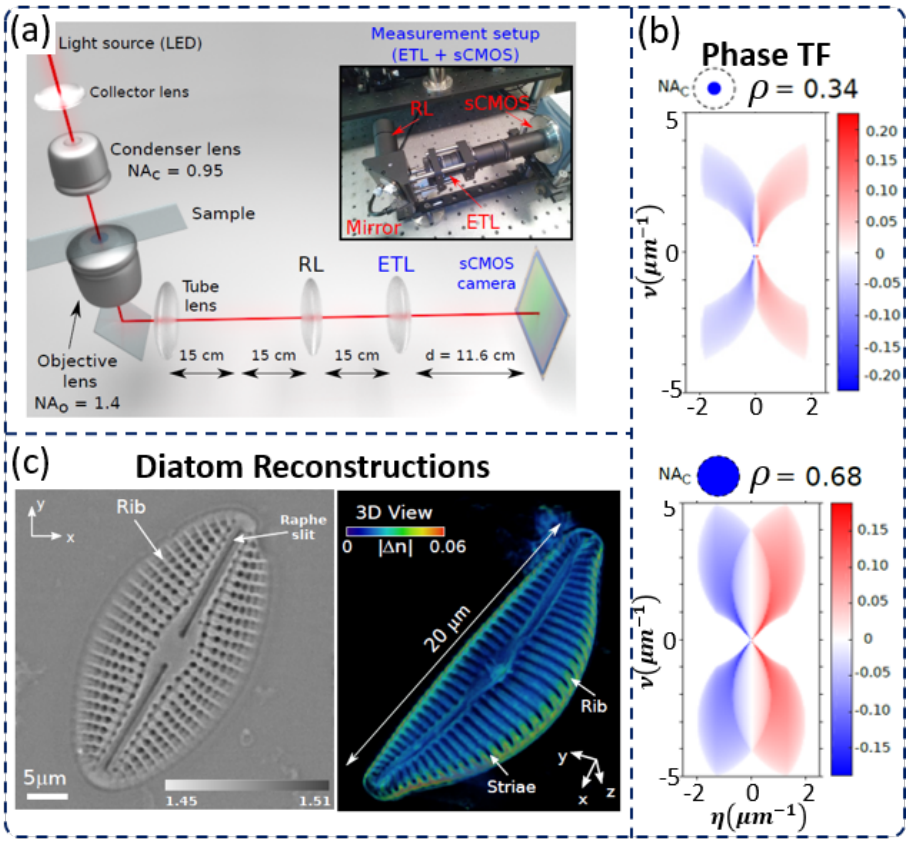

Figure 2·3: Overview of the PC-ODT imaging setup and 3D QPI capabilities. (a) Imaging system diagram and hardware image showing optical path and ETL for rapid focal scanning through the sample. (b) The 3D phase TF for PC-ODT under high spatial coherence (Top) and low spatial coherence (Bottom) illumination. The lower spatial coherence shows enhanced bandwidth enabling better system 3D resolution. (c) Example diatom reconstruction from PC-ODT showing RI recovery and identification of specific rib, raphe slit, and striae structures in the sample. Figure adapted from [4].

A prime implementation of through-focus scanning tomography under partial coherence comes from Soto et al. [4]. Their implementation, termed Partial Coherence Optical Diffraction Tomography (PC-ODT) (Fig. 2·3), combines high-NA illumination and collection with an electrically tunable lens (ETL) in a standard transmis-

sion microscope setup for rapid, high-resolution 3D QPI (Fig. 2·3(a)). Implementing the non-paraxial forms of Eq. (2.31), (2.32) from [58], PC-ODT uses low coherence circular illumination for acquisition with a coherence parameter $\rho = 0.68$, where $\rho = \mathrm{NA}_{ill}/\mathrm{NA}_0$, showing close to incoherent sample illumination. This approach uses a $\mathrm{NA}_0 = 1.4$ high-NA objective to acquire high-resolution $\approx$ 200nm and $\approx$ 500nm lateral and axial resolution for 3D complex RI recovery on biological samples. The optimized 3D TFs for this setup are shown in Fig. 2·3(b) to highlight the bandwidth enhancement under partially coherent illumination. For efficient object reconstruction, this work simplifies the complex RI recovery by assuming the object has significantly weak absorption such that $V_{\mathrm{im}} = \alpha V_{\mathrm{re}}$. α is manually chosen to set a linear relation between the object's phase and absorption, enabling the object's complex physical information to be recovered from a single effective TF that reduces halo artifacts [4]

$$H_E = H_{\mathrm{re}} + \alpha H_{\mathrm{im}}, \tag{2.33}$$

thus allowing 3D QPI directly using the inverse solution in Eq. (2.24).

3D QPI reconstructions using PC-ODT can be seen in Fig. 2·3(c) for a diatom sample. The use of low coherence illumination with through-focus scanning tomography provides improved 3D resolution of the diatom sample and recovers easily identifiable biological structures including rib structures, the raphe slit, and striae with a quantified RI. Using high-NA objectives also helps reduce the spatial frequency loss from the classic missing cone problem that reduces the object's axial resolution. These results show the utility of this intensity tomography technique for 3D QPI and more recent work has illustrated its high-speed imaging capabilities using the ETL for rapid through-focus scanning [47].

One of the elements of PC-ODT shown to provide additional improvements to 3D QPI is the computational illumination geometry and the setup's experimental illu-

mination [5, 61]. While PC-ODT originally considers uniform circular illumination across the back focal plane, this assumption does not always hold for the experimental illumination and mismatches in the assumptions used when generating the 3D TFs and the experimental imaging condition quickly lead to blurred object reconstructions and resolution loss. This effect was highlighted in [61], where matching the illumination and TF assumptions shows enhanced resolution recovery on calibration samples. Furthermore, the use of specially designed illumination schemes, such as gaussian illumination [61] or annular illumination [5], can provide additional improvements based on the conditioning of the 3D TFs.

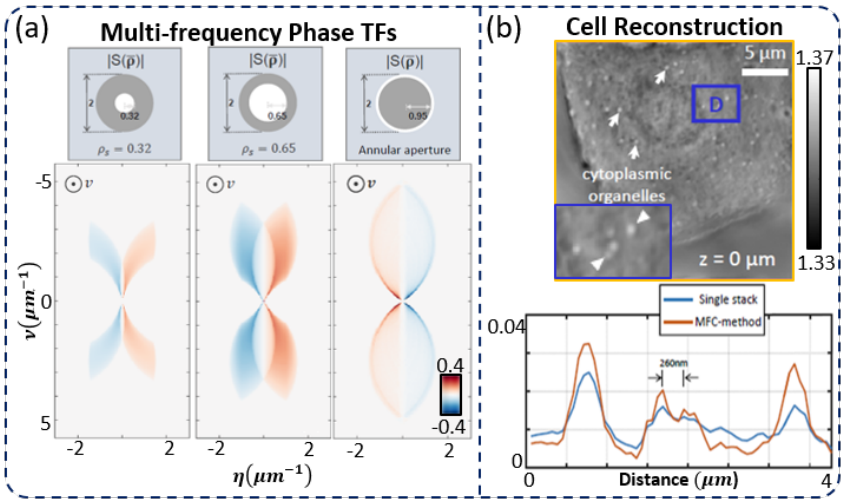

Figure 2·4: Spatial coherence under different illumination schemes with PC-ODT. (a) illumination masks (Top) and corresponding phase 3D TFs (Bottom) under high coherence, low coherence, and annular low coherence illumination using the multi-filter frequency PC-ODT method. (b) Epithelial buccal cell RI reconstruction showing high-resolution feature recovery using low annular spatial coherence illumination within the sample in the blue outset and cross-section plot. Figure adapted from [5].

This result was shown particularly in work from Li et al. [5] that combined multiple through-focus scans with programmed illumination designs for improving the reconstructed tomogram. This approach used three illumination designs with differ-

ent coherence parameters of $\rho = [0.32, 0.65, 0.95]$ with two circular and one annular illumination design to evaluate the object. As shown in Fig. 2·3(a), the use of multiple illumination schemes of varying coherence provides improved weighting to low or high spatial frequencies within the recovered bandwidth. These weight variations provides better conditioning in the reconstruction across the object's recovered spectrum and provides stable, high-quality RI reconstructions as shown on the epithelial buccal cell segment of Fig. 2·3(b). Implementing this approach requires additional data and a modified form of Eq. (2.24) for reconstruction discussed elsewhere [5].

2.3.3 Through-focus scanning tomography with Differential Phase Contrast

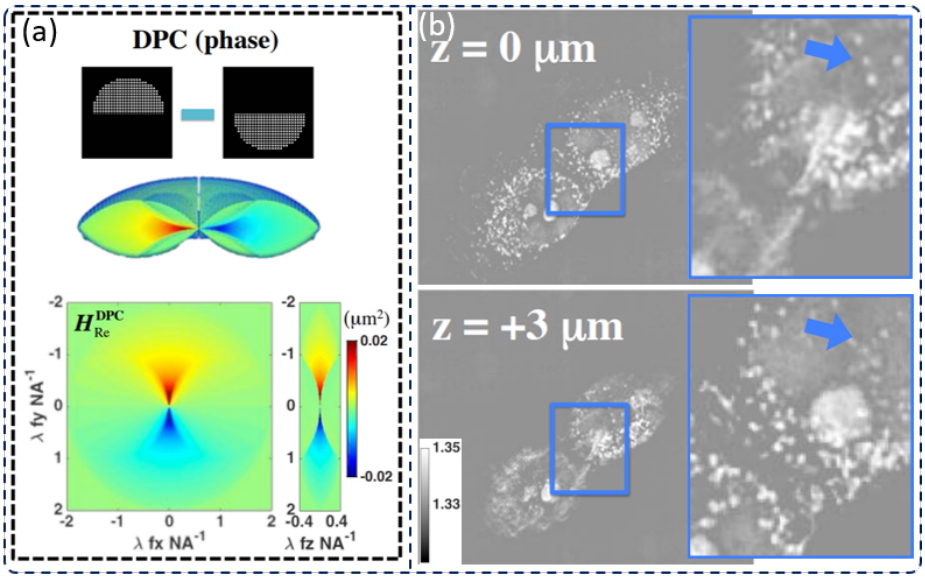

Figure 2·5: Overview of the 3D TF and reconstruction capabilities of 3D DPC. (a) 3D DPC TF exhibiting TF asymmetry under differential half-circle LED programmed illumination. (b)MCF10A cell reconstructions at two different axial planes with outsets highlighting the depth sectioning and quantitative recovery of 3D DPC on biological volumes. Figure adapted from [6].

The use of multiple, low coherence illuminations to provide enhanced object re-

covery with through-focus scanning tomography has also been investigated using Differential Phase Contrast (DPC) [6]. DPC recovers an object's phase by evaluating the difference of intensity image pairs acquired under opposing asymmetric half-circle (Fig. 2·5(a)) [6, 62], annular [62], or other more complex illumination schemes [63, 64]. These difference images enhance the encoded phase of the object measured under oblique illumination and can quantitatively recover the object using a corresponding inverse scattering model.

The key to DPC results from the odd and even functions of the phase and absorption TF of Eq. (2.31), (2.32). The object's absorption information is symmetric about the origin in the Fourier plane, while the phase information is asymmetric noted by the minus sign of Eq. (2.31). At the focal plane under incoherent illumination, this asymmetry is often problematic as it means that illuminating the sample from symmetric points in the Fourier plane will remove the object's phase information [62]. This cancellation can be seen in Fig. 2·3(b) and Fig. 2·4(a), where the central axial plane of the phase 3D TF exhibits no phase information. By taking the difference of two intensity images with opposing illumination designs (Fig. 2·5(a)), however, the difference image will enhance the object's phase information while cancelling out absorption features. Equivalently, the summation of these images provides a brightfield image containing only the object's absorpting features at the focal plane. Using half-circle illuminations [6], the images for DPC recovery of an object's complex scattering potential become

$$I_{abs} = \frac{I_T + I_B + I_L + I_R - 2|I_0|}{2|I_0|}, I_{phase} = \frac{I_{T/L} - I_{B/R}}{|I_0|} \tag{2.34}$$

where the half-circle images are denoted as Top (T), Bottom (B), Left, (L), and Right (R) and $|I_0|$ is the estimated background intensity from the intensity images. Fig. 2·5(a) illustrate the 3D TFs for recovering the phase and absorption from these

images.

Following previously discussed through-focus tomography methods, 3D DPC requires intensity image acquisition at multiple focal planes throughout the sample for volumetric recovery. Since differential images are required, this approach requires four images at each axial position for full bandwidth recovery. A closed-form reconstruction then simultaneously recovers the 3D object using Tikhonov regularization to prevent high-frequency artifacts corrupting the image [62].

Example reconstructions with 3D DPC are shown on human mammary epithelial MCF10A cells in Fig 2·5(b) using a conventional brightfield microscope equipped with a programmable LED array controlling the illumination and a 0.65 NA objective. The recovered cells show depth-sectioning of different cellular structures across the recovered volume and overall high-quality reconstructions similar to other through-focus scanning tomography setups.

While these results show impressive tomographic results, the utility of this technique is limited in biological situations compared to the previously discussed through-focus tomography techniques. In using DPC with intensity image pairs, this approach requires a substantially larger dataset for 3D object recovery. This larger dataset is less appealing for 3D QPI adoption and adds temporal constraints for evaluating living biological specimens.

2.3.4 Through-focus scanning tomography with object rotation

One limitation common to the prior through-focus scanning tomography techniques is the classic missing cone artifact limiting axial resolution. While imaging a sample at high NA can reduce this artifact [4], the lack of axial frequency information due to the limited illumination angles available under brightfield transmission imaging means this artifact always corrupts the 3D reconstruction. As with TIE tomography

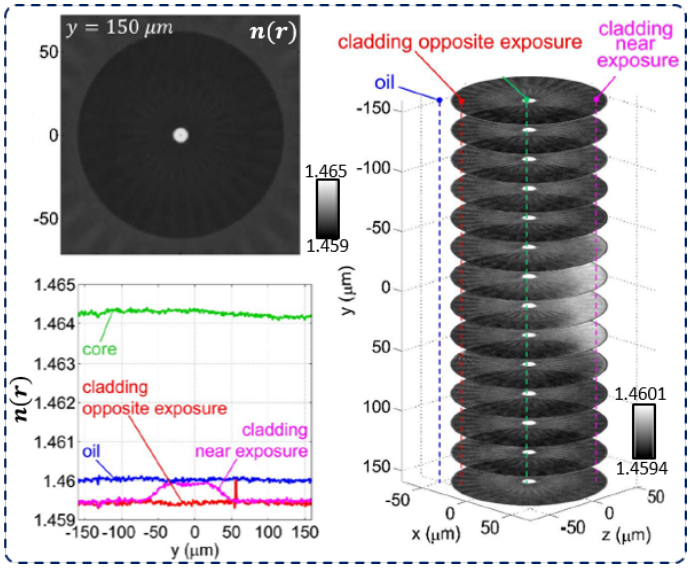

Figure 2·6: Through-focus RI tomography reconstruction of single-mode fiber with object rotation [7]. Results show high sensitivity reconstructions of fiber's core and cladding without missing cone artifacts from the addition of object rotation. Figure adapted from [7].

and ODT, this problem can be easily solved through the use of object rotation. While requiring additional data and optical hardware, resolving the full object of interest without artifacts is often desirable for the best quality reconstruction. This approach is well illustrated in work by Jenkins and Gaylord [7] which uses a first Rytov-based TF derivation and partial coherence for their rotation through-focus scanning tomography setup.

For the first Rytov-based derivation, the model utilizes the field and scattered field complex phase defined in Eq. (2.15) and (2.18), respectively. Under partially coherent illumination, the intensity is

$$I(\boldsymbol{r}|\boldsymbol{\nu}_l) = S(\boldsymbol{\nu}_l)e^{2Re[\psi(\boldsymbol{r}|\boldsymbol{\nu}_l)]} \tag{2.35}$$

to account for the object illuminated with spatial frequencies $\boldsymbol{\nu}_l$. Due to the non-linear relation between the object's complex phase and the intensity, the first Rytov

approximation requires a weak complex phase assumption, $2Re[\psi(\boldsymbol{r}|\boldsymbol{\nu}_l)] \ll 1$, such that a Taylor expansion can be applied to linearize the phase relation with intensity

$$I(\boldsymbol{r}|\boldsymbol{\nu}_l) = S(\boldsymbol{\nu}_l)\big(1 + 2Re[\psi(\boldsymbol{r}|\boldsymbol{\nu}_l)]\big). \tag{2.36}$$

With this approximation, the application of Eq. (2.18) generates the same intensity definition as obtained in Eq. (2.30) allowing for identical TF generation as the prior cases.

For object recovery in [7], the main variation in the processing pipeline results from evaluating multiple through-focus scans of a rotated object. The through-focus scans are acquired at angle increments $\Delta\theta$ and must be rotated and co-registered for the final deconvolution using Eq. (2.24). An additional processing step to improve recovery of the object's low and high-frequency complex RI is also implemented and described elsewhere [7]. For simplicity, the authors assume negligible absorption and evaluate a pure phase object.

Experimental results from this rotation-based through-focus tomography setup can be seen for a fiber optic cable in Fig. 2·6. While rotation-based artifacts are present in the recovered volumetric object, the sample exhibits no missing cone artifacts as observed in non rotation-based architectures. From the line profiles in Fig. 2·6, this tomographic approach also shows sensitivity to small RI variations in the optical fiber core and cladding highlighting the technique's utility. With the requirement of additional datasets and adding optical hardware, the rotation-based scanning tomography setups show impressive 3D QPI capabilities.

2.4 Summary on scanning-based 3D QPI methods

The previous sections introduced a number of different existing scanning 3D QPI techniques, reviewed their linear forward models, and their phase encoding strate-

gies. We first reviewed the derivation of the inhomogeneous Helmholtz equation to understand the assumptions made on the objects and imaging volume for its validity and understand the basis for QPI physical models. From there, a number of techniques were discussed that used the TIE solution to the Helmholtz equation to recover an object's 3D structure using the defocus-based phase encoding strategies. To recover 3D, these techniques utilized both geometric and diffraction-based 3D models in addition to TIE to recover the object volume with varying levels of model-based artifacts. Following these techniques, we reviewed the first Born approximation describing the field behavior of weakly scattering objects and the general forward model structure using this approximation. We reviewed different instances of through-focus scanning tomography that continued the trend of defocus-based phase encoding for 3D QPI. These techniques incorporated different illumination strategies for resolution enhancement and also investigated object rotation to enhance the recovered object's axial resolution. These existing techniques, their linear scattering models, and easily implementable reconstruction methods highlight the capabilities of these technologies for 3D QPI and their potential utility in biological imaging.

The fundamental limitation with these imaging modalities is their reliance on mechanical scanning for recovering phase from defocus. While this phase encoding strategy can be simply implemented using just the focusing knob on a microscope, the technique experiences difficulties when evaluating living biological samples. Worms, tardigrades, and other micro-organisms as well as living cells are of interest for imaging live, but any rapid movements require high acquisition speeds to capture their phase information without artifacts. This temporal constraint can be overcome with more expensive equipment or ETLs [47], but the added cost and specialization of the microscope can limit the appeal of adopting 3D QPI for biology. Alternative investigations have shown motion deblurring using computational methods for QPI [65] but

have not gained much traction in the community.

Chapter 3

Intensity Diffraction Tomography

3.1 Overview

In response to the limitations of scanning-based 3D QPI techniques, many recent modalities have investigated alternative phase encoding strategies recovering phase from scanless intensity methods [66, 67, 8]. Scan-free techniques recover the volumetric object from single 2D intensity image datasets using simpler optical hardware without mechanically moving components. One of the most popular scanless tomography implementations has utilized computational illumination for this process due to the development of programmable light sources, such as LED arrays, that can be electronically scanned for rapid data acquisition. These setups modify an existing standard optical microscope with an off-the-shelf [38, 68, 8, 9] or customized LED array [69] in the Fourier plane of the sample. As each LED acts as a quasi-monochromatic, partially coherent illumination source, this hardware enables similar limited angle tomography imaging to ODT without the risk of coherent noise from laser-based illumination. With significant utility already in 2D QPI for multimodal imaging [70], large FOV quantitative analysis with high-resolution [38], and high-speed QPI with asymmetric illuminations [62], recent works have shown success in achieving scanless tomography with LED array-based imaging [8, 71, 9, 67].

Here, we discuss the intensity diffraction tomography setup known as IDT. Developed by Ling et al. [8], this modality couples an LED array microscope with a linear scattering model to provide efficient 3D QPI reconstructions of an object in a *slice-wise* reconstruction approach. This implementation provides a significant improvement over scanning methods by requiring no moving parts, and its linear model derivation allows for arbitrary sizes of object volumes to be reconstructed from the set of 2D intensity measurements. This has significant potential for biological imaging applications, as the adaptive nature of the 3D reconstruction enables the user to adapt the reconstruction volume size to their required specifications purely in the post-acquisition stage. This allows the user to evaluate large or small-volume objects easily without requiring specialized imaging constraints during acquisition. Coupled with its low-cost hardware, IDT offers an easily adoptable 3D QPI instrument that can be easily added to the arsenal of imaging techniques in biological research labs.

We first review the derivation of the IDT forward model in detail from [8]. This derivation provides an understanding of the assumptions and imaging conditions required for the imaging setup and object's physical parameters to provide a valid model. We then discuss the deterministic reconstruction method used for recovering the 3D object from 2D intensity measurements, and finally discuss the imaging setup originally used for IDT and its experimental results. Finally, we discuss the limitations of this technique that motivated the main works in this thesis.

3.2 IDT Forward Model

The IDT forward model utilizes many of the similar approximations made in the 3D QPI setups discussed in the prior chapter. Mainly, this forward model relies on the Born approximation discussed is based on the first Born approximation discussed in section 2.3.1 for solving the inhomogeneous Helmholtz equation from Eq. (2.10).

As with other 3D QPI methods, this model utilizes only the first order expansion of the Born approximation to model the scattered field from the object to maintain linearity between the object's RI and the measured intensity. The main difference for the IDT model results from its treatment of the object's volumetric scattering, which we discuss below.

Field Definition and Axial Discretization

Under the first Born approximation, the field in the object volume for a single IDT intensity image can be defined as

$$U(\boldsymbol{r}|\boldsymbol{\nu}_l) = U_0(\boldsymbol{r}|\boldsymbol{\nu}_l) + \int_{\Gamma} U_0(\boldsymbol{r'})V(\boldsymbol{r'})G(\boldsymbol{r}-\boldsymbol{r'})d^3\boldsymbol{r'}. \tag{3.1}$$

as initially derived in Eq. (2.27). For IDT, we assume the incident field is a monochromatic plane wave acting on the sample at a given illumination angle

$$U_0(\boldsymbol{r}_\perp, z|\boldsymbol{\nu}_l) = \sqrt{S(\boldsymbol{\nu}_l)}e^{j2\pi(\boldsymbol{\nu}_l\cdot r_\perp + \eta(\boldsymbol{\nu}_l)z)}, \tag{3.2}$$

where we have separated lateral and axial spatial coordinates into $\boldsymbol{r}_\perp$ and z, respectively, and the lateral and axial spatial frequency coordinates into $\boldsymbol{\nu}$ and $\eta(\boldsymbol{\nu}) = \sqrt{\lambda^{-1} - |\boldsymbol{\nu}|^2}$ for ease of notation for the IDT model.

For the scattered field, we must make a few manipulations before obtaining a form of the equation easily usable for the forward model. We first expand the 3D integral and apply the Weyl expansion [44]

$$G(\boldsymbol{r}_\perp - \boldsymbol{r}'_\perp, z-z') = j\int_{-\infty}^{\infty} \frac{e^{\boldsymbol{\nu}_\perp\cdot(\boldsymbol{r}_\perp - \boldsymbol{r}'_\perp)+\eta(\boldsymbol{\nu})(z-z')}}{\eta(\boldsymbol{\nu})}d^2\boldsymbol{\nu}, \tag{3.3}$$

form of the free-space Green's function defining scattering behavior from a point source in the Fourier space. Here, we have made a further assumption to the Green's

function that evanescent fields are not present in the total field. Substituting Eq. (3.3) into Eq. (3.1), applying the definition of the scattering potential $V(\boldsymbol{r})$ from Eq. (2.11), applying a lateral Fourier transform to the field, and simplifying we obtain

$$\hat{U}_s(\boldsymbol{\nu}, z|\boldsymbol{\nu}_l) = \frac{jk^2\sqrt{S(\boldsymbol{\nu}_l)}}{4\pi}\frac{e^{j2\pi\eta(\boldsymbol{\nu})z}}{\eta(\boldsymbol{\nu})}\int_{z'}\Delta\hat{\epsilon}(\boldsymbol{\nu}-\boldsymbol{\nu}_l, z')e^{j2\pi(\eta(\boldsymbol{\nu})-\eta(\boldsymbol{\nu}_l)z')}dz', \tag{3.4}$$

defining the scattered field spectra, where $\hat{\cdot}$ denotes the Fourier transform of a function and the permittivity $\Delta\epsilon(\boldsymbol{r}) = n(\boldsymbol{r})^2 - n_0^2$ has been introduced to succinctly represent the object's RI variations compared to the surrounding medium.

Compared to prior 3D QPI methods, IDT only applies the lateral integration over the object volume $\boldsymbol{r}'_\perp$ and maintains the axial coordinates in the real space. This choice is made to allow for reconstructing the 3D volume from IDT's 2D intensity measurements. Because IDT implements the first Born approximation, the model only accounts for the initial scattering event between the incident field and each point in the object volume with RI differing from the surrounding medium. This assumption means that all scattering events are *independent* of one another and provide separate scattered field contributions to the image plane. For IDT, this means that the 3D volume can be *axially discretized* into a set of slices that accumulate independent scattering signals into the final intensity image. For reconstruction, each slice of this volume can be independently reconstructed from 2D intensity measurements if the additional phase propagation can be accounted for to recover each slice. This innovation is the key factor allowing IDT to recover volumes of arbitrary size from intensity image stacks.

To implement this axial discretization from Eq. (3.4), we assume the object is discretized into a series of M slabs with thickness Δz such that the object's RI is

constant within each slab. We can describe this mathematically as

$$\sum_{m=1}^{M} \Delta\hat{\epsilon}(\boldsymbol{\nu}-\boldsymbol{\nu}_l, m) \int_{\frac{1}{2}(m-\Delta z)}^{\frac{1}{2}(m+\Delta z)} \Pi\Big(\frac{z'-m\Delta z}{\Delta z}\Big) e^{j2\pi(\eta(\boldsymbol{\nu})-\eta(\boldsymbol{\nu}_l)z')} dz', \tag{3.5}$$

where

$$\Pi(z') = \begin{cases} 1, & |z'| \leq \frac{1}{2} \\ 0, & \text{otherwise} \end{cases} \tag{3.6}$$

defines the rectangular function for the axial slab and the object's permittivity depends only on the slice m. Solving this integral, we obtain a discretized form of the axial integral

$$\text{sinc}(\Delta z(\eta(\boldsymbol{\nu})-\eta(\boldsymbol{\nu}_l))\Delta z \sum_{m=1}^{M} \Delta\hat{\epsilon}(\boldsymbol{\nu}-\boldsymbol{\nu}_l, m) e^{j2\pi(\eta(\boldsymbol{\nu})-\eta(\boldsymbol{\nu}_l)m\Delta z)}, \tag{3.7}$$

where the terms are similar to the continuous case of Eq. (3.4) save for the introduction of a sinc function and a scaling factor Δz in the coefficient. This term results from the axial discretization step of IDT and can artificially modify the field depending on the choice of the slab thickness and the difference of the object and incident field's axial spatial frequencies. To satisfy the assumption that the object's RI is constant in each slice, the axial thickness is assumed to match the microscope's Depth-of-Field (DOF=$\lambda(NA_0^2)^{-1}$) defining the system's axial resolution. Under transmission imaging conditions, the system's sampling of low axial spatial frequencies generally requires the system to have a large DOF [57]. This limitation, coupled with the low-valued, slowly varying values from the spatial frequency difference term, often result in this function being close to unity and the term being left out of the IDT model.

With the approximation of the sinc function as unity and the assumption that the system is set at the focal plane ($z = 0$), we obtain a simplified and axially discretized

term for the total field in the Fourier domain

$$\hat{U}(\boldsymbol{\nu}, 0|\boldsymbol{\nu}_l) = \sqrt{S(\boldsymbol{\nu}_l)}\delta(\boldsymbol{\nu} - \boldsymbol{\nu}_l) + j\frac{\Delta z k^2 \sqrt{S(\boldsymbol{\nu}_l)}}{4\pi\eta(\nu)} \sum_{m=1}^{M} \Delta\hat{\epsilon}(\boldsymbol{\nu} - \boldsymbol{\nu}_l, m) e^{j2\pi(\eta(\boldsymbol{\nu}) - \eta(\boldsymbol{\nu}_l) m\Delta z)}, \tag{3.8}$$

where the incident plane wave becomes a delta function translated depending on the illumination's lateral spatial frequency.

This resulting field definition is significant from its treatment of the scattered field discretization. The discretization includes both the object permittivity and an axially-dependent exponential term. The object's discretization allows us to easily account for its 3D volume, while the exponential term accounts for the additional phase accumulation experienced by the field from each slice reaching the detector and allows for the volumetric reconstruction when the model is inverted. This result is more readily apparent in the IDT model's TFs generated from the measured intensity discussed below.

Transfer Function Derivation

Given the total field in the IDT model in Eq. (3.8), the forward model relating the intensity image captured by the camera to the object's unknown parameters can now be developed. The approach follows the exact guidelines discussed in section 2.3.1, where the field is low-pass filtered by a pupil function $P(\boldsymbol{\nu})$ with bandlimit $\boldsymbol{\nu}_{max} = \mathrm{NA}_0\lambda^{-1}$ based on the microscope objective's NA, NA_0, and the modulus squared of the field is taken following Eq. (2.28). Applying this process to the field definition in the IDT model, we obtain the following intensity spectra terms for a given slice m

based on Eq. (2.29a)-(2.29d)

$$\hat{I}_{0,0}(\boldsymbol{\nu}|\boldsymbol{\nu}_l) = S(\boldsymbol{\nu}_l)|P(\boldsymbol{\nu})|^2\delta(\boldsymbol{\nu}) \tag{3.9a}$$

$$\hat{I}_{0,s}(\boldsymbol{\nu}, m|\boldsymbol{\nu}_l) = -jCS(\boldsymbol{\nu}_l)P(\boldsymbol{\nu}_l)P^*(\boldsymbol{\nu}-\boldsymbol{\nu}_l)\frac{e^{-j2\pi(\eta(\boldsymbol{\nu}-\boldsymbol{\nu}_l)-\eta(\boldsymbol{\nu}_l))m\Delta z}}{\eta(\boldsymbol{\nu}-\boldsymbol{\nu}_l)}\Delta\hat{\epsilon}^*(-\boldsymbol{\nu}, m), \tag{3.9b}$$

$$\hat{I}^*_{0,s}(\boldsymbol{\nu}, m|\boldsymbol{\nu}_l) = jCS(\boldsymbol{\nu}_l)P^*(\boldsymbol{\nu}_l)P(\boldsymbol{\nu}+\boldsymbol{\nu}_l)\frac{e^{j2\pi(\eta(\boldsymbol{\nu}+\boldsymbol{\nu}_l)-\eta(\boldsymbol{\nu}_l))m\Delta z}}{\eta(\boldsymbol{\nu}+\boldsymbol{\nu}_l)}\Delta\hat{\epsilon}(\boldsymbol{\nu}, m), \tag{3.9c}$$

where we have introduced the constant $C = \frac{\Delta z k^2}{4\pi}$ for clarity and omitted the final term (Eq. (2.29d)) since it is ignored in this model.

As mentioned in Section 2.3.1, the first term acts as a background signal centered at the origin of the Fourier plane and is typically subtracted from the intensity images. The second and third terms capture the scattered field behavior from the cross-interference of the incident and scattered fields and provide the linear relation between the object's RI or permittivity and the intensity spectra. Because of the IDT model's discretization, the total intensity consists of a summation of these cross terms for each slice in the entire object volume. This discretization allows for separate recovery from the intensity given a full forward model

To finalize the forward model from Eq. (3.9b) and (3.9c), we add an assumption that the object's permittivity is complex

$$\Delta\epsilon(\boldsymbol{r}) = \Delta\epsilon_{\mathrm{re}}(\boldsymbol{r}) + j\Delta\epsilon_{\mathrm{im}}(\boldsymbol{r}), \tag{3.10}$$

with $\Delta\epsilon_{\mathrm{re}}, \Delta\epsilon_{\mathrm{im}}$ existing in the real space. This assumption allows for the cross-interference terms to be separated based on the object's complex permittivity such that we can develop a forward model based on the background-subtracted intensity

$$\hat{I}^N(\boldsymbol{\nu}, 0|\boldsymbol{\nu}_l) = \sum_{m=1}^{M} H_{\mathrm{re}}(\boldsymbol{\nu}, m|\boldsymbol{\nu}_l)\Delta\hat{\epsilon}_{\mathrm{re}}(\boldsymbol{\nu}, m) + H_{\mathrm{im}}(\boldsymbol{\nu}, m|\boldsymbol{\nu}_l)\Delta\hat{\epsilon}_{\mathrm{im}}(\boldsymbol{\nu}, m) \tag{3.11}$$

where

$$H_{\mathrm{re}}(\boldsymbol{\nu}, m|\boldsymbol{\nu}_l) = jCS(\boldsymbol{\nu}_l)\Big\{P(\boldsymbol{\nu}_l)P^*(\boldsymbol{\nu}-\boldsymbol{\nu}_l)\frac{e^{-j[\eta(\boldsymbol{\nu}-\boldsymbol{\nu}_l)-\eta(\boldsymbol{\nu}_l)]m\Delta z}}{\eta(\boldsymbol{\nu}-\boldsymbol{\nu}_l)} - P^*(\boldsymbol{\nu}_l)P(\boldsymbol{\nu}+\boldsymbol{\nu}_i)\frac{e^{j[\eta(\boldsymbol{\nu}+\boldsymbol{\nu}_l)-\eta(\boldsymbol{\nu}_l)]m\Delta z}}{\eta(\boldsymbol{\nu}+\boldsymbol{\nu}_l)}\Big\}, \tag{3.12a}$$

$$H_{\mathrm{im}}(\boldsymbol{\nu}, m|\boldsymbol{\nu}_l) = -CS(\boldsymbol{\nu}_l)\Big\{P(\boldsymbol{\nu}_l)P^*(\boldsymbol{\nu}-\boldsymbol{\nu}_l)\frac{e^{-j[\eta(\boldsymbol{\nu}-\boldsymbol{\nu}_l)-\eta(\boldsymbol{\nu}_l)]m\Delta z}}{\eta(\boldsymbol{\nu}-\boldsymbol{\nu}_l)} + P^*(\boldsymbol{\nu}_l)P(\boldsymbol{\nu}+\boldsymbol{\nu}_l)\frac{e^{j[\eta(\boldsymbol{\nu}+\boldsymbol{\nu}_l)-\eta(\boldsymbol{\nu}_l)]m\Delta z}}{\eta(\boldsymbol{\nu}+\boldsymbol{\nu}_l)}\Big\}, \tag{3.12b}$$

define the real and imaginary TFs of the IDT forward model, respectively. Here, the superscript N is used to denote the background-subtracted intensity image.

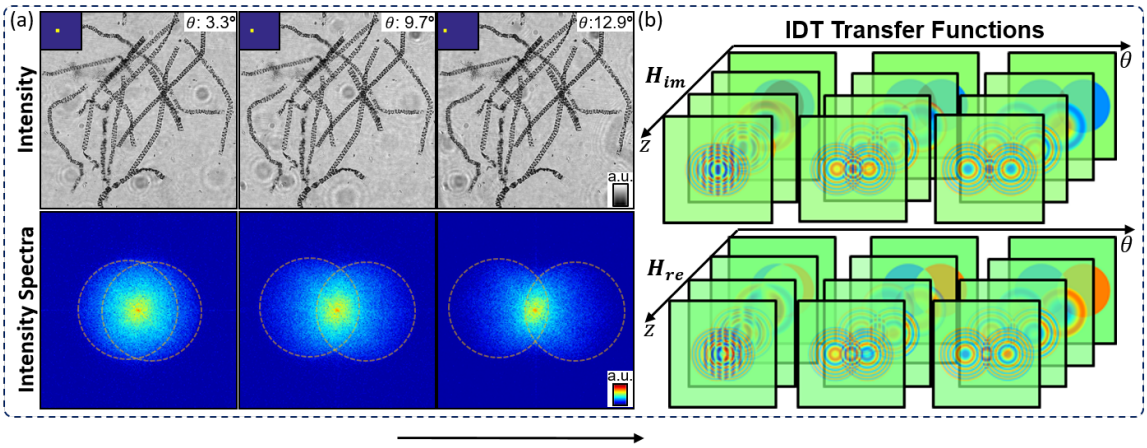

Figure 3·1: Example intensity images, spectra, and TFs for IDT. (a) Example intensity images of *spirogyra* algae and their intensity spectra under increasingly oblique illuminations highlighting the pupil translation with angle. (b) Real and imaginary TFs for different axial positions and illumination angles. Comparison between (a) and (b) shows the model captures the pupil translation seen in experimental data and the model includes defocus correction enabling 3D reconstruction. Figure adapted from [8].

These TF terms highlight three critical features of IDT and can be seen in Fig. 3·1 with comparisons to experimental data. First, the translated pupil functions $P(\boldsymbol{\nu}\pm\boldsymbol{\nu}_i)$ result from using oblique illumination on the sample as discussed in Section 2.3.1 and result in an enhancement of the object's bandwidth following synthetic aperture prin-

ciples. This enhancement allows the encoding of the object's bandwidth up to the incoherent resolution limit, allowing the final recovered object to have a maximum resolution of $2NA_0\lambda^{-1}$. Second, the TFs' exponential terms account for the phase accumulation as the fields from different slices propagate to the focal plane. This is intuitively understood from evaluating the axial spatial frequency term under paraxial imaging conditions as $\eta(\boldsymbol{\nu}-\boldsymbol{\nu}_l) \approx \lambda(\boldsymbol{\nu}_l \cdot \boldsymbol{\nu} - |\boldsymbol{\nu}|^2/2)$. At small illumination angles, this exponential term accounts for object translation as a function of axial position akin to light field techniques [66] with diffraction effects from the second term. This term accounts for the encoding of the object's complex permittivity from different axial slices and allows for its correction when inverting the model. Finally, the real TF recovering the object's phase information exhibits asymmetric behavior aligning with observations seen in differential phase contrast [62]. Under low-angle illumination, this asymmetric behavior generates significant overlap between Eq. (3.9b) and Eq. (3.9c) that loses phase information due to the twin image problem. This indicates that IDT works best when using illumination angles with minimal overlap. These factors from the forward model enable IDT to account for a 3D object's phase and absorption information from only 2D intensity images and makes it an easily implementable imaging modality for 3D QPI.

3.3 Object Reconstruction

With the above forward model, an adequate reconstruction process is required to provide efficient recovery of the object and maintain computational simplicity for easy adoption of IDT in the biological imaging community. In the initial publication on IDT [8], Tikhonov deconvolution was used as it provides a closed-form, non-iterative reconstruction method for recovering the object. As mentioned in the prior chapter, this deconvolution approach is common in 3D QPI because of its simplicity and

efficient reconstruction capabilities for linear models.

For the IDT deconvolution problem, the inverse problem is formulated as a minimization problem with regularization on the energy of the object's complex permittivity

$$\underset{\Delta\hat{\epsilon}_{\text{re}},\Delta\hat{\epsilon}_{\text{im}}}{\operatorname{argmin}} \sum_{l=1}^{L} \left|\left|\hat{I}_l^N - (H_{\text{im},l}\Delta\hat{\epsilon}_{\text{im}} + H_{\text{re},l}\Delta\hat{\epsilon}_{\text{re}})\right|\right|_2^2 + \tau_{\text{im}}\left|\left|\Delta\hat{\epsilon}_{\text{im}}\right|\right|_2^2 + \tau_{\text{re}}\left|\left|\Delta\hat{\epsilon}_{\text{re}}\right|\right|_2^2, \quad (3.13)$$

solving for both terms in the object's complex permittivity where L defines the total number of intensity images used in the measurement, $\hat{I}_l^N$ is the l^{th} normalized, background-subtracted intensity image from the measurement, and τ_{re}, τ_{im} denote the manually selected regularization weights on the energy. We note here that the notation is simplified for readability.

The first term in the minimization provides the data fidelity term estimating the error between the normalized, background-subtracted intensity of each image and the predicted intensity from the IDT model. While this term is differentiable allowing for a minimum to be solved, the ill-posed nature of this model and QPI models in general requires the addition of regularization to prevent the object from being lost to noise [59]. As such, the $L2$ norm is added for both the object's real and imaginary complex permittivity as it is a differentiable function allowing for the minimization problem to provide a closed-form solution. Applying the gradient and solving for the closed-form solution obtains the following term

$$\Delta\hat{\epsilon}_{\text{re}}(\boldsymbol{\nu}, m) = \frac{1}{T}\left[\Big(\sum_{l=1}^{L}\left|H_{\text{im},l}\right|^2 + \tau_{\text{im}}\Big)\Big(\sum_{l=1}^{L} H_{\text{re},l}^{*}\hat{I}_l^N\Big) - \Big(\sum_{l=1}^{L} H_{\text{re},l}^{*}H_{\text{im},l}\Big)\Big(\sum_{l=1}^{L} H_{\text{im},l}^{*}\hat{I}_l^N\Big)\right] \quad (3.14a)$$

$$\Delta\hat{\epsilon}_{\text{im}}(\boldsymbol{\nu}, m) = \frac{1}{T}\left[\Big(\sum_{l=1}^{L}\left|H_{\text{re},l}\right|^2 + \tau_{\text{re}}\Big)\Big(\sum_{l=1}^{L} H_{\text{im},l}^{*}\hat{I}_l^N\Big) - \Big(\sum_{l=1}^{L} H_{\text{im},l}^{*}H_{\text{re},l}\Big)\Big(\sum_{l=1}^{L} H_{\text{re},l}^{*}\hat{I}_l^N\Big)\right] \quad (3.14b)$$

where

$$T = \Big(\sum_{l=1}^{L} |H_{\mathrm{re},l}|^2 + \tau_{\mathrm{re}}\Big)\Big(\sum_{l=1}^{L} |H_{\mathrm{im},l}|^2 + \tau_{\mathrm{im}}\Big) - \Big(\sum_{l=1}^{L} H_{\mathrm{re},l} H^*_{\mathrm{im},l}\Big)\Big(\sum_{l=1}^{L} H^*_{\mathrm{re},l} H_{\mathrm{im},l}\Big). \quad (3.15)$$

The simple implementation of this inverse problem provides a number of benefits for providing rapid reconstructions of arbitrary object size. First, the reconstruction approach requires only two tunable parameters, τ_{re} and τ_{im}, to be manually determined for the reconstruction process compared to more advanced optimization techniques [72]. From the related Wiener deconvolution approach [59], the optimal value for these tunable parameters is the inverse of the Signal-to-Noise Ratio (SNR) of the imaging system. While this value is unknown and must be found for each experimental measurement, the use of an imaging system with relatively stable noise characteristics coupled with IDT's limitation to weakly scattering objects places limits the potential SNR range and empirically allows for a short scan range to be used to find the optimal regularization weights. The fast, single-shot reconstruction of this deconvolution method also allows the optimal weight to be quickly determined. Second, this minimization is done in a slice-wise manner to independently reconstruct each object slice. While this approach requires multiple reconstruction steps to get a 3D volume, the recovery of individual slices allows for the user to reconstruct different amounts of the object volume depending on their requirements. For evaluating thin objects, this reconstruction method becomes highly efficient and recover only the few required object slices. For large volumes, the user can reconstruct as many slices as necessary with this model to capture the entire volume. These factors allow the IDT algorithm to efficiently recover the necessary volumetric phase information from the object and can be implemented with minimal computing resources, making it advantageous for biological research facilities where powerful computational tools may not be readily available. Coupled with the simple optical hardware needed for IDT

discussed below, this technology has many advantages posing it to be easily adopted for biological research.

3.4 Imaging System

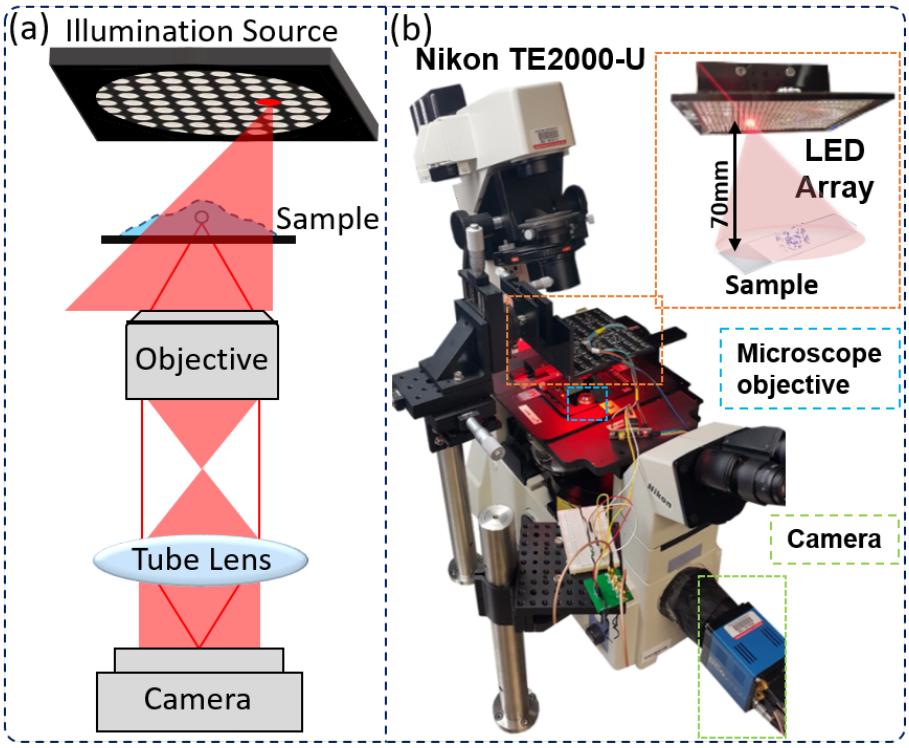

Figure 3·2: Schematic and implementation of the IDT setup. (a) Schematic showing the basic elements required for a transmission-mode IDT setup. At its simplest, the setup requires a programmable illumination source and 4F lens relay collecting field onto a camera. (b) The IDT setup used in [8]. The setup utilized a commercial Nikon TE2000-U microscope equipped with a programmable rectangular LED array, various Nikon objectives, and a PCO camera detailed below. Figure adapted from [8].

The simplicity of the IDT imaging setup is one of its key benefits for providing easy access to 3D QPI. The basic elements required for IDT consist of a controllable light source providing diverse illuminations on the sample, a sample holder for the object of interest, and a 4F lens configuration relaying the total field to the camera

image plane (Fig. 3·2(a)). The majority of this system can be obtained commercially, as the collection side of this setup is satisfied easily with a transmission-mode brightfield microscope. The primary element differing from this standard microscope is the source which must satisfy constraints from both the model and experimental imaging conditions. Specifically, this source must provide: 1) wide-field plane-wave illumination with 2) monochromatic or quasi-monochromatic illumination from 3) known illumination angles at 4) sufficiently fast acquisition speeds to prevent motion artifacts in the measurement of live samples.

A number of source designs already exist satisfying such illumination conditions and have been used in various QPI setups. Commercially available ODT systems utilize digital micromirror devices (DMD) coupled with collimated laser illumination for rapid imaging of samples under plane wave illumination [26, 73], and a number of intensity-only QPI systems have shown utility with galvo or rapidly scanning mirrors with various sources [41, 74]. These sources can provide precise plane wave illuminations to the sample with controlled angles up to video-rate imaging capabilities depending on the implementation. The main downside with such techniques is that their higher costs and complexity can act as a barrier from use in a system otherwise needing simple hardware.

Instead of these source designs, the optimal illumination source for IDT has become the LED array. These sources have become popular in microscopy with the development of Fourier ptychography [38] from their low cost and easy implementation into a commercial microscope. LED sources satisfy the model constraints of IDT when placed in the far field compared to the object plane. While the LED exhibits a lambertian source profile with illumination matching better aligned with spherical waves [69], positioning the source far away from the sample results in low-NA, approximately plane wave illumination described by the Van-Cittert Zernike theorem [44].

Empirically, this condition has shown to be valid in IDT even with 37-40mm source-object separation enabling relatively compact system designs [9]. These sources also emit small wavelength range with coherence lengths approximately around 50μm and can be estimated as quasi-monochromatic sources. These commercial arrays are developed in planar, circular, or domed geometries that have well-regulated spacing making the initial prediction of their illumination angles easy to determine [69, 74]. Finally, their programmable nature and the rise in faster communication protocols allows IDT setups to acquire data at camera-limited acquisition speeds [9]. These factors make LED arrays ideal for IDT, and the existing literature on IDT has shown that commercial microscopes with off-the-shelf LED arrays are commonly used [8, 9, 71, 75]. Recent work has even shown that simple 3D-printed microscope setups for classroom use can implement this technique [76].

In the first IDT implementation by ling et al. [8], the LED array microscope in Fig. 3·2(b) was used for the proof-of-concept measurements. This setup utilized the Nikon TE 2000-U microscope for the collection optics equipped with a customized rectangular planar LED array source ($\lambda = 632nm$) for the programmable illumination source. Compared to later IDT setups, this design used a large source-sample separation of 79mm allowing for closer plane-wave illuminations and hundreds of LEDs to provide oblique illuminations within the microscope objective's passband. This customized source was controlled using a microcontroller that coordinated measurements with the sCMOS (PCO Edge 5.5) camera acquiring the intensity measurements. The 4F collection path passing the total field to this camera consisted of a 200mm tube lens with various Nikon microscope objectives under low NA (0.25NA, 10×, MRL00102) and high NA (0.65 NA, 40×,MRL00402) conditions. Given the differences in collection NA, these configurations utilized up to 89 and 697 LEDs from this planar array, respectively, for evaluating the sample of interest. We review the results from this

setup in the next section.

3.5 Results

When developing a new physics model in 3D QPI, the model must first be validated to confirm its reconstruction results are trustworthy. Despite being derived from fundamental scattering models, the axial discretization assumption in IDT or other elements of the model could introduce error causing incorrect structures or RI to be recovered with the 3D QPI technique. To alleviate these concerns, Ling et al. validated the IDT model against standardized phase imaging methods as well as simulated and experimental measurements of a manufactured sample to determine its reconstruction capabilities in recovering 3D phase structures and RI values, respectively.

3.5.1 Validation against Phase Contrast Microscopy

Before evaluating unknown specimens and making claims regarding their phase and 3D structure, Ling et al. first validated the IDT model against the phase constrast (PhC) microscope imaging modality [77]. Briefly, this imaging approach provides qualitative visualization of a sample's phase features at the focal plane by illuminating the sample with an annular illumination ring and capturing the light with a custom microscope objective. This objective introduces a 90° phase shift to this incident illumination with some attenuation to maximize the scattered field contrast compared to the background illumination and generate interference from the object's phase features. By scanning through a 3D sample, this method provides qualitative recovery of the object's 3D phase features. This measurement provides an adequate reference to evaluate whether the recovered structures with IDT are real within the sample and the model is valid.

The results from comparing IDT with PhC on clusters of formaldehyde-fixed MCF-

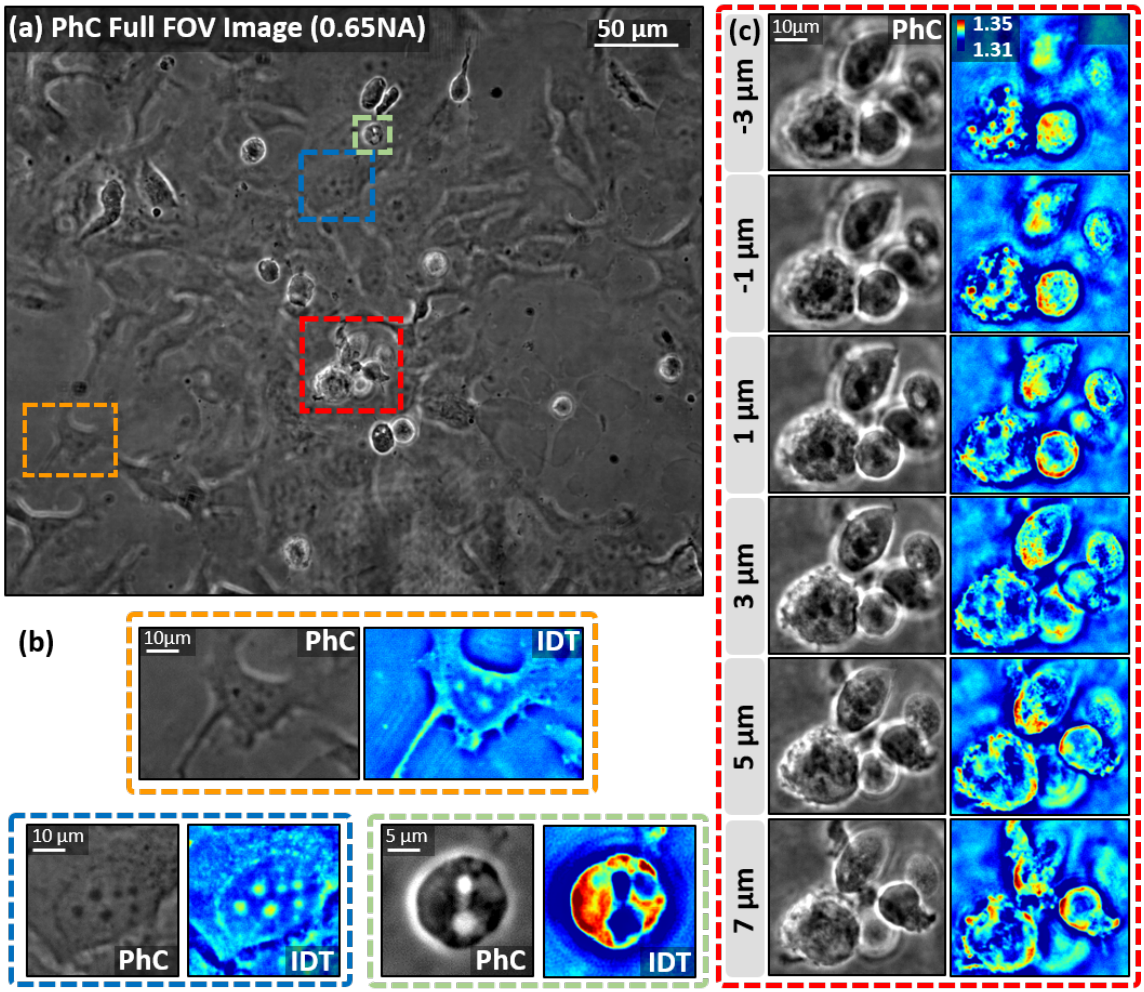

Figure 3·3: Comparison of IDT and PhC on MCF-7 breast cancer cells. (a) The full PhC image acquired at 40× magnification with a 0.65NA objective. (b) Outsets comparing PhC with IDT reconstructions on thin, adhered cells and thick, spherical cancer cells floating in the medium. The similar features show IDT recovers the object regardless of thickness. (c) Through-focus comparison on spherical cancer cells between PhC and IDT. The similar resolution and feature reconstruction highlights that IDT's model works in recovering phase structures across different axial planes. Figure adapted from [8].

7 cancer cells are replicated from [8] in Fig. 3·3. A collection NA of 0.65 was used for both IDT and PhC to provide equivalent resolution of the sample for direct comparison. The structures have opposing sign between PhC and IDT, as the contrast in

PhC exhibits an inverse relationship with stronger, higher scattering features while IDT contrast shows direct relationships with the same features. Fig. 3·3(a) shows the entire PhC FOV while (b) and (c) compare the IDT and PhC reconstructions of different flat and spherical cells within the sample.

Across all observed axial planes, the PhC features recovered from scanning through the sample match the IDT reconstructed phase features at the same depth. Because IDT implements a deconvolution setp, the features recovered at a given axial slice also exhibit better depth sectioning and improved clarity compared to the PhC results. This result is echoed for both the flat and spherical cells within the sample, indicating the IDT model does not exhibit object-dependent reconstruction problems. These results validated that the slice-wise reconstruction method for IDT correctly recovers the sample's phase structures from 2D intensity images and provides trustworthy feature recovery.

3.5.2 Validation of RI recovery against experimental, simulated objects

Validating the IDT model's RI recovery, or any 3D QPI setup, experimentally is a difficult task. The majority of manufactured resolution targets and samples used for characterizing a setup are absorption-based and provide no known phase information, making experimental validations of phase systems more difficult. Furthermore, the samples must also produce weak scattering to match the model assumptions of the many previously discussed QPI techniques and requires careful RI matching. As a result, few phase calibration samples existed with manufactured 3D phase objects being developed only recently [78]. Here, Ling et al. used both simulated and experimentally measured strongly scattering phase resolution targets to provide some characterization of the technique's RI recovery and its limitations.

The simulated and experimentally measured phase sample can be seen in Fig. 3·4,

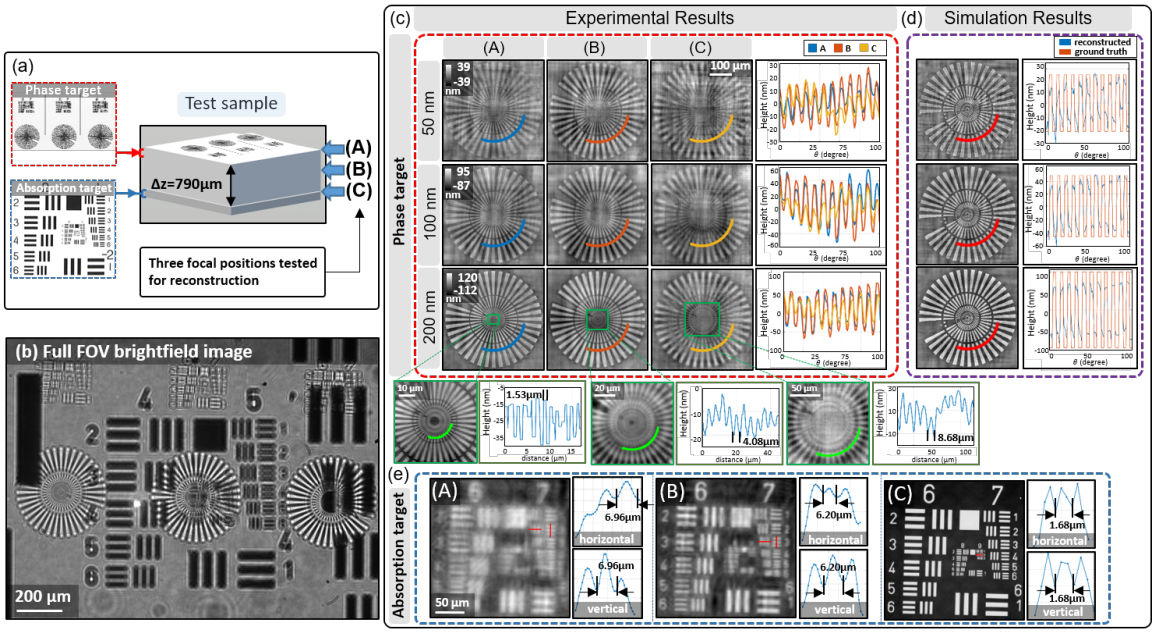

Figure 3·4: Validation of IDT reconstruction on a manufactured and simulated strongly scattering object. (a)Schematic showing the layered phase and absorption target's design and the microscope's focal planes during the measurement. (b) An example brightfield image showing the full FOV of the complex target. (c) IDT reconstructions of the 50nm, 100nm, and 200nm phase star targets from three different microscope focal positions with corresponding cross-section comparisons. Resolution loss is observed in the reconstructions due to LED misalignment errors, and the multiply-scattering nature of this target causes height underestimations due to IDT's linear model. (d) Illustration of IDT's underestimation of strongly scattering objects in simulated star target reconstructions. (e) absorption target reconstructions from three focal planes shows resolution loss when the object is reconstructed from large defocus positions. Figure adapted from [8].

reprinted from [8], along with the corresponding reconstructions from IDT. The object consisted of a layered absorption (58-198, Edmund Optics) and phase resolution target (QPT, Benchmark Technologies) separated 790μm axially to provide a 3D object with two slices of interest (Fig. 3·4(a),(b)). The phase target consisted of glass $n_g = 1.52$ in air $n_0 = 1$ with raised star and USAF resolution targets on an otherwise flat surface. Three of these raised phase objects with sample heights of 50nm, 100nm, and 200nm

were imaged with the IDT setup's 0.25NA, 10× objective and 89 illuminations. For each object type, measurements at three different focal planes were also acquired to evaluate the consistency of IDT's reconstruction when recovering the same object from different depth positions. The objects were then reconstructed with IDT at each target plane with a large slice thickness ($\Delta z = 10\mu m$) approximately matching the system's DOF. For confirming the experimental results, simulations of the phase target were generated and reconstructed to validate IDT's behavior with a known ground truth object.

The results in reconstructing this sample in experiment and simulation highlight the capabilities and limitations of the IDT modality and linear model. The main difficulty in evaluating this object is the large RI mismatch between air and glass ($\Delta n = 0.52$). This large change in density between the sample and medium means the object will be multiply-scattering and generate non-negligible nonlinear scattering (Eq. (2.29d)) invalidating IDT's linear model assumptions. Because the IDT model cannot account for this additional scattering, this nonlinearity adds object-dependent noise reducing the recovered RI values with the IDT model. This is observable in Fig. 3·4(c) and (d), where the recovered object height obtained from converting the IDT model's permittivity to height following $\tilde{h}(\boldsymbol{r}) = (\Delta\tilde{\epsilon}(\boldsymbol{r})\Delta z)/(n_g^2 - 1)$, where $\tilde{\epsilon}(\boldsymbol{r})$ denotes the reconstruction's recovered permittivity contrast, becomes underestimated compared to the known heights of the experimental and simulated star targets. The IDT model does shows adequate performance for the 50nm tall object where it short height allows for the object to generate shorter phase delays and more closely match the weakly scattering condition. The underestimation does not significantly affect the recovered structure, however, visible in the image and profiles of Fig. 3·4(c)-(d). The structure only shows degradation when the object is reconstructed from different defocus planes (Fig. 3·4(c)) which is attributed to the presence of small angle

miscalibrations between the true and estimated illumination angles. This behavior is echoed in the recovery of the absorption target shown in Fig. 3·4(e). Overall, these results indicate that the IDT model works to recover the RI so long as the object is known to occupy the weakly scattering imaging assumptions made in the IDT model.

3.5.3 Application to Biological Sample

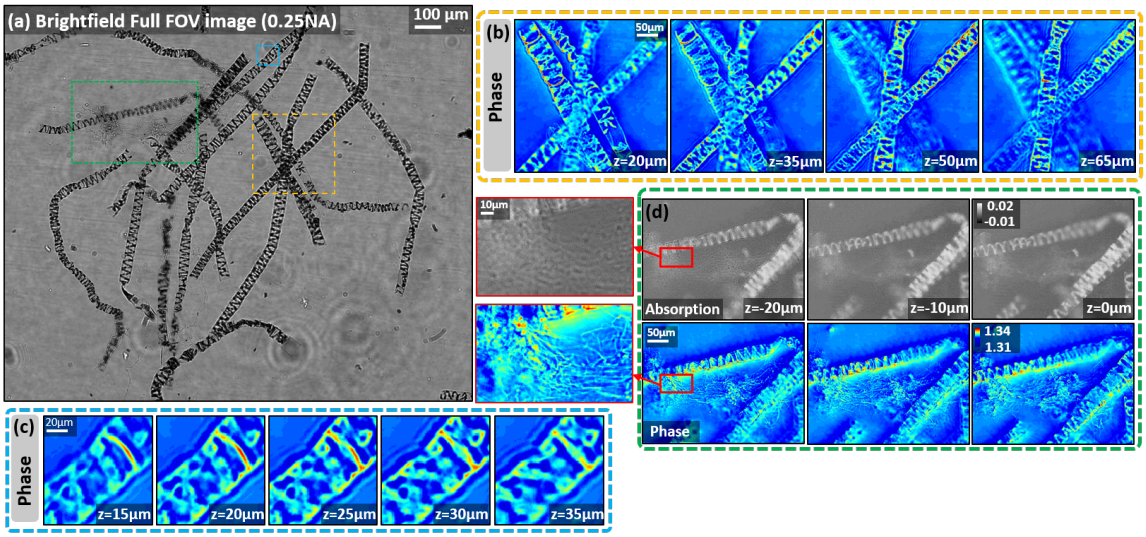

Figure 3·5: IDT reconstructions of *spirogyra* samples. (a)A full FOV brightfield image showing the algae distribution in the sample with outsets highlighted from (b)-(d). (b) Example IDT reconstructions of *spirogyra* across multiple axial planes highlighting the different phase features recovered at each plane. (c) Zoom-in algae region showing the reconstruction of different helical structures along z. (d) Absorption and phase reconstructions showing that unstained filament structures invisible to absorption-based imaging techniques become resolved with IDT. Figure adapted from [8].

Following validation, the IDT setup was applied to a stained and fixed biological *spirogya* sample (S68786, Fisher Scientific) to evaluate the 3D features recoverable with IDT from a specimen (Fig. 3·5). The sample was evaluated with the IDT setup's 0.25NA, 10× objective and 89 LED illuminations in the same configuration as the manufactured sample imaging conditions. The slice thickness was set at 5μm to

upsample the object volume and reconstructed over a 220μm volume to visualize large regions of the object. The summed brightfield image of the sample from all LEDs is shown in Fig. 3·5(a) with reconstructions of the object's complex permittivity at different axial planes labeled as phase and absorption, respectively, in Fig. 3·5(b)-(d).

The reconstructions of the sample highlight the impressive 3D QPI capabilities of IDT. In Fig. 3·5(b) and (c), the IDT model recovers different sections of the *spirogyra* algae's helical structure as the object is distributed through the 3D volume. Comparing the absorption and phase reconstructions, IDT shows that various filaments previously unobserved in the brightfield measurements become visible from IDT's recovery of phase objects. For biological samples where such features are typically invisible with absorption-based imaging, the IDT model's result is very promising for recovering purely phase features with IDT from biological samples with high sensitivity.

3.6 Discussion and limitations of IDT

This initial work from Ling et al. [8] presented a proof-of-concept evaluation of the highly promising 3D QPI modality of IDT. Ling's worked provided the derivation of the forward model enabling slice-wise object reconstructions of an object's complex RI distribution along with a single-shot inverse problem solution for rapid reconstruction of the object volume. Using two different objectives, the work validated the phase structures recovered with this technique compared to PhC microscopy and its validity range for recovering the RI of objects in simulated and experimental conditions. Finally, this work showed an example application of this technology to interesting biological samples with unique 3D structures and features visible only with 3D QPI. These results provided a strong baseline of the potential for IDT in the 3D QPI realm for biological imaging.

Despite the strengths shown for IDT, a number of limitations exist for the initial implementation of this modality. One of the main limitations of this technology is its limited acquisition speed. Despite some preliminary illumination design testing detailed in [8], this IDT implementation utilizes hundreds of illuminations for a single acquisition. Given the system's camera-limited acquisition speed of 50Hz, the setup has slow acquisition rates around 0.1Hz for higher magnification objectives due to the large number of LEDs in the setup's back focal plane. This limitation requires IDT to evaluate only fixed biological samples and removes the benefit of QPI in evaluating unperturbed, unlabeled biological specimens. As a result, enhancing the system's acquisition speed is a critical factor to improving the limitations of this 3D QPI modality to become an easily adoptable biological imaging tool.

A second main limitation of this technique is its linear model. As shown in Fig. 3·4, this technique significantly underestimates the object's RI when the sample exhibits multiple-scattering behavior. This limitation poses difficulties when evaluating unknown biological samples as the sample's scattering behavior will be unknown and the linear model could provide incorrect results. Multiple-scattering models can be adopted in both interferometric and intensity-based 3D QPI to recover multiple-scattering signals [42, 31, 43, 79, 41], but the added computational complexity of such methods drastically increases the reconstruction computation time. Furthermore, these models can no longer assume independent scattering behavior from the object's axial slices and must reconstruct the entire volume simultaneously. When pushing to live sample imaging, these computational constraints limit the ability to quickly evaluate dynamic living samples in 3D. The added complexity also provides another barrier to easy adoption of 3D QPI in biological research fields. Thus, there is a need for an efficient method for inverting the scattered signal from multiply-scattering complex biological specimens.

Finally, one of the remaining limitations of IDT is its axial resolution. As specified in Section 3.2, the axial resolution of this system is limited by the microscope objective DOF. The objective's DOF is limited based on the transmission imaging geometry of the setup, which only captures the slowly varying axial spatial frequencies from the object [57, 44]. For a brightfield transmission-mode system capturing the object's bandwidth up to the incoherent resolution limit, the best axial resolution possible is DOF=$\lambda(\mathrm{NA}_0^2)^{-1}$. Short visible wavelengths and high NA objectives are therefore required to achieve high axial resolution, but this requires a sacrifice of the total FOV due to the space-bandwidth product limit. With high axial resolution, IDT could improve its resolution of 3D subcellular structures such as the endoplasmic reticulum, the nucleus, and mitochondria to help evaluate their morphology for biological research applications. This limitation reveals a need for high axial resolution IDT.

In the following chapters, we introduce solutions to each of these limitations through the work done in this thesis. Chapters 3 and 4 discuss solutions enabling high-speed, high volume-rate IDT. Chapters 5 and 6 provide a deep learning approach and new reflection-mode linear model for recovering multiple-scattering samples and high axial resolution reconstructions, respectively. These solutions show that IDT can be significantly enhanced beyond this initial work to provide rapid 3D QPI of complex biological samples in an easily implementable hardware package.

Chapter 4

High-throughput quantitative phase imaging with multiplexed intensity diffraction tomography

4.1 Introduction

The prior chapter reviewed the initial IDT publication by Ling et al. providing a proof of concept of the IDT model and imaging setup for 3D QPI [8]. In this implementation, all LEDs within the microscope objective passband were treated as equally important, and the object of interest was reconstructed from hundreds of sequential illuminations of the sample. This illumination design provided high quality reconstructions but left the question on whether all such illuminations were required unanswered. While additional tests were done evaluating some reconstructions with fewer illuminations in the original work [8], this investigation was cursory and did not find optimal illumination designs for IDT. This naïve illumination scheme is adequate for fixed samples such as the *spirogyra* sample evaluated in the work, but the large dataset size and long acquisition times prevent this IDT implementation from evaluating living biological samples. Since QPI operates without needing sample augmentations, this limiting factor is a severe roadblock for IDT from being used for

studying native biological samples. Here, we investigate a solution to this speed bottleneck by optimizing the illumination design to provide high volume-rate IDT with model-based multiplexed illumination.

The work discussed in this chapter builds off a wealth of work already investigating designed computational illumination schemes in CI. Optimized illumination has been used in 2D QPI for Fourier Ptychography [68, 80, 81] and Differential Phase Contrast (DPC) techniques, among others [63, 82]. Existing techniques utilize nonlinear optimization [68, 80], learned illumination designs [63, 81, 82], and multi-spectral systems [64, 83] to pattern the illumination for maximized object information in reduced dataset sizes. Significant work has also incorporated model-based design in DPC to enhance object Fourier coverage through non-uniform illumination patterning [62, 84, 85, 86]. These various approaches optimize 2D object information recovery instead of volumetric objects and may not translate to IDT and other tomographic QPI approaches. The approach used here develops illumination design constraints based on IDT's physical model for achieving high-speed IDT with minimal reconstruction artifacts. This method maintains the system's resolution, complex object recovery, and volumetric reconstruction capabilities in a design adoptable for any microscope with a programmable source array.

This chapter presents the multiplexed Intensity Diffraction Tomography (mIDT) illumination scheme for real-time biological sample imaging (Fig. 4·1). This mIDT implementation provides a software-only approach for high volume-rate imaging based on the linear IDT model in [87]. This approach optimizes the illumination by balancing the multiplexed system's Fourier weight distribution, akin to minimizing the condition number of the underlying system TF. mIDT utilizes illumination downsampling, Poisson disk random sampling [88], and geometric constraints to achieve hardware-limited 4Hz acquisition rates with minimal reductions in reconstruction

quality (Fig. 4·1(b)-(d)). For directly comparing our multiplexed designs with conventional IDT without introducing significant human error, we derive a semi-automated recipe for selecting the Tikhonov regularization parameter based on the mIDT scheme's image and multiplexed illumination numbers. Using low multiplexing, highly downsampled mIDT schemes, we recover quantitative volumetric reconstructions of living *Caenorhabditis elegans* (*C. elegans*) worms (Fig. 4·1(e)), *C. elegans* embryos, and epithelial buccal cells. Our mIDT scheme provides an illumination design framework applicable to any diverse illumination source enabling high-speed acquisition with minimal loss to reconstruction quality for dynamic sample imaging.

4.2 Theory

4.2.1 mIDT forward model

We consider the derived IDT linear model in Chapter 3 and [8] when designing our illumination patterns. From Section 3.2, the normalized, background subtracted intensity spectra for a single-illumination IDT measurement can be described as a discrete summation of the object's complex permittivity $\Delta\epsilon_{\text{re}}$, $\Delta\epsilon_{\text{im}}$ from each axial slice of the object multiplied by the IDT real and imaginary TFs, H_{re} and H_{im}, in the Fourier space (Eq. (3.11)). When considering different illumination angles from the IDT images, the only variables dependent upon this angle are IDT's TFs. These TFs account for the pupil function translation and changes to the axial spatial frequency coverage defining the section of the object's bandwidth being encoded onto the intensity image. For multiplexing illuminations to provide high-speed IDT, we focus on how these TFs combine to optimally capture as much of this bandwidth information in as few images as possible.

When multiplexing, we assume each LED in our array (Fig. 4·1(a)-(b)) is monochromatic and mutually incoherent. For L total mIDT images under this assumption, the

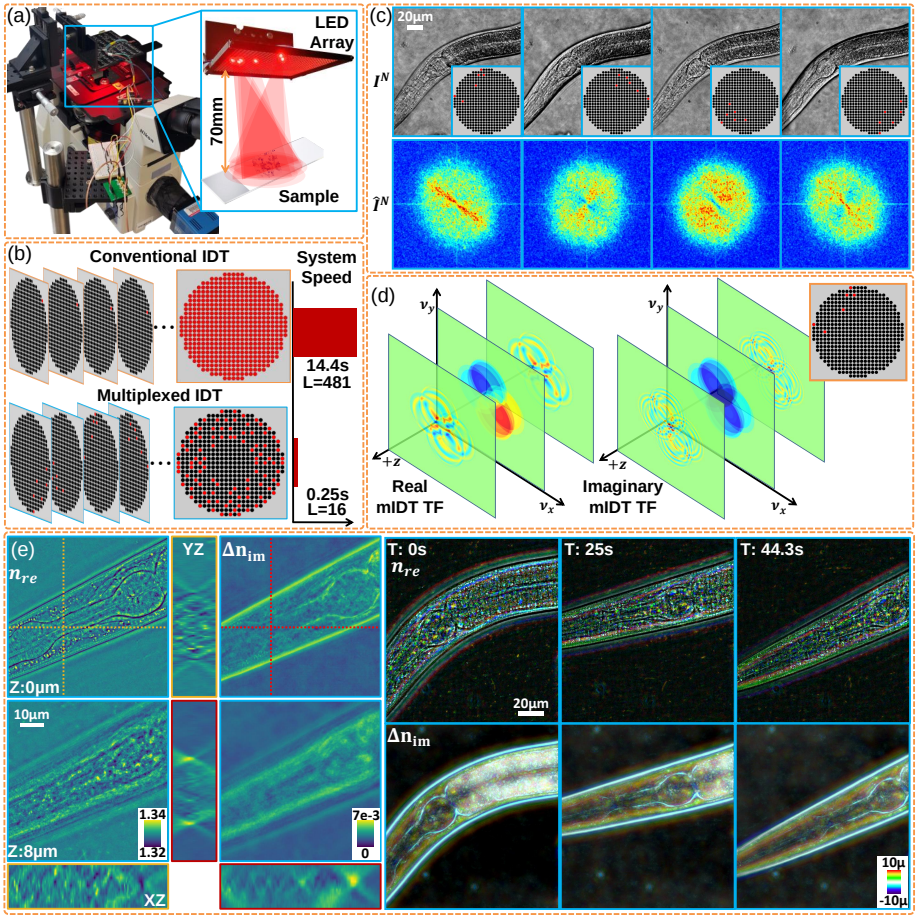

Figure 4·1: (a) mIDT imaging system composed of an inverted microscope equipped with an LED array. (b) mIDT reduces both acquisition speeds and image numbers. (c) Example mIDT ($N_s = 6$,$L = 16$) intensity images (top) and spectra (bottom) for a live *C. elegans* worm . (d) Example mIDT real and imaginary TFs across multiple depths. (e) Real and imaginary refractive index reconstructions and depth-coded projections of live *C. elegans* worm volumetric reconstructions, demonstrating minimal motion artifacts across a 1-minute acquisition period.

l^{th} mIDT measurement will simply contain the linear superposition of simultaneously illuminated single-LED intensities indexed by $s \in \{1, 2, \cdots, N_s^l\}$, where N_s^l denotes the number of multiplexed LEDs in the l^{th} image. We can represent the normalized,

background-subtracted intensity spectra as

$$\hat{I}_l(\boldsymbol{\nu}|N_s^l) = \sum_{m=1}^{M} \Big\{ H_{\mathrm{re}}(\boldsymbol{\nu}, m|N_s^l)\Delta\hat{\epsilon}_{\mathrm{re}}(\boldsymbol{\nu}, m) + H_{\mathrm{im}}(\boldsymbol{u}, m|N_s^l)\Delta\hat{\epsilon}_{\mathrm{im}}(\boldsymbol{\nu}, m) \Big\}. \tag{4.1}$$

where the multiplexed TF is the sum of the corresponding single-LED TFs due to linearity:

$$H_{\mathrm{re(im)}}(\boldsymbol{\nu}, m|N_s^l) = \sum_{s=1}^{N_s^l} H_{\mathrm{re(im)}}(\boldsymbol{\nu}, m|\boldsymbol{\nu}_s). \tag{4.2}$$

We note the illumination spatial frequency $\boldsymbol{\nu}_s$ uses the subscript s instead of l from Chapter 3 to account for multiple illumination angles encoded in a single intensity image.

This summation is critical due to the TF characteristics described by Eqs. (3.12a) and (3.12b). As discussed in Section 3.2, the TFs from IDT account for the resolution enhancement in the object reconstruction following synthetic aperture principles, the additional phase accumulation from defocused object features allowing for 3D reconstruction, and the potential for phase information loss from overlap between the pupil function and its complex conjugate. Examples of these features can be observed in the generated TFs of Fig. 4·1(c)-(d). Without considering these factors, the TF overlap from excessive multiplexing or improperly chosen LEDs can result in poor resolution, phase feature loss (Fig. 4·2(b), [87]), and low coherence limiting 3D recovery. This overlap is unavoidable when multiplexing, so the illumination designs across the full mIDT measurement must be jointly considered to maintain the object's information.

4.2.2 mIDT forward model in matrix form

We consider the full mIDT system using matrix notation to help analyze the optimal illumination design for mIDT. For an $N \times N \times M$ object recovered using L $N \times N$-pixel images with N_s unique multiplexed LEDs for each image, the forward model is

represented as

$$\hat{\mathbf{I}} = \mathbf{H}\boldsymbol{\Delta}\hat{\boldsymbol{\epsilon}} \tag{4.3}$$

where $\hat{\mathbf{I}}$ is an $LN^2 \times 1$ vector containing all L intensity spectra, $\boldsymbol{\Delta}\hat{\boldsymbol{\epsilon}}$ is a $2MN^2 \times 1$ vector of the object's complex permittivity contrast, and $\mathbf{H}$ is the system TF composed of an $LN^2 \times 2MN^2$ matrix with all real and imaginary multiplexed TFs, respectively. This system TF has the form

$$\mathbf{H} = \begin{bmatrix} H_{\mathrm{re}}[1, N_s^1] & \dots & H_{\mathrm{re}}[M, N_s^1] & H_{\mathrm{im}}[1, N_s^1] & \dots & H_{\mathrm{im}}[M, N_s^1] \\ \vdots & \ddots & \vdots & \vdots & \ddots & \vdots \\ H_{\mathrm{re}}[1, N_s^L] & \dots & H_{\mathrm{re}}[M, N_s^L] & H_{\mathrm{im}}[1, N_s^L] & \dots & H_{\mathrm{im}}[M, N_s^L] \end{bmatrix} \tag{4.4}$$

where $H_{\mathrm{re}}[m, N_s^l]$ and $H_{\mathrm{im}}[m, N_s^l]$ represent the TFs for the l^{th} multiplexed intensity image at the m^{th} axial slice, written in the form of $N^2 \times N^2$ diagonal matrices. Because our IDT model is derived from the first Born approximation [8], resulting in independent scattering contribution from each axial slice, the system TF can be simplified for recovering the m^{th} slice of the object

$$\mathbf{H}_m = \begin{bmatrix} H_{\mathrm{re}}[m, N_s^1] & H_{\mathrm{im}}[m, N_s^1] \\ \vdots & \vdots \\ H_{\mathrm{re}}[m, N_s^L] & H_{\mathrm{im}}[m, N_s^L] \end{bmatrix}. \tag{4.5}$$

to enable slice-wise recovery under multiplexed conditions. We apply SVD analysis to this forward model to optimize illumination patterns for achieving high volume-rate mIDT.

4.2.3 mIDT illumination scheme design

Our multiplexing scheme considers two categories for illumination design: 1) the multiplexed TF, and 2) the single-LED TF characteristics. From the multiplexed TF, we develop a custom metric evaluating the Fourier space weighting within the 3D bandwidth to ensure uniform coverage. The metric is derived by applying the

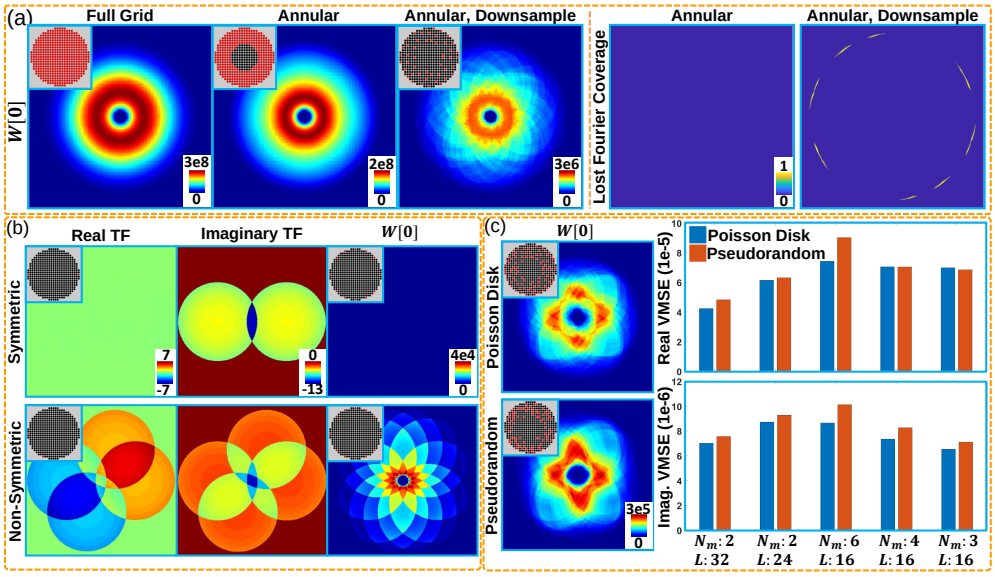

Figure 4·2: (a) The in-focus weight distribution $W[0]$ of conventional IDT, Annular illumination IDT, and downsampled annular illumination TFs without multiplexing. Removing LEDs from the grid provides equivalent Fourier coverage while reducing the number of images required for IDT. (b) The real and imaginary TF behavior for multiplexed symmetric (top) and non-symmetric (bottom) illuminations. The loss of phase information for symmetric illumination necessitates geometric illumination constraints to maximize the object's recovered phase. (c) The weight distribution and VMSE comparison of mIDT designs using pseudorandom and poisson disk random sampling for LED selection. Poisson disk sampling provides equivalent or lower VMSE to pseudorandom sampling because it reduces TF overlap by spatially separating multiplexed illuminations.

singular value decomposition (SVD) to the multiplexed system to obtain a weight distribution for every axial slice. Our metric, $W[m]$, is derived by analyzing the multiplexed TF via SVD and represents the Fourier weighting for the system TF at slice q for a given mIDT design

$$W[m] = \left(\sum_{\ell=1}^{L} \left|H_{\mathrm{re}}[m, N_s^{\ell}]\right|^2\right) \odot \left(\sum_{\ell=1}^{L} \left|H_{\mathrm{im}}[m, N_s^{\ell}]\right|^2\right) - \left(\sum_{\ell=1}^{L} H_{\mathrm{re}}^{*}[m, N_s^{\ell}] H_{\mathrm{im}}[m, N_s^{\ell}]\right) \odot \left(\sum_{\ell=1}^{L} H_{\mathrm{re}}[m, N_s^{\ell}] H_{\mathrm{im}}^{*}[m, N_s^{\ell}]\right), \tag{4.6}$$

where $\odot$ denotes element-wise multiplication. Notably, this term matches the denominator for Tikhonov-based reconstruction (in Eq. (3.14a) and (3.14b)) and controls the system conditioning for a single object slice. By optimizing this term for equal Fourier weighting across the available bandwidth, we improve the inverse problem's overall stability without sacrificing resolution.

An example of this distribution for the standard IDT is shown in Fig. 4·2(a). We preserve this weight distribution when selecting multiplexed illumination designs using the metric

$$D = \max \frac{\sum_{m=1}^{M} \mathrm{tr}(W[m] \geq \alpha)}{\sum_{m=1}^{M} \mathrm{tr}(W[m] < \alpha)}, \tag{4.7}$$

where $\mathrm{tr}(\cdot)$ takes the trace of a matrix and α is a thresholding parameter. Essentially, D optimizes the system TFs to provide weight distributions above the threshold α for all available spatial frequencies. The ideal α matches the system's Signal-to-Noise ratio (SNR) to prevent information loss. In practice, this value is unknown and dependent on both the system and signal. Because the signal must maintain weak scattering conditions for the IDT model's validity, the signal strength is limited and the dominant control for α results from the system noise. This parameter requires manual testing to find optimal α values for each imaging system using mIDT. Because this metric is non-differentiable, we implement a random search procedure through the available LED combinations with a fixed number of 100 realizations to determine the illumination pattern that maximizes D.

With this random search, we implement model-based design constraints on the available illuminations for each multiplexed image. First, we remove low angle illuminations with NA$\leq$ 0.3 (Fig. 4·2(a)) because they provide minimal phase information. Second, we downsample the total available LED grid (Fig. 4·2(a)) to remove redundant Fourier coverage. Next, we geometrically restrict the available LEDs in each image to one quadrant of the Fourier space to prevent symmetric illumination multiplexing from cancelling out object phase information [80, 82]. This behavior is highlighted in Fig. 4·2(b). Finally, we implement Poisson disk random sampling to enforce spatial separation between the remaining multiplexed LEDs [88]. This constraint reduces TF overlap and helps preserve the propagation phase for higher quality volumetric object recovery. We show this improvement in Fig. 4·2(c), where mIDT designs using poisson disk sampling show lower Volumetric Mean-Squared Error (VMSE) object reconstructions compared to conventional IDT than designs using pseudorandom LED sampling. With these constraints and our $W[m]$ metric, the final mIDT design procedure follows the steps below

1. Select desired number of illuminations and LED downsampling,
2. Define axial range for evaluating TF weight distributions,
3. Implement poisson disk sampling with model-based constraints,
4. Calculate metric with Eq. (4.7),
5. Repeat M times and select the design with largest value of D.

4.2.4 Regularization with mIDT

In following the work by Ling et al. [8], the reconstruction approach utilizes the Tikhonov-based deconvolution following Eq. (3.14a) and (3.14b). The multiplexing of illuminations changes the image number and TFs for this inverse problem, but the

inverse problem remains identical to that in [8]. The critical change important for mIDT is the choice of regularization weights τ_{re} and τ_{im}. The value of τ relates directly to the measurement SNR and depends both on the scattered signal and measurement noise [59]. Since the SNR is never known exactly, selecting the appropriate τ requires manually judging reconstructions using a range of regularization values, and an incorrect choice can artificially alter the recovered object. This choice becomes more important for comparing mIDT results with IDT, as the multiplexed illumination and varying image count will modify the SNR and require new regularization weight choices. Before evaluating new biological samples, we first investigate the relation between τ, the multiplexed illumination quantity N_s, and the image number L to automatically select the regularization for each simulated mIDT design.

To determine the optimal τ, we evaluate the signal SNR behavior under multiplexed illumination and multi-image conditions following the Wiener deconvolution analysis [59]. We consider the cost functional for a phase-only object $\widehat{\Delta\epsilon}_{\mathrm{re}}$ as a random field in the presence of additive white gaussian noise $\widehat{w}$

$$D = \underset{G_\ell}{\operatorname{argmin}}\, \mathbb{E}\left\{ \left\| \widehat{\Delta\epsilon}_{\mathrm{re}} - \sum_{\ell}^{L} G_\ell \widehat{I}_\ell \right\|^2 \right\} \tag{4.8}$$

where G_ℓ is each multiplexed intensity's TF and $I_\ell = H_{\mathrm{re}}[m, N_s^\ell]\widehat{\Delta\epsilon}_{\mathrm{re}} + \frac{\hat{w}}{N_s}$. We assume unit magnitude illumination from each multiplexed plane wave on the sample such that the reference field intensity has value N_s. Since we normalize the intensity image and remove this background signal, the noise is reduced by N_s. Applying the gradient over G_ℓ and setting it to zero, we obtain the following optimal choice of G_ℓ:

$$G_\ell = \frac{H_{\mathrm{re}}^*[m, N_s^\ell]}{\sum_\ell^L |H_{\mathrm{re}}[m, N_s^\ell]|^2 + \tau_{mux}} \tag{4.9}$$

where $\gamma = W/S$ is the SNR of each single LED illuminated intensity image given the

power spectral densities of the noise W and permittivity contrast S, respectively, and

$$\tau_{mux} = \frac{L\gamma}{N_s}, \tag{4.10}$$

defining the behavior of the regularization parameter as a function of the image number L and multiplex number N_s. The value of γ will vary between each intensity image due to fluctuations in the image-specific SNR, but this global approximate enables each mIDT scheme's regularization value to be automatically predicted from the conventional IDT regularization. This enables semi-automatic regularization choices and fair comparison across reconstructions using different multiplexing designs.

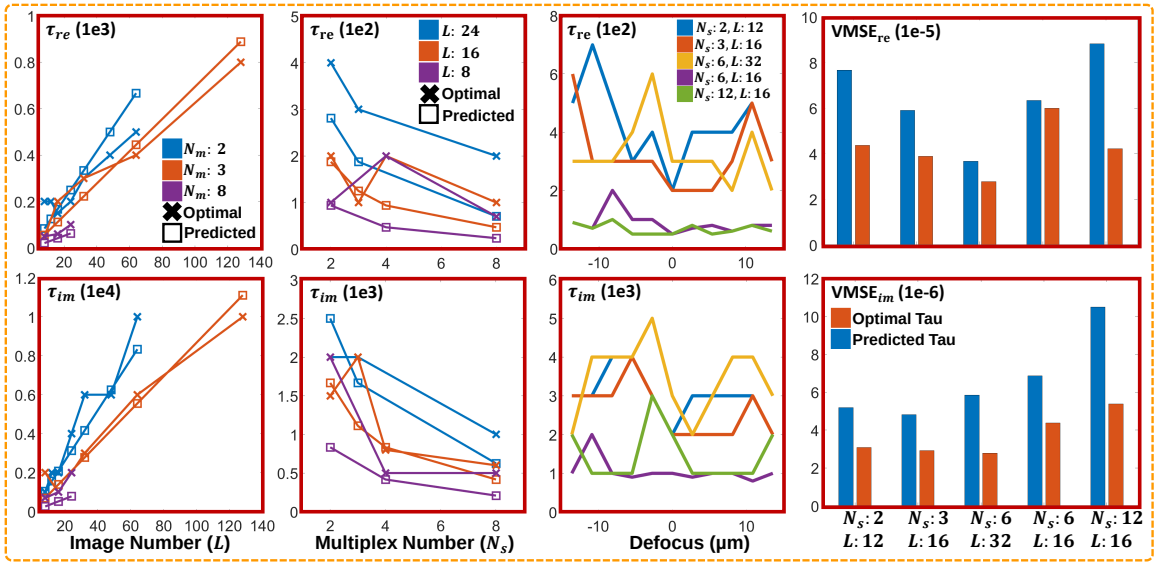

Figure 4·3: Predicted and manually determined Tikhonov regularization values for (a) fixed N_s and variable L, (b) fixed L and variable N_s, (c) fixed L and N_s with variable defocus, and (d) VMSEs comparing mIDT and conventional IDT using predicted and manually determined Tikhonov values. We observe linearly increasing τ with L and linearly decreasing τ with N_s as predicted from our derivations. Our VMSE is increased with our predictions but are still considered small for finding optimal mIDT designs.

We validate this predictive τ term through comparison with the manually found τ across different mIDT conditions shown in Fig. 4·3. We evaluate τ with fixed mul-

tiplexed illumination N_s and variable image counts L (Fig. 4·3(a)), variable N_s with fixed L (Fig. 4·3(b)), and regularization across different axially reconstructed slices (Fig.4·3(c)). To quantify the reconstruction quality, we compare the VMSEs for predicted and optimal τ reconstructions with conventional IDT (Fig. 4·3(d)). For these predictions, we use the manually tuned γ for the conventional IDT reconstructions.

The manually found τ follows directly proportional and inversely proportional relationships with L and N_s, respectively, as predicted with our derived τ relationship (Fig. 4·3(a)-(b)). Our prediction does not exactly match the manually found τ, but this is expected since both the predicted and manually found regularization values are inherently based on user-selected values. We do observe that our predictions are within one order of magnitude of the manual τ which is acceptable for Tikhonov regularization [59]. We also observe the manual τ value varies within an order of magnitude across all axial reconstructions, indicating that a fixed regularization parameter is viable across all reconstructed slices. Furthermore, the VMSEs show a small increase in error using the predicted τ for both the real and imaginary permittivity contrast reconstructions. This error is still an order of magnitude smaller than the error introduced with mIDT and is considered insignificant. These results indicate our predictive τ choice gives us a semi-automated approach to uniformly regularizing all mIDT conditions for evaluating our available mIDT designs. We use this relation of the regularization weights for automatically regularizing mIDT measurements for comparison with conventional IDT.

4.3 Results

4.3.1 Optimal multiplexed illumination

We now evaluate mIDT designs for the optimal combination of illumination multiplexing, image number, and acquisition speed for high volume-rate mIDT. We consider the

visual volumetric object reconstruction, the VMSE compared to conventional IDT, and the theoretical acquisition speed for finding the optimal design. Each mIDT design is simulated using conventional IDT measurements of a $\sim 110 \times 120 \times 40\mu\text{m}^3$ diatom biological structure fixed in glycerin ($n = 1.47$). For the reconstruction, we use the regularization from Eq. (4.10) allowing for direct comparison across mIDT designs.

Figure 4·4 highlights the key factors of our evaluation. For non-multiplexed, downsampled illumination schemes, we observe the real permittivity contrast depth-coded projection (Fig. 4·4(a), rows) and VMSEs (Fig. 4·4(b)) provide low error compared to conventional IDT. Reconstruction artifacts become significant, however, with the introduction of multiplexing (Fig. 4·4(a), columns). We attribute these artifacts to the system point-spread function (PSF) under multiplexed conditions. Our multiplexed illumination designs attempt to generate uniform weight distribution over the recovered object bandwidth, but the TF overlap between different illuminations creates uneven distributions in the system TF (Fig. 4·2(b)-(c)). The resulting non-uniform system PSF from this result creates object-dependent structural artifacts and corrupts the reconstruction quality. This is evident in the blurry mIDT reconstructions shown in Fig. 4·4.

This degradation from the PSF, however, still provides lower VMSE when multiplexing without downsampling (Fig. 4·4(b)). With more images, the patterned system TF becomes smoothed out and reduces these artifacts. The most significant degradation occurs when both downsampling and multiplexing are implemented in mIDT. These results suggest the best mIDT reconstructions result providing the fastest acquisition speeds result from measurements using sparse illumination with minimal multiplexing.

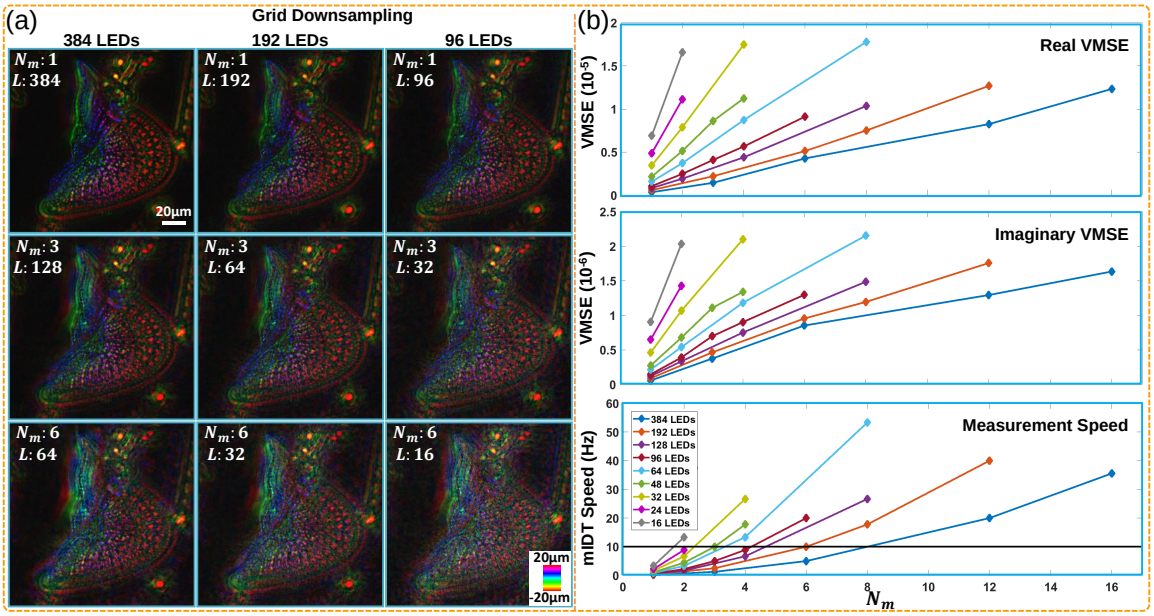

Figure 4·4: (a) Depth-coded projections of conventional IDT (Upper Left) reconstructions compared with various mIDT designs. Each row is fixed with a specific multiplexing value and each column has a fixed downsampled LED grid. Downsampling without multiplexing preserves the reconstruction quality while multiplexing illuminations increases the reconstruction artifacts. (b) Volumetric mean-square errors (VMSEs) of mIDT designs using different downsampling and multiplexing conditions and their corresponding theoretical acquisition speed. Each mIDT case is compared to the conventional IDT reconstruction. The results show multiplexing and downsampling are necessary to achieve a theoretical 10Hz acquisition rate with our hardware setup.

4.3.2 Multiplexed vs. conventional IDT

Based on our simulations, we evaluated whether multiplexing itself is necessary. The large illumination quantity and long exposure time of 30-40ms required for conventional IDT in our setup initially motivated the use of multiplexed illumination. The artifacts introduced through mIDT, however, may provide larger VMSE than conventional IDT measurements using fewer LEDs at a lower SNR. To investigate this case, we compared IDT and mIDT under equivalent theoretical acquisition speeds using downsampled illumination grids with shorter exposure times.

For these measurements, we used our experimental setup (Fig. 4·1(a)) consisting of a Nikon TE 2000-U microscope equipped with a custom programmable 632nm LED array [80]; a 0.65NA, 40x objective (Nikon, MRL00402), and an sCMOS camera (PCO.Edge 5.5). In all cases, we evaluated the same diatom sample discussed in the prior section. For conventional IDT, we used the previously evaluated L=96 illumination case and an annular illumination design using high NA illuminations (NA=0.575) inspired by the work of Li et al. [9]. These choices consider whether many low SNR measurements or a few high SNR, high NA illuminations provide better conventional IDT reconstructions, respectively. We acquired multiple IDT measurements under different exposure times to match the theoretical acquisition speeds of the $N_s = 3, L = 32$, $N_s = 6, L = 32$, and $N_s = 6, L = 16$ mIDT measurements at 2Hz, 4.7Hz, and 9.5Hz, respectively. We also acquired L=384 conventional IDT measurements for our reference object and mIDT measurements to compare the visual reconstruction quality and VMSE.

The results from this experiment are presented in Fig. 4·5. We show the depth-coded projections (Left) from each reconstruction on a fixed scale and the real VMSE (Right) as a function of the measurement SNR. We estimate the SNR as the average standard deviation ratio between the signal and background ($\sigma_{\text{sig}}/\sigma_{\text{bk}}$) over all illuminations, where $\sigma_{\text{sig}} = \sigma_{\text{image}} - \sigma_{\text{bk}}$ denotes the standard deviation difference between the entire image and a blank image region. In agreement with our simulation, the $L = 96$ conventional IDT case shows the lowest VMSE under standard exposure times Fig. 4·5, Right) but loses reconstruction quality with decreasing SNR. This case matches our expectations for noise-limited IDT measurements where the quality reduces with additional system noise. The mIDT measurements exhibit the next lowest error, followed by a counter-intuitive VMSE increase with longer exposure times for the $L = 16$ case. This behavior can be better understood from the

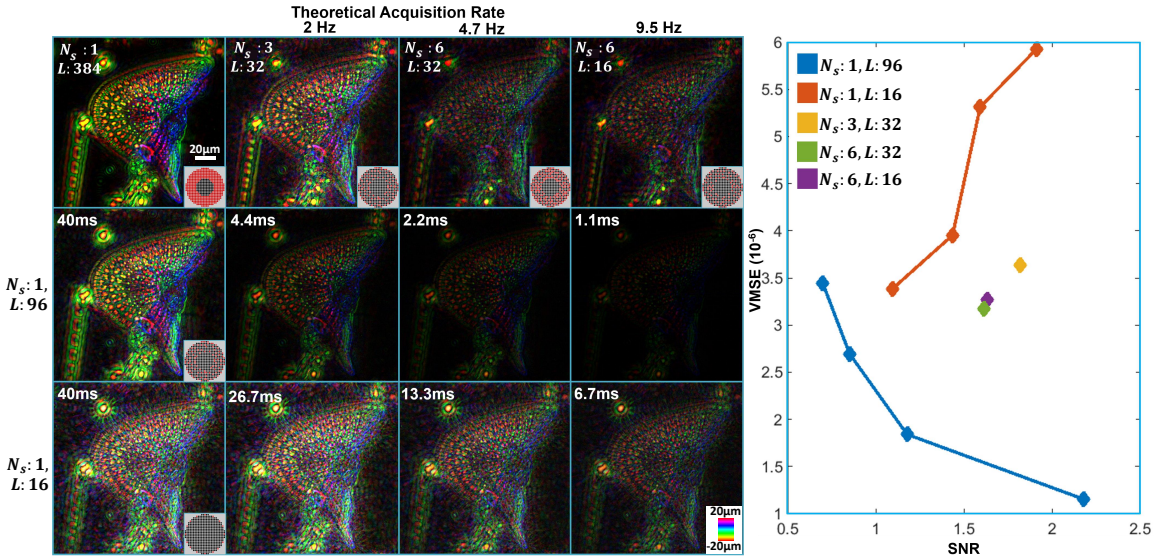

Figure 4·5: Depth-Coded Projections (Left) and Volumetric Mean-Square errors (Right) for conventional IDT and mIDT measurements under different SNR conditions. The $N_s = 1, L = 96$ case shows noise-limited reconstruction quality with increasingly underestimated object permittivity while both the mIDT and $N_s = 1, L = 16$ show higher contrast, better permittivity recovery with object-dependent structural artifacts. These artifacts cause the VMSE to increase with longer exposure times.

depth-coded projections (Fig. 4·5, Left). Both the $L = 16$ and mIDT measurements generate structural artifacts in their reconstruction due to their sparse illuminations creating patterned weight distributions for the system TF (Fig. 4·2). Because these cases maintain higher SNR with longer exposure times, they recover higher contrast object features better matching the $L = 384$ conventional IDT case but also amplify these artifacts. This is particularly evident for the $L = 16$ case's star-shaped reconstructions and VMSE trend. The end result is a trade-off between slow, noise-limited conventional IDT measurements and fast measurements with object-dependent structural noise. For imaging dynamic samples, these results indicate the best solution is a high-speed illumination source without significant downsampling or multiplexing.

Physical system constraints unfortunately make this optimal condition difficult.

The system utilized here is fundamentally limited by the LED Array's 60Hz refresh rate. Regardless of exposure time and camera acquisition speed, this system can only acquire images with six different illumination patterns for achieving 10Hz live sample imaging. This large reduction in image quantity would result in significant VMSE from the system's uneven weight distribution. To achieve high-speed imaging with the lowest available VMSE, we are thus limited by our system constraints to mIDT measurements with large N_s and small L. For the following experiments, we use an mIDT design with $N_s = 6$ and $L = 16$ for an acquisition rate of 4Hz. Despite larger error and slower acquisition speeds, we show quantitative recovery of bacterial, cellular, and tissue 3D structure on living organisms using mIDT.

4.3.3 Static object reconstructions with mIDT

We first compare mIDT with phase contrast microscopy (PhC) and conventional IDT on fixed biological samples. This step experimentally validates whether our mIDT design provides adequate volumetric object reconstructions without introducing severe artifacts. To provide ground-truth phase information in the sample volume, we acquire a stack of axially-scanned PhC images on epithelial buccal cells in aqueous media. We subsequently capture mIDT and conventional IDT measurements at a fixed axial plane and reconstruct the object to compare with PhC over the volume. The PhC objective used here matched the magnification and NA of our IDT objective. These results are shown in Fig. 4·6. Both IDT and mIDT recover the same features as PhC across the defocus planes. Due to the specific PhC objective used for this measurement, the corresponding phase features are inverted compared to IDT and mIDT. As expected from simulation, mIDT provides reduced quality reconstructions compared to conventional IDT from the use of multiplexed illumination. However, mIDT has a much faster acquisition speeds of 0.2s compared to conventional IDT at 12s and the axially-scanning PhC measurements at 40min. This trade-off between

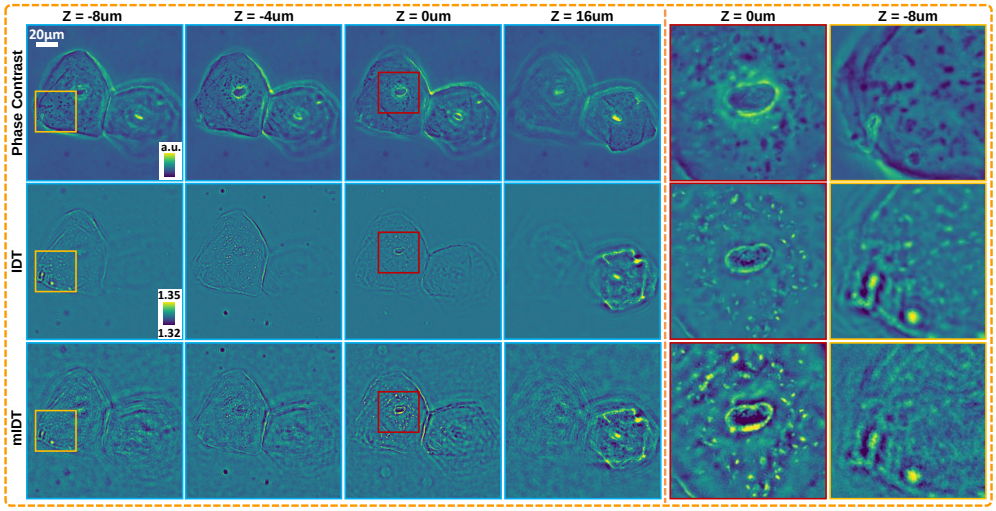

Figure 4·6: Comparison of Phase Contrast (Top), conventional IDT (Middle), and mIDT (Bottom) measurements on two epithelial buccal cells. The phase contrast measurements show inverted phase information compared to IDT. mIDT recovers identical features to PhC and conventional IDT across different depths but includes slightly more artifacts as discussed in the main text.

speed and reconstruction quality makes mIDT advantageous for live sample imaging where IDT's slow acquisition speed will generate significant motion artifacts. These artifacts increase the reconstruction error in conventional IDT beyond that seen in mIDT. We show this improvement with mIDT on living *C. elegans* worms and embryos as well as epithelial buccal cell specimens.

4.3.4 Dynamic object reconstructions with mIDT

We show the high-volume rate imaging capabilities of mIDT on a *C. elegans* worm in Fig. 4·1(e), 4·7, and in Visualization 1. mIDT's large Field-of-View (FOV) simultaneously recovers the worm's pharynx, pharyngeal bulbs, and intestine (Fig. 4·7(a)) as well as high-resolution tissue features across multiple depths (Fig. 4·7(b)). In particular, mIDT captures fine-details including granular structures (Fig. 4·7, red arrows), the worm's grinder (Fig. 4·7(b), white arrow), and the pharyngeal-intestinal

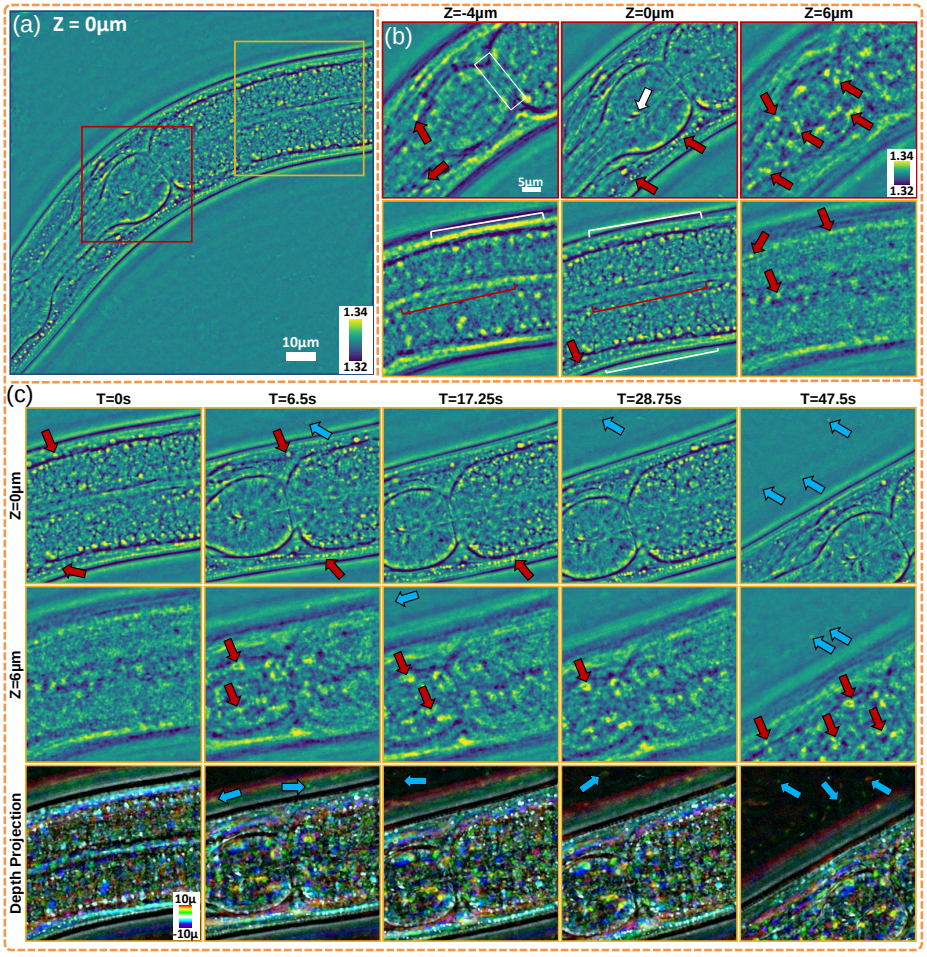

Figure 4·7: (a) Full-field refractive index reconstruction of a live *C. elegans* worm at the in-focus plane at time $T = 0$s. The full video of the reconstruction is provided in Visualization 1. (b) Outsets at $T = 0$s of the live worm across multiple depths. The markers highlight the following structures: lipid droplets and granular structures (red arrows), the grinder (white arrow), The pharyngeal-intestinal valve (white box), the intestinal tract (red bar), and wall muscle (white bar). mIDT reconstruction artifacts are more prominent at defocused slice reconstructions, but some structures are still recoverable. (c) Time lapse images of the *C. elegans* worm moving through outset regions at $Z = 0\mu$m (Top), $Z = 6\mu$m (Middle), and depth projections (Bottom) through the object volume. Lipid droplets (red arrows) and external native bacteria (blue arrows) are highlighted showing finely detailed features are captured with mIDT. The various colors in the depth projection show tissues and bacteria are recovered across the reconstructed volume.

valve (Fig. 4·7, white box). The worm's wall muscles (Fig. 4·7, white bracket) and intestinal tract (Fig. 4·7, red bracket) are also visible across multiple depths. With mIDT's high-speed acquisition, we can monitor these 3D features in time (Fig. 4·7(c), Visualization 1) and observe external organisms, such as bacteria (Fig. 4·7(c), blue arrows), interact with the worm. mIDT's larger reconstruction error does appear more prominently with increasing defocus (Fig. 4·7(b)-(c)), but lipid droplets and other features are still apparent at these depths. These results highlight the potential utility of mIDT as an easily implementable tool for evaluating 3D morphology and multicellular organism response to its environment and external variables.

We note here that motion artifacts still occur with our mIDT design under periods of rapid *C. elegans* motion in Visualization 1. Our system is hardware-limited by the LED array's 60Hz refresh rate to 4Hz acquisition rates and thus is too slow for rapidly moving living samples. This problem solvable with the use of faster LED arrays, which we hope to investigate in future work.

We further show the utility of mIDT for embryogenesis using *C. elegans* embryos (Fig. 4·8, Visualization 2). Using our mIDT design, we recover the volumetric morphology of two embryos in the three-fold (red arrow) and quickening (orange arrow) stages of development. mIDT easily resolves developing tissues including the worm's buccal cavity (Fig. 4·8, white box) and evaluates a cross-section of the worm's intestine (Fig. 4·8, blue box). A native bacteria (Fig. 4·8, blue arrow) is also capture at a defocus plane with mIDT. Our mIDT architecture's high-speed acquisition rate enables longitudinal monitoring of the embryo development, which shows significant promise for this technique in developmental biology applications.

mIDT also shows promise for bacteria-cell interactions as shown in Fig. 4·9 and Visualization 3. Live epithelial buccal cells are evaluated in saliva and temporal projections show 3D native bacteria motion throughout the measurement (Fig. 4·9(a)).

We observe diplococci bacteria, likely native *Escherichia coli*, interacting near the cells (Fig. 4·9(b)) as well as an unknown bacterial cluster moving within a membrane (Fig. 4·9(b)). A feature within this cluster is highlighted with a red arrow. Furthermore, we can track bacterial movement in 3D as shown in the maximum intensity projections of our temporally coded reconstructions (Fig. 4·9(c)). mIDT provides quantitative volumetric information on both cells and bacteria that could be used for tracking, cell-bacteria interaction studies, and numerous other applications. These results show mIDT is highly promising for cytopathology and immunological research fields where these interactions are critical to understanding disease propagation and infection.

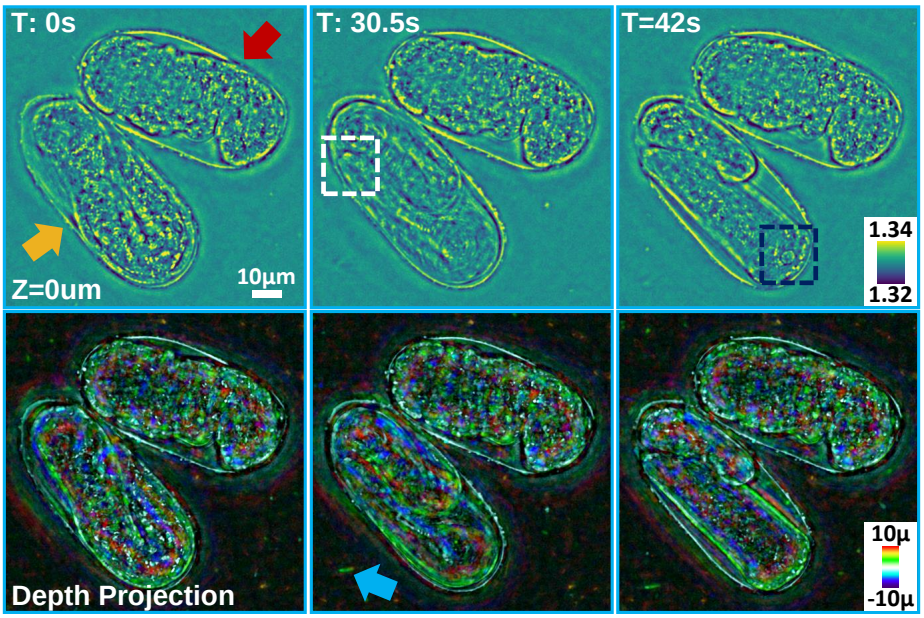

Figure 4·8: (Top) In-focus refractive index reconstruction of *C. elegans* embryo temporal measurement and (Bottom) depth-coded projections of volumetric reconstruction. The full video of the reconstruction is provided in Visualization 2. mIDT's reconstruction quality enables the identification of the embryos in the three-fold (red arrow) and quickening (orange arrow) development stages. Individual developing tissues including the buccal cavity (white box), intestine (blue box), and native bacteria (blue arrow) are clearly recovered with mIDT.

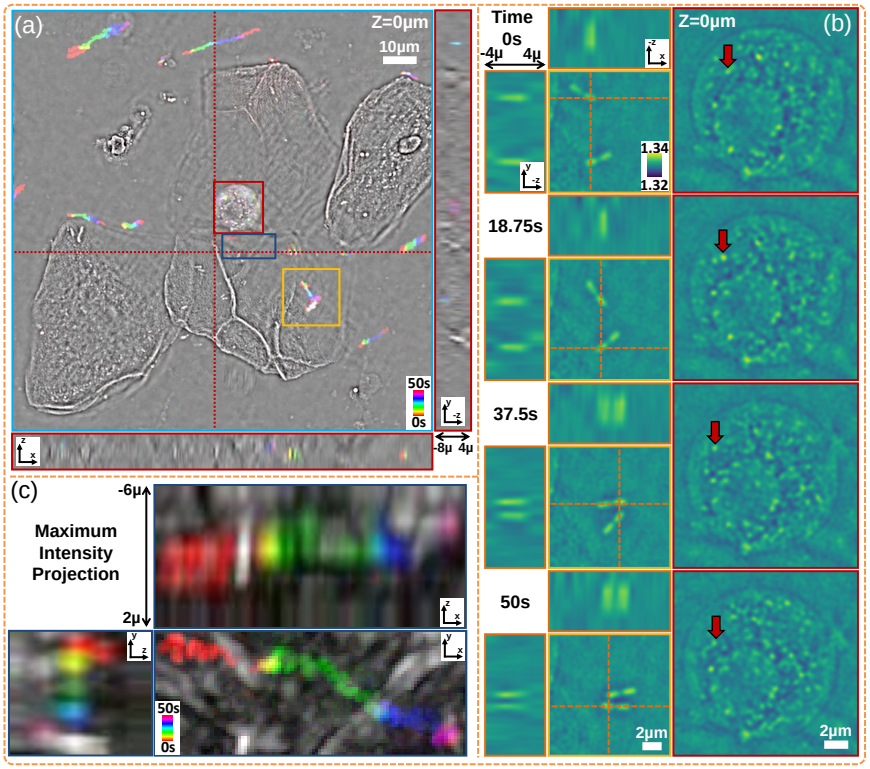

Figure 4·9: (a) Temporally color-coded in-focus reconstruction of epithelial buccal cells and native bacteria. The volumetric reconstruction cross-sections capture moving bacteria across multiple depths. The full video of the reconstruction is provided in Visualization 3. (b) The refractive index reconstructions of diplococci bacteria (left) and a native bacterial cluster (right) across a one minute acquisition period. Both outsets show bacteria motion is quantitatively captured without artifacts using mIDT. The red arrow highlights a dynamic feature of the native bacterial cluster. (c) Maximum intensity projections of temporally encoded refractive index volume reconstructions of a single bacteria. The cross-sections recover 3D particle motion across multiple axial planes during the measurement highlighting mIDT's potential for particle tracking.

4.4 Discussion

Quantitative phase image modalities provide a unique platform for evaluating the morphology of biological specimens in their natural state. Acquiring data in native environments quickly becomes difficult because high-speed, large FOV volumetric

imaging with adequate resolution is required to capture dynamic biological samples. These parameters typically requires expensive setups or sample fixation to evaluate the object without motion artifacts. mIDT removes this limitations in an easily-implementable, scan-free imaging system. Our model-based illumination design maximized the recovered object bandwidth within each image and minimized redundant sample information and phase information loss. From these designs, we achieved reconstructions with minimal quality loss at near real-time acquisition rates. We validated the reconstruction quality against both conventional IDT and PhC systems and showed its utility on dynamic samples including *C. elegans* worms, embryos, and epithelial buccal cell samples. This modality provides a straight-forward, easily accessible tool for wide-spread biological research applications.

Our mIDT design could be significantly improved with specializing the illumination design. Our evaluation of mIDT designs suggests the optimal reconstruction quality is achieved from highly downsampled illumination grids with no multiplexing. This result suggests that specializing the illumination hardware to use a few high power, high NA illuminations to capture the object's information at maximum object bandwidth would improve the reconstruction quality and provide high-speed imaging. We showed this approach is successful in a separate high volume-rate IDT paper [9]. This work utilized a specialized annular LED arrays providing angles matching the objective NA. This choice enhanced the object bandwidth and reduced TF overlap to provide high-quality reconstructions from 8 illuminations with even weighting distributions for the system TF. Specializing the illumination hardware is not always advantageous, however, when multi-modal illuminations are required. Using generic square LED arrays enables other microscopy techniques, such as Dark-field [89], Fourier Ptychography [38, 68, 80] and Differential Phase Contrast [62], that can be advantageous for numerous research applications. Our mIDT design only

modifies the illumination pattern and thus provides a flexible alternative approach to achieve high volume-rate IDT.

Another factor of consideration in our design is the procedure used for LED design selection. Our SVD-based metric is non-differentiable and thus requires search-based procedures to find optimal LED combinations. As specific illumination designs will be system-dependent, the optimal illumination choice requires significant computation time. To conserve time, we limit this search to 100 realizations and provide adequate reconstruction quality (Fig. 4·4) despite not achieving a true optimal mIDT design. To further improve the results, learning based illumination designs [82, 81] and phase recovery [90, 91, 92, 93] may be a fruitful area of future research.

Finally, mIDT's reconstruction quality and robustness to large biological structures could be improved by considering multiple-scattering. mIDT's underlying physical model relies on the first Born approximation [87] and thus is limited to weakly scattering structures. This limitation creates a trade-off between the object's refractive index contrast and overall height to provide an accurate reconstruction. Both model-based [67, 31, 94, 43, 41, 42] and machine learning-based [95, 96, 97, 30] approaches have shown excellent results in extracting useful information from multiple scattering. We will expand mIDT to consider multiple-scattering in future work following these methods.

Chapter 5

High-speed intensity diffraction tomography via annular illumination

5.1 Overview

One of the critical challenges described in Chapter 3 is that of the IDT system's acquisition speed preventing the evaluation of living samples. In Chapter 4, we presented the first solution to this limitation known as multiplexed IDT (mIDT). This technique provided a multiplexed illumination framework enabling hardware-limited 4Hz volume-rate imaging capable of evaluating the 3D structures of live *C. elegans* worms and embryos, cell samples, and bacteria quantitatively [71]. The appeal of mIDT is in its hardware-agnostic illumination scheme allowing for faster IDT regardless of the system's hardware. This design is advantageous for multi-modal computational microscopes where having generic illumination sources, such as rectangular LED arrays, enable numerous CI modalities to be implemented in a single setup [89, 70]. The main downside of this technique, as mentioned in Section 4.3.2, is its trade-off of reduced reconstruction quality for faster acquisition. The use of multiplexed illuminations within each image generated unequal weighting of spatial frequencies in the

TFs that led to strong, object-dependent missing cone artifacts in the reconstruction. The optimization from mIDT suggested that the best case illumination design was to utilize sparse, high angle illumination avoiding TF overlap and enhancing the setup's resolution without multiplexing illuminations. While such illumination schemes are possible with rectangular arrays, the structure of such arrays is suboptimal to encode the object's full bandwidth in very few illuminations [98]. This limitation requires the adoption of new illumination hardware to achieve high volume-rate IDT with minimal reconstruction quality loss.

In this chapter, we present the annular IDT (aIDT) modality for high-speed 3D QPI. This hardware-based solves the IDT speed limitations by replacing the rectangular LED array of the initial IDT setup with a 24-LED ring-geometry commercial array for sparse, high-angle sample illumination. The key element of this new array is that it can be optimally positioned to match the microscope objective's NA and provide the highest angle illumination on the sample. We show this design enables the maximum recovery of both low and high spatial frequencies of the object's bandwidth from each illumination and can achieve fast, high-resolution reconstructions of dynamic biological samples sample with as few as 8 LED illuminations. This technique reduces the data requirement by more than 60×, achieving more than 10 Hz volume-rates for imaging a $\sim 350 \times 100 \times 20 \mu\text{m}^3$ volume with near diffraction-limited lateral resolution of 487 nm and axial resolution of 3.4 μm in the 3D RI reconstruction. In addition, we introduce an illumination angle calibration algorithm based on [74] for improving the volumetric reconstruction quality to achieve incoherent resolution limits over the entire volume. These improvements enable *in vitro* dynamic 3D RI characterizations of living biological samples without motion artifacts or the reconstruction artifacts of mIDT. We show that aIDT can provide useful subcellular information on multiple specimens including unicellular diatom microalgae, clustered

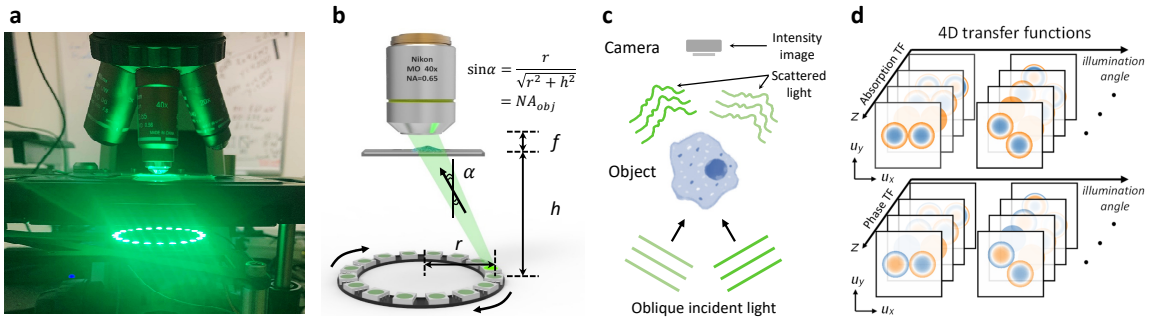

Figure 5·1: Illustration of the aIDT imaging system. (a) The aIDT system setup consisting of a standard microscope equipped with an annular LED array. A visualization demonstrating the system operation is shown in Video 1 of [9]. (b) An LED ring illumination unit is placed underneath the sample. The distance Z is tuned such that the illumination angle α is matched with the objective NA. (c) Each IDT image measures the interference between the scattered and the unperturbed fields. (d) The absorption and phase transfer functions at various illumination angles and sample depths.

epithelial buccal cells, and live (*C. elegans*) multi-cellular specimens. Finally, we simulate our aIDT system to show accurate reconstructions within 1×10^{-3} of the object's true RI and sensitivity to RI changes of 2×10^{-4} under our system's SNR for weakly scattering objects.

5.2 Methods

5.2.1 aIDT principle

The key element of the aIDT imaging system is its choice of annular LED arrays for the illumination hardware. As shown in Fig. 5·1(a), the system follows the setup of the initial IDT setup in Chapter 3 but instead couples a commercial transmission-mode brightfield microscope with a ring-geometry LED array. This axial distance Z is critical, as the source-sample separation and the LED's lateral position with respect to the optical axis defines the illumination angle from geometric optics principles. Denoting the LED ring radius as r_{ring}, the illumination NA ($\mathrm{NA_{illum}}$) defining the

incident angle of each LED is set by

$$\mathrm{NA}_{\mathrm{illum}} = \frac{r_{ring}}{\sqrt{r_{ring}^2 + Z^2}}, \tag{5.1}$$

To match the microscope objective's maximum collection NA NA_0, the array's height must simply be adjusted to the proper value of Z. This distance must also maintain sufficient distance from the sample to provide plane-wave illumination, although this work found that shorter separations than those used in Chapter 3 still satisfy this condition. This configuration can acquire up to 24 intensity images with separate illumination angles(Fig. 5·1c) and faster acquisition rates are possible by leveraging optimal illumination selection with LED downsampling in similar form to [71].

The optimal selection of LED illuminations follows similar model-based design constraints considered for mIDT in [71]. As discussed in Chapter 3 and [8], the TFs describing the IDT forward model exhibit shifted circles, resulting from the low-pass filtering of the scattered field by the system's pupil function $P(\boldsymbol{\nu})$, in the Fourier space depending upon the illumination angle following synthetic aperture principles (Fig. 5·1c). These circles shift in opposite directions due to the interference of the scattered and reference fields with the complex conjugates of each field. When these circles intersect in the Fourier space, the phase features within this passband are largely cancelled due to the overlap of the field and its conjugate. This behavior is captured in the asymmetric structure of the phase TF in Eq. (3.12a). To optimally capture the object's bandwidth information with as few illuminations as possible, the LEDs in the annular array must be chosen to similarly to mIDT and provide maximum bandwidth coverage with minimal phase TF overlap.

The benefits of this optimization in aIDT are present in Fig. 5·2. Fig. 5·2(a) illustrates the loss of phase information due to the overlap of the phase TF at low illumination angles while Fig. 5·2(b) shows the benefits of using the high-angle il-

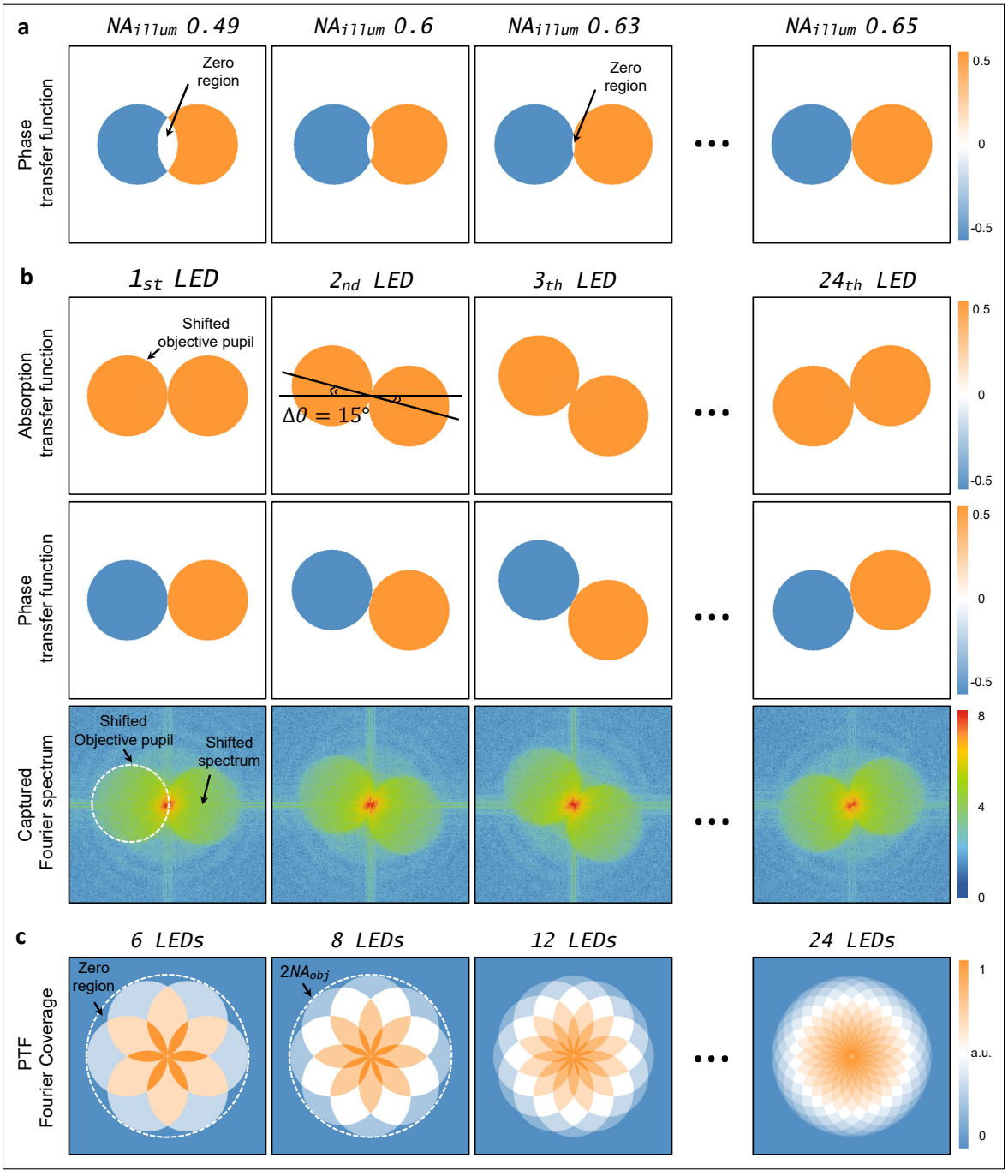

Figure 5·2: aIDT transfer function illustration. (a,b) The absorption and phase transfer functions of aIDT and the corresponding experimentally obtained intensity Fourier spectrums. (c) Fourier coverage of PTF with different illumination LED number.

lumination of aIDT. When the illumination NA nearly matches the objective's NA ($\mathrm{NA_{illum}} \approx \mathrm{NA_{obj}}$), the overlap between the shifted pupil functions is minimal and allows for low spatial frequency feature recovery from the object. In addition, the maximally shifted pupil function also enhances the high spatial frequency content recovered from the object. In Fig. 5·2(c), the weighting matrix $W[m]$ introduced in [71] and Chapter 4 is shown for the focal plane ($m = 0$) for aIDT under various downsampled illumination conditions. Due to the radially symmetric design of the ring LED array, the LEDs optimally encode nearly the entire object's bandwidth in as few as 8 unique illumination angles. This strategy provides an elegant solution to IDT's slow acquisition problem that can be easily implemented in existing microscopes in a lab for evaluating dynamic biological samples.

5.2.2 aIDT forward and inverse model

The beauty of the aIDT implementation is that it provides optimal illumination designs capable of high volume-rate imaging without modifying the IDT forward model from [8]. Since each acquired intensity image captures a single illumination, the forward model requires no augmentations like that of mIDT to model the intensity and invert the scattering to recover the object. This result means that the simplicity of the original IDT model is maintained and the setup only required a more specialized LED array to provide high volume-rate imaging. We refer the reader to Sections 3.2 and 3.3 for a full discussion on the forward and inverse model implemented for reconstructing the 3D object volumes with aIDT.

5.2.3 System setup

The aIDT setup is built on an upright brightfield microscope (E200, Nikon) equipped with a ring LED array (1586, Adafruit) instead of its standard broadband source. The radius of the ring LED unit is ≈30mm and is placed ≈35mm away from the

sample centered along the microscope's optical axis. Each LED approximately provides spatially coherent quasi-monochromatic illumination with central wavelength λ =515nm with a ≈20nm bandwidth. All experiments were conducted using either a 40× microscope objective (MO) (0.65 NA, CFI Plan Achro) or a 10× (0.25 NA, CFI Plan Achro) objective. Images were taken with an sCMOS camera (PCO. Panda 4.2, 6.5μm pixel size) synchronized with the LED source to provide camera-limited acquisition speed. The LED array is controlled using an off-the-shelf microcontroller (Arduino Uno) connected to a computer.

During the experiments of imaging living *C. elegans*, a rectangular field of view consisting of 2048×600 pixels was optimized to match the sample size and achieve 85 Hz acquisition rates. All the processing was done using MATLAB 2018b on a personal computer. The processing time to perform LED position calibration (using a 400×400×24 intensity stack) is about 2 seconds. The 3D reconstruction for a 1024×1024×51 RI stack takes about 50 seconds.

5.2.4 Self-calibration method

A critical issue described in Chapter 3 was that of resolution loss when recovering objects at axial planes outside of the focal plane. This loss was attributed to mismatches between the assumed and true illumination angles of the sample. With an incorrect illumination angle, both the translation of $P(\boldsymbol{\nu})$ and the axial spatial frequency term $\eta(\boldsymbol{\nu}-\boldsymbol{\nu}_l)$ in Eq. (3.12a) and Eq. (3.12b) introduce error and blur to the reconstruction by removing lateral spatial frequencies with incorrect pupil positions and insufficiently correcting the phase accumulation from defocused planes, respectively. This error has been shown to be partially corrected through the addition of a post-processing step calibrating the illumination angles based on the intensity spectra [74]. Here, we modify this algorithm with an additional geometric constraint to further enhance the calibration procedure.

We first perform this numerical self-calibration procedure before reconstructing the object with two geometric constraints. First, the distribution of our LED ring is expected to obey a circular geometry

$$u_l^2 + v_l^2 = \frac{{\mathrm{NA}_0}^2}{\lambda}, \tag{5.2}$$

where u_l, v_l denote the separated lateral spatial frequencies of $\boldsymbol{\nu}_l$ for the l^{th} LED illumination. Second, the LEDs are expected to be equally spaced based on the controlled design of the LED array's circuit board layout. Correspondingly, each pair of neighboring LEDs occupy a $\pi/12$ radian angular space. The initial estimate of the angular coordinates θ_l of each LED follows

$$\theta_l = \mathrm{atan2}\Big(\frac{v_l}{u_l}\Big),\ \theta_l \in \Big[-\pi : \frac{\pi}{12} : \pi\Big), \tag{5.3}$$

where atan2 computes the angle of the inverse tangent function in the unit of radian.

Our self-calibration algorithm starts with an initial guess $u_l^{\text{init}}, v_l^{\text{init}}$ from the algorithm in [74], whose estimated LED positions are often contaminated by noise. Accordingly, the final calibrated LED positions $u_l^{\text{cal}}, v_l^{\text{cal}}$ are parameterized as

$$\begin{aligned} u_l^{\text{cal}} &= \Delta u + \mathrm{NA}_{\text{obj}} \cos\left(\theta_l + \Delta\theta\right)/\lambda, \\ v_l^{\text{cal}} &= \Delta v + \mathrm{NA}_{\text{obj}} \sin\left(\theta_l + \Delta\theta\right)/\lambda, \end{aligned} \tag{5.4}$$

and are found by solving the optimization problem

$$\min_{u_l^{\text{cal}}, v_l^{\text{cal}}} \sum_{l=1}^{24} \left[\left(u_l^{\text{cal}} - u_l^{\text{init}}\right)^2 + \left(v_l^{\text{cal}} - v_l^{\text{init}}\right)^2 \right]. \tag{5.5}$$

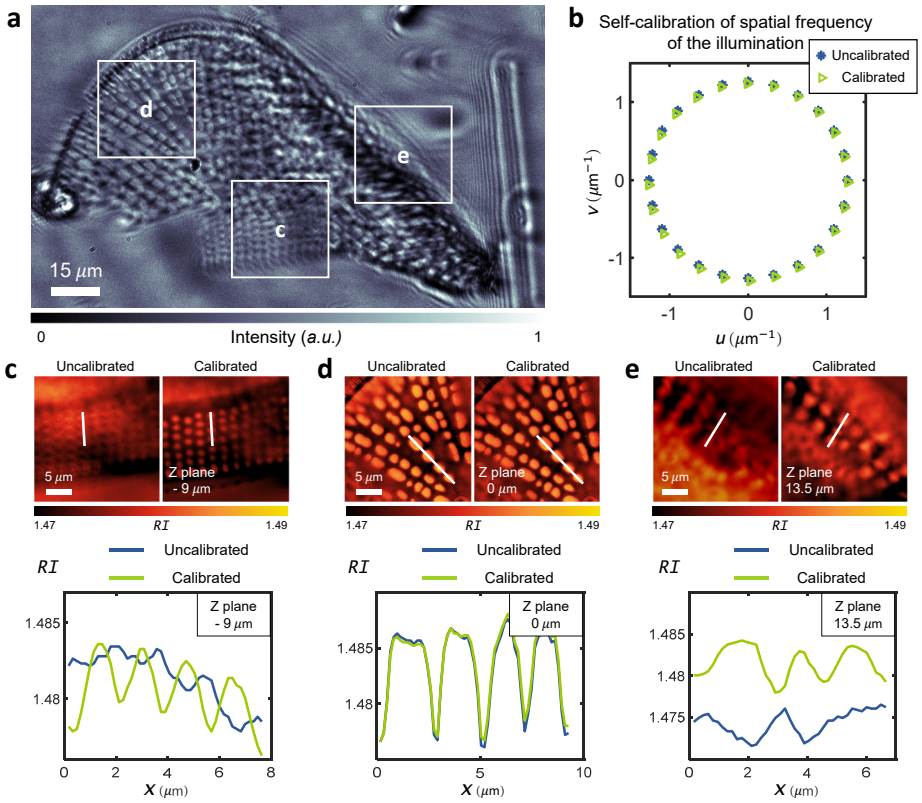

Figure 5·3: Results using the proposed LED self-calibration method. (a) A sample intensity image of a diatom under a certain single-LED illumination. (b) LED positions from manual alignment (termed uncalibrated, marked in blue star) and our self-calibration methods (termed calibrated, marked in green triangle) as plotted in the spatial frequency coordinates. (c-e) Comparison of the reconstructed RI slides before and after calibration. (c) $z = -9\mu$m, (d) $z = 0\mu$m, and (e) $z = 13.5\mu$m. More detailed comparisons across the whole volume is provided in Video 2 of [9].

5.3 Results

5.3.1 Angle self-calibration and performance characterization

Achieving high-quality 3D QPI reconstructions require accurate LED positioning, especially when imaging large-volume objects under high NA illuminations. In practice, removing all residual errors in the LED positions using only manual alignment

and physical calibration procedures is non-trivial. We instead develop an algorithmic self-calibration method for finely tuning the LED positions and demonstrate our technique's improvement of 3D reconstructions.

Our self-calibration method combines two main principles for high-accuracy measurements. First, our TF analysis shows that each intensity image's Fourier spectrum should contain distinct circular regions with center positions defining the illumination angle. A previously developed algorithm [74] already utilizes these features, which we adopted to provide initial LED position estimates. In practice, this algorithm's susceptibility to noise can introduce position error exceeding the LED array's engineering and alignment tolerance. To correct this error, we subsequently incorporate two geometric constraints refining the LED positions to form a ring shape with equal angular spacing using a nonlinear fitting algorithm. This is warranted because the surface-mount technology has high positioning accuracy when placing devices in printed circuit board manufacturing and our illumination unit's printed LED circuits have expected engineering tolerances below 5μm.

We demonstrate the effectiveness of this method on diatom microalgae (S68786, Fisher Scientific) fixed in glycerine gelatin imaged with a 0.65 NA MO. An example intensity image is shown in Fig. 5·3(a). The low-absorbing features (i.e. "phase" features) are already visible due to asymmetric illumination, akin to differential phase contrast [99]. Figure 5·3b compares the LED positions from manual alignment (blue stars) and our self-calibration method (green triangles). This is illustrated in greater detail in Fig. 5·4 as well. The RI reconstruction improvements from our technique are shown in three outsets highlighting features located at different axial positions.

As shown in Fig. 5·3(d), the LED mis-calibrations have minimal effect for structure reconstructions at the objective's focal plane ($z = 0\mu$m). Significant RI degradation from incorrect illumination angles is observed at defocus reconstruction planes

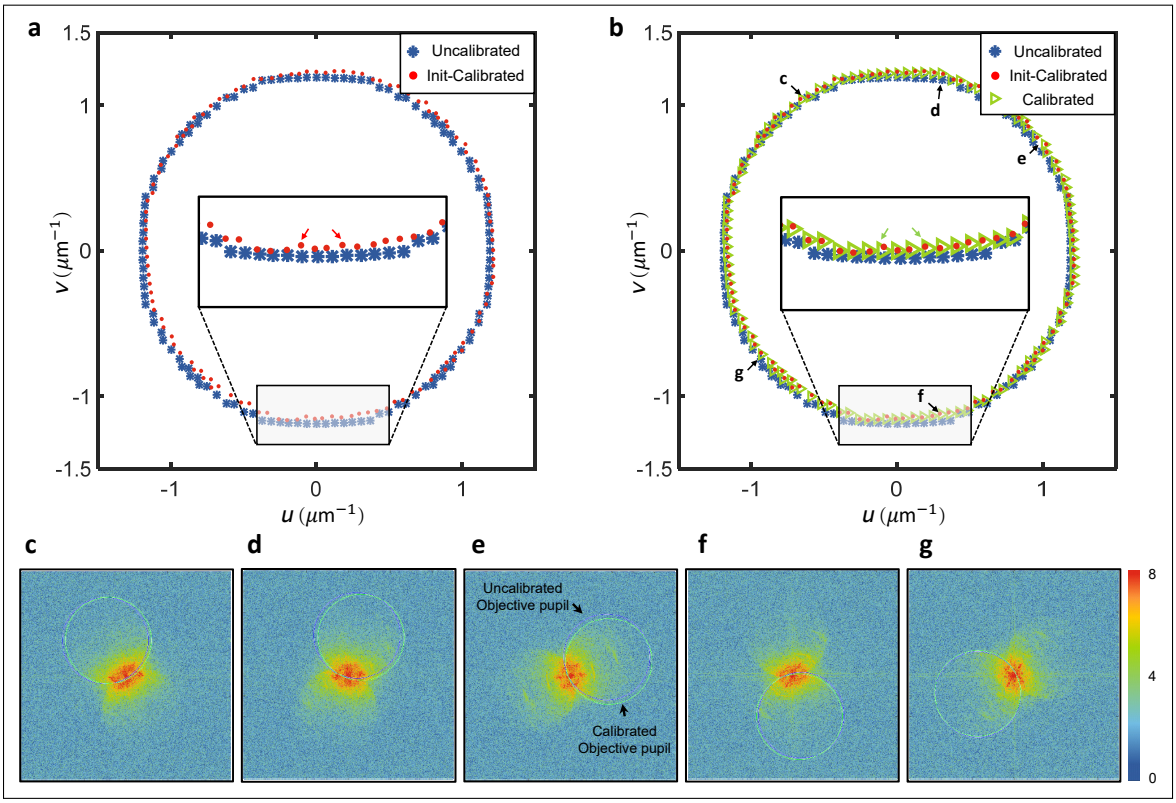

Figure 5·4: Demonstration of the LED matrix self calibration method. (a) The LED positions from manual alignment (termed uncalibrated, marked in blue star) and initial guess of calibration (termed Init-calibrated, marked in red dot), plotted in the spatial frequency coordinates. (b) Calibrated spatial frequency positions of LEDs (green triangle). (c-g) Captured Fourier spectrum using the corresponding LED (marked with arrows) along with calibrated pupil positions (marked by circles).

(Fig. 5·3(c),(e)). This degradation is intuitively explained under the "light field" [100, 66] effect: for a fixed angular error, a larger defocus induces a larger feature displacement error. Our self-calibration method largely mitigates these errors to provide high-quality RI reconstructions (Fig. 5·3(c)-(e)). Both the lateral resolution and contrast are preserved across the entire volume and recovers diatom frustules previously lost at large defocus due to mis-calibration (Fig. 5·3(e)). This calibration procedure allows us to provide high-quality RI distributions with aIDT and is used in our

subsequent results.

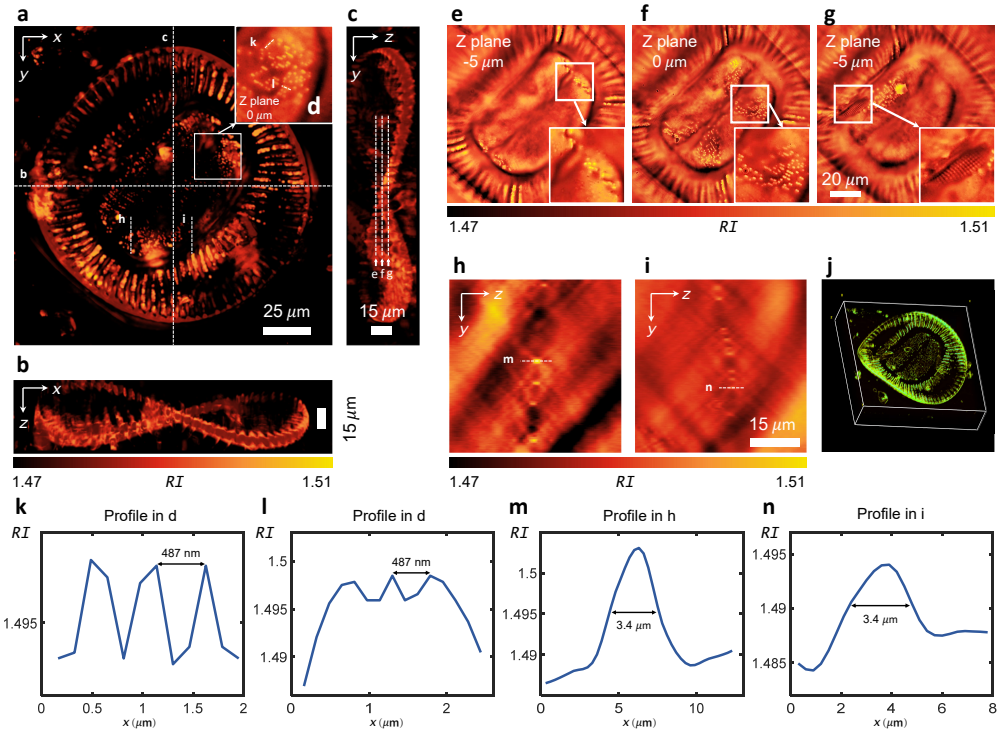

Figure 5·5: RI tomography of Surirella spiralis. (a-c) The maximum RI projection views of the recovered 3D RI distribution in the $x-y$, $x-z$, and $y-z$ planes. (d) Zoom-in on closely packed frustule structures. (e-g) Reconstructed 2D cross sectional RI slices at -5μm, 0μm and 5μm planes. (h-i) YZ-cross sectional views of the reconstructed RI. (j) A 3D rendering view of the reconstructed RI distribution. Additional cross-sectional reconstruction and 3D rendering view from different perspectives are shown in Video 3 of [9]. (k-n) Line profiles across frustule structures to quantify the reconstructed lateral and axial resolution.

5.3.2 Tomographic characterization of Surirella spiralis

We demonstrate aIDT's ability to characterize complex single cell organisms with intracellular resolution on a Surirella spiralis diatom sample. We acquired 24 intensity images under oblique illuminations and reconstructed the sample's RI across a 50 μm volume as shown in Fig. 5·5. The benefit of this technique is clearly shown

in its recovery of multi-scale features of the sample. aIDT recovers the characteristic Surirella spiralis saddle shape spanning the full 50 μm reconstructed volume (Fig. 5·5a-c). Within this large saddle, fine structures including silica frustules are also visible and well-resolved across multiple reconstructed slices (Fig. 5·5d-g) and the YZ cross-sectional views (Fig. 5·5h-i). To further illustrate this structure, Fig. 5·5(j) displays the RI rendered as a 3D volume [101] of Surirella spiralis. Line profiles across these 10 μm tall frustules in Fig. 5·5(k-n) demonstrate near diffraction-limited lateral resolution of 487nm and axial resolution of 3.4 μm.

5.3.3 RI tomography on cell clusters

aIDT quantitatively recovers both full cell-sized features and intracellular structures easily using a small set of intensity images from a single focal plane. These results make aIDT advantageous for biological research applications containing complex environments requiring simultaneous, multi-scale sample evaluation. In addition, the lack of sample scanning with this technique increases its utility for dynamic sample imaging where living objects easily move out-of-focus. We show aIDT's application to both of these cases in the subsequent sections.

We next apply aIDT to evaluating complex biological cell clusters and environments. Existing 2D phase imaging techniques are often used when imaging monolayers of cells. These integrated phase map techniques contain less useful information, however, when imaging cell clusters more commonly found in biological systems. Our aIDT technique overcomes this problem by recovering multiple, independent RI cross-sections across extended volumes. This approach enables better depth-sectioning of the sample such that larger biological structures with greater complexity can be evaluated without significant information loss.

We demonstrate this ability to recover complex biological environments on clusters of unstained human epithelial buccal cells distributed on a glass sample slide. A

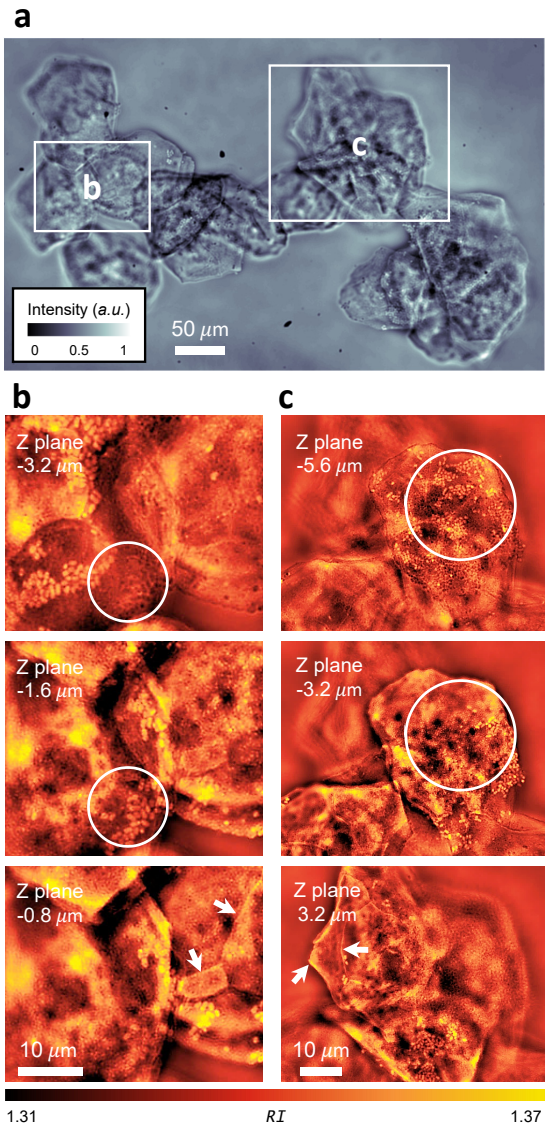

Figure 5·6: Single cell RI tomography of unstained human cheek cell clusters. (a) A sample raw intensity image under annular illumination. (b,c) Reconstructed RI cross-sections demonstrate the sectioning capability enabled by the aIDT. Additional examples are shown in Video 4 of [9].

sample normalized intensity image is shown in Fig. 5·6a showing the cell cluster's complexity and its defocused regions highlighting the sample's large volume. We take 24 intensity images and reconstruct the RI across a 16 μm volume. We expand two regions of the reconstructed RI in Fig. 5·6b,c highlighting our depth-sectioned

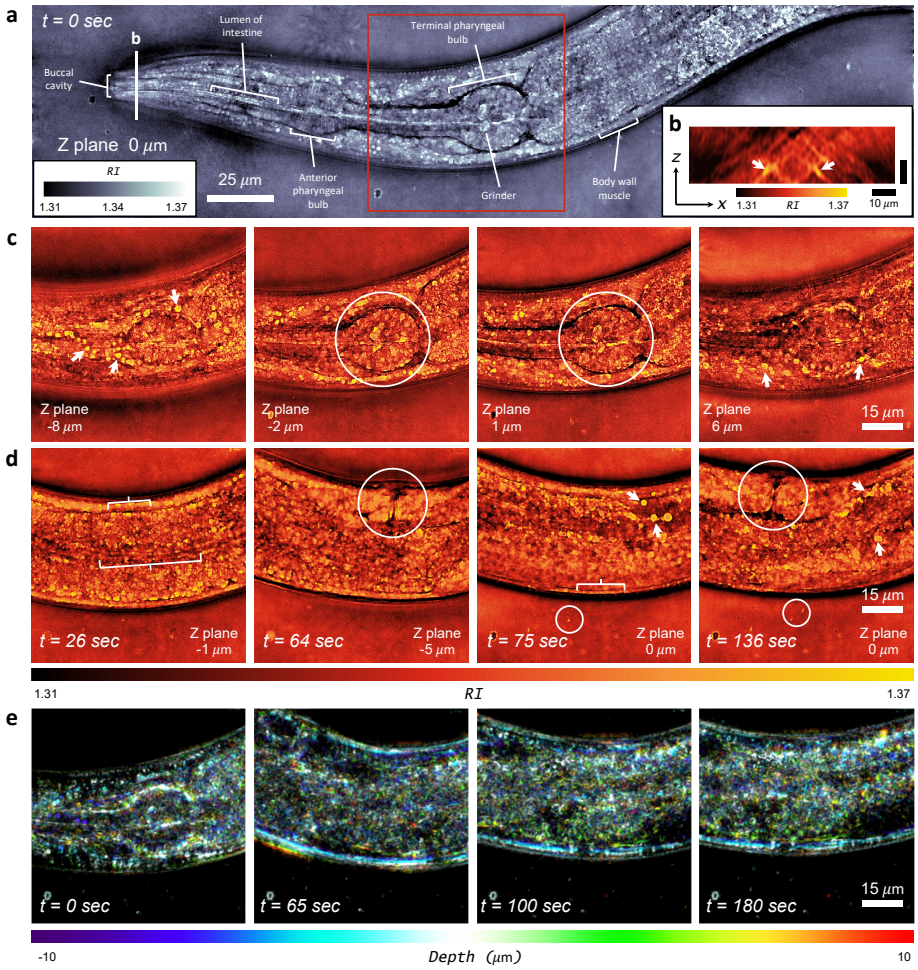

Figure 5·7: Time-lapse *in vitro* tomographic imaging of *C. elegans*. (a) Recovered RI slice located at central plane at $t = 0$ *sec*. The full *C. elegans* worm reconstruction visualization is shown in Video 5 of [9]. (b) RI stack section in $x - z$ plane close to the mouth of *C. elegans*. Buccal cavity of *C. elegans* is distinguishable (indicated by the white arrows). (c) RI distribution of worm at different z planes in the marked red square region at t = 0 sec. Time-lapse details are demonstrated in Video 6. (d) Visualizations and RI quantification of the *C. elegans* internal tissue structures at different time points and axial planes. (e) Depth color coding of 3D RI measurements of sample in the selected sub-region with fix position in the field of view. 4 different time points to illustrate the time lapse results of *C. elegans*.

reconstructions.

The benefit of aIDT when imaging complex environments is seen in its high-

resolution reconstructions across the entire cell volume. At each reconstructed slice we observe cellular membrane folds, cell boundaries, nuclei, and intracellular features with high resolution (Fig. 5·6b,c arrows). In addition, we recover native bacteria, likely a staphylococcus strain, distributed on the cells throughout the sample (Fig. 5·6b,c circles).

Quantifying the 3D RI distribution of entire cells, their subcellular structures, and external environment features such as bacteria has significant potential in biological research applications. The recovered volumetric RI distributions of cellular features enables the calculation of dry and buoyant mass, sphericity, and other morphometric descriptors used for cell profiling [102, 103]. Because subcellular and bacterial structures are also resolved, these parameters can be applied to subcellular features with aIDT. With aIDT's fast acquisition rates and large volume recovery, shown experimentally in the next section, longitudinal maps of structure mass and volume changes can be mapped in real-time throughout multi-cellular complex environments. Quantifying these factors could be highly beneficial to immunology and pathophysiology applications ,where longitudinal studies of parasite and bacterial interactions and induced morphological changes in cells carry critical information for understanding and mitigating infection [33, 104]. Furthermore, quantifying volumetric morphological changes of cellular and subcellular information also has significant utility in oncology for both differentiating cancer types and evaluating their response to drug and therapy treatments [34, 105, 106].

5.3.4 Dynamic RI tomography of C. elegans in vitro

A major advancement enabled by aIDT is the ability to perform high-speed *in vitro* tomographic imaging of biological samples using a small number of intensity-only measurements. This allows us to visualize 3D dynamical biological phenomena with minimal motion artifacts, which is particularly challenging using existing RI tomog-

raphy techniques. We demonstrate this ability on unstained, live *C. elegans* worms [107, 108] at a 10.6 Hz volume rate. We image a volume containing $333\times98\times21$ μm^3. In a time-lapse series, each image stack includes 8 frames (for reconstructing each RI volume) that were recorded with a 4.4 ms exposure time over a 3 min period to evaluate fast motions in a living *C. elegans*.

The reconstructed RI of the *C. elegans* worm is shown in Fig. 5·7. Reconstructed RI $x-y$ and $x-z$ cross-sections at the $z=0\mu$m plane at $t=0$ sec are shown in Fig. 5·7a and Fig. 5·7b, respectively. Figure 5·7c shows the RI distribution of the worm at different z planes in the marked region at $t=0$ sec. Figure 5·7d illustrates the RI distribution of the *C. elegans* internal tissue structures at different time points and axial planes. Depth-coded projections of our reconstructions are also provided in Fig. 5·7e, where the volumetric RI distribution is shown for several different time points. The full *C. elegans* worm reconstruction visualization is shown in Video 5 of [9]. The results show that aIDT is robust to motion artifacts and resolves internal features during high-speed worm motion, as clearly demonstrated in Video 6 of [9].

Our technique easily visualizes and provides RI quantification of the *C. elegans* internal tissues. The anterior and terminal pharyngeal bulbs are clearly resolved in our reconstruction (Fig. 5·7a,c) as well as the grinder and intestines (Fig. 5·7c circles, Fig. 5·7d long bracket). Lipid droplets and lysosomes are also distinguished in the worm head at different axial layers (Fig. 5·7c arrows). Within the worm body, we recover the vulva (Fig. 5·7d circles) across multiple axial slices, body wall muscles (Fig. 5·7d short brackets), and features resembling the worm's nerve cord (Fig. 5·7d). We also observe *E. coli* bacteria living and moving independently of the *C. elegans* (Fig. 5·7d small circles). Additional results on fixed *C. elegans* can be found in supplementary material and Video S2 of [9].

aIDT enables a simple, label-free approach for volumetric imaging in the bio-

logical research community. The tissues shown in Fig. 5·7 and Video 5 of [9] often undergo phenotypic changes from genetic mutations during biological studies [109]. Quantifying these tissue changes and studying their effect on live worm behavior in a natural, label-free setting would be highly beneficial in understanding the effects of targeted genetic mutations on living organisms. Because our technique captures bacteria motion concurrently with the *C. elegans*, aIDT could also evaluate multi-organism interactions and provide 3D bacteria tracking during longitudinal studies. The versatility of this technique in visualizing multiple tissue types means it has utility spanning from neurology to pathogenesis and wound healing [109].

5.3.5 aIDT reconstruction accuracy and sensitivity analysis

Having shown aIDT's utility for label-free dynamic biological sample imaging, we further evaluate the modality's *accuracy* and *sensitivity*. While the experimentally recovered volumes exhibit RI ranges matching expected biological values, the inherent variability of these specimens prevents quantitative analysis of the system's accuracy and sensitivity for recovering the true RI distribution and detecting small RI variations, respectively. These parameters were briefly explored for conventional IDT [110], but the lack of manufactured, well-characterized objects limited the accuracy and sensitivity analysis to thin glass structures with high-contrast RI distributions. These structures are not representative of most biological samples' RI range or size, and their high-contrast nature generates multiple-scattering behavior that invalidates the IDT model. Recent works [111, 112] show such experimental sensitivity analyses are possible in quantitative phase systems with rigorous testing using expensive hardware that was not readily available for the aIDT system. Thus, determining aIDT's accuracy and sensitivity is a challenging task. Here, we instead evaluate aIDT in simulation to determine its theoretical accuracy and sensitivity over the RI range present in our experimental data.

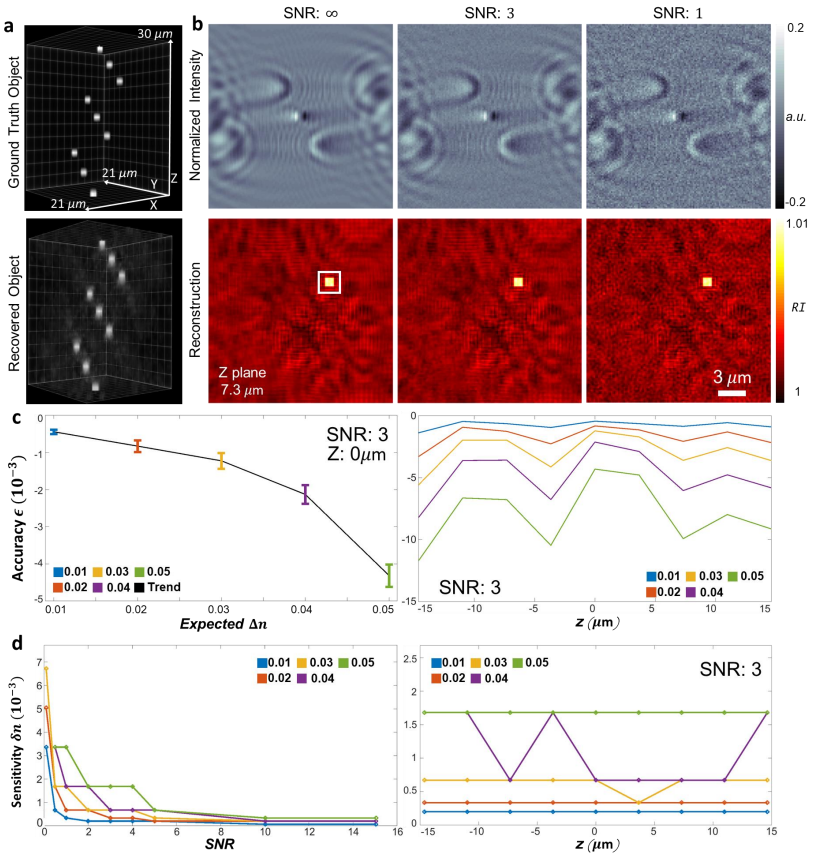

Figure 5·8: Simulation evaluating aIDT's accuracy and sensitivity. (a) The simulated cuboid array (Top) occupying a 21μm$\times 21\mu$m$\times 30\mu$m volume with its aIDT reconstruction (Bottom). (b) Simulated intensity images with decreasing SNR (Top) and their reconstructions at Z= 7.3μm (Bottom). The white box region is used to obtain the cuboid's RI. (c) Left: aIDT accuracy (ϵ) with object RI. The plot shows the average difference between the aIDT reconstruction and true RI across 100 realizations. The bars show the error's standard deviation. Right: aIDT accuracy with axial position. aIDT provides accurate RI recovery under low contrast ($\Delta n = 0.01 - 0.03$) objects and loses accuracy from highly scattering features ($\Delta n = 0.05$). The accuracy is stable over the object volume but fluctuates due to boundary artifacts. (d) aIDT sensitivity (δn) analysis as a function of SNR (Left) and axial position (Right) under the experimental SNR. aIDT's sensitivity to small RI variations depends on the object's RI contrast but maintains sensitivity above $\delta n = 0.002$ even at high RI contrast for SNR= 3. The sensitivity is constant along z for low-contrast objects and varies with increasing RI.

Our simulations were performed in MATLAB with three primary components: 1) a ground-truth object, 2) a rigorous forward model simulating the field through the object, and 3) our aIDT inversion algorithm. For the object, we generated 3×3 cuboid arrays inside a $21\times21\times30\mu\text{m}^3$ volume with variable RI (Fig. 5·8a). Each cuboid occupied a $0.97\times\ 0.97\times1.2\mu\text{m}^3$ volume and was spatially separated by 3.25μm and 2.4μm in lateral and axial dimensions, respectively. This separation recovers a single cuboid for each reconstructed aIDT slice over the same volume considered in our experiment. For the cuboid RI, we assumed a homogeneous imaging medium ($n_m = 1$) and generated arrays with RI range $RI = [1.0033, 1.0567]$ following the equation $RI = n_{\text{base}} + \delta n$, where $n_{\text{base}} = [1.01, 1.02, 1.03, 1.04, 1.05]$ and $\delta n = [-.0067, 0.0067]$. This large RI range allowed us to evaluate aIDT's accuracy over the contrast range observed in our experiments ($\Delta RI \leq 0.05$) and test aIDT's sensitivity to small RI variations at each n_{base} level. Here, the selected range of δn values corresponded to object phase variations between 1 and 100 mrad following $\phi = 2\pi\lambda^{-1}\Delta n\Delta h$. These parameters allowed the evaluation of both aIDT's accuracy and its sensitivity to small RI changes across a large contrast range.

With these objects, we simulated aIDT intensity images using the convergent Born series model [113]. This forward model efficiently simulates multiple-scattering through large object volumes using a convergent Born series expansion, making it ideal for evaluating aIDT's recovery capabilities. Using the illumination angles from our 8-LED illumination aIDT case, we simulated the scattered field through the cuboid array and propagated the final field through a 0.65 NA, 40× objective lens to obtain our intensity image stack. We repeated this simulation process for each cuboid array with differing refractive index and reconstruct the object volume using our aIDT algorithm. Furthermore, we added white Gaussian noise to the intensity images generating a Signal-to-Noise Ratio (SNR) ranging from 0 to 15, and generate

100 realizations for each SNR level. The SNR is quantified by the ratio between the signal contrast and noise level as SNR= $\sigma_{\text{Signal}}/\sigma_{\text{Noise}}$, where σ denotes the standard deviation. To determine the reconstruction accuracy, we compared the median recovered RI over each cuboid area (Fig. 5·8b, white square) with the ground-truth (GT) object filtered to match the reconstruction bandwidth. For the reconstruction sensitivity, we evaluated the separation between the small RI variations δn from the central RI value n_{base}. We used the Ashman's D test [114] for separating bimodal distributions to determine the minimum RI variation detectable for each SNR condition and considered two RI values to be separable when $D > 2$.

The simulation results for accuracy and sensitivity are summarized in Fig. 5·8c and d, respectively. Under SNR matching our experimental condition, Fig. 5·8c shows the average RI mismatch between our reconstruction and the ground truth across RI (Left) and axial position (Right) over the 100 realizations simulated for this SNR condition. The error bars show the standard deviation in this mismatch over these realizations. We obtain nearly equivalent RI recovery under low contrast ($\Delta n = 0.01-0.03$) and large underestimations for high-contrast objects at $\Delta n = 0.05$. Underestimations for large RI contrast objects was expected due to the presence of multiple-scattering invalidating the assumption of weak scattering in the aIDT model. An offset still exists between aIDT and the GT object for weakly scattering objects, which indicates the approximations we make in the aIDT model do reduce our system's accuracy. Across different axial positions, we observe mostly constant ϵ with greater offsets occurring for high-contrast features. Across all RI cases, we observe a periodic loss in accuracy over the tested axial range. This periodic loss corresponds to the cuboid appearing close to the volume boundary, suggesting that boundary condition issues exist in our simulation. Under weakly scattering conditions, we observe that this axial-dependent behavior is within our model's ϵ offset and are

considered to be minimal. We will solve these boundary condition issues in future work.

Figure 5·8d shows aIDT's theoretical sensitivity range over the imaging volume and across multiple SNR conditions. At SNR = 3, we have a minimum sensitivity to $\delta n = 2 \times 10^{-4}$ for low-contrast objects and $\delta n = 2 \times 10^{-3}$ for high-contrast features. Across different axial positions, aIDT's sensitivity shows mostly static sensitivity with greater fluctuations for objects with stronger contrast. These results indicate that aIDT exhibits high sensitivity to RI variations across the full reconstructed volume under low-contrast imaging conditions.

Our simulations show aIDT can provide high-accuracy and high-sensitivity RI recovery of volumetric biological samples under the proper conditions. Given weakly scattering samples within our model's validity range, aIDT can recover correct accurate RI values and detect small fluctuations to variations in the object's RI. This analysis is promising for biological sample evaluation where these small RI variations could correspond to the presence of pathogens in cells [33]. While this accuracy and sensitivity will suffer from experimental factors including objective aberrations and illumination misalignments, our simulations shown here indicate aIDT provides accurate, highly-sensitive volumetric recoveries of biological samples.

5.4 Discussion

We introduced aIDT, a high-speed, label-free, scanless non-interferometry based quantitative imaging tool for the 3D evaluation of unlabeled weakly scattering specimens. By combining an LED ring illumination unit with a standard brightfield microscope, we capture obliquely illuminated intensity images and perform 3D deconvolution to recover the slice-wise 3D RI distribution. The geometry fitting between illumination angle with the objective NA optimally encodes both low and high spatial frequen-

cies into each acquired image. This illumination scheme reduces the system's data requirement and allows us to image large 3D volumes of weakly-scattering samples at high speeds. We demonstrated the success of aIDT on various biological samples, from fixed microalgae, cheek cells, to living *C. elegans*. Finally, we showed aIDT's has high theoretical accuracy and sensitivity limits in simulation under a range of noisy imaging conditions. We believe this method will set an excellent foundation for other research projects and applications, and the aIDT has the potential as a tool of great biological interest by showing its use in monitoring cell morphology and dynamics in noninvasive high-speed measurements.

By illuminating at NAs matching the objective NA, the achievable phase imaging resolution can be extended to the incoherent diffraction limit. The proposed technique is mainly focus on high-speed *in vitro* biological sample imaging, so the limits of the RI mapping resolution of this work is the tradeoff between the working distance and objective NA. The quantification of the phase sensitivity is important for the aIDT imaging system as angle calibration quality, object RI, and the assumed slice thickness will also effect the aIDT's sensitivity. However, this requires more complicated setups and control samples to experimentally evaluate the system sensitivity, and more detailed analysis and enchantment of phase sensitivity are beyond the scope of this work.

The IDT model is currently limited by the single scattering approximation that cannot accurately recover multiple scattering objects. Recently, several groups have demonstrated multiple scattering models suitable for solving large-scale imaging problems [100, 31, 41, 42] that could be used with the aIDT setup. Our model-based reconstruction approach is also constrained by unknown experimental variabilities that are difficult to be fully parameterized via an analytical model, which may be overcome using emerging learning-based inversion techniques [92, 93, 91, 90, 97, 115, 116, 117].

Chapter 6

Multiple-scattering object recovery with intensity diffraction tomography using physical model simulator-trained neural networks

6.1 Overview

So far in this thesis, we have focused on the speed limitations of IDT and proposed two separate methods providing high volume-rate 3D QPI. The first approach in Chapter 4 provided a software-based speed improvement using multiplexed illumination optimized following the IDT linear model. This strategy sacrificed reconstruction quality to preserve the potential multi-modal imaging capabilities of the setup while using generic rectangular LED arrays [71]. In Chapter 5, a hardware-based speed improvement was discussed that simply replaced this rectangular array with an annular LED ring. This implementation optimized the illumination hardware based on the linear model to provide high-quality 3D QPI at 10Hz volume rates [9]. In all these implementations, the linear IDT model from [8] plays the pivotal role in deciding the illumination design and the reconstruction technique. This model's simple implemen-

tation, modularized 3D reconstruction capabilities, and efficient reconstruction of 3D objects make it a powerful tool already showing utility when evaluating a number of different biological specimens.

Despite its strengths, IDT's model limits the modality from recovering complex biological specimens. As discussed in Chapter 3, the model relies on the first Born approximation for solving the inhomogeneous Helmholtz equation and neglects all scattering events outside of the initial interaction between the incident field and the object. For dense samples with high RI contrast and large volume objects containing many scatterers, the nonlinear scattering events resulting from the continued interaction of the scattered field with the object become significant and non-negligible. Under such conditions, the IDT model and other linear models become invalid and underestimate the object's RI as shown in Sections 5.3.5 and 3.5.2) and the existing literature [41, 9, 42, 79]. This limitation prevents the quantitative analysis of complex biology including tissue biopsies and organoids. Recent efforts have shown improved RI estimates can be achieved using multiple-scattering model based iterative reconstruction algorithms [67, 31, 41, 42, 79]. However, this improved accuracy requires greater computation times that limit the evaluation of dynamic samples and large-scale objects in time-series studies. This trade-off in traditional model-based reconstruction methods between accuracy and computational efficiency has become a signficant limitation to the adoption of 3D QPI techniques for evaluating any arbitrary biological specimen.

In this chapter, we introduce a modern approach to overcome this bottleneck by melding closed-form single-scattering solutions with a fast and generalizable deep learning model. We illustrate this synergistic approach using the aIDT setup described in the prior chapter providing high volume-rate 3D QPI [9]. Our prior work demonstrated efficient 3D phase recovery with 10.6 Hz volume rates based on a linear

single-scattering model (Fig. 6·1(a)) [9]. To maintain fast and quantitative 3D phase imaging, we combine aIDT with the proposed deep learning model for live sample imaging with minimal artifacts on multiple-scattering specimens.

Deep learning has revolutionized the fields of computational microscopy with its ability to efficiently solve complex nonlinear inverse problems [117]. Existing DL models utilize different learning strategies from full "end-to-end" models for direct inversion [90, 93] to "guided" learning with embedded physical models or priors [82, 118, 119, 120, 121, 91]. The physics-guided approach is appealing as it encourages predicting physics-constrained features and reduces the "black box" nature of DL models. While many DL QPI developments have been in 2D [90, 93], recent works have expanded to 3D QPI using the physical approximant-guided learning approach [118, 121, 30]. These methods successfully improved RI predictions on red blood cells [118] and high-contrast manufactured samples [30, 121]. However, the generalizability of existing networks is limited due to the similarities between the training and testing data. For biological applications where objects of interest vary between specimen types, the potential for overfitting in existing learning approaches significantly limits their broad application. Furthermore, all existing networks for 3D QPI utilize 3D network structures and contain a large number of trainable parameters that further complicate the training data size and computational requirements for tomographic recovery.

Here, we overcome these existing limitations by leveraging multiple-scattering model simulation, efficient network architectures, and single-scattering approximants to achieve efficient multiple-scattering object recovery on dynamic biological samples. First, we develop a physical model simulator-based training approach bypassing the need for experimentally acquiring diverse training datasets with accessible ground truth information. To facilitate multiple-scattering feature recovery, we generate sim-

ulated object volumes using a fast and accurate Split-Step Non-Paraxial (SSNP) [42] multiple-scattering model (Fig. 6·1(b)). We enforce model generalizability with these object volumes by generating them from diverse natural images available from multiple open-source databases. Using aIDT's single-scattering based 3D estimates of these objects as the network's input, we train the network to enhance the 3D RI recovery and correct model-based artifacts using an approximant-guided learning strategy. Second, our network features a lightweight 2D "U-Net" structure to perform 3D reconstruction (Fig. 6·1(c), Fig. 6·3). We achieve efficient learning with this network by feeding five consecutive axial slices selected randomly from larger object volumes as a multi-channel input and predict only the central object slice (Fig. 6·1(c)). We show this approach efficiently encodes the depth and diffraction information and enables effective suppression of missing-cone and multiple-scattering artifacts in a highly scalable and computational efficient manner as compared to alternative 3D networks or other complex architectures [118, 121]. Third, to provide uniform prediction quality regardless of scattering strength, we devise a model-based data normalization procedure for homogenizing sample contrast prior to the model prediction. This novel data preprocessing procedure dramatically improves the model's generalizability in terms of RI contrast. In combination, we show that our network can be generalized to recover complex 3D biological samples of arbitrary size and structure.

We experimentally demonstrate our network's superior generalization capacity by predicting live epithelial buccal cells, *Caenorhabditis elegans* (*C. elegans*) worm samples (Fig. 6·1(d)), and fixed algae samples acquired using different experimental setups (Fig. 6·6, 6·7). We further highlight the robustness of our network by making time-series predictions on a living, dynamic worm. To quantitatively assess the reliability of our network's predictions, we adapt an image-space based evaluation procedure by feeding the network predicted RI into the multiple-scattering model and comparing

the calculated intensity and experimental measurements. Even for "unseen" illumination angles that are unused during model training or prediction, the calculated intensities from our predictions match well with experimental data. We show a 2-3× error reduction using our network over the aIDT linear model's estimates. Our result highlights that leveraging large-scale multiple-scattering modeling can obviate major overhead in physical data acquisition and train a reliable, highly generalizable deep learning model for imaging complex 3D biology.

6.2 Network design for optimal recovery

To optimally combine aIDT's reconstruction pipeline with a learning model, the network architecture must satisfy four key properties: 1) preserve the modality's speed, 2) provide arbitrary volume size recovery, 3) remove single-scattering approximation and missing-cone induced artifacts, and 4) equivalently recover weak and strongly scattering samples. The first two properties preserve the main benefits from the aIDT platform and linear model, while the latter two properties require improved performance over aIDT's model-based implementation. These factors require the network to learn efficient object predictions robust to scattering strengths without sacrificing aIDT's fast acquisition speed.

Satisfying the defined properties required specific choices in the data generation, training process, and network architecture as shown in Fig. 6·1 and Fig. 6·2. In generating a robust network for evaluating arbitrary object samples under supervised learning conditions, a significant constraint exists in acquiring sufficiently diverse experimental measurements to properly train a network without overfitting to specific object types. This limitation often restricts networks to recovering specific sample types [118, 121]. Here, we completely bypass this issue by *simulating* object volumes for training the network from diverse, readily available open-source natural image

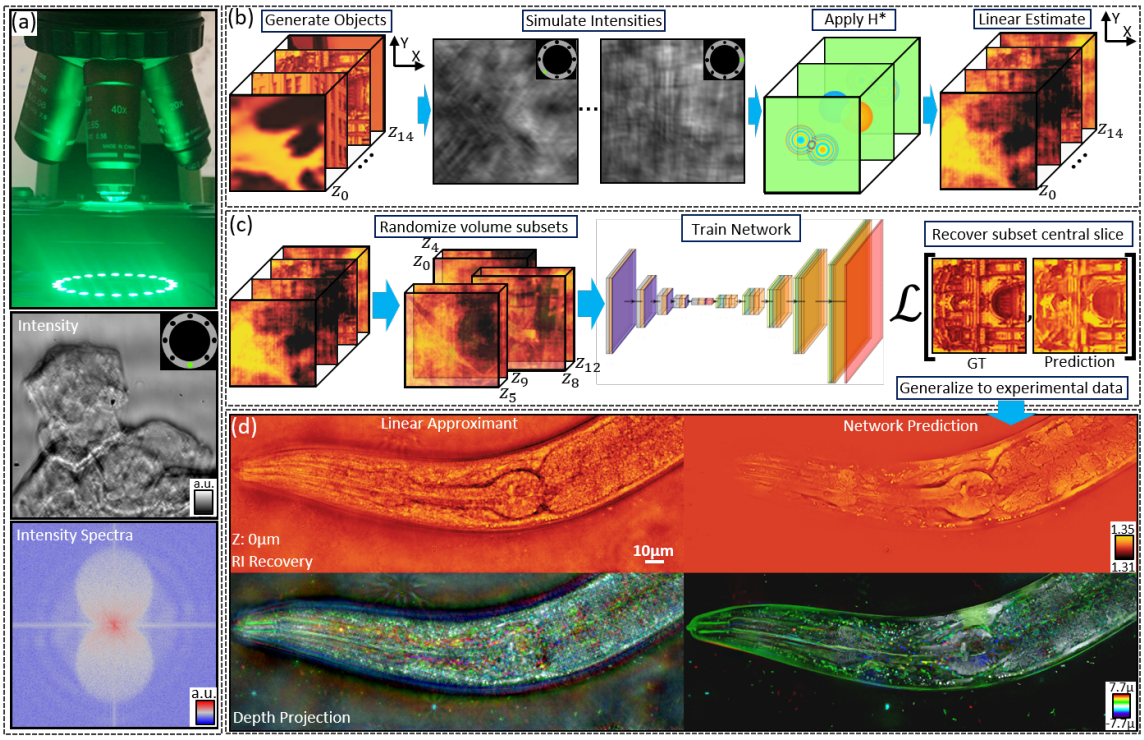

Figure 6·1: Overview of the physical model simulator-trained neural network for computational 3D phase imaging. (a) aIDT imaging setup (top) with example intensity image (middle) and intensity spectra (bottom) under single-LED oblique illumination. (b) Network training data simulation process. Natural images are randomly sorted into volumes with randomized RI, the SSNP multiple-scattering forward model is used to simulate the aIDT intensity images for each volume, and linear approximants are generated using the IDT model. (c) Training process for the proposed neural network. The simulated object volume approximants are randomly segmented into five slice subsets on each training mini-batch and fed into the network to recover the central volume slice. (d) Example application of the network on an experimentally measured *C. elegans* worm compared to the aIDT linear object estimate with in-focus RI slice reconstructions (top) and color-coded depth projections (bottom). Results demonstrate network generalization, enhanced depth sectioning, and improved feature recovery using the proposed network.

datasets. Randomly selecting natural images from these datasets, we stack these images into 3D volumes and assign them random RI values to create weak and strongly scattering media. We then leverage a highly efficient and accurate SSNP forward

model [42] to generate intensity images with the same physical parameters as the experimental aIDT setup (Fig. 6·1(b)) [9]. This simulator provides a rigorous physical model of the multiple-scattering through an object using a non-paraxial beam propagation-based approach accounting for both the scattered field and its first-order axial derivative at each object slice [42]. Using SSNP allows easy, rapid generation of a large diverse dataset for training the network while the use of natural images helps prevent overfitting from their high entropy [122]. With these images, we can obtain linear model approximants of the object volumes using the aIDT model, which we use as the network inputs for training. Details on the simulation process for this dataset are found in the materials and methods section below.

With this simulated training dataset, we next develop a training process to help the network recover volumes of arbitrary RI contrast and size. A significant challenge in recovering both weak and strongly scattering objects with a single learning model is the heterogeneity of the data distribution. When training directly on the simulated dataset, we observe that the larger approximant error from strongly scattering objects results in network overfitting to correct high scattering strength features while over-smoothing weak scattering structures. We overcome this issue with a linear model-based data normalization scheme, detailed in the materials and methods, to homogenize the dataset and enable high-quality object predictions regardless of scattering strength.

To enable arbitrary volume prediction, we introduce a randomized sampling procedure to the training process. Due to the sparse illumination and undersampling of the object's 3D Fourier information in aIDT's limited angle tomography design, the object's linear approximant exhibits anisotropic, axially varying, and object-dependent missing cone artifacts throughout the volume. These artifacts exhibit unique behavior for each object and axial slice that necessitate the network to learn the entire 3D

multiple-scattering process. To facilitate this process, we present random consecutive five slice subsets of an object as the input within each training mini-batch and predict the central slice from each subvolume using a modified 2D U-Net (Fig. 6·1(c), Fig. 6·3). This procedure presents 3D information as the multi-channel input (i.e. feature maps), from which the network can extract 3D information with an efficient and easily trainable 2D network. By randomizing the subvolume input during training, the network is forced to learn object recovery only from relative inter-slice relations allowing for arbitrary volume predictions. Details on the training procedure for this network and its architecture can be found in the materials and methods section. Once trained, this network can be sequentially applied through the entire object volume to perform 3D predictions and has been tested on both unseen simulated objects and experimental data such as the *C. elegans* worm in Fig. 6·1(d). We go into detail on the elements of this simulator-trained deep learning pipeline with aIDT in the following section.

6.3 Materials and Methods

6.3.1 aIDT experimental imaging setups

The primary experimental aIDT setup consists of a commercial transmission microscope (E200, Nikon) equipped with an off-the-shelf LED ring (1586, Adafruit), a 0.65 NA, 40× objective (MRL00402, Nikon), and an sCMOS camera (Panda 4.2, PCO, pixel size 6.5μm). The LED ring is placed $\approx$ 35mm from the sample plane to generate oblique quasi-plane wave with illumination angles $NA_i \approx 0.63$. Each aIDT measurement used for approximant generation included eight intensity images from a subset of the ring's 24 LEDs using green (515nm) illumination. Each image was acquired with a 10ms exposure time providing a camera-limited 10.6 Hz acquisition speed for a single measurement. Additional information regarding this setup and the

post-processing calibration procedures are discussed in detail in [9].

Two alternative aIDT setups were also tested to evaluate the network's generalization capabilities for samples measured with different illumination sources and lower NA objectives. The diatom algae samples shown in the main text Fig. 5(b), (d) and Fig. 6·6 were acquired using a higher density LED source array (Adafruit, 607) with 120 annular illuminations ($NA_i \approx 0.63$) used for image space comparison in Fig. 5(b),(d). The low NA ($NA = 0.25$) imaging setup utilized the same dense array with 36 annular illuminations ($NA_i \approx 0.24$) of the fixed *spirogyra* sample shown in Fig. 6·7. Matching the main setup, only eight annular intensity images were used for each sample to perform the model-based reconstruction. Each measurement set underwent equivalent post-processing calibration procedures prior to reconstruction as used in the main setup [9].

6.3.2 Training dataset generation

Creating the training data for the learned IDT implementation required three steps: 1) generating sufficient large-volume object quantities with unique features, 2) simulating intensity images using a multiple-scattering forward model, and 3) recovering object approximants using the aIDT linear inversion model. Unique object volumes were generated from randomly selecting 128×128 natural image patches obtained from multiple open-source databases including SUN397 [123], Faces-LFW [124], Caltech256 [125], NWPU-RESISC45 [126], Stanford Online Products [127], CIFAR-10 [128], and Stanford Dogs [129] datasets. This random selection process was done from an equal selection of patches from each database to allow for equal probability of image type selection. For each object volume, fifteen random selections were made with a 70/30 probability of selecting from the natural image list or a null slice containing no scatterers, respectively. This process was empirically found to allow for sparse, weakly scattering samples and dense, multiple-scattering objects to be created

simultaneously. The final image volumes consisted of $128 \times 128 \times 15$ voxels with a voxel size of $0.1625 \times 0.1625 \times 1.1\mu m^3$. The axial voxel size was chosen to match the microscope's depth-of-field (DOF). Following volume generation, the volume was normalized between $[-1, 1]$ and multiplied by a random RI value $n \in [0, 0.05]$ to generate the scattering object volume. A background RI value matching water ($n = 1.33$) was subsequently added to mimic evaluating biological samples in aqueous media.

The intensity images for each volume were generated using the recently developed SSNP multiple-scattering simulator [42] using version 3.6.9 of the Python programming platform. For simulation, the generated volumes were padded with uniform values matching the background RI and the edges between this padding and the image were Gaussian filtered to reduce boundary artifacts. The volume was remeshed axially to a size of $256 \times 256 \times 150$ voxels to provide smaller step sizes for generating valid SSNP simulations. The simulation parameters used for SSNP matched the experimental aIDT setup, and a total of eight intensity images were generated for each object matching aIDT's illumination scheme. The images were subsequently normalized and background-subtracted following the aIDT procedures [9].

The IDT linear inverse scattering model was implemented for recovering approximants of each object for training [9]. Fifteen transfer functions were generated to recover the original 15 simulated object slices with illumination angles, pupil size, imaging wavelength, and sample thickness matching the aIDT experimental setup [9]. Tikhonov regularization with a manually determined threshold value of 100 was implemented to recover each slice of the simulated object volume. This regularization parameter, while traditionally chosen separately for each object based on an estimate of its signal-to-background (SBR) ratio [71], was fixed for this training set to provide examples of under-regularized and over-regularized objects to the network that can occur in practice due to user error. This process of object generation, image simu-

lation, and reconstruction was repeated until 10,000 training objects were obtained. 9,990 of these objects were used for training with five volumes reserved for validation and testing, respectively. Additionally, a separate testing set of 1000 objects were generated using the same procedure with the previously unseen Food-101 dataset [11] for evaluating the network performance in simulation without potential overfitting issues.

6.3.3 Model-based linear fitting

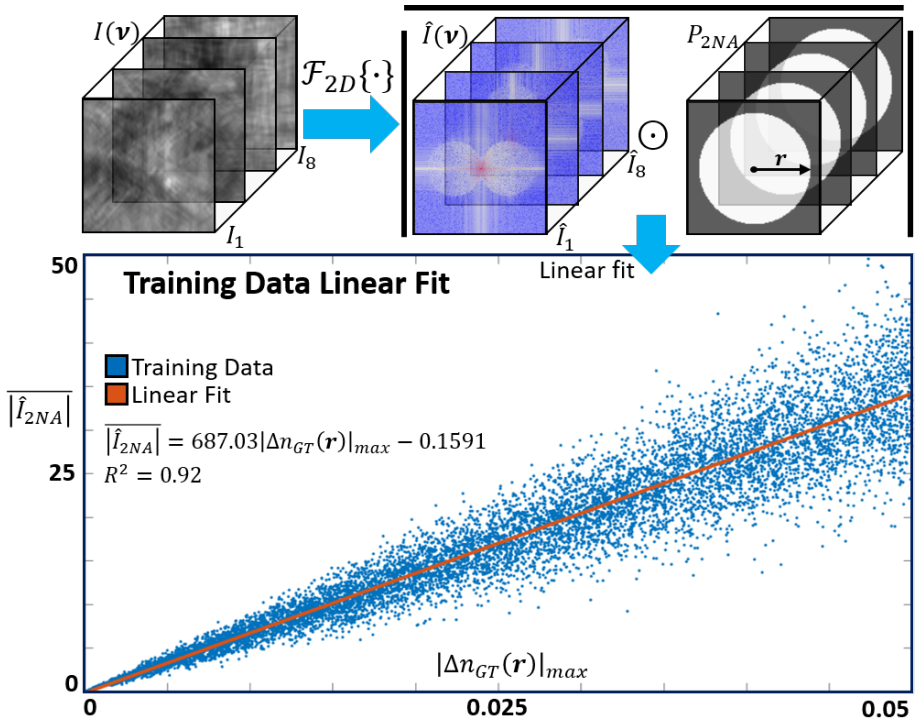

Figure 6·2: Pipeline for obtaining the linear fit between the average intensity spectral magnitude and the ground truth refractive index. The intensity images simulated using the SSNP forward model for the training dataset are Fourier transformed and filtered using a circular binary filter matching the incoherent bandwidth ($r = 2\text{NA}$). The magnitude of each spectral term is obtained, averaged over the eight simulated intensity images, and plotted as a function of the object's maximum RI. This result provides a linear fit with a strong correlation ($R^2 = 0.92$).

The linear fitting procedure used to homogenize the input object's distribution is shown in Fig. 6·2. We generate this fit using the simulated intensity images of our training dataset generated using the SSNP physical model and the underlying object's peak RI. Because the intensity spectra scales with the object's RI and quantity of scattering features [44], we apply a Fourier transform to the eight intensity images and filter spectra based on the maximum incoherent bandwidth ($r = 2NA$) recovered in the experimental setup. This approach captures all field information from the sample and was empirically found to provide the best normalization procedure. For the fit, we take the magnitude of this bandwidth information and find the average value over all eight intensity images

$$\overline{|\hat{I}(\boldsymbol{\nu}) \odot P_{2NA}(\boldsymbol{\nu})|} = \alpha \Delta n_{max} + \beta, \tag{6.1}$$

where $\hat{I}(\boldsymbol{\nu})$ denotes the intensity spectra with spatial frequency coordinates $\boldsymbol{\nu}$, $\odot$ is the Hadamard product, $P_{2NA}(\boldsymbol{\nu})$ is the circular bandwidth binary mask with radius 2NA (Fig. 6·2), α, β are the linear coefficients, and Δn_{max} is the true object's peak RI. The resulting fit from applying this approach to our simulated training dataset shows a strong linear correlation ($R^2 = 0.92$) between the intensity spectra and peak RI with coefficients found to be $\alpha = 687.03$ and $\beta = -0.1591$. This linear correlation shows less agreement at stronger RI contrast ($\Delta n > 0.03$) due to the increasing nonlinear scattering spectral contribution and the variation in scatterer quantity within each natural image object volume. Despite these factors generating worse agreement, the resulting linear fit provides an efficient, sufficiently strong method for estimating the object's peak RI from the intensity spectra. With this RI estimate, we can normalize the aIDT model object approximant close to $[-1, 1]$ enabling dataset homogenization and uniform object recovery from the network regardless of RI.

6.3.4 Network training and architecture

Following normalization, the network was trained using using the simulated dataset for 100 epochs using the mean absolute error (MAE) loss function, Adam optimization [130] with a 10^{-3} learning rate and batch size of 20. The network used five consecutive randomly selected slices from the object approximants as inputs to predict the central slice of each subvolume. This subvolume was randomly selected from the training data on each mini-batch during training to improve arbitrary volume generalization. After training, the network is applied iteratively through the slices of the model-based object estimate and multiplied by the estimated peak RI to recover the final object volume.

6.3.5 Network architecture

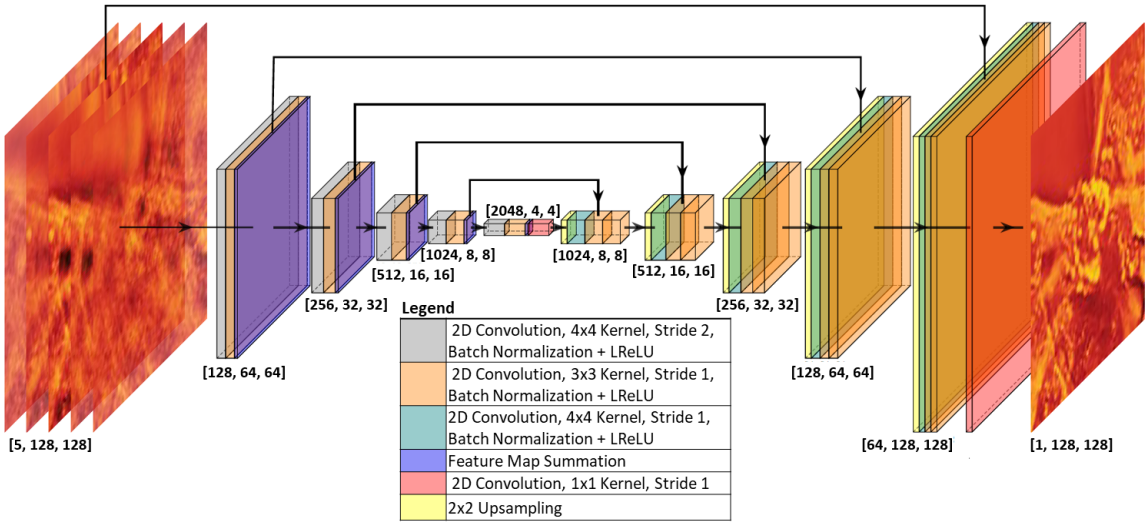

Figure 6·3: Proposed modified 2D U-Net architecture. Five consecutive axial slices from the aIDT linear approximant are fed into the network and the central slice is predicted on the output. Architecture details are provided in section 6.3. Network visualization generated using [10].

Our network follows a modified 2D U-Net architecture [131] and was implemented

using Tensorflow 2.0.0 with Keras. The network, shown in Fig. 6·3, consists of five encoding and decoding layers with 128 initial filter channels and skip connections preserving high-resolution object features throughout the network. The encoding blocks consist of two 2D convolution operations followed by a summation of their output feature maps in a residual connection. The first convolution downsamples the prior feature map using a 4×4 filter kernel size with a stride of 2, while the second convolution maintains feature size with a 3×3 kernel size with a stride of 1. Both convolutions are followed by batch normalization and a Leaky Rectified Linear Unit (LReLU) activation function [132]. At the bottleneck, the network uses an additional 2D convolution with a 1×1 filter kernel with a stride of 1 for blending the latent feature information of the 3D input. The resulting feature map is decoded using a process of 2×2 upsampling followed by a 4×4 2D convolution with a stride of 1 and two sets of 2D convolution operations with 3×3 convolution kernels also with a stride of 1. Each convolution operation is followed by batch normalization and LReLU. This design recovers the original image size without incurring checkerboard artifacts from transpose convolution operations and provides sufficient filters for learning image features. For the final prediction, the network performs a 2D convolution with 1×1 kernels with no nonlinear activation to predict the central object slice.

6.4 Results

6.4.1 Predictions on unseen simulated object volumes

We first show our network's predictions on unseen simulated object volumes in Fig. 6·4. Here, we compared the network and model-based reconstructions of 1000 unseen simulated object volumes generated from the food-101 open-source dataset [11]. These objects avoid potential network overfitting issues by utilized unseen simulated volumes and a new dataset not used in the training dataset generation. Fig. 6·4(a) shows ex-

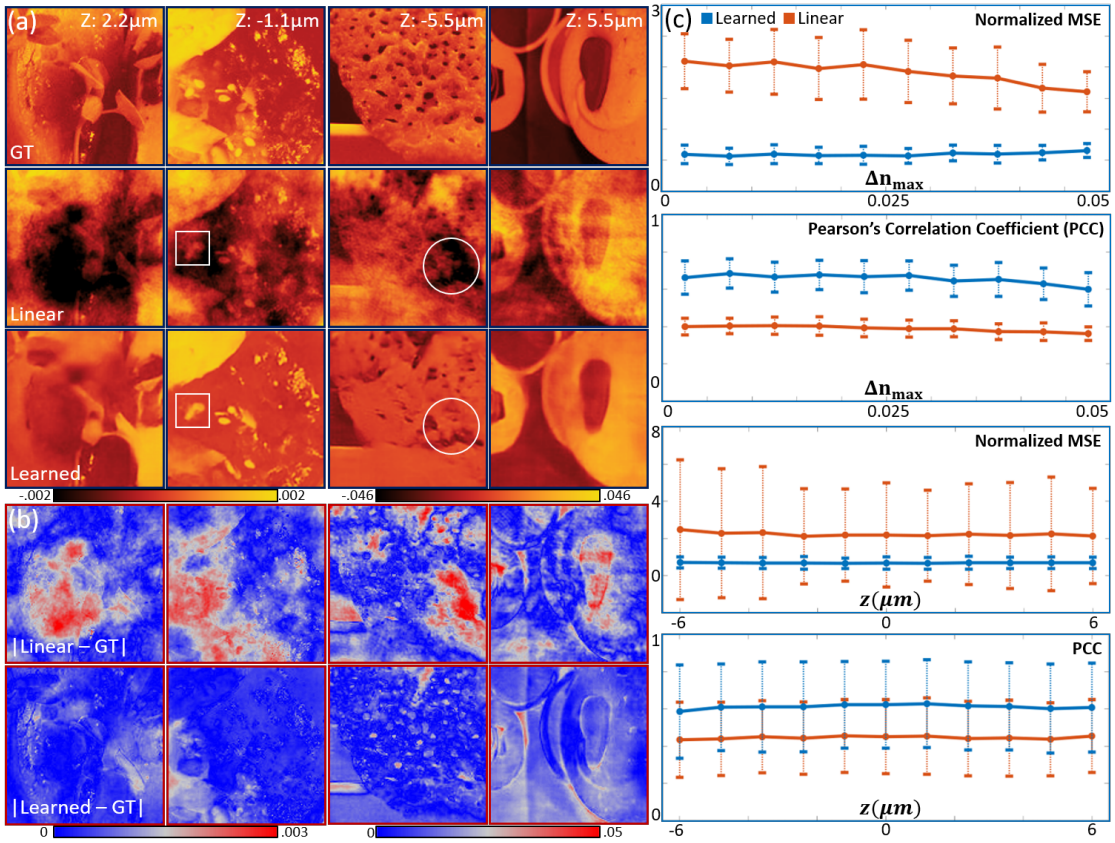

Figure 6·4: Predictions on unseen simulated object volumes generated from the Food-101 open-source dataset [11]. (a) compares the ground truth (GT), linear aIDT model, and learned network prediction of weakly scattering (left) and strongly scattering (right) simulated object volumes at two different axial positions. (b) shows pixel-wise absolute error maps for the axial positions shown in part (a) with larger error being shown in the linear model results. (c) shows the network and linear model error as a function of the GT peak RI (Top) and object axial slice (Bottom) using the normalized mean-squared error (nMSE) and Pearson's Correlation Coefficient(PCC) on 1000 unseen simulated volumes. The learned prediction shows lower nMSE, higher PCC, and smaller standard deviation (error bars) than the linear model indicating improved object recovery.

ample visual comparisons between ground truth object volumes, aIDT linear model reconstructions, and learned object predictions for weak (Left) and strongly scattering (Right) samples along with their pixel-wise absolute error maps (Fig. 6·4(b)). In

Fig. 6·4(c), we show the average error for the linear and learned volume predictions of 1000 simulated volumes as a function of peak RI (Top) and axial slice (Bottom). For evaluating the error in the recovered RI, we use the normalized Mean-Squared Error (nMSE) metric

$$nMSE = \frac{||\widetilde{\Delta n}(\boldsymbol{r}) - \Delta n(\boldsymbol{r})||^2}{||\Delta n(\boldsymbol{r})||^2}, \tag{6.2}$$

where $\widetilde{\cdot}$ denotes the model-based or network-based volume estimate and $\boldsymbol{r}$ denotes the spatial coordinates. We use the Pearson's Correlation Coefficient (PCC) metric for evaluating our network's performance in recovering the object's features and structural content

$$PCC = \frac{\sum_{\boldsymbol{r}} (\widetilde{\Delta n}(\boldsymbol{r}) - \mu_{\widetilde{\Delta n}})(\Delta n(\boldsymbol{r}) - \mu_{\Delta n})}{\sqrt{\sum_{\boldsymbol{r}} (\widetilde{\Delta n}(\boldsymbol{r}) - \mu_{\widetilde{\Delta n}})^2} \sqrt{\sum_{\boldsymbol{r}} (\Delta n(\boldsymbol{r}) - \mu_{\Delta n})^2}}, \tag{6.3}$$

where μ denotes the average value of the estimated or ground truth volume. For evaluating the error with scattering strength, we quantize the volumetric error from the dataset based on the ground truth peak RI into ten bins centered at $\Delta n_{max} = [0.0025, 0.0475$ with a step-size and width of 0.005. This binning process accumulates approximately 100 volumes per point from which we obtain an average error and standard deviation. For evaluating the prediction stability through the volume, we also average the slice-wise error across the dataset to determine whether slice-dependent variations exist in the network predictions. Because nMSE and PCC cannot be applied to null slices, the predictions of these slices are removed for the error measurements compared with slice position.

The network prediction results shown in Fig. 6·4 highlight the improvements of our network prediction over the linear model. Fig. 6·4 shows the linear reconstruction limits the recovery of certain object features due to the presence of low-frequency, missing cone-generated artifacts (Fig. 6·4(b)). The network shows these artifacts are

predominantly removed based on the lower valued error maps of Fig. 6·4(b), and high-resolution features are recoverable in these corrupted regions (Fig. 6·4(a), white square). The network experiences greater difficulty under strong scattering conditions, however, when the strength of these artifacts can completely mask a feature of interest (Fig. 6·4(a), white circle). As shown in Fig. 6·4(b), this stronger corruption does result in high-frequency feature loss and larger overall error in the network prediction. When compared over 1000 unseen simulated objects in Fig. 6·4(c), the network outperforms the linear model despite this increased error at high scattering strength. Over the full volume, Fig. 6·4(c) shows the learned prediction exhibits lower nMSE with smaller variation in the predictions than the linear model while having a higher PCC. These results indicate the network is recovering both the object's RI values and structural content well despite being from unseen simulated objects. Across all the recovered slices, we further see minimal variation in the nMSE and PCC indicating stable object recovery regardless of axial position (Fig. 6·4(c), bottom). These results indicate our network is robust to recovering objects regardless of RI and structure with feature loss attributed primarily to losses in the linear model input.

6.4.2 Weakly scattering object recovery

Following application of our network on unseen simulated data, we applied our trained network to weakly scattering epithelial buccal cell clusters in aqueous media ($n_0 = 1.33$) (Fig. 6·5). Figure 6·5(a) compares the linear (lower left) and learned (upper right) depth-coded projections of the cell cluster volumes with outset comparisons of the RI at different slices in Fig. 6·5(c). Fig. 6·5(b) shows a volume rendering of a cell cluster segment from our network with maximum intensity projections (MIP) in XY, YZ, and XZ.

Compared with the linear case, the learned object prediction shows significant

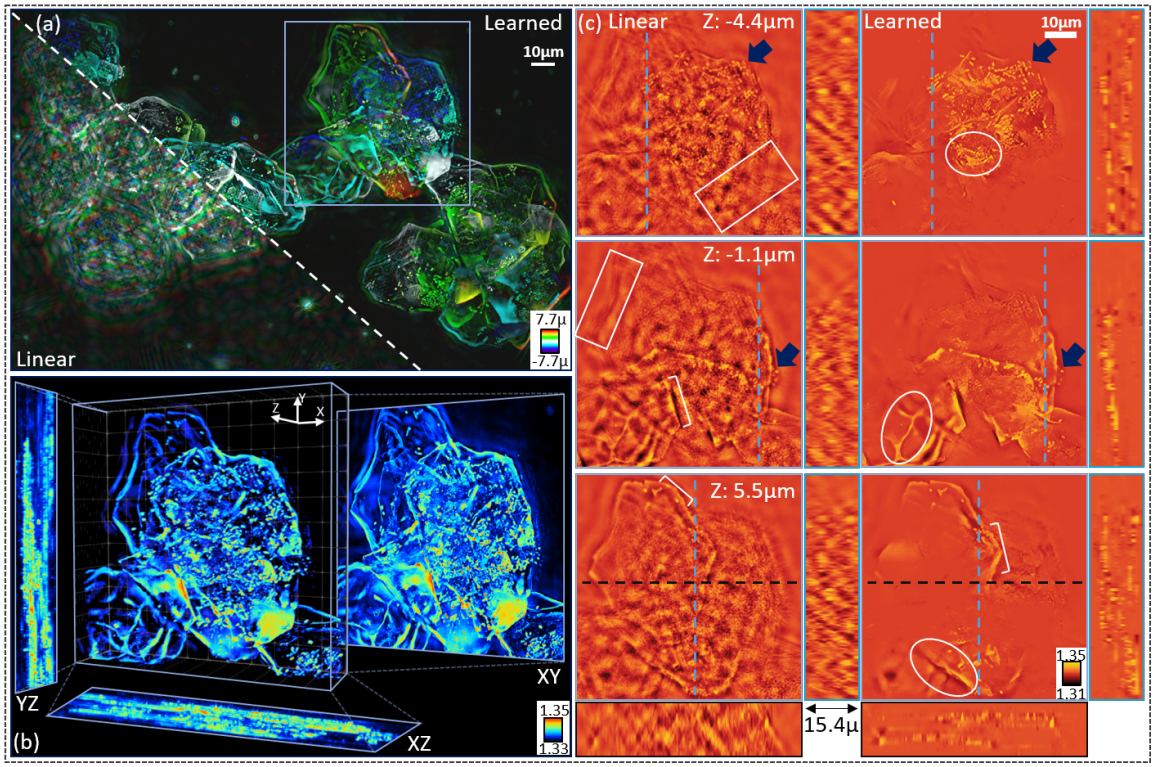

Figure 6·5: Prediction results of weakly scattering epithelial buccal cells. (a) Color-coded depth projections using the aIDT linear model (lower left) and learned result (upper right). (b) 3D rendering of the learned reconstruction outset from the purple region in (a). (c) RI slice reconstructions, XZ, and YZ cross-sections from the linear (left) and learned (right) volume predictions. White squares show poor depth sectioning in the linear model that is corrected with the learned results, while blue arrows highlight native bacteria features and white circles show enhanced cell edge detection in the learned result.

noise suppression and object feature enhancement. Shown in the projection of Fig. 6·5(a) and the cross-sections of Fig. 6·5(c), the linear model generates strong missing cone artifacts corrupting the reconstructed features. While lateral cross-section images show cell edges (Fig. 6·5(c), white brackets) and native bacteria (Fig. 6·5(c), blue arrows) are visible with the linear estimate, the missing cone artifacts reduce feature visibility and confound the true morphology of cellular structures (Fig. 6·5(c), white boxes). In contrast, the learned result maintains or improves recovery of these bi-

ological features (Fig. 6·5(c), white circles) and removes the model-induced missing cone artifacts as shown in the XZ and YZ cross-sections. These improvements provide clearly distinguishable 3D volumes of the cellular structure (Fig. 6·5(b)) allowing easier evaluation of the sample's morphology. Furthermore, the similar recovered RI values of the cell's edges and bacteria between the linear estimate and network prediction suggests the network recovers the correct quantitative values in weakly scattering media. We further evaluate this quantitative recovery in section 6.4.6. These results provide encouraging evidence that our network generalizes well to recovering weakly scattering, experimentally measured biological samples of arbitrary size, structure, and contrast.

6.4.3 Network generalization to unseen samples, imaging systems

Showing good generalization from simulated to experimental data, we further evaluated the capabilities of our network in predicting object volumes within different imaging mediums and a different optical setup. These volumes consisted of a diatom sample embedded in glycerin ($n_0 = 1.45$) and a *spirogyra* sample measured using a low magnification (NA = 0.25, 10×) aIDT configuration. The first sample changes the assumed imaging medium from that used in training, while the second sample changes the physical imaging setup. These factors alter the missing cone artifact strength and structure throughout the volume and present unseen physical modifications that test whether the network generalizes to recovering objects under different imaging conditions. We discuss each of these conditions in more detail below.

Diatom sample in high contrast media

The model-based reconstructions and network predictions of a diatom algae sample embedded in glycerin ($n_0 = 1.45$) are shown in Fig. 6·6. The depth-coded projection

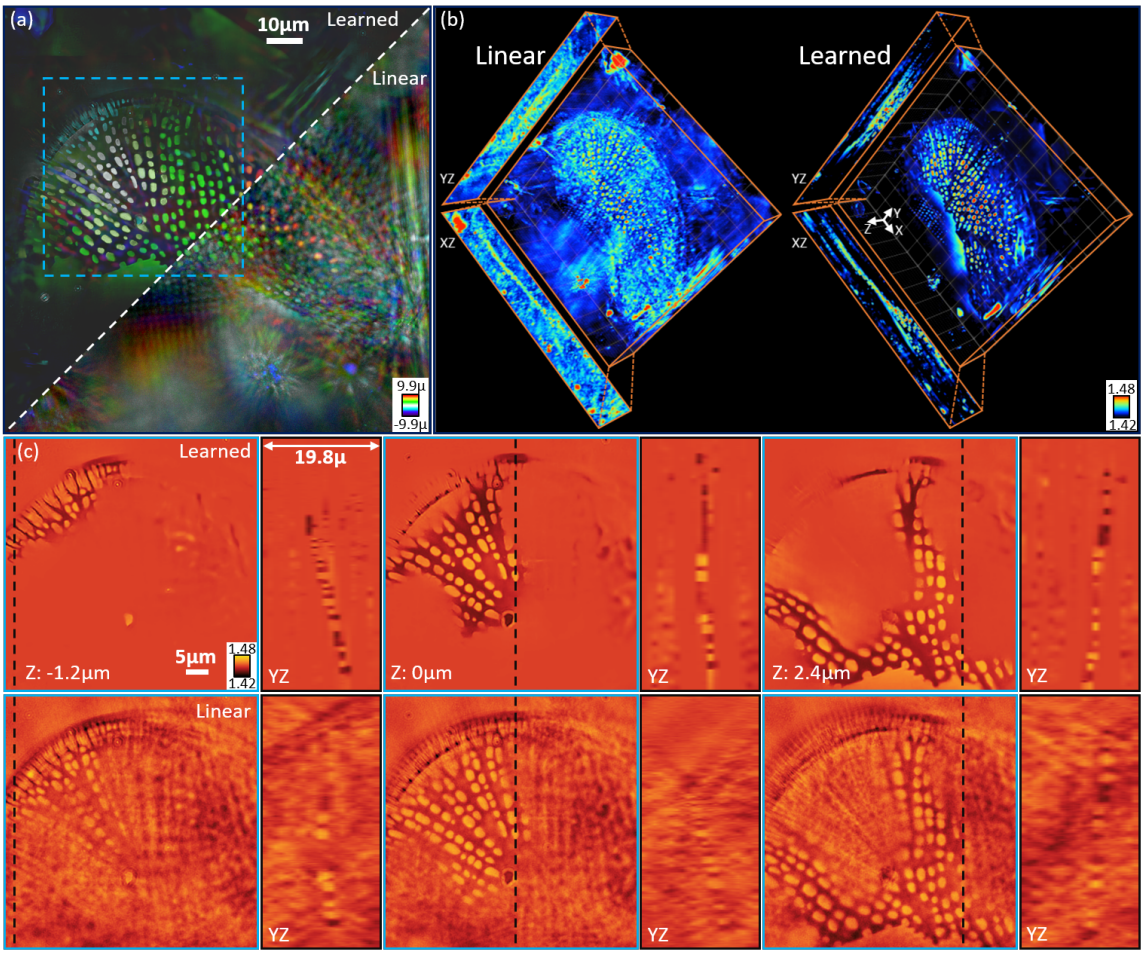

Figure 6·6: Linear and learned reconstructions of a diatom algae sample in glycerin media ($n_0 = 1.45$). (a) shows the depth-coded projection through the learned (upper left) and linear (lower right) recovered object volumes with significant denoising and feature recovery present with the learned result. (b) compares the 3D renderings and maximum intensity projections (MIP) for the reconstructed volumes showing enhanced visibility with the learned result. (c) shows slice-wise XY and YZ comparisons of the recovered biological diatom sample's RI throughout the volume. The learned result removes missing cone artifacts and cleanly separates the sample features throughout the volume. Renderings generated using [12].

through the sample comparing the linear and predicted objects is shown in Fig. 6·6(a) with 3D rendering comparisons in (b), and RI slice and cross-section comparisons of the model-based and network-recovered objects in (c). Following the prediction

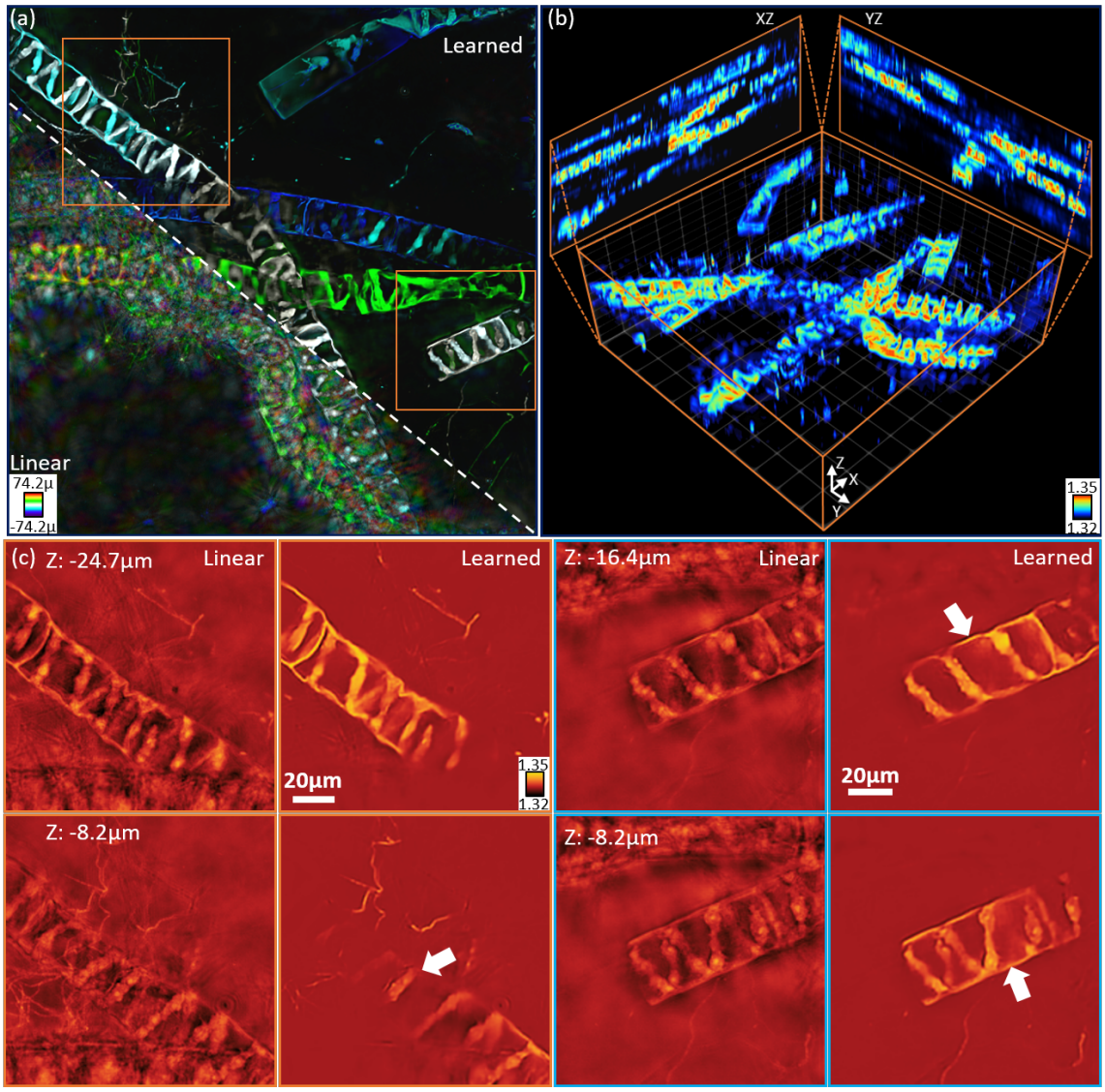

Figure 6·7: Linear and learned reconstruction comparison of *Spirogyra* in aqueous media ($n_0 = 1.33$) using a low NA aIDT setup ($NA = 0.25$). (a) Depth-coded projection comparing the linear and learned object predictions spanning 148μm, (b) 3D rendering of the learned *spirogyra* sample recovery with XZ and YZ MIP. The artifact removal and strong feature recovery provide enhanced depth sectioning throughout the volume. (c) RI slice-wise comparisons of the linear and learned reconstructions through the volume. The learned network's better depth sectioning removes defocused sample features (white arrows) and show stronger RI recovery than the linear model. Renderings generated using [12].

results shown in the main text, the network provides missing cone artifact removal, enhanced depth sectioning, and improved feature recovery over the aIDT linear model reconstructions. Despite the different RI medium, the diatom structure is well recovered with the network and the structure is clearly defined throughout the volume (Fig. 6·6(b) MIP,(c) YZ sections). Compared to the linear model, the network shows significant depth sectioning improvement of the diatom's structure that results in improved lateral sample views as well. These results illustrate our network's implementation is robust to sample imaging mediums, opening the ability to evaluate other samples embedded in higher or lower density media.

Spirogyra samples with low NA setup

Reconstructions of the *Spirogyra* sample evaluated with the low NA aIDT setup are shown in Fig. 6·7. Comparisons of the linear and learned reconstructions as depth projections are shown in Fig. 6·7(a) with a rendering of the network-recovered volume in (b), and (c) compares individual recovered RI slices of both reconstruction techniques. Despite the new imaging setup, the object predictions show artifact-free recovery of the algae sample with enhance depth sectioning providing clear visuals of the algae fragments (Fig. 6·7(b), XZ and YZ MIP). This is further highlighted in Fig. 6·7(c), where white arrows show the *spirogyra*'s helical structure is now well separated into different axial planes without the missing cone artifacts of the linear mode reconstruction. This separation is also visible in the color coding variation of the algae helical structure in Fig. 6·7(a). In addition, these features exhibit higher RI indicating the linear model could be underestimating the object's RI. These results show our network generalizes well to different imaging setup configurations as well as different sample types.

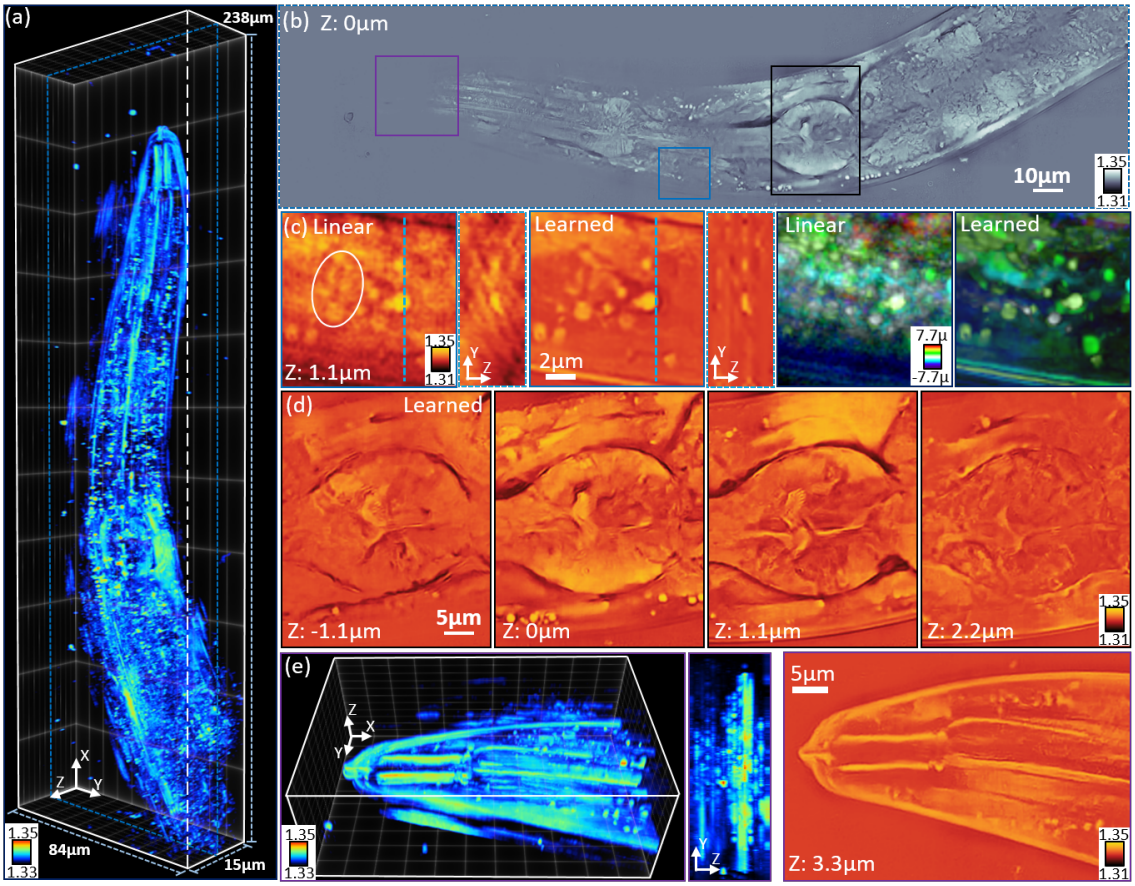

Figure 6·8: Prediction results of multiple-scattering *C. elegans* worm sample. (a) Volume rendering of the prediction showing the full volume network recovery. (b) Central slice reconstruction with outsets of lipid droplets (light blue), pharyngeal bulb (black) and buccal cavity (purple). (c) Outset comparing the linear aIDT reconstruction and learned prediction of lipid droplets in the sample with RI slice, YZ cross-sections, and color-coded projections. (d) Consecutive axial slices of the terminal pharyngeal bulb with clear recovery of the worm's grinder organ. High-resolution features are recovered with our network at 1.1μm, (e) Rendering, maximum intensity projection along YZ plane, and RI slice of the worm's buccal cavity. Results show features at defocused planes are well recovered with our network.

6.4.4 Multiple-scattering object recovery

To evaluate the network's capabilities on stronger scattering media, we applied our learned model to a *C. elegans* worm sample as shown in Figure 6·8. Here, the

figure shows a 3D rendered worm segment (Fig. 6·8(a)) with the central recovered RI slice (Fig. 6·8(b)) and outsets of tissue structures including lipid droplets (Fig. 6·8(c)), the terminal pharyngeal bulb with grinder (Fig. 6·8(d)), and the buccal cavity (Fig. 6·8(e)). Immediately apparent in the learned prediction of the worm is the enhanced clarity and RI contrast of the worm's tissue structures. The network's removal of missing cone artifacts and improved RI prediction show clean recovery of worm features across the entire segment in Fig. 6·8(b) and additional lipid droplets being recovered in Fig. 6·8(c). Our learned approach further shows fine, continuous features are recoverable through the volume such as the grinder from the worm's digestive tract (Fig. 6·8(d)) and the pharyngeal epithelium at defocused planes in Fig. 6·8(e). While these features are also recovered using aIDT's linear model, the network's artifact removal and enhanced feature recovery significantly improves the depth sectioning of the reconstruction. This is particularly evident with the buccal cavity centralized at 5μm whose missing cone artifacts have been nearly completely removed from the central slice (Fig. 6·8(b) purple square, 6·8(e)). These results highlight the network's capabilities to generalize well on multiple-scattering multi-cellular organisms.

6.4.5 Dynamic sample volumetric recovery

A key objective for combining aIDT with our learning architecture is to maintain fast reconstruction of complex samples for imaging living dynamic biological samples. To demonstrate this capability, we applied our trained network to *C. elegans* time-series measurements from [9]. Results are shown for specific time points in Figure 6·9 and the video reconstruction is provided in [133]. Figure 6·9 highlights the wealth of information recovered by the network from the complex, dynamic biological samples. From Fig. 6·9(a), the network predictions' removal of missing cone artifacts provides clear visualizations of the worm's movement through the entire 3-minute measurement

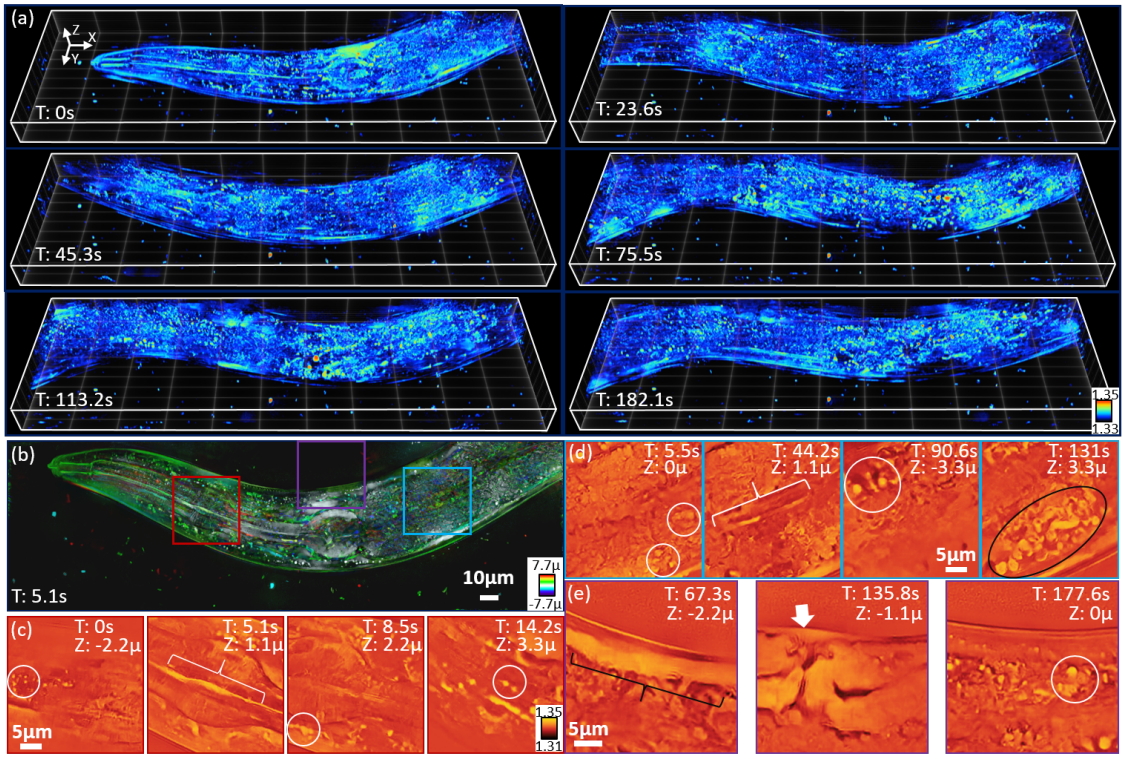

Figure 6·9: Predictions of a dynamic *C. elegans* worm. (a) Learned object prediction 3D renderings across different time points of an aIDT longitudinal measurement. (b) Color-coded depth projection through the learned reconstruction at 5.1 seconds. Network prediction shows minimal missing cone artifacts and clear feature recovery, (c)-(e) outsets of reconstruction FOV highlighting recovered *C. elegans* organs and tissues during video reconstruction. White circles highlight lipid droplets and high-resolution circular structures, white brackets illustrate recovered intestinal tract, black brackets show worm muscle wall, black circles indicate complex tissue features being recovered, and the white arrow indicates the worm's vulva and reproductive organs.

period. The network also enhances the depth sectioning capabilities as seen previously, which is particularly evident in the well-separated features in the color-coded depth projection of Fig. 6·9(b). During this time period, the learned model provides recovery of the digestive tract (white brackets) and lipid droplets (white circles) in Fig. 6·9(c) and Fig. 6·9(d) with complex internal organ features clearly recovered in Fig. 6·9(d) (black oval). Figure 6·9(e) shows new feature recovery previously outside

of the FOV including muscle walls and the worm's vulva (white arrow).

The network's enhanced recovery of such features in temporal data highlights its utility for arbitrary dynamic sample imaging. Despite training on simulated natural images, the network's generalization recovers a complex biological sample's features consistently in time with minimal degradation. This result opens the possibility for the network's application to evaluating temporal dynamics of biological samples with significantly enhanced feature recovery over conventional model-based aIDT. This possibility highlights the significant potential of our deep learning augmented aIDT approach.

6.4.6 Prediction reliability analysis

While the network predictions on simulated objects show close agreement with the ground truth (Fig. 6·4), the network's reliability when predicting experimental data remains an outstanding question. Despite replicating our aIDT setup's experimental parameters in simulation, variations in experimental measurements, such as noise, illumination angle, source homogeneity, imaging wavelength, and aberrations could introduce artifacts to aIDT's object approximant. These variations could generate unreliable object predictions that cannot be evaluated due to the lack of ground-truth information in experimental measurements. Understanding the network reliability is crucial for applying this pipeline in biology where artificial features could cause misclassification of features and/or disease mis-diagnoses. To investigate this issue, we developed an image space analysis metric to evaluate the reliability of our network's predictions on experimental data.

Our image space metric expands upon the method in [118]. This approach implements a physical forward model simulator to generate intensity images from the linear and learned object volumes that are then compared with the experimental measurements. With a sufficiently rigorous physical simulator, deviations between

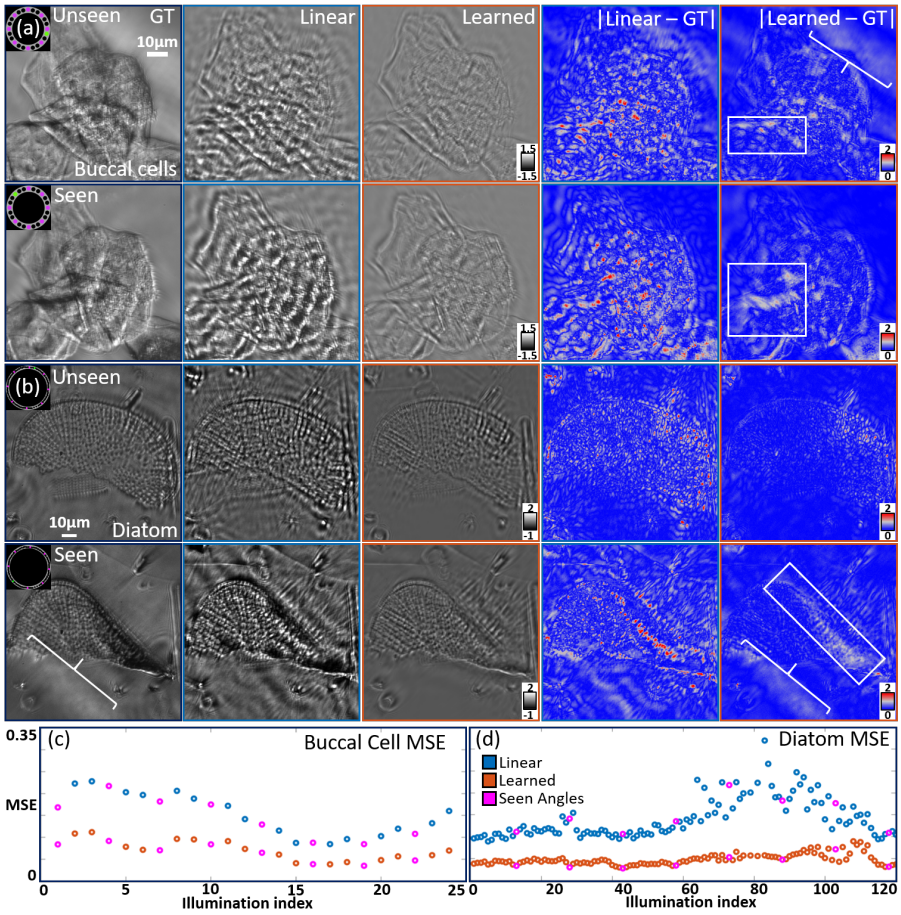

Figure 6·10: Quantitative reliability analysis of network's predictions. We compare intensity images computed using the multiple-scattering model from the linear and learned object and compare them with the experimentally measured intensity images for (a) epithelial buccal cells and (b) a diatom sample. The learned object predictions show closer intensity image contrast and lower errors than intensity images computed from the IDT linear model-based reconstructions indicating closer object predictions to the ground truth. The MSE between the computed and experimental measured images across both seen and unseen angles for (c) epithelial buccal cells and (d) a diatom sample. The results show consistently lower error using the learned model regardless whether the illuminations are used in the model training.

the simulated and experimental images can be related to errors in the predicted RI and structure of the recovered volumes. This comparison utilizes the ground-truth object information encoded in the experimental measurements to evaluate the predicted

object estimates quantitatively. Here, we compare intensity images from illumination angles used in our model-based approximant (seen) and illumination angles unused in the aIDT model and network prediction (unseen). If the network "overfits" to the features recovered using seen illuminations, the simulated images from *unseen* illuminations would exhibit increased error from network hallucinated object features.

We first evaluate epithelial buccal cells using 24 illuminations in Fig. 6·10(a) and (c) using the main setup in Fig. 6·1(a). To further evaluate the effect of experimental setup variations with this metric, we compute the metrics on diatom algae samples measured with a different LED array setup (Adafruit, 607) with 120 illuminations in Fig. 6·10(b) and (d). We utilize the SSNP model for generating the intensity images using both the linear (Fig. 6·10, blue) and learned (Fig. 6·10, orange) estimates and compared them with experimental measurements using pixel-wise absolute error maps (Fig. 6·10(a,b)) and the mean squared error (MSE) of each intensity image as a function of the illumination index (Fig. 6·10(c,d)). Seen illuminations are noted in magenta with green illuminations highlighting the specific LED used for the intensity images shown in Fig. 6·10(a,b).

The network's object predictions show strong agreement with the experimental measurements regardless of the illumination angle. In both the cells and diatom sample, the learned network intensity images show closer contrast and lower error to the experimental data than the linear model's results. This result is consistent regardless of whether the illumination angle was used for the reconstruction (Fig. 6·10(a,b), Seen vs. Unseen). The main differences between the network and experimental images appears due to low spatial frequency loss (Fig. 6·10(a,b), white boxes) creating "flatter" images and source inhomogeneities in the experimental measurements (Fig. 6·10(a,b), white brackets). These error contributions are attributed to the linear model input to the network lacking low spatial frequency information and the LED

sample illumination not ideally matching plane wave illumination, respectively. These issues, however, are not tied to the network's behaviors and show the network is not introducing hallucinations or artifacts that would skew predictions of experimental objects.

Evaluating the image-wise MSE in Fig. 6·10(c,d) further confirms the network predicts the underlying object volume. Plotted as a function of the illumination index, the MSE for the seen and unseen illumination angles show no substantial difference in error for both sample types. Across all illuminations, the images from the learned object volume prediction show consistently lower error than the linear model, which is partially attributed to the removal of missing cone artifacts in the predicted volume. The dominant error variations of Fig. 6·10(d) instead result from illumination angle misalignments remaining after implementing the calibration procedures of [9]. These misalignments are most present in illuminations 70-90 for the diatom sample where the illumination angles were close to the objective's maximum 0.65 NA cut-off and were difficult to calibrate. While these angle-based error fluctuations are most present in the aIDT model-based results, the network shows a stable MSE regardless of the illumination angle. This stability is attributed to the removal of missing cone artifacts, as these features would generate significant error due to small fluctuations in the illumination angle. These results highlight that our learned IDT framework provides reliable object estimates without network-induced hallucinations.

6.5 Discussion

Our results highlight the significant potential of deep learning in computational 3D phase imaging. With only simulated objects, we showed a lightweight 2D network can be trained following approximant-guided learning methods to recover the 3D phase of biological samples of arbitrary size and scattering strength. The network corrects not

only missing cone artifacts but also improves the prediction accuracy of the object's RI. We showed better RI and object feature recovery on unseen simulated data and illustrated improved object predictions on experimental data acquired using a range of experimental setups. Finally, we showed this network can be readily applied to recover high-quality volumetric reconstructions of dynamic biological samples using a *C. elegans* worm video in [133].

A main limitation of this approximant-guided learning approach is the network's reliance on the initial model-based object estimate for feature prediction. aIDT uses transfer functions based on the interference of the incident illumination and first order scattering to recover the object's 3D structure [110]. These transfer functions exhibit finite support and remove significant portions of the intensity measurements' nonlinear scattering signal that becomes non-negligible under multiple-scattering conditions [41]. This information loss limits the information available for the network to learn from, which contributes to the network's failure to predict object features including low axial spatial frequencies outside the linear model's bandwidth. This limitation could be solved through the incorporation of higher order physical approximants [30].

Our learned IDT approach holds promise for improving the image quality in low-cost optical setups. Recent works have developed low-cost, open-source optical imaging setups enabling affordable multi-modal imaging in a push for the "democratization" of science to the general public [134, 76]. Particularly, recent work from Diederich *et al.* has shown that aIDT can be included in such multi-modal setups enhancing both the capabilities of these platforms and accessibility to the imaging modality [76]. By using cheaper optical components, however, the reconstructed volume can suffer in quality from having less precision over the source array alignment. Because our learned approach generalizes well to object recovery in different optical

setups, the use of this lightweight framework on low-cost setups could drastically improve the object volume predictions and potentially be implemented on cellphones for real-time processing [135]. This generalizability could also correct the stronger model-induced artifacts present from multiplexed illumination schemes used for high-speed imaging [71]. Prior work showed that combining illuminations in each IDT intensity image trades image reconstruction quality and stronger missing cone artifacts for faster acquisition speeds to image live dynamic samples [71]. Since our network shows strong removal of these artifacts, this learned IDT approach could potentially be applied to multiplexed IDT setups to achieve faster volume rates without losing reconstruction quality. This improvement would enable IDT to evaluate more dynamic biological features and enable high-speed imaging in low-cost optical setups as well.

The enhanced recovery of object RI features using our approach also has significant potential in recently developed virtual labeling technologies [136, 137, 138, 139]. These methods showed that deep learning models coupled with the morphological features present in phase imaging modalities can digitally synthesize fluorescent labels on unlabeled cell samples. This approach effectively adds specificity to the phase images for differentiating biological structures and creates a "computational multimodal" setup expanding the phase modality's capabilities. The enhanced 3D structures provided with this work could be utilized for such networks to provide computational specificity to the recovered RI volumes. This avenue would provide a substantial boon for the biological imaging community by providing digital staining of 3D biological samples for analysis.

Finally, the generalizable network achieved using our physical model simulator shows the power of simulation-only training for applying deep learning for imaging in complex media applications. We showed here that the SSNP framework sufficiently

models the multiple-scattering process for the network to recover experimentally measured samples from training only on natural image-based volumes. This learning approach overcomes the bottleneck of acquiring diverse experimental measurements for deep learning, and the model's efficient field simulation through large-scale multiple-scattering objects could be used for numerous other imaging advancements, such as imaging and light manipulation through diffuse media [97, 96, 140, 141, 142, 143].

Chapter 7

Reflection-mode inverse scattering model for high axial resolution phase imaging

7.1 Overview

The prior chapters in this thesis introduced improvements to IDT's acquisition speed and object reconstruction using model-based illumination design and simulator-trained learning strategies. In all this development, the assumed optical setup evaluated the sample using transmission-mode microscopes that aligned with the IDT forward model in Chapter 3 and [8]. While this imaging geometry is common in microscopy, the evaluation of a sample in transmission always suffers from low axial resolution under limited-angle tomography conditions [57]. In transmission, the recovered scattering corresponds to forward-scattered light from the object and contains only *slowly varying* axial spatial frequencies. For IDT, this is observed in the exponential term of Eq. (3.12a). Under incoherent illumination achieving the maximum axial resolution, this low frequency sampling coupled with a transmission system's 3D TF results in axial resolution defined by the DOF and a toroidal-shaped TF [57]. These factors result in high-resolution biological structures, such as subcellular features, from being

well resolved and creates missing cone artifacts in the reconstruction. Although the learning strategy proposed in Chapter 6 can solve the missing cone artifacts, achieving high axial resolution with transmission-based IDT still remains a difficult task preventing isotropic 3D resolution in this imaging modality. For biological imaging, this capability would be highly advantageous for studying dynamic subcellular structures and interactions in unlabeled cell cultures.

One approach to recover high axial resolution information is to utilize *reflection*-geometry imaging systems. Such systems are important because they: 1) can measure backscattered fields carrying high frequency content sensitive to fine details in the object's axial structures [18, 144, 145, 146, 147, 148, 149, 150, 151, 152] and/or 2) can be applied to both thin [148, 144, 153, 146, 147, 149, 154, 155, 156, 150] and thick biological samples [145, 157, 158, 159, 144, 160, 161]. Recent modalities have expanded reflection systems to QPI for recovering the object's RI [162, 163, 164, 165, 148, 166, 167, 168, 169]. Existing approaches often utilize interferometry [168, 166, 148, 170, 171, 165, 161, 172, 173] with successful high-resolution, high-sensitivity quantitative recovery of cellular and subcellular features [148, 164, 165, 166, 168, 161, 174, 169]. Such interferometric techniques often require specialized optical setups that can be less accessible for certain biological applications. In addition, QPI in reflection can require accurate scattering models that vary significantly with the imaging modality design [175, 176, 177, 173, 171] and desired application [175, 176, 178, 179, 180, 181]. Specifically, the presence of boundaries or structures near the object can generate additional scattering requiring complex models [167, 180, 182, 179, 183] or can result in transmission-like imaging conditions [160, 184, 185, 186]. These constraints suggest that QPI in reflection with standard microscope designs and computationally efficient, easily implementable inverse scattering models would be highly advantageous for biological research. Recently, *intensity-only* techniques using diverse illumination paired

with inverse scattering models have achieved great success for QPI in transmission and are easily built into standard microscopes [68, 62, 80, 100, 6, 8, 9, 187, 71]. Here, we explored such an intensity-only reflection QPI approach using diverse illumination of a sample fixed on a glass slide. This implementation investigated where reflection IDT was possible for high axial resolution imaging of cell samples grown on glass slides or petri dishes.

One of the critical requirements to investigate IDT in reflection is the development of a linear scattering model. Linear reflection models have been explored previously for applications including metrology [175] and quantitative tissue imaging [178, 170, 177, 175]. Classical reflection models such as the Kirchhoff approximation are easily implemented and have found utility in metrology for confocal microscopy [188, 189, 190, 191]. This model is less applicable to biomedical imaging, where material inhomogeneities, optical roughness, and volumetric scattering of biological structures invalidate the approximation's underlying assumptions. Furthermore, this model relies on direct field detection for quantitative recovery and requires interferometry or point-scanning the sample to unambiguously recover phase from the object's height [188, 191]. This chapter instead evaluates a *volumetric* model using the first Born approximation for describing light scattered from an inhomogeneous object of variable height and permittivity. This approximation is used elsewhere in reflection [178, 170, 177, 180, 175], but we consider a partially reflective boundary interface below the object that creates additional scattering to model a biological sample fixed on a glass slide. This case is similar to [180, 182, 192, 183] where vectorial inverse scattering models are evaluated for recovering the phase of nanoscale structures. These approaches are successful and evaluate both interferometric and intensity-only techniques but consider only nano-scale objects with complex optical setups or computationally intensive phase recovery techniques. To develop an efficient

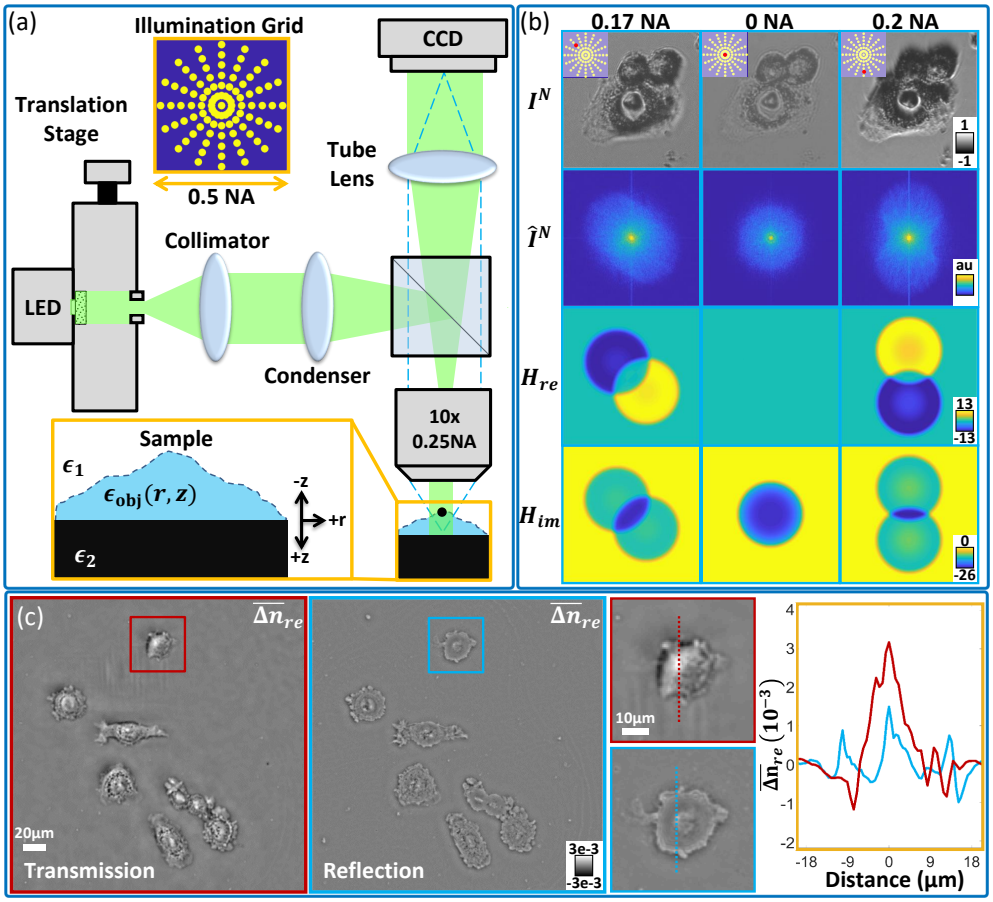

Figure 7·1: (a) Reflection intensity phase microscope design with illumination grid and imaging geometry. A scannable LED in a conjugate plane to the objective's back focal plane enables programmable oblique illumination up to 0.25NA. (b) Normalized reflection images, Fourier coverage, and model transfer functions for illuminations at 0.17, 0, and 0.2NA. The phase transfer function show asymmetric behavior at oblique illumination and cancellation for on-axis illumination. (c) The average real refractive index (RI) contrast reconstructions from transmission Intensity Diffraction Tomography [8] (Red) and our reflection system (Blue). Transmission better recovers large nuclear structures while reflection captures thin membrane features.

model suitable for commonly encountered biological conditions, we consider a scalar model with a scattering object above a semi-infinite, partially reflecting interface.

In this chapter, we evaluate a linearized reflection phase model and develop a new imaging modality for performing phase imaging in reflection originally published

in [193]. We show this imaging condition captures both forward and back-scattered fields from the object that are *linear* and *nonlinear* with object height, respectively. Using only the forward-scattered field information, we derive a linear inverse scattering model and show this field is twice as sensitive to the object's phase than transmission. This enhanced phase sensitivity allows the recovery of objects at nanometer length-scales but induces a rapid breakdown of the model's validity range for increasingly tall objects. We validate this behavior using rigorous discrete dipole approximation simulations of the imaging condition and illustrate its effects in experiment on fixed HeLa cells. This work presents promising developments for QPI in reflection using simplified intensity-only imaging modalities.

7.2 Theory

We consider the imaging geometry in Fig. 7·1(a). An object of unknown RI or permittivity and height is distributed between two homogeneous media with permittivities satisfying $\epsilon_1 < \epsilon_2$. We set the interface of these media as the $z = 0$ plane with the object contained entirely in ϵ_1 (i.e. $z \leq 0\mu$m). With this geometry, the total field must consider the reflections of both the object's scattered field and the illumination from the interface differing from the transmission IDT condition discussed in Chapter 3 and [8]. Assuming quasi-monochromatic plane waves with central wavelength λ illuminate the object at arbitrary oblique angles up to the system's numerical aperture (NA), the total illumination with this boundary is

$$U_0(\boldsymbol{r}_\perp, z|\boldsymbol{\nu}_l) = Ae^{j2\pi\boldsymbol{\nu}_l\cdot\boldsymbol{r}_\perp}\left(e^{j2\pi\eta(\boldsymbol{\nu}_l)z} + R(\boldsymbol{\nu}_l)e^{-j2\pi\eta(\boldsymbol{\nu}_l)z}\right), \tag{7.1}$$

containing the incident plane wave U_i and its reflection U_r (Fig. 7·2(a)). As before, $\boldsymbol{r}_\perp$ and z denote the lateral and axial spatial coordinates, respectively; $\boldsymbol{\nu}_l$ and $\eta(\nu_l) = \sqrt{\lambda^{-2} - |\boldsymbol{\nu}_l|^2}$ denote the illumination's lateral and axial spatial frequencies,

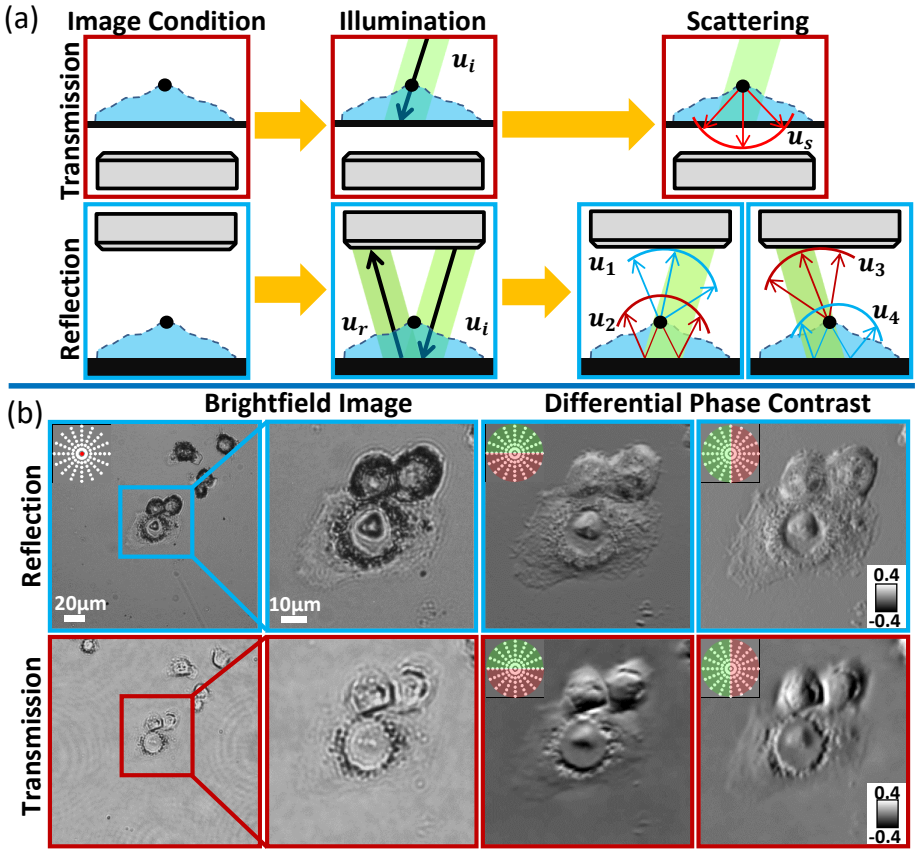

Figure 7·2: (a) Illumination and expected scattering behavior under transmission and reflection geometries. (b) Comparison of on-axis brightfield and differential phase contrast (DPC) images of Henrietta Lacks (HeLa) cells in reflection and transmission. DPC images were generated from the difference of the images taken with the shown illuminations (Green - Red). The additional forward-scattering in reflection enhances thin cellular feature contrast.

respectively; the amplitude $A = \sqrt{S(\boldsymbol{\nu}_l)}P(-\boldsymbol{\nu}_l)$; S is the incoherent primary source function; and P is the pupil function. To calculate the reflected field, we use the average TE and TM wave Fresnel coefficients $R(\boldsymbol{\nu}_l) = \frac{1}{2}[|R_{\mathrm{TE}}(\boldsymbol{\nu}_l)| + |R_{\mathrm{TM}}(\boldsymbol{\nu}_l)|]$ to model the reflection amplitude of the unpolarized illumination from the boundary [194].

As in the case for transmission IDT, we consider a weakly scattering object with a *slowly varying* permittivity distribution $\epsilon(\boldsymbol{r}_\perp, z)$ characterized by the scattering potential $V(\boldsymbol{r}_\perp, z) = k^2\Delta\epsilon(\boldsymbol{r}_\perp, z)/4\pi$ with $\Delta\epsilon(\boldsymbol{r}_\perp, z) = \epsilon(\boldsymbol{r}_\perp, z) - \epsilon_0$ and wavenumber $k = 2\pi\lambda^{-1}$. Following the first Born approximation, the total field is modified from

the transmission case defined by Eq. (3.1)

$$U(\boldsymbol{r}_\perp, z|\boldsymbol{\nu}_l) = U_r(\boldsymbol{r}_\perp, z|\boldsymbol{\nu}_l) + \int_{-\infty}^{0}\iint_{-\infty}^{\infty} V(\boldsymbol{r}'_\perp, z')U_0(\boldsymbol{r}'_\perp, z'|\boldsymbol{\nu}_l)G(\boldsymbol{r}_\perp - \boldsymbol{r}'_\perp, z - z')d^2\boldsymbol{r}'_\perp dz', \quad (7.2)$$

where only the reflected illumination U_r acts as a reference field instead of the incident field illuminating the sample. Because the scattering is generated from both the incident and reflected plane waves, the object's scattered field U_s after illumination accounts for the the total incidence U_0. Due to the boundary interface, the free-space Green's function used in IDT cannot be directly implemented in this case. Here, we instead use the half-space Green's function G in Weyl expansion form [180] to account for both the forward and back-scattered fields in the presence of two separate media(Fig. 7·2(a))

$$G(\boldsymbol{r}_\perp - \boldsymbol{r}'_\perp, z - z') = j\iint_{-\infty}^{\infty} \frac{1}{\eta(\boldsymbol{\nu})} e^{j2\pi(\boldsymbol{\nu}\cdot(\boldsymbol{r}_\perp - \boldsymbol{r}'_\perp) - \eta(\boldsymbol{\nu})z)}[e^{j2\pi\eta(\boldsymbol{\nu})z'} + R(\boldsymbol{\nu})e^{-j2\pi\eta(\boldsymbol{\nu})z'}]d^2\boldsymbol{\nu}, \quad (7.3)$$

where $\boldsymbol{\nu}$ and $\eta(\boldsymbol{\nu}) = \sqrt{\lambda^{-2} - |\boldsymbol{\nu}|^2}$ are the scattered field's lateral and axial spatial frequencies, respectively, and $R(\boldsymbol{\nu})$ is the scatter-angle ($\boldsymbol{\nu}$) dependent Fresnel coefficient. We constrain z' over the object's height $h(\boldsymbol{r}'_\perp)$ by $z' \in [-h(\boldsymbol{r}'_\perp), 0]$ to obtain the scattered field

$$U_s(\boldsymbol{r}_\perp, z|\boldsymbol{\nu}_l) = j\frac{Ak^2}{4\pi}\iint_{-\infty}^{\infty}\iint_{-\infty}^{\infty}\int_{-h(\boldsymbol{r}'_\perp)}^{0} \frac{1}{\eta(\boldsymbol{\nu})} e^{j2\pi(\boldsymbol{\nu}\cdot\boldsymbol{r}_\perp - \eta(\boldsymbol{\nu})z)}\Big[e^{j2\pi\eta^+(\boldsymbol{\nu})z'} + R(\boldsymbol{\nu_i})e^{j2\pi\eta^-(\boldsymbol{\nu})z'}$$
$$+ R(\boldsymbol{\nu})e^{-j2\pi\eta^-(\boldsymbol{\nu})z'} + R(\boldsymbol{\nu_i})R(\boldsymbol{\nu})e^{-j2\pi\eta^+(\boldsymbol{\nu})z'}\Big]\Delta\epsilon(\boldsymbol{r}'_\perp, z')e^{-j2\pi\boldsymbol{\nu}^-\cdot\boldsymbol{r}'_\perp}dz'd^2\boldsymbol{r}'_\perp d^2\boldsymbol{\nu}, \quad (7.4)$$

where $\boldsymbol{\nu}^- = \boldsymbol{\nu} - \boldsymbol{\nu}_l$, $\eta^+(\boldsymbol{\nu}) = \eta(\boldsymbol{\nu}) + \eta(\boldsymbol{\nu}_l)$, and $\eta^-(\boldsymbol{\nu}) = \eta(\boldsymbol{\nu}) - \eta(\boldsymbol{\nu}_l)$. In similar form to the assumptions for transmission IDT in Chapter 3, we assume the object's permittivity is axially uniform for each lateral position in $h(\boldsymbol{r}'_\perp)$. Following axial

integration and a Fourier transform of the field, we obtain the Fourier scattered field

$$\hat{U}_s(\boldsymbol{\nu}, z|\boldsymbol{\nu}_l) = j\frac{Ak^2}{4\pi}\frac{e^{-j2\pi\eta(\boldsymbol{\nu})z}}{\eta(\boldsymbol{\nu})}\iint_{-\infty}^{\infty}\Big[\hat{\mathrm{F}}(\boldsymbol{\nu}, \boldsymbol{r}'_\perp|\boldsymbol{\nu}_l) + \hat{\mathrm{B}}(\boldsymbol{\nu}, \boldsymbol{r}'_\perp|\boldsymbol{\nu}_l)\Big]e^{-j2\pi\boldsymbol{\nu}^-\cdot\boldsymbol{r}'_\perp}d^2\boldsymbol{r}'_\perp, \quad (7.5)$$

where

$$\hat{\mathrm{F}}(\boldsymbol{\nu}, \boldsymbol{r}'_\perp|\boldsymbol{\nu}_l) = \Delta\epsilon(\boldsymbol{r}'_\perp)h(\boldsymbol{r}'_\perp)\mathrm{sinc}(\pi\eta^-(\boldsymbol{\nu})h(\boldsymbol{r}'_\perp))[R(\boldsymbol{\nu}_l)e^{-j\pi\eta^-(\boldsymbol{\nu})h(\boldsymbol{r}'_\perp)} + R(\boldsymbol{\nu})e^{j\pi\eta^-(\boldsymbol{\nu})h(\boldsymbol{r}'_\perp)}] \quad (7.6)$$

$$\hat{\mathrm{B}}(\boldsymbol{\nu}, \boldsymbol{r}'_\perp|\boldsymbol{\nu}_l) = \Delta\epsilon(\boldsymbol{r}'_\perp)h(\boldsymbol{r}'_\perp)\mathrm{sinc}(\pi\eta^+(\boldsymbol{\nu})h(\boldsymbol{r}'_\perp))[e^{-j\pi\eta^+(\boldsymbol{\nu})h(\boldsymbol{r}'_\perp)} + R(\boldsymbol{\nu})R(\boldsymbol{\nu}_l)e^{j\pi\eta^+(\boldsymbol{\nu})h(\boldsymbol{r}'_\perp)}] \quad (7.7)$$

denote the *slowly* oscillating forward-scattering (F) and *rapidly* oscillating back-scattering (B) axial phase contributions. F and B map to the lower and upper regions of the sample's Fourier space providing low and high-resolution information of the axial features, respectively [24]. This additional feature content enhances the captured phase information over transmission (Fig. 7·2), but the rapidly oscillating phase in B and non-elementary integration due to $h(\boldsymbol{r}'_\perp)$ make quantitative phase recovery difficult and possibly nonlinear or ambiguous [178]. Thus, additional assumptions on the field behavior are required to maintain a simplified physical model.

To determine appropriate assumptions, we use a Discrete Dipole Approximation (DDA) [195] model from Marseilles Fresnel Institute [196, 197] to rigorously simulate our imaging condition from first principles. We simulate $1.8 \times 1.8\mu m^2$ cuboid objects (Fig. 7·3(a)) with varying heights ($h(\boldsymbol{r}_\perp \in [0.12, 1]\mu$m) and real permittivity contrasts ($\Delta\epsilon \in [0.02, 0.44]$) on a 256×256×256 pixel grid with 30nm sampling. We convert the object's permittivity to refractive index (RI) contrast in our results, as it is more commonly used in the QPI field. The corresponding real RI contrast has a range of $\Delta n_{\mathrm{re}} \in [0.01, 0.2]$.

We generate simulated intensity images for each object using a 0.25NA, 10× magnification objective and oblique illuminations up to 0.2 NA. This design and max-

imum illumination angle matched our experimental setup's maximum illumination as discussed in greater detail below. Because the intensity encodes greater phase and scattering information from the object with oblique illumination (Fig. 7·1(b)), we evaluate the image contrast under 0.2 NA illumination for each simulated object (Fig. 7·3(b)). We use the average of the image's full-width half-maximum (FWHM) as our contrast metric

$$C = \overline{FWHM(|I^N|)}, \tag{7.8}$$

where $I^N = (I - \bar{I})/\bar{I}$ is the normalized, background-subtracted intensity image. This approach captures the object's average scattering contrast without significant influence from the low-valued background or extreme, high-valued saturated pixels.

The recovered intensity contrast values for various simulations are shown in Figure 7·3(c)-(e). We evaluate the contrast across different object heights at fixed RI and wavelength $\lambda = 530$nm (Fig. 7·3(c)), across different imaging wavelengths (Fig 7·3(d)), and with increasing RI at fixed object heights and wavelength $\lambda = 530$nm (Fig. 7·3(e)). For weakly scattering objects, we observe *linearly* increasing scattering contrast plus a *nonlinear* sinusoidal oscillation with respect to the object's height (Fig. 7·3(c) blue,(d_1)). Across different imaging wavelengths, this height-dependent nonlinearity is preserved with an oscillation period matching $\lambda/2$ (Fig. 7·3(d_1)). With increasing RI contrast, this behavior breaks down across all imaging wavelengths as the object becomes strongly scattering (Fig. 7·3(c),(d_2)). Furthermore, the intensity contrast shows a linear relationship with increasing RI contrast at fixed heights until the object becomes strongly scattering (Fig. 7·3(e)).

These results agree with our Born-based derivation in Eq. (7.5) but show the difficulty of reflection QPI with linear models for intensity-only measurements. The linear intensity trends in object height and RI can be attributed to the forward-scattered phase of Eq. (7.6). This phase is inherently nonlinear, but its slowly varying na-

ture is adequately approximated with linear functions as shown in transmission systems [110, 100]. This results in a directly proportional, linear relationship between the object's physical parameters and the field amplitude. The oscillating nonlinear intensity contrast results from the backscattering phase of Eq. (7.7). This field oscillates with a period of $\lambda/2$ as a function of object height, matching the behaviors observed in Fig. 7·3(c)-(d). The inherent nonlinearity of the backscattering means that a linear model is insufficient to capture the full scattered field behavior for quantitative recovery in reflection. We can therefore only recover the *forward-scattered* object features with a linear model for this imaging condition.

7.2.1 Linear Scattering Model

To evaluate whether a linear reflection model still provides relevant morphological information, we generate a forward model that ignores the backscattered field contribution of Eq. (7.7). Specifically, we consider this entire backscattered term as an unrecoverable nonlinear error that reduces our linear model's validity. Without this nonlinear term in Eq. (7.5), we assume the forward-scattered field in Eq. (7.6) will slowly accumulate phase through the object and is linearizable. Following an application of Euler's formula and the definition of the sinc$(\cdot)$ function, we obtain the reformulation of Eq. (7.6):

$$\hat{\mathrm{F}}(\boldsymbol{\nu}, \boldsymbol{r}'_{\perp}|\boldsymbol{\nu}_l) = \frac{\Delta\epsilon(\boldsymbol{r}'_{\perp})}{j2\pi\eta^{-}(\boldsymbol{\nu})}\left[R(\boldsymbol{\nu}_l)(1 - e^{-j2\pi\eta^{-}(\boldsymbol{\nu})h(\boldsymbol{r}'_{\perp})}) + R(\boldsymbol{\nu})(e^{j2\pi\eta^{-}(\boldsymbol{\nu})h(\boldsymbol{r}'_{\perp})} - 1)\right] \quad (7.9)$$

from which a Taylor expansion on the height-dependent exponential terms provides the field linearization: $\mathrm{F}(\boldsymbol{\nu}, \boldsymbol{r}'_{\perp}|\boldsymbol{\nu}_l) = \Delta\epsilon(\boldsymbol{r}'_{\perp})h(\boldsymbol{r}'_{\perp})[R(\boldsymbol{\nu}_l) + R(\boldsymbol{\nu})]$. Solving Eq. (7.5) with this term, we obtain a linear Fourier scattered field

$$U_s(\boldsymbol{v}, z|\boldsymbol{\nu}_l) = j\frac{Ak^2}{4\pi}\frac{e^{-j2\pi\eta(\boldsymbol{\nu})z}}{\eta(\boldsymbol{\nu})}\mathcal{R}(\boldsymbol{\nu}|\boldsymbol{\nu}_l)\widehat{\Phi}(\boldsymbol{\nu}^{-}), \quad (7.10)$$

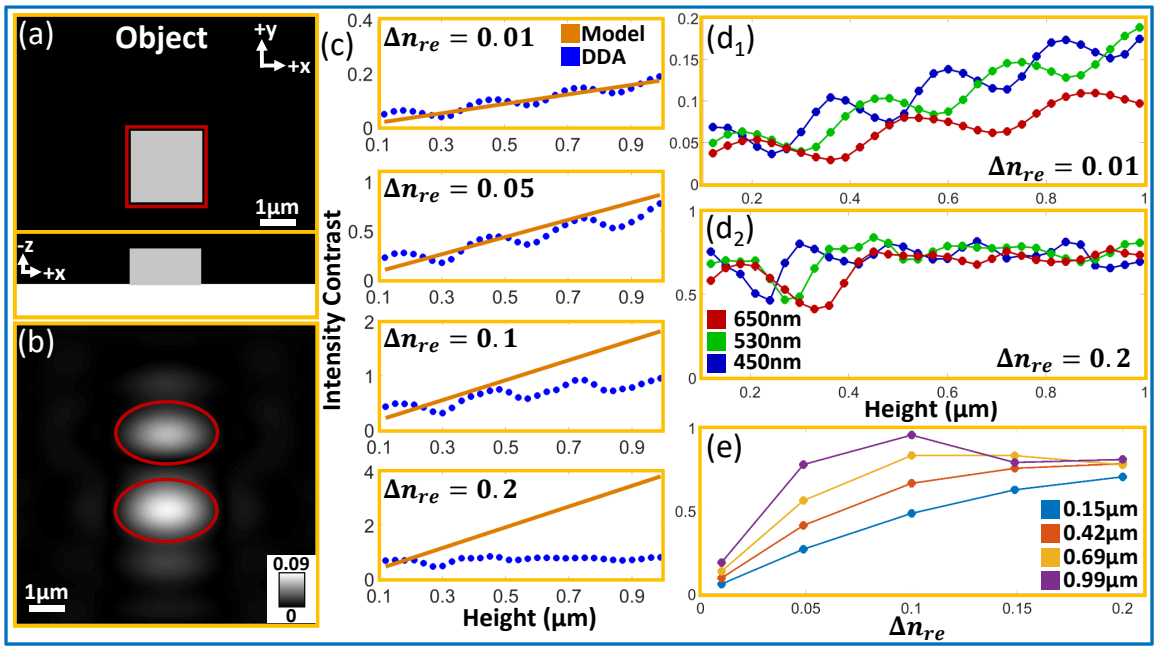

Figure 7·3: (a) 3D Cuboid distribution above partially reflective surface from DDA simulations. (b) Cuboid intensity contrast ($\Delta n_{\text{re}} = 0.01$, $h = 210$nm, $\lambda = 530$nm) with red ovals highlighting evaluated contrast region. (c) Linear reflection model (Orange) and DDA simulation (blue) intensity contrast under 0.2NA illumination for objects with heights $0.12 - 1\mu m$ and increasing RI contrast for $\lambda = 530$nm. The linear model adequately predicts the contrast at weak object permittivities but overestimates larger RI object contrast. (d) Intensity contrast at fixed real RI ($\Delta n_{\text{re}} = 0.01, 0.2$ for $\text{d}_{1,2}$ respectively) with increasing height across multiple wavelengths. The nonlinear term's period follows $\lambda/2$ until high RI contrast objects are evaluated. (e) Intensity contrast highlighting linear trends for increasing RI contrast at fixed object heights.

where $\widehat{\Phi}(\boldsymbol{\nu}^-) = \mathcal{F}\{\Delta\epsilon(\boldsymbol{r}_\perp)h(\boldsymbol{r}_\perp)\}$ is the Fourier transform ($\mathcal{F}$) of the object-dependent phase introduced to the scattered field and is discussed in greater detail below, while the lateral frequency variable $\boldsymbol{\nu}^-$ describes the frequency shifted scattered field from oblique illumination providing enlarged Fourier coverage, akin to synthetic aperture and the pupil function translations in transmission-mode IDT. $\mathcal{R}(\boldsymbol{\nu}|\boldsymbol{\nu}_l) = [R(\boldsymbol{\nu}_l) + R(\boldsymbol{\nu})]$ is the modified Fresnel coefficient that accounts for the two forward-scattered field contributions. The phase term $e^{-j2\pi\eta(\boldsymbol{\nu})z}$ accounts for the additional

phase induced by microscope defocus at position z. As discussed in Chapter 3, this defocus is often set to zero for simplicity.

With this field, we derive transfer functions (TF) for the image intensity to complete our linear model. Assuming L oblique illuminations, the intensity I_l in the l^{th} image is the result of the total field u_{tot} filtered by the pupil function P

$$I_l(\boldsymbol{r}_\perp, z|\boldsymbol{\nu}_l) = |\mathcal{F}^{-1}\{U_{\text{tot},l}(\boldsymbol{\nu}, z|\boldsymbol{\nu}_l)P(\boldsymbol{\nu})\}|^2, \tag{7.11}$$

which contains four terms including the intensities of the reference field, scattered field, and their interference terms. With our first Born approximation, we neglect the weak intensity contribution from the scattered field's intensity and perform background subtraction to remove the reference intensity. The remaining interference terms describe a *linear* relation between the object permittivity and the measured intensity.

We decompose the object's complex permittivity contrast $\Delta\epsilon(\boldsymbol{r}_\perp, z) = \Delta\epsilon_{\text{re}}(\boldsymbol{r}_\perp, z) + j\Delta\epsilon_{\text{im}}(\boldsymbol{r}_\perp, z)$ into real and imaginary components and solve for them separately, following the work discussed in prior chapters and [62, 8]. These terms carry different physical meanings and are considered decoupled and separable during reconstruction. We obtain the Fourier scattered field with respect to our TFs using normalized, background-subtracted intensity images I_l^N

$$\widehat{I}_l^N(\boldsymbol{\nu}, z|\boldsymbol{\nu}_l) = C\big[H_{\text{re}}(\boldsymbol{\nu}, z|\boldsymbol{\nu}_l)\widehat{\Phi}_{\text{re}}(\boldsymbol{\nu}) + H_{\text{im}}(\boldsymbol{\nu}, z|\boldsymbol{\nu}_l)\widehat{\Phi}_{\text{im}}(\boldsymbol{\nu})\big], \tag{7.12}$$

where $C = -(|A|^2 R(\boldsymbol{\nu}_l)k^2)/4\pi$ is a constant coefficient. The real and imaginary TFs are

$$H_{\mathrm{im},l}(\boldsymbol{\nu}, z|\boldsymbol{\nu}_l) = P(\boldsymbol{\nu}_l)P^*(\boldsymbol{\nu}^-)D(\boldsymbol{\nu}^-, z)\mathcal{R}(\boldsymbol{\nu}^-|\boldsymbol{\nu_i}) + P^*(\boldsymbol{\nu}_l)P(\boldsymbol{\nu}^+)D^*(\boldsymbol{\nu}^+, z)\mathcal{R}(\boldsymbol{\nu}^+|\boldsymbol{\nu}_l), \tag{7.13a}$$

$$H_{\mathrm{re},l}(\boldsymbol{\nu}, z|\boldsymbol{\nu}_l) = j\Big\{P(\boldsymbol{\nu}_l)P^*(\boldsymbol{\nu}^-)D(\boldsymbol{\nu}^-, z)\mathcal{R}(\boldsymbol{\nu}^-|\boldsymbol{\nu}_l) - P^*(\boldsymbol{\nu}_l)P(\boldsymbol{\nu}^+)D^*(\boldsymbol{\nu}^+, z)\mathcal{R}(\boldsymbol{\nu}^+|\boldsymbol{\nu}_l)\Big\}. \tag{7.13b}$$

where $D(\boldsymbol{\nu}, z) = e^{j2\pi\eta^-(\boldsymbol{\nu})z}/\eta(\boldsymbol{\nu})$ is the objective's defocus with an obliquity factor closely matching Eq. (3.12a) and (3.12b).

Most critically, this linear model predicts a contrast enhancement in reflection over transmission. The model recovers the sample's phase $\Phi_{\mathrm{re}}(\boldsymbol{r}_\perp) = \Delta\epsilon_{\mathrm{re}}(\boldsymbol{r}_\perp)h(\boldsymbol{r}_\perp)$, which is related to the sample's optical path length: $\Delta\epsilon_{\mathrm{re}}(\boldsymbol{r}_\perp)h(\boldsymbol{r}_\perp) \approx 2\Delta n(\boldsymbol{r}_\perp)n_1(\boldsymbol{r}_\perp)h(\boldsymbol{r}_\perp)$ ($n_1 = \sqrt{\epsilon_1}$, $n_{\mathrm{re}} = \sqrt{\epsilon_{\mathrm{re}}}$, and $\Delta n = n_{\mathrm{re}} - n_1$). This result resembles that of [191] and shows the phase through the object is doubled compared to transmission. Thin features typically unobservable in transmission will thus provide better contrast in reflection from accumulating additional phase in the forward-scattered field. This is observed qualitatively in the DPC [62] images of Fig. 7·2(b), where the cellular membrane and filopodial structures are more apparent in reflection. With more rapid phase accumulation, however, the linearity range of the forward-scattered phase is halved. We thus expect a reduced range of object heights recoverable with this linearized model, which also limits the potential for achieving 3D reconstructions in reflection with this approach.

This model maintains many of the similar behaviors observed in transmission IDT discussed in Chapter 3 and [8]. This reflection forward model includes synthetic aperture behavior from oblique illumination with two shifted pupil functions, $P(\boldsymbol{\nu})$ and its complex conjugate $P^*(\boldsymbol{\nu})$, centered at $\boldsymbol{\nu}^+ = \boldsymbol{\nu} + \boldsymbol{\nu}_l$, and $\boldsymbol{\nu}^- = \boldsymbol{\nu} - \boldsymbol{\nu}_l$. These functions exhibit frequency shifts in opposite directions based on the illumination spatial frequency $\pm\boldsymbol{\nu}_l$. As shown in the intensity image I^N and the normalized in-

tensity spectra $\hat{I}^N$ of Fig. 7·1(b), the use of oblique (0.2 NA) versus on-axis (0 NA) illumination captures higher resolution information by enhancing the recovered object's bandwidth. This enhancement follows synthetic aperture principles [8] as seen in transmission and can be extended by increasing the illumination angle until the incident field exceeds the objective NA. At illuminations matching the objective NA, the pupil function shifts by the objective NA to achieve a maximum resolution of $\lambda/2\text{NA}$ matching the incoherent resolution limit. In practice, hardware limitations prevent these high angles and less oblique illuminations are acquired. We encounter this limitation here and use lower angle illumination as discussed below.

The TFs also exhibit different symmetries as previously observed in transmission [62, 8]. The real and imaginary TFs are asymmetric and symmetric, respectively. As the real TF recovers the object's *phase*, the TF's asymmetry provides increasingly better phase contrast and recovery with larger oblique illuminations (Fig. 7·1(b)) [8, 62]. The imaginary TF is symmetric and recovers object features generating a loss of energy to the total illumination. Because of the reflection imaging condition, this TF recovers both the object's *absorbing* features and the object's *reflectivity*. This behavior is shown experimentally in Fig. 7·5 where the cell's scattering structures are present in both the real and imaginary reconstructions.

Finally, the phase of $D(\boldsymbol{\nu}, z)$ is best understood under paraxial conditions with oblique illumination: $\eta^-(\boldsymbol{\nu}^+) \approx -\lambda(\boldsymbol{\nu}_l \cdot \boldsymbol{\nu} + |\boldsymbol{\nu}|^2/2)$. This term provides a linear geometric shift akin to lightfield [66] and Fresnel diffraction, respectively. These factors enable the post-correction of focusing errors during object reconstruction and have similar form for $\eta^-(\boldsymbol{\nu}^-)$.

To evaluate this forward model, we generate the expected intensity contrast using Eq. (7.12) on the same objects and imaging conditions as the DDA simulation in Fig. 7·3(c)(Orange). Our model adequately estimates the intensity contrast's linear

component for objects with weak phase (Fig. 7·3(c)) but quickly overestimates more strongly scattering objects. Since these overestimated objects are typically considered weakly scattering in transmission, our model's failure in this range highlights its reduced validity range from the enhanced phase sensitivity. When reconstructing the object with this reflection model, we will thus recover thin structures and underestimate taller objects. We confirm this in simulation and experiment in Section 7.3 using the reconstruction method described below.

7.2.2 Object Reconstruction

For recovering the object phase, we follow the same minimization problem described in Section 3.3. We consider all L measurements and implement Tikhonov deconvolution for recovering the complex object by solving

$$\underset{\widehat{\Phi}_{\mathrm{re}},\widehat{\Phi}_{\mathrm{im}}}{\operatorname{argmin}} \sum_{l=1}^{L} \left|\left|\widehat{I}_l^N - (H_{\mathrm{im},l}\widehat{\Phi}_{\mathrm{im}} + H_{\mathrm{re},l}\widehat{\Phi}_{\mathrm{re}})\right|\right|_2^2 + \tau_{\mathrm{im}}\left|\left|\widehat{\Phi}_{\mathrm{im}}\right|\right|_2^2 + \tau_{\mathrm{re}}\left|\left|\widehat{\Phi}_{\mathrm{re}}\right|\right|_2^2, \tag{7.14}$$

where τ_{im} and τ_{re} are regularization parameters. We obtain the following closed-form solution

$$\hat{\Phi}_{\mathrm{re}}(\boldsymbol{r}_\perp) = \frac{1}{T}\Big[\Big(\sum_{l=1}^{L}\left|\mathcal{H}_{\mathrm{im},l}\right|^2 + \tau_{\mathrm{im}}\Big)\Big(\sum_{l=1}^{L}\mathcal{H}_{\mathrm{re},l}^*\hat{I}_l^N\Big) - \Big(\sum_{l=1}^{L}\mathcal{H}_{\mathrm{re},l}^*\mathcal{H}_{\mathrm{im},l}\Big)\Big(\sum_{l=1}^{L}\mathcal{H}_{\mathrm{im},l}^*\hat{I}_l^N\Big)\Big] \tag{7.15a}$$

$$\hat{\Phi}_{\mathrm{im}}(\boldsymbol{r}_\perp) = \frac{1}{T}\Big[\Big(\sum_{l=1}^{L}\left|\mathcal{H}_{\mathrm{re},l}\right|^2 + \tau_{\mathrm{re}}\Big)\Big(\sum_{l=1}^{L}\mathcal{H}_{\mathrm{im},l}^*\hat{I}_l^N\Big) - \Big(\sum_{l=1}^{L}\mathcal{H}_{\mathrm{im},l}^*\mathcal{H}_{\mathrm{re},l}\Big)\Big(\sum_{l=1}^{L}\mathcal{H}_{\mathrm{re},l}^*\hat{I}_l^N\Big)\Big] \tag{7.15b}$$

where $T = \big(\sum_{l=1}^{L}|\mathcal{H}_{\mathrm{re},l}|^2+\tau_{\mathrm{re}}\big)\big(\sum_{l=1}^{L}|\mathcal{H}_{\mathrm{im},l}|^2+\tau_{\mathrm{im}}\big) - \big(\sum_{l=1}^{L}\mathcal{H}_{\mathrm{re},l}\mathcal{H}_{\mathrm{im},l}^*\big)\big(\sum_{l=1}^{L}\mathcal{H}_{\mathrm{re},l}^*\mathcal{H}_{\mathrm{im},l}\big)$. This reconstruction is performed once to recover the object's real and imaginary phase, similar to [62]. Optimal values for τ_{re},τ_{im} were chosen based on manually evaluating the reconstructions from a range of regularization values.

7.3 Results

7.3.1 Reconstruction from Simulated Cuboids

We further evaluate our linear model's validity range by reconstructing the DDA-simulated objects. We use the average pixel-wise difference between the reconstructed and ground-truth objects as our error metric. Given the reconstruction's maximum bandwidth of 0.45NA, we filter the ground-truth object with a 0.45NA circular pupil to directly compare the best object resolvable with the system and the linear model's reconstructions. In addition, we convert our recovered phase Φ and the ground-truth filtered object to the average RI contrast $\overline{\Delta n}$ for both real and imaginary components. For an object of uniform permittivity contained entirely within the objective DOF, the average permittivity contrast is equivalent to $\overline{\Delta\epsilon}(\boldsymbol{r}_\perp) = \Phi(\boldsymbol{r}_\perp)/\text{DOF}$, where $\text{DOF} = \lambda/\text{NA}^2$. We subsequently convert this value to average RI contrast $\overline{\Delta n}$ based on the relation of permittivity and RI. This choice enables direct comparison between our reflection model's reconstructions and the transmission reconstructions of Section 7.3. We convert our simulation outputs to the average RI contrast as well for consistency.

Visuals of the reconstructed cuboids are shown in Fig. 7·4(a) with color scales adjusted to match the expected average RI contrast for each object. Fig. 7·4(b)-(d) shows the error for our reconstructions for fixed RI contrasts with object height (Fig. 7·4(b)), fixed heights with varying RI (Fig. 7·4(c)), and fixed RI contrast with object height across multiple wavelengths (Fig. 7·4(d)). For weak RI contrast objects, we adequately predict the average of the object's phase and show primarily sinusoidal error due to the missing backscattering phase contribution (Fig. 7·4(a)-(b)). With increasing RI values, the linear model underestimates taller objects as the forward-scattered field accumulates phase and exits the Taylor expansion's validity range (Fig. 7·4(a)-(b)). With the missing backscattered phase from Eq. (7.7), we observe nonlinear, sinusoidal error as a function of object height with oscillation

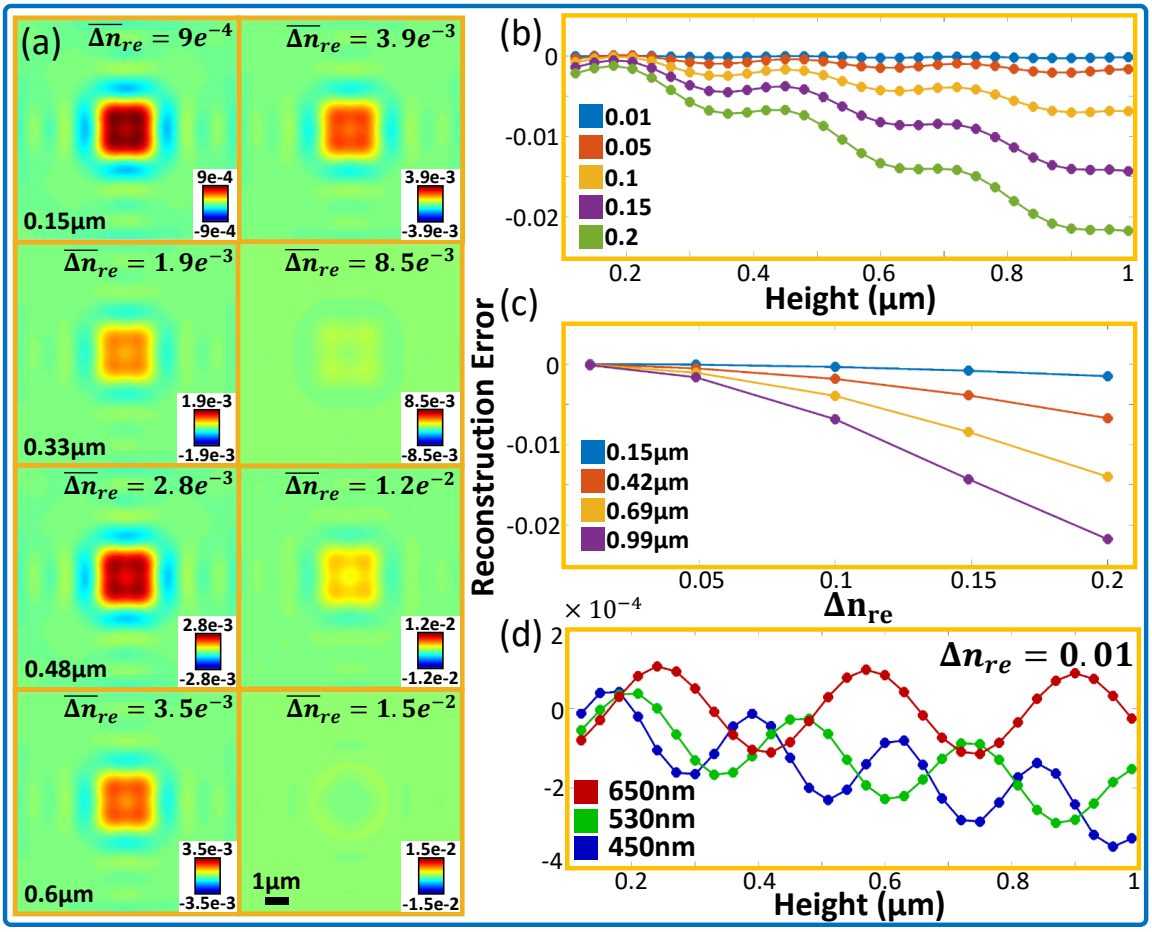

Figure 7·4: (a) Linear model reconstructions of cuboid average permittivity contrast. The color scales are adjusted based on the ground truth object's properties to show correctly recovered cuboids in red. Weak permittivity (left) objects are more accurately recovered compared to strong permittivity (right) structures. (b) Cuboid reconstruction error at $\lambda = 530$nm across different object heights at fixed permittivity contrast values. Nonlinear error is always present from backscattering, and increasingly tall objects quickly become underestimated from the enhanced sensitivity of our model. (c) Cuboid reconstruction error at $\lambda = 530$nm across different permittivity contrasts for fixed object heights. The error is linear with permittivity contrast following Eq. (7.5). (d) Cuboid reconstruction error for a $\Delta n_{\text{re}} = 0.01$ object across multiple heights at different wavelengths ($\lambda = 450, 530, 650$nm). We observe nonlinear error also shifts with period following Fig. 7·3(d).

period varying with the illumination wavelength (Fig. 7·4(b),(d)). The linearity with RI contrast is still preserved (Fig. 7·4(c)).

These results confirm our linear model's validity range is considerably more limited than transmission intensity-only approaches. Without evaluating the object in an imaging medium of nearly equivalent RI, the reflection imaging case provides reasonable phase recovery only for thin structures at nanometer length-scales. This is restrictive for biological sample imaging where structures, such as cells and bacteria, have varied size distributions that are both within and outside the validity range of this model. This validity range is further reduced for objects with high variance in both size and RI, as the object's physical parameters would become ambiguous in our reconstruction. Despite these factors, we show reliable object recovery on thin cellular structures with high contrast below.

7.3.2 Reconstructions from Experiment

We experimentally investigate the validity range of our reflection model using the setup in Fig. 7·1(a). A 530nm LED (Lighthouse LEDs, 10 Watt Jade Green) placed behind a white diffuser (Edmund Optics, 34473) and a 300μm pinhole (Thorlabs, P300H) composes the illumination source. This source resides inside a motorized (Thorlabs, Z806) XY translation stage (Thorlabs, ST1XY) and follows the Köhler geometry for oblique illumination up to 0.2NA. This illumination angle was chosen based on the scannable light source's maximum range of motion. A 4F setup provides 3.3× magnification generating a 1mm diameter source (0.025NA, coherence parameter = 0.1) at the back-focal plane of the objective lens (10×, 0.25NA, Nikon). The detection path collects the field through the objective and relays it to the camera (Thorlabs,CS2100M-USB) with a 200mm tube lens. The system's total NA is 0.45 with a $\sim$1.2μm lateral resolution. In each experiment, 97 images were acquired over an approximate five minute measurement period. The samples consist of unstained

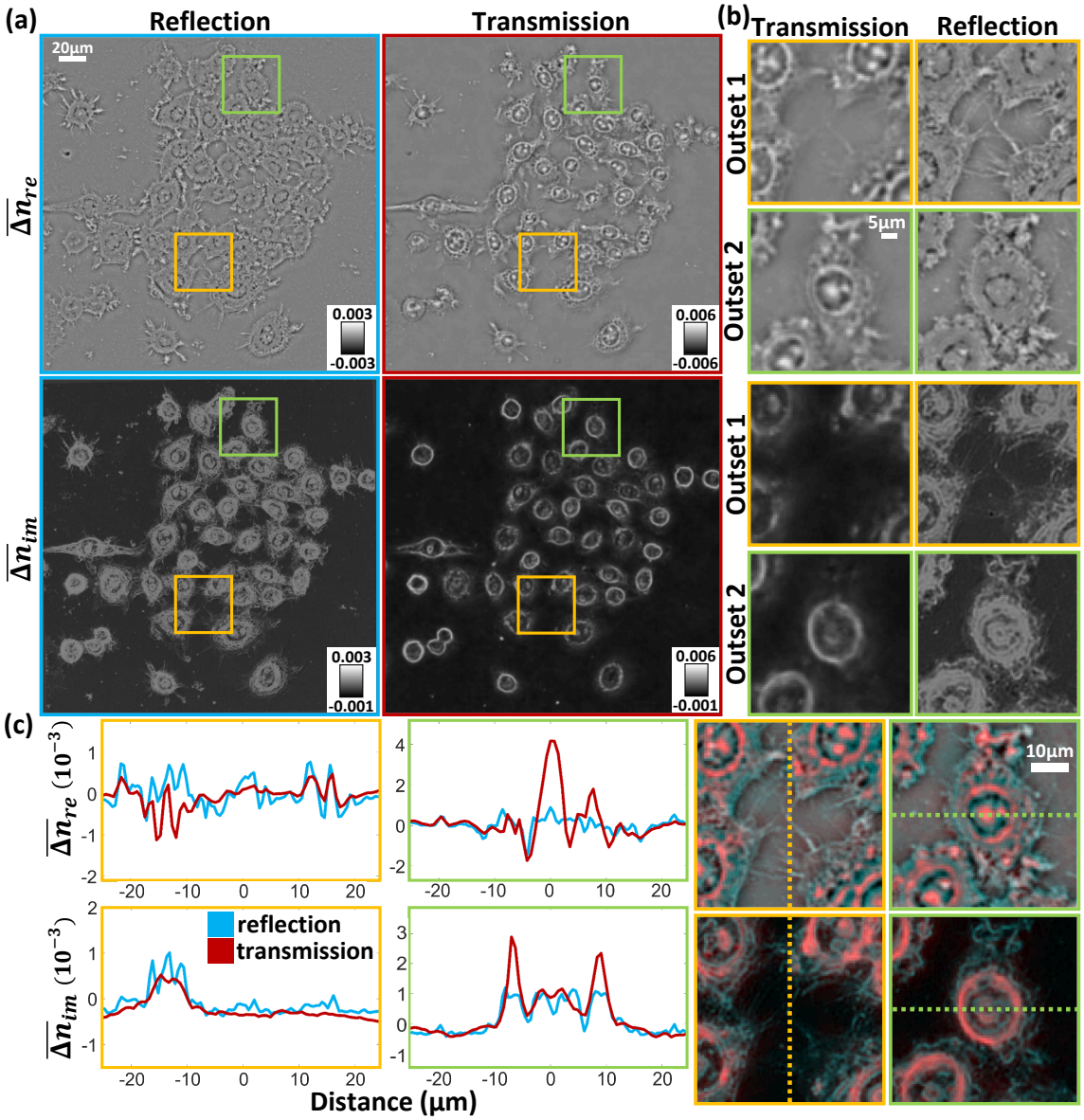

Figure 7·5: (a) Full FOV complex RI contrast reconstructions for reflection and transmission (HeLa cells); (b) Outset regions show (1) cell boundaries and filopodia, and (2) cell nuclei reconstructions; (c) Cross-sections compare reflection and transmission average RI contrast reconstructions and overlays of transmission and reflection reconstructions. Outset 1 show better membrane structure contrast in reflection than transmission with agreement on the recovered average RI contrast values. Outset 2 shows reflection underestimates the RI contrast of tall nuclear features as expected from simulation.

HeLa cells fixed with ethanol (Fig. 7·5) and formalin (Fig. 7·1).

For comparison, the transmission-based IDT technique [8] was also applied to the same samples using 87 images and up to 0.25 NA illumination (630nm LED array) on the same objective lens. This system's specifications and reconstruction process are detailed in [8].

We evaluate the recovered average RI contrast of the HeLa cells from both techniques in Fig. 7·5. Full field-of-view (FOV) reconstructions are shown in Fig. 7·5(a) with corresponding subcellular regions highlighted in outsets 1 and 2 (Fig. 7·5(b)). The cross-sections through these outsets are also presented in Fig. 7·5(c) with overlays directly comparing the two methods' reconstructions. Outsets 1 shows cellular membrane boundaries and filopodia and outset 2 highlights features within the cell nucleus.

Outset 1 highlights the improved contrast our reflection model provides over the transmission technique (Fig. 7·5(b)-(c)). The observed filopodial structures range down to 100nm in diameter [198] while cellular membranes can be only a few nanometers in thickness. Comparing the reconstructions shows enhanced contrast from reflection and agreement in average RI contrast value with transmission for both the real and imaginary contrast (Fig. 7·5(c), orange). These results indicate our reflection model reliably recovers these features despite the greater error from the height-dependent nonlinear back-scattered field.

Outset 2 shows our reflection model's underestimation of large objects. Nuclear structures maintain similar RI contrast to the surrounding cellular material but are much taller than the surrounding membrane. The green cross-sections in Fig. 7·5(c) show transmission measurements capture tall, higher contrast features while reflection underestimates the object RI in both the real and imaginary reconstructions. This underestimation agrees with our results in Fig. 7·4 where our linear reflection model

could not adequately recover tall features at large RI contrast.

The image overlays of Fig. 7·5(c) highlight the complementary nature of the transmission and reflection QPI measurements. We observe dominant reflection reconstructions (blue) in the membrane features with weak phase while transmission (red) recovers nuclear features with larger phase. Combining these modalities provides a more complete cell evaluation, where the cell boundaries become clearly visible from reflection and the nucleus is adequately measured in transmission. This results suggests that this linear reflection model could still provide useful information for biological research applications when combined with transmission QPI modalities.

7.4 Discussion

We derived and evaluated intensity-only linear scattering models for recovering phase in reflection from an object above a partially reflective boundary interface. Our derivation showed both forward-scattered and back-scattered fields are measured in reflection from an illuminated object in the presence of this interface in similar fashion to the mirror tomographic approaches [180, 182]. These contributions provide slowly varying, approximately linear phase behavior in the forward case and rapidly oscillating, nonlinear behavior in the backscattering case dependent on object height. Through rigorous DDA simulations, we confirmed this linear and height-dependent nonlinear phase behavior across objects of varying height, RI, and with different imaging wavelengths. We presented a simplified linear model recovering only the *forward*-scattered phase from the object that accepts the nonlinear field behavior as error in the object reconstruction. Through DDA simulations and object reconstructions, we showed the reflection case provides enhanced phase sensitivity and contrast for thin objects with weak permittivity contrast and underestimates taller, higher RI contrast structures. We confirmed this result by measuring fixed HeLa cells on a

glass slide in reflection and transmission using our approach and IDT, respectively. This sample showed thin membrane structures are recovered with greater contrast in reflection, but tall nuclear features are underestimated with our approach when compared with transmission. Our physical model shows linear approximations for intensity-only imaging systems are more restrictive in reflection than transmission due to the backscattered field's nonlinear behavior with object height. Despite this limitation, very thin object features can be recovered with minimal reconstruction error using a linear model. Given this model's strict limitations to thin objects, this intensity-only reflection phase system is best utilized in tandem with transmission modalities to provide thin feature recovery with the thick structures recovered in transmission.

The nonlinear behavior of the backscattered field can be better understood through an evaluation of the Ewald's sphere [49]. The back-scattered field relates to the upper half of the Ewald's sphere containing high-frequency, high-resolution axial information about the object. For low NA illumination in a quasi-monochromatic imaging system, this upper half of the sphere is effectively measured only at $\lambda/2$ with the back-scattered field. This under-sampling results in oscillations with object height as observed in our DDA simulations. Using higher NA objectives and illumination enhance this axial bandwidth to achieve improved axial resolution but requires additional hardware specialization and complexity [182, 183].

Compared to the existing reflection interferometric modalities using temporal gating [164, 145, 169], our intensity-only system is limited by the sample thickness due to its lack of adequate depth sectioning as compared to the backscatter signal oscillation period. Nevertheless, performing phase imaging on thick samples using intensity-only measurements *without* temporal gating is still possible, as recently demonstrated by oblique back-illumination microscopy (OBM) [160]. OBM exploits multiply scattered

diffuse photons to generate oblique trans-illumination in a reflection imaging geometry [160]. Consequently, OBM also relies on the dominant forward-scattering signal from the object, similar to our model. The volumetric scattering medium effectively suppresses the object's backscattering contribution enabling a similar, yet less stringent linear phase imaging approach providing enhanced contrast and phase gradient information [184, 186] as well as quantitative phase recovery [185].

One avenue for improving our model's validity range is through reducing the permittivity contrast between the object and surrounding medium. Evaluating a cell sample in aqueous media with closer permittivity would solve this problem and enable researchers to evaluate their cultures directly, but a significant issue arises with the boundary interface. With larger imaging medium permittivity, we reduce the mismatch between the medium and boundary layer that generates the forward-scattering necessary for this model. The weakened forward-scattering field strength would reduce the linearity of the scattering field and also limit the model's validity range. Using a higher permittivity boundary would be possible but necessitates specializing the imaging platform which makes it less accessible for biological research. In addition, the reflections from the aqueous media's surface would alter the physical model proposed here. For these reasons, we used the strongly scattering HeLa cell sample in our experiment to illustrate our technique's capabilities on glass slides commonly used for biological research.

Another avenue for improvement is to develop *nonlinear* scattering models that can better account for the scattering process. Computationally efficient and accurate multiple scattering models have recently been demonstrated for transmission-mode phase tomography [100, 31, 199, 43, 41, 42]. Adapting such models to reflection is possible [192] and will be considered in our future work.

Beyond the *model*-based inverse scattering framework, the alternative *learning*-

based tomographic reconstruction framework has drawn significant interest. Promising inverse scattering results have been demonstrated in transmission systems [97, 95, 96, 30, 91, 200], with the closest application of learning-based tomography discussed in Chapter 6 [133]. The success of such algorithms in transmission suggests they could also be implemented to enhance multiple-scattering in reflection and recover the nonlinear backscattered field. Recovering this nonlinear signal would enable the discussed imaging setup to provide 3D QPI with high axial resolution in reflection.

Chapter 8

Conclusions

8.1 Thesis Summary

This thesis focused on enhancing the intensity-based, scanless 3D QPI modality known as intensity diffraction tomography. From the background discussed in Chapters 1 and 2, the IDT modality offers significant advantages over other 3D QPI techniques by avoiding the coherent noise artifacts in interferometry-based ODT and providing a scanless phase-encoding strategy encoding the object's phase using diverse illumination instead of defocus-based mechanisms. The model and initial implementation of IDT, reviewed in Chapter 3 from work by Ling et al. [8], discussed how this system benefited not only from its low-cost hardware but from its use of an assumption of axially-independent scattering behavior enabling *slice-wise* computationally efficient reconstructions of an object's 3D volume. This initial work validated the technique in experiment and simulation and showed the imaging modality could recover phase features in biological samples that were previously invisible to absorption-based imaging methods. The IDT implementation, despite its strong performance, suffered from a number of limitations including: 1) non-optimized illumination designs limiting its acquisition speed, 2) its linear model failing on multiple-scattering objects, and 3) its low axial resolution preventing fine axial detail recovery of subcellular structures.

Chapters 4 and 5 presented two solutions to the slow acquisition speed of the IDT modality preventing the analysis of live biological samples. These methods relied on an understanding of the linear model's TF to provide software-based and hardware-based illumination strategies to recover high-quality 3D QPI of dynamic biological specimens. Chapter 4 showed that heavily downsampled, well spread out multiplexed LED illuminations could evaluate biological samples at hardware-limited 4Hz volume rates while sacrificing minimal reconstruction quality. Chapter 5 advanced upon this development by showing that sparse annular illumination from ring-geometry LED arrays could provide better reconstruction quality of living specimens at camera-limited 10Hz volume rates using only eight intensity images per reconstruction. These advancements were significant in providing simple, cost-effective solutions for high-speed IDT that could be just as easily adopted by biological imaging labs for 3D QPI.

Using the annular IDT method from Chapter 5, the limitations of IDT's linear model were addressed using learning-based approaches in Chapter 6. This section showed that training a lightweight 2D network on purely simulated natural image-based object volumes could provide generalized recovery of 3D biological volumes regardless of the object or imaging system used for experimental measurements. This learning approach could be rapidly trained in hours and showed enhanced RI and improved structure recovery without the missing cone artifacts present from the linear model reconstruction. Because most multiple-scattering models require significant computation to recover complex biological specimens, this work showed an alternative, reliable method to recover multiple-scattering objects in a computationally efficient manner.

Finally, an investigation into the potential for IDT in reflection was discussed in Chapter 7. While a reflection imaging mode captures the backscattered signal con-

taining high axial resolution object information, the model development, simulations, and experimental testing in this section showed that *linear* 3D models in reflection were not possible for IDT-designed setups. A 2D model was shown to be possible and provided enhanced sensitivity to cellular membranes and other thin biological structures in a complementary fashion to transmission-mode IDT.

8.2 Advancing transmission-mode IDT

The advancements shown in IDT have only expanded the possibilities for further improving the modality. One immediate result of the work done in this thesis is the potential for performing 3D QPI in even simpler optical setups. As shown in recent works [134, 76], low-cost, open-source optical imaging setups are becoming increasingly popular in improving the accessibility of various imaging modalities to the general public. With the simple hardware and software for IDT, the creation of similar low-cost setups for IDT is also possible and has already been tested by Diederich *et al.* [76]. This result indicates that IDT can be incorporated as another imaging modality in a multi-modal, affordable optical setup for biological sample imaging by anyone interested in science. The main downside of such devices is their lower machining precision that can cause significant reductions in IDT's reconstruction quality from illumination angle misalignments as discussed in Chapter 3. As shown in Chapter 5, however, post-processing calibration algorithms can ameloriate this potential problem. Recent developments in deep learning strategies suggest that such hardware-based confounding factors could also be corrected rapidly with learned approaches [201, 202]. Such learning methods could also correct for the stronger mIDT reconstruction artifacts and enable even faster acquisition speeds. Furthermore, the computational simplicity of IDT and the learning method discussed in Chapter 6 could be integrated onto a cellphone for real-time volumetric 3D QPI in similar form

to [135]. This real-time processing could be highly beneficial in rapidly evaluating living biological samples for numerous applications ranging from teaching students in classrooms about QPI to studying a cell culture's response to drugs or other exogenous agents.

Another region of improvement available to IDT is in the learning approach discussed in Chapter 6. The current implementation relies on approximant-guided learning where the only object information provided to the network is from the linear model's reconstruction. In cases where the IDT model cannot adequately recover the object's structure, the network will also likely fail to recover the object's features. Recently, alternative network designs have shown promising recovery object recovery using dynamic machine learning [121], adding image information to the input [203], or the incorporation of the physical model into the learning process [204]. The first two methods would introduce additional nonlinear information to the model for better learning how to recover the multiple-scattering object. This last option is particularly appealing, as the use of physical models in the learning model can elucidate the workings of the learning approach to provide reliable object predictions. For biologists, knowing the behavior of the network would significantly improve their trustworthiness in using these learning models for evaluating any complex biological specimen.

In line with developing more advanced learning models for IDT, this modality can also be expanded into a multi-modal system through the application of virtual staining techniques [136, 137, 138, 139]. These methods have utilized the recovered structural content from phase imaging techniques to synthesize fluorescent labels onto unlabeled biological specimens. The significant potential for this approach is that it can add specificity to the phase object to better evaluate the specimen's structures using a "computational multimodal" setup. While this has primarily been explored in

2D, the realm of evaluating 3D fluorescence for digital staining is largely unexplored. This avenue would provide a substantial boon for the biological imaging community by providing digital staining of 3D biological samples for analysis.

8.3 Advancing reflection-mode IDT

Despite the shortfalls encountered with 3D reflection-mode IDT, a number of advancements could still be made to the setup described in Chapter 7. Most critically, the reflection-mode IDT technique would significantly benefit from being expanded to full 3D imaging. In the linear model space, recent works have shown this is possible in deep tissue imaging [205, 185, 160] where the nonlinear backscattered signal is removed by the tissue's multiple-scattering behavior. For samples on a glass slide, however, alternative strategies are required for recovering both the forward and backscattered signal unambiguously to reconstruct the 3D object. Given the ability to simulate objects in reflection, one avenue for 3D object recovery is to implement a similar simulator-trained network learning strategy as Chapter 6 for reflection. This route could extend the reflection case to recover 3D, but the greater complexity of the DDA simulation tool used in Chapter 7 for reflection would require significantly greater computation to generate a training dataset. End-to-end network models recovering the 3D object from the system's intensity images could also be explored in this case as well. These learning-based solutions would bypass the need for a more complex reflection model and maintain computational efficiency while expanding the reflection IDT system's capabilities.

Another option for enhancing the reflection IDT case is to modify the reflection setup with an additional collection path below the sample. Following similar designs to the I^5M and 4π microscopes [206, 207], this design would capture both the forward and backscattered fields from the object containing both the low and high axial reso-

lution object information. Because the transmitted field through the glass substrate would not contain the ambiguous mixing of forward and backscattered fields, the transmission could aid in separating and recovering the nonlinearities present from the backscattering. This design is possible due to the assumption of an imperfectly reflecting boundary layer, and the imaging condition would require a new imaging model for the reconstruction. While sacrificing IDT's system complexity and requiring a new and more rigorous physical model, this design could enable high-resolution 3D imaging of the sample with isotropic resolution.

Bibliography

[1] G. Gbur and E. Wolf, "Diffraction tomography without phase information," *Optics Letters*, vol. 27, no. 21, pp. 1890–1892, Nov. 2002. [Online]. Available: http://ol.osa.org/abstract.cfm?URI=ol-27-21-1890

[2] A. Barty, K. Nugent, A. Roberts, and D. Paganin, "Quantitative phase tomography," *Optics Communications*, vol. 175, no. 4-6, pp. 329–336, 2000.

[3] G. Gbur, M. A. Anastasio, Y. Huang, and D. Shi, "Spherical-wave intensity diffraction tomography," *Journal of the Optical Society of America A*, vol. 22, no. 2, pp. 230–238, Feb. 2005. [Online]. Available: http://josaa.osa.org/abstract.cfm?URI=josaa-22-2-230

[4] J. M. Soto, J. A. Rodrigo, and T. Alieva, "Label-free quantitative 3d tomographic imaging for partially coherent light microscopy," *Optics Express*, vol. 25, no. 14, pp. 15 699–15 712, 2017.

[5] J. Li, Q. Chen, J. Sun, J. Zhang, J. Ding, and C. Zuo, "Three-dimensional tomographic microscopy technique with multi-frequency combination with partially coherent illuminations," *Biomedical Optics Express*, vol. 9, no. 6, pp. 2526–2542, 2018.

[6] M. Chen, L. Tian, and L. Waller, "3D differential phase contrast microscopy," *Biomedical Optics Express*, vol. 7, no. 10, pp. 3940–3950, Oct 2016. [Online]. Available: http://www.osapublishing.org/boe/abstract.cfm?URI=boe-7-10-3940

[7] M. H. Jenkins and T. K. Gaylord, "Three-dimensional quantitative phase imaging via tomographic deconvolution phase microscopy," *Applied Optics*, vol. 54, no. 31, pp. 9213–9227, 2015.

[8] R. Ling, W. Tahir, H.-Y. Lin, H. Lee, and L. Tian, "High-throughput intensity diffraction tomography with a computational microscope," *Biomedical Optics Express*, vol. 9, no. 5, pp. 2130–2141, 2018.

[9] J. Li, A. C. Matlock, Y. Li, Q. Chen, C. Zuo, and L. Tian, "High-speed in vitro intensity diffraction tomography," *Advanced Photonics*, vol. 1, no. 6, p. 066004, 2019.

[10] H. Iqbal, "Plotneuralnet v1.0.0," Zenodo, Dec. 2018, https://doi.org/10.5281/zenodo.2526396. [Online]. Available: https://doi.org/10.5281/zenodo.2526396

[11] L. Bossard, M. Guillaumin, and L. Van Gool, "Food-101 – mining discriminative components with random forests," in *European Conference on Computer Vision*, 2014.

[12] L. A. Royer, M. Weigert, U. Günther, N. Maghelli, F. Jug, I. F. Sbalzarini, and E. W. Myers, "Clearvolume: open-source live 3d visualization for light-sheet microscopy," *Nature methods*, vol. 12, no. 6, pp. 480–481, 2015.

[13] D. T. Ginat and R. Gupta, "Advances in computed tomography imaging technology," *Annual review of biomedical engineering*, vol. 16, pp. 431–453, 2014.

[14] J. Hsieh, *Computed tomography: principles, design, artifacts, and recent advances*. SPIE press, 2003, vol. 114.

[15] P. Sarder and A. Nehorai, "Deconvolution methods for 3-D fluorescence microscopy images," *IEEE Signal Processing Magazine*, vol. 23, no. 3, pp. 32–45, May 2006.

[16] R. Ng, M. Levoy, M. Bredif, G. Duval, M. Horowitz, and P. Hanrahan, "Light field photography with a hand-held plenoptic camera," Stanford, Tech. Rep. CTSR 2005-02, 2005.

[17] L. Gao, J. Liang, C. Li, and L. V. Wang, "Single-shot compressed ultrafast photography at one hundred billion frames per second," *Nature*, vol. 516, no. 7529, pp. 74–77, 2014.

[18] D. Jin, R. Zhou, Z. Yaqoob, and P. So, "Tomographic phase microscopy: Principles and applications in bioimaging," *Journal of the Optical Society of America B*, vol. 34, no. 5, pp. B64–B77, 2017.

[19] T. Kim, R. Zhou, L. L. Goddard, and G. Popescu, "Solving inverse scattering problems in biological samples by quantitative phase imaging," *Laser & Photonics Reviews*, vol. 10, no. 1, pp. 13–39, 2016.

[20] B. Bhaduri, C. Edwards, H. Pham, R. Zhou, T. H. Nguyen, L. L. Goddard, and G. Popescu, "Diffraction phase microscopy: principles and applications in materials and life sciences," *Advances in Optics and Photonics*, vol. 6, no. 1, p. 57, Mar 2014. [Online]. Available: http://dx.doi.org/10.1364/AOP.6.000057

[21] P. A. Sandoz, C. Tremblay, S. Equis, S. Pop, L. Pollaro, Y. Cotte, G. F. Van Der Goot, and M. Frechin, "Label free 3d analysis of organelles in living cells by refractive index shows pre-mitotic organelle spinning in mammalian stem cells," *BioRxiv*, p. 407239, 2018.

[22] V. Nandakumar, L. Kelbauskas, K. F. Hernandez, K. M. Lintecum, P. Senechal, K. J. Bussey, P. C. Davies, R. H. Johnson, and D. R. Meldrum, "Isotropic 3d nuclear morphometry of normal, fibrocystic and malignant breast epithelial cells reveals new structural alterations," *PloS one*, vol. 7, no. 1, p. e29230, 2012.

[23] Y. Park, M. Diez-Silva, G. Popescu, G. Lykotrafitis, W. Choi, M. S. Feld, and S. Suresh, "Refractive index maps and membrane dynamics of human red blood cells parasitized by plasmodium falciparum," *Proceedings of the National Academy of Sciences*, vol. 105, no. 37, pp. 13 730–13 735, 2008.

[24] E. Wolf, "Three-dimensional structure determination of semi-transparent objects from holographic data," *Optics Communications*, vol. 1, no. 4, pp. 153–156, September/October 1969.

[25] Y. Sung, W. Choi, C. Fang-Yen, K. Badizadegan, R. R. Dasari, and M. S. Feld, "Optical diffraction tomography for high resolution live cell imaging," *Optics Express*, vol. 17, no. 1, pp. 266–277, December 2009.

[26] S. Shin, K. Kim, J. Yoon, and Y. Park, "Active illumination using a digital micromirror device for quantitative phase imaging," *Optics Letters*, vol. 40, no. 22, pp. 5407–5410, 2015.

[27] Y. Cotte, F. Toy, P. Jourdain, N. Pavillon, D. Boss, P. Magistretti, P. Marquet, and C. Depeursinge, "Marker-free phase nanoscopy," *Nature Photonics*, 2013.

[28] J. Lim, A. Wahab, G. Park, K. Lee, Y. Park, and J. C. Ye, "Beyond born-rytov limit for super-resolution optical diffraction tomography," *Optics express*, vol. 25, no. 24, pp. 30 445–30 458, 2017.

[29] J. W. Lim, K. R. Lee, K. H. Jin, S. Shin, S. E. Lee, Y. K. Park, and J. C. Ye, "Comparative study of iterative reconstruction algorithms for missing cone problems in optical diffraction tomography," *Optics Express*, vol. 23, no. 13, pp. 16 933–16 948, June 2015.

[30] A. Goy, G. Rughoobur, S. Li, K. Arthur, A. I. Akinwande, and G. Barbastathis, "High-resolution limited-angle phase tomography of dense layered objects using deep neural networks," *Proceedings of the National Academy of Sciences*, vol. 116, no. 40, pp. 19 848–19 856, 2019.

[31] U. S. Kamilov, I. N. Papadopoulos, M. H. Shoreh, A. Goy, C. Vonesch, M. Unser, and D. Psaltis, "Learning approach to optical tomography," *Optica*, vol. 2, no. 6, pp. 517–522, 2015.

[32] J. Yoon, K. Kim, H. Park, C. Choi, S. Jang, and Y. Park, "Label-free characterization of white blood cells by measuring 3d refractive index maps," *Biomedical optics express*, vol. 6, no. 10, pp. 3865–3875, 2015.

[33] R. Chandramohanadas, Y. Park, L. Lui, A. Li, D. Quinn, K. Liew, M. Diez-Silva, Y. Sung, M. Dao, C. T. Lim *et al.*, "Biophysics of malarial parasite exit from infected erythrocytes," *PloS one*, vol. 6, no. 6, p. e20869, 2011.

[34] Y. Sung, W. Choi, N. Lue, R. R. Dasari, and Z. Yaqoob, "Stain-free quantification of chromosomes in live cells using regularized tomographic phase microscopy," *PloS one*, vol. 7, no. 11, p. e49502, 2012.

[35] "Tomocube inc." http://www.tomocube.com/, accessed: 2021-05-20.

[36] "Nanolive label-free live cell imaging and analysis," https://www.nanolive.ch/, accessed: 2021-05-20.

[37] G. Gbur and E. Wolf, "Hybrid diffraction tomography without phase information," *Journal of the Optical Society of America A*, vol. 19, no. 11, pp. 2194–2202, Nov. 2002. [Online]. Available: http://josaa.osa.org/abstract.cfm?URI=josaa-19-11-2194

[38] G. Zheng, R. Horstmeyer, and C. Yang, "Wide-field, high-resolution Fourier Ptychographic microscopy," *Nature Photonics*, vol. 7, no. 9, pp. 739–745, 2013. [Online]. Available: http://www.nature.com/nphoton/journal/v7/n9/abs/nphoton.2013.187.html

[39] T. H. Nguyen, M. E. Kandel, M. Rubessa, M. B. Wheeler, and G. Popescu, "Gradient light interference microscopy for 3D imaging of unlabeled specimens," *Nature Communications*, vol. 8, no. 1, p. 210, 2017.

[40] Z. Wang, L. Millet, M. Mir, H. Ding, S. Unarunotai, J. Rogers, M. U. Gillette, and G. Popescu, "Spatial light interference microscopy (SLIM)," *Optics Express*, vol. 19, no. 2, pp. 1016–1026, Jan. 2011. [Online]. Available: http://www.opticsexpress.org/abstract.cfm?URI=oe-19-2-1016

[41] S. Chowdhury, M. Chen, R. Eckert, D. Ren, F. Wu, N. Repina, and L. Waller, "High-resolution 3d refractive index microscopy of multiple-scattering samples from intensity images," *Optica*, vol. 6, no. 9, pp. 1211–1219, 2019.

[42] J. Lim, A. B. Ayoub, E. E. Antoine, and D. Psaltis, "High-fidelity optical diffraction tomography of multiple scattering samples," *Light: Science & Applications*, vol. 8, no. 1, pp. 1–12, 2019.

[43] W. Tahir, U. S. Kamilov, and L. Tian, "Holographic particle localization under multiple scattering," *Advanced Photonics*, vol. 1, no. 3, p. 036003, 2019.

[44] M. Born and E. Wolf, *Principles of Optics*, 7th ed. Cambridge Univ. Press, 1999.

[45] M. A. Anastasio, D. Shi, Y. Huang, and G. Gbur, "Image reconstruction in spherical-wave intensity diffraction tomography," *Journal of the Optical Society of America A*, vol. 22, no. 12, pp. 2651–2661, Dec. 2005. [Online]. Available: http://josaa.osa.org/abstract.cfm?URI=josaa-22-12-2651

[46] J. A. Rodrigo and T. Alieva, "Rapid quantitative phase imaging for partially coherent light microscopy," *Optics express*, vol. 22, no. 11, pp. 13 472–13 483, 2014.

[47] J. A. Rodrigo, J. M. Soto, and T. Alieva, "Fast label-free microscopy technique for 3d dynamic quantitative imaging of living cells," *Biomedical Optics Express*, vol. 8, no. 12, pp. 5507–5517, 2017.

[48] M. R. Teague, "Deterministic phase retrieval: a Green's function solution," *Journal of the Optical Society of America*, vol. 73, no. 11, pp. 1434–1441, 1983.

[49] N. Streibl, "Phase imaging by the transport equation of intensity," *Optics Communications*, vol. 49, no. 1, pp. 6–10, 1984.

[50] C. J. Sheppard, "Three-dimensional phase imaging with the intensity transport equation," *Applied optics*, vol. 41, no. 28, pp. 5951–5955, 2002.

[51] L. Waller, L. Tian, and G. Barbastathis, "Transport of intensity phase-amplitude imaging with higher order intensity derivatives," *Optics Express*, vol. 18, no. 12, pp. 12 552–12 561, 2010. [Online]. Available: http://www.opticsexpress.org/abstract.cfm?URI=oe-18-12-12552

[52] M. Soto and E. Acosta, "Improved phase imaging from intensity measurements in multiple planes," *Applied optics*, vol. 46, no. 33, pp. 7978–7981, 2007.

[53] C. Zuo, Q. Chen, Y. Yu, and A. Asundi, "Transport-of-intensity phase imaging using savitzky-golay differentiation filter-theory and applications," *Optics express*, vol. 21, no. 5, pp. 5346–5362, 2013.

[54] C. Zuo, J. Li, J. Sun, Y. Fan, J. Zhang, L. Lu, R. Zhang, B. Wang, L. Huang, and Q. Chen, "Transport of intensity equation: a tutorial," *Optics and Lasers in Engineering*, p. 106187, 2020.

[55] A. C. Kak and M. Slaney, *Principles of Computerized Tomographic Imaging*. IEEE, 1988.

[56] J. Li, Q. Chen, J. Zhang, Z. Zhang, Y. Zhang, and C. Zuo, "Optical diffraction tomography microscopy with transport of intensity equation using a light-emitting diode array," *Optics and lasers in engineering*, vol. 95, pp. 26–34, 2017.

[57] N. Streibl, "Three-dimensional imaging by a microscope," *Journal of the Optical Society of America A*, vol. 2, no. 2, pp. 121–127, 1985. [Online]. Available: http://josaa.osa.org/abstract.cfm?URI=josaa-2-2-121

[58] Y. Bao and T. K. Gaylord, "Quantitative phase imaging method based on an analytical nonparaxial partially coherent phase optical transfer function," *Journal of the Optical Society of America A*, vol. 33, no. 11, pp. 2125–2136, 2016.

[59] M. Bertero and P. Boccacci, *Introduction to inverse problems in imaging*. Taylor & Francis, 1998.

[60] J. Goodman, *Introduction to Fourier optics*, 3rd ed., Crisp, J. & Elliott, B., Ed. Roberts & Co., 2005.

[61] J. M. Soto, J. A. Rodrigo, and T. Alieva, "Partially coherent illumination engineering for enhanced refractive index tomography," *Optics letters*, vol. 43, no. 19, pp. 4699–4702, 2018.

[62] L. Tian and L. Waller, "Quantitative differential phase contrast imaging in an LED array microscope," *Optics Express*, vol. 23, no. 9, pp. 11 394–11 403, May 2015. [Online]. Available: http://www.opticsexpress.org/abstract.cfm?URI=oe-23-9-11394

[63] B. Diederich, R. Wartmann, H. Schadwinkel, and R. Heintzmann, "Using machine-learning to optimize phase contrast in a low-cost cellphone microscope," *PloS one*, vol. 13, no. 3, p. e0192937, 2018.

[64] Z. F. Phillips, M. Chen, and L. Waller, "Single-shot quantitative phase microscopy with color-multiplexed differential phase contrast (cdpc)," *PloS one*, vol. 12, no. 2, p. e0171228, 2017.

[65] M. Kellman, M. Chen, Z. F. Phillips, M. Lustig, and L. Waller, "Motion-resolved quantitative phase imaging," *Biomedical optics express*, vol. 9, no. 11, pp. 5456–5466, 2018.

[66] L. Tian, J. Wang, and L. Waller, "3D differential phase-contrast microscopy with computational illumination using an LED array," *Optics Letters*, vol. 39, no. 5, pp. 1326–1329, Mar. 2014. [Online]. Available: http://ol.osa.org/abstract.cfm?URI=ol-39-5-1326

[67] L. Tian and L. Waller, "3d intensity and phase imaging from light field measurements in an led array microscope," *Optica*, vol. 2, no. 2, pp. 104–111, 2015.

[68] L. Tian, X. Li, K. Ramchandran, and L. Waller, "Multiplexed coded illumination for Fourier ptychography with an LED array microscope," *Biomedical Optics Express*, vol. 5, no. 7, pp. 2376–2389, Jul 2014. [Online]. Available: http://www.opticsinfobase.org/boe/abstract.cfm?URI=boe-5-7-2376

[69] Z. F. Phillips, M. V. D'Ambrosio, L. Tian, J. J. Rulison, H. S. Patel, N. Sadras, A. V. Gande, N. A. Switz, D. A. Fletcher, and L. Waller, "Multi-contrast imaging and digital refocusing on a mobile microscope with a domed led array," *PLoS ONE*, vol. 10, no. 5, p. e0124938, 05 2015. [Online]. Available: http://dx.doi.org/10.1371%2Fjournal.pone.0124938

[70] K. Guo, S. Dong, and G. Zheng, "Fourier ptychography for brightfield, phase, darkfield, reflective, multi-slice, and fluorescence imaging," *IEEE Journal of Selected Topics in Quantum Electronics*, vol. 22, no. 4, pp. 77–88, 2016.

[71] A. Matlock and L. Tian, "High-throughput, volumetric quantitative phase imaging with multiplexed intensity diffraction tomography," *Biomedical Optics Express*, vol. 10, no. 12, p. 6432, Nov 2019. [Online]. Available: http://dx.doi.org/10.1364/BOE.10.006432

[72] S. Boyd, "Alternating direction method of multipliers," Presentation. [Online]. Available: http://www.stanford.edu/~boyd/papers/pdf/admm_slides.pdf

[73] D. Jin, R. Zhou, Z. Yaqoob, and P. T. So, "Dynamic spatial filtering using a digital micromirror device for high-speed optical diffraction tomography," *Optics express*, vol. 26, no. 1, pp. 428–437, 2018.

[74] R. Eckert, Z. F. Phillips, and L. Waller, "Efficient illumination angle self-calibration in fourier ptychography," *Applied Optics*, vol. 57, no. 19, p. 5434, Jun 2018. [Online]. Available: http://dx.doi.org/10.1364/AO.57.005434

[75] J. Li, A. Matlock, Y. Li, Q. Chen, L. Tian, and C. Zuo, "Resolution-enhanced intensity diffraction tomography in high numerical aperture label-free microscopy," *Photonics Research*, vol. 8, no. 12, pp. 1818–1826, 2020.

[76] B. Diederich, R. Lachmann, S. Carlstedt, B. Marsikova, H. Wang, X. Uwurukundo, A. S. Mosig, and R. Heintzmann, "A versatile and customizable low-cost 3d-printed open standard for microscopic imaging," *Nature communications*, vol. 11, no. 1, pp. 1–9, 2020.

[77] F. Zernike, "Phase contrast, a new method for the microscopic observation of transparent objects," *Physica*, vol. 9, pp. 686–698, 1942.

[78] M. Ziemczonok, A. Kuś, P. Wasylczyk, and M. Kujawińska, "3d-printed biological cell phantom for testing 3d quantitative phase imaging systems," *Scientific reports*, vol. 9, no. 1, pp. 1–9, 2019.

[79] M. Chen, D. Ren, H.-Y. Liu, S. Chowdhury, and L. Waller, "Multi-layer born multiple-scattering model for 3d phase microscopy," *Optica*, vol. 7, no. 5, pp. 394–403, 2020.

[80] L. Tian, Z. Liu, L.-H. Yeh, M. Chen, J. Zhong, and L. Waller, "Computational illumination for high-speed in vitro Fourier ptychographic microscopy," *Optica*, vol. 2, no. 10, pp. 904–911, 2015.

[81] M. Kellman, E. Bostan, M. Chen, and L. Waller, "Data-driven design for fourier ptychographic microscopy," in *2019 IEEE International Conference on Computational Photography (ICCP)*. IEEE, 2019, pp. 1–8.

[82] M. R. Kellman, E. Bostan, N. A. Repina, and L. Waller, "Physics-based learned design: optimized coded-illumination for quantitative phase imaging," *IEEE Transactions on Computational Imaging*, vol. 5, no. 3, pp. 344–353, 2019.

[83] W. Lee, D. Jung, S. Ryu, and C. Joo, "Single-exposure quantitative phase imaging in color-coded led microscopy," *Optics Express*, vol. 25, no. 7, pp. 8398–8411, 2017.

[84] J. Li, Q. Chen, J. Zhang, Y. Zhang, L. Lu, and C. Zuo, "Efficient quantitative phase microscopy using programmable annular led illumination," *Biomedical optics express*, vol. 8, no. 10, pp. 4687–4705, 2017.

[85] H.-H. Chen, Y.-Z. Lin, and Y. Luo, "Isotropic differential phase contrast microscopy for quantitative phase bio-imaging," *Journal of biophotonics*, vol. 11, no. 8, p. e201700364, 2018.

[86] Y. Fan, J. Sun, Q. Chen, X. Pan, L. Tian, and C. Zuo, "Optimal illumination scheme for isotropic quantitative differential phase contrast microscopy," *Photonics Research*, vol. 7, no. 8, p. 890, Jul 2019. [Online]. Available: http://dx.doi.org/10.1364/PRJ.7.000890

[87] R. Ling, W. Tahir, H.-Y. Lin, H. Lee, and L. Tian, "High-throughput intensity diffraction tomography with a computational microscope," *Biomedical Optics Express*, vol. 9, no. 5, p. 2130, Apr 2018. [Online]. Available: http://dx.doi.org/10.1364/BOE.9.002130

[88] R. Bridson, "Fast poisson disk sampling in arbitrary dimensions." in *SIGGRAPH sketches*, 2007, p. 22.

[89] Z. Liu, L. Tian, S. Liu, and L. Waller, "Real-time brightfield, darkfield, and phase contrast imaging in a light-emitting diode array microscope," *Journal of Biomedical Optics*, vol. 19, no. 10, pp. 106 002–106 002, 2014.

[90] A. Sinha, J. Lee, S. Li, and G. Barbastathis, "Lensless computational imaging through deep learning," *Optica*, vol. 4, no. 9, pp. 1117–1125, 2017.

[91] Y. Rivenson, Y. Zhang, H. Günaydın, D. Teng, and A. Ozcan, "Phase recovery and holographic image reconstruction using deep learning in neural networks," *Light: Science & Applications*, vol. 7, no. 2, p. 17141, 2018.

[92] T. Nguyen, Y. Xue, Y. Li, L. Tian, and G. Nehmetallah, "Deep learning approach for fourier ptychography microscopy," *Optics express*, vol. 26, no. 20, pp. 26 470–26 484, 2018.

[93] Y. Xue, S. Cheng, Y. Li, and L. Tian, "Reliable deep-learning-based phase imaging with uncertainty quantification," *Optica*, vol. 6, no. 5, pp. 618–629, 2019.

[94] U. S. Kamilov, I. N. Papadopoulos, M. H. Shoreh, A. Goy, C. Vonesch, M. Unser, and D. Psaltis, "Optical tomographic image reconstruction based on beam propagation and sparse regularization," *IEEE Transactions on Computational Imaging*, vol. 2, no. 1, pp. 59–70, March 2016.

[95] Y. Sun, Z. Xia, and U. S. Kamilov, "Efficient and accurate inversion of multiple scattering with deep learning," *Optics Express*, vol. 26, no. 11, pp. 14 678–14 688, 2018.

[96] S. Li, M. Deng, J. Lee, A. Sinha, and G. Barbastathis, "Imaging through glass diffusers using densely connected convolutional networks," *Optica*, vol. 5, no. 7, pp. 803–813, 2018.

[97] Y. Li, Y. Xue, and L. Tian, "Deep speckle correlation: a deep learning approach toward scalable imaging through scattering media," *Optica*, vol. 5, no. 10, pp. 1181–1190, 2018.

[98] K. Guo, S. Dong, P. Nanda, and G. Zheng, "Optimization of sampling pattern and the design of fourier ptychographic illuminator," *Optics express*, vol. 23, no. 5, pp. 6171–6180, 2015.

[99] S. Mehta and C. Sheppard, "Quantitative phase-gradient imaging at high resolution with asymmetric illumination-based differential phase contrast," *Optics Letters*, vol. 34, no. 13, pp. 1924–1926, 2009.

[100] L. Tian and L. Waller, "3D intensity and phase imaging from light field measurements in an LED array microscope," *Optica*, vol. 2, pp. 104–111, 2015.

[101] J. Schindelin, I. Arganda-Carreras, E. Frise, V. Kaynig, M. Longair, T. Pietzsch, S. Preibisch, C. Rueden, S. Saalfeld, B. Schmid *et al.*, "Fiji: an open-source platform for biological-image analysis," *Nature methods*, vol. 9, no. 7, pp. 676–682, 2012.

[102] J. Lobo, E. Y.-S. See, M. Biggs, and A. Pandit, "An insight into morphometric descriptors of cell shape that pertain to regenerative medicine," *Journal of tissue engineering and regenerative medicine*, vol. 10, no. 7, pp. 539–553, 2016.

[103] T. A. Zangle and M. A. Teitell, "Live-cell mass profiling: an emerging approach in quantitative biophysics," *Nature methods*, vol. 11, no. 12, p. 1221, 2014.

[104] Z. Sadrearhami, F. N. Shafiee, K. K. K. Ho, N. Kumar, M. Krasowska, A. Blencowe, E. H. Wong, and C. Boyer, "Antibiofilm nitric oxide releasing polydopamine coatings," *ACS applied materials & interfaces*, 2019.

[105] Y. Li, M. J. Fanous, K. A. Kilian, and G. Popescu, "Quantitative phase imaging reveals matrix stiffness-dependent growth and migration of cancer cells," *Scientific reports*, vol. 9, no. 1, p. 248, 2019.

[106] A. Zhikhoreva, A. Belashov, V. Bespalov, A. Semenov, I. Semenova, G. Tochilnikov, N. Zhilinskaya, and O. Vasyutinskii, "Morphological changes in the ovarian carcinoma cells of wistar rats induced by chemotherapy with cisplatin and dioxadet," *Biomedical optics express*, vol. 9, no. 11, pp. 5817–5827, 2018.

[107] T. Stiernagle, "Maintenance of c. elegans. wormbook. the c. elegans research community," *WormBook*, 2006. [Online]. Available: http://www.wormbook.org/chapters/www_strainmaintain/strainmaintain.html

[108] E. Kim, L. Sun, C. V. Gabel, and C. Fang-Yen, "Long-term imaging of caenorhabditis elegans using nanoparticle-mediated immobilization," *PloS one*, vol. 8, no. 1, p. e53419, 2013.

[109] A. K. Corsi, B. Wightman, and M. Chalfie, "A transparent window into biology: a primer on caenorhabditis elegans," *Genetics*, vol. 200, no. 2, pp. 387–407, 2015.

[110] R. Ling, W. Tahir, H. Y. Lin, H. Lee, and L. Tian, "High-throughput intensity diffraction tomography with a computational microscope," *Biomedical Optics Express*, vol. 9, no. 5, pp. 2130–2141, 2018.

[111] P. Hosseini, R. Zhou, Y.-H. Kim, C. Peres, A. Diaspro, C. Kuang, Z. Yaqoob, and P. T. So, "Pushing phase and amplitude sensitivity limits in interferometric microscopy," *Optics letters*, vol. 41, no. 7, pp. 1656–1659, 2016.

[112] T. Juffmann, A. de los Ríos Sommer, and S. Gigan, "Local optimization of wavefronts for optimal sensitivity phase imaging (lowphi)," *Optics Communications*, vol. 454, p. 124484, 2020.

[113] G. Osnabrugge, S. Leedumrongwatthanakun, and I. M. Vellekoop, "A convergent born series for solving the inhomogeneous helmholtz equation in arbitrarily large media," *Journal of computational physics*, vol. 322, pp. 113–124, 2016.

[114] K. M. Ashman, C. M. Bird, and S. E. Zepf, "Detecting bimodality in astronomical datasets," *arXiv preprint astro-ph/9408030*, 1994.

[115] S. Feng, Q. Chen, G. Gu, T. Tao, L. Zhang, Y. Hu, W. Yin, and C. Zuo, "Fringe pattern analysis using deep learning," *Advanced Photonics*, vol. 1, no. 2, p. 025001, 2019.

[116] M. Lyu, H. Wang, G. Li, S. Zheng, and G. Situ, "Learning-based lensless imaging through optically thick scattering media," *Advanced Photonics*, vol. 1, no. 3, p. 036002, 2019.

[117] G. Barbastathis, A. Ozcan, and G. Situ, "On the use of deep learning for computational imaging," *Optica*, vol. 6, no. 8, pp. 921–943, 2019.

[118] J. Lim, A. B. Ayoub, and D. Psaltis, "Three-dimensional tomography of red blood cells using deep learning," *Advanced Photonics*, vol. 2, no. 2, p. 026001, 2020.

[119] Z. Wu, Y. Sun, A. Matlock, J. Liu, L. Tian, and U. S. Kamilov, "Simba: Scalable inversion in optical tomography using deep denoising priors," *IEEE Journal of Selected Topics in Signal Processing*, vol. 14, no. 6, pp. 1163–1175, 2020.

[120] K. C. Zhou and R. Horstmeyer, "Diffraction tomography with a deep image prior," *Optics Express*, vol. 28, no. 9, pp. 12 872–12 896, 2020.

[121] I. Kang, A. Goy, and G. Barbastathis, "Dynamical machine learning volumetric reconstruction of objects' interiors from limited angular views," *Light: Science & Applications*, vol. 10, no. 1, pp. 1–21, 2021.

[122] M. Deng, S. Li, Z. Zhang, I. Kang, N. X. Fang, and G. Barbastathis, "On the interplay between physical and content priors in deep learning for computational imaging," *Optics Express*, vol. 28, no. 16, pp. 24 152–24 170, 2020.

[123] J. Xiao, J. Hays, K. A. Ehinger, A. Oliva, and A. Torralba, "Sun database: Large-scale scene recognition from abbey to zoo," in *2010 IEEE computer society conference on computer vision and pattern recognition*. IEEE, 2010, pp. 3485–3492.

[124] G. B. Huang, M. Mattar, T. Berg, and E. Learned-Miller, "Labeled faces in the wild: A database forstudying face recognition in unconstrained environments," in *Workshop on faces in'Real-Life'Images: detection, alignment, and recognition*, 2008.

[125] G. Griffin, A. Holub, and P. Perona, "Caltech-256 object category dataset," *California Institute of Technology*, 2007. [Online]. Available: https://resolver.caltech.edu/CaltechAUTHORS:CNS-TR-2007-001

[126] G. Cheng, J. Han, and X. Lu, "Remote sensing image scene classification: Benchmark and state of the art," *Proceedings of the IEEE*, vol. 105, no. 10, pp. 1865–1883, 2017.

[127] H. Oh Song, Y. Xiang, S. Jegelka, and S. Savarese, "Deep metric learning via lifted structured feature embedding," in *Proceedings of the IEEE conference on computer vision and pattern recognition*, 2016, pp. 4004–4012.

[128] A. Krizhevsky and G. Hinton, "Learning multiple layers of features from tiny images," *Citeseer*, 2009. [Online]. Available: https://www.cs.toronto.edu/~kriz/cifar.html

[129] A. Khosla, N. Jayadevaprakash, B. Yao, and F.-F. Li, "Novel dataset for fine-grained image categorization: Stanford dogs," in *Proceedings on CVPR Workshop on Fine-Grained Visual Categorization*, vol. 2, no. 1, 2011.

[130] D. P. Kingma and J. Ba, "Adam: A method for stochastic optimization," *arXiv preprint arXiv:1412.6980*, vol. abs/1412.6980, 2014. [Online]. Available: http://arxiv.org/abs/1412.6980

[131] O. Ronneberger, P. Fischer, and T. Brox, "U-net: Convolutional networks for biomedical image segmentation," in *International Conference on Medical image computing and computer-assisted intervention*. Springer, 2015, pp. 234–241.

[132] B. Xu, N. Wang, T. Chen, and M. Li, "Empirical evaluation of rectified activations in convolutional network," *arXiv:1505.00853*, 2015.

[133] A. Matlock and L. Tian, "Physical model simulator-trained neural network for computational 3d phase imaging of multiple-scattering samples," *arXiv preprint arXiv:2103.15795*, 2021.

[134] J. S. Cybulski, J. Clements, and M. Prakash, "Foldscope: origami-based paper microscope," *PloS one*, vol. 9, no. 6, p. e98781, 2014.

[135] B. Diederich, P. Then, A. Jügler, R. Förster, and R. Heintzmann, "cellstorm—cost-effective super-resolution on a cellphone using dstorm," *PloS one*, vol. 14, no. 1, p. e0209827, 2019.

[136] E. M. Christiansen, S. J. Yang, D. M. Ando, A. Javaherian, G. Skibinski, S. Lipnick, E. Mount, A. O'Neil, K. Shah, A. K. Lee, P. Goyal, W. Fedus, R. Poplin, A. Esteva, M. Berndl, L. L. Rubin, P. Nelson, and S. Finkbeiner, "In silico labeling: predicting fluorescent labels in unlabeled images," *Cell*, vol. 173, no. 3, pp. 792–803, 2018.

[137] Y. Rivenson, T. Liu, Z. Wei, Y. Zhang, K. de Haan, and A. Ozcan, "Phasestain: the digital staining of label-free quantitative phase microscopy images using deep learning," *Light: Science & Applications*, vol. 8, no. 1, pp. 1–11, 2019.

[138] M. E. Kandel, Y. R. He, Y. J. Lee, T. H.-Y. Chen, K. M. Sullivan, O. Aydin, M. T. A. Saif, H. Kong, N. Sobh, and G. Popescu, "Phase imaging with computational specificity (pics) for measuring dry mass changes in sub-cellular compartments," *Nature communications*, vol. 11, no. 1, pp. 1–10, 2020.

[139] S. Cheng, S. Fu, Y. M. Kim, W. Song, Y. Li, Y. Xue, J. Yi, and L. Tian, "Single-cell cytometry via multiplexed fluorescence prediction by label-free reflectance microscopy," *Science advances*, vol. 7, no. 3, p. eabe0431, 2021.

[140] S. Yoon, M. Kim, M. Jang, Y. Choi, W. Choi, S. Kang, and W. Choi, "Deep optical imaging within complex scattering media," *Nature Reviews Physics*, vol. 2, no. 3, pp. 141–158, 2020.

[141] S. Rotter and S. Gigan, "Light fields in complex media: Mesoscopic scattering meets wave control," *Reviews of Modern Physics*, vol. 89, no. 1, p. 015005, 2017.

[142] B. Rahmani, D. Loterie, E. Kakkava, N. Borhani, U. Teğin, D. Psaltis, and C. Moser, "Actor neural networks for the robust control of partially measured nonlinear systems showcased for image propagation through diffuse media," *Nature Machine Intelligence*, vol. 2, no. 7, pp. 403–410, 2020.

[143] N. Borhani, E. Kakkava, C. Moser, and D. Psaltis, "Learning to see through multimode fibers," *Optica*, vol. 5, no. 8, pp. 960–966, 2018.

[144] N. N. Boustany, S. A. Boppart, and V. Backman, "Microscopic imaging and spectroscopy with scattered light," *Annual review of biomedical engineering*, vol. 12, pp. 285–314, 2010.

[145] E. Beaurepaire, A. C. Boccara, M. Lebec, L. Blanchot, and H. Saint-Jalmes, "Full-field optical coherence microscopy," *Optics letters*, vol. 23, no. 4, pp. 244–246, 1998.

[146] L. Cherkezyan, I. Capoglu, H. Subramanian, J. Rogers, D. Damania, A. Taflove, and V. Backman, "Interferometric spectroscopy of scattered light can quantify the statistics of subdiffractional refractive-index fluctuations," *Physical review letters*, vol. 111, no. 3, p. 033903, 2013.

[147] J. Yi, Y. Stypula-Cyrus, C. S. Blaha, H. K. Roy, and V. Backman, "Fractal characterization of chromatin decompaction in live cells," *Biophysical journal*, vol. 109, no. 11, pp. 2218–2226, 2015.

[148] P. Wang, R. K. Bista, W. E. Khalbuss, W. Qiu, S. Uttam, K. Staton, L. Zhang, T. A. Brentnall, R. E. Brand, and Y. Liu, "Nanoscale nuclear architecture for cancer diagnosis beyond pathology via spatial-domain low-coherence quantitative phase microscopy," *Journal of biomedical optics*, vol. 15, no. 6, pp. 066 028–066 028, 2010.

[149] R. K. Bista, P. Wang, R. Bhargava, S. Uttam, D. J. Hartman, R. E. Brand, and Y. Liu, "Nuclear nano-morphology markers of histologically normal cells detect the "field effect" of breast cancer," *Breast cancer research and treatment*, vol. 135, no. 1, pp. 115–124, 2012.

[150] J. Ortega-Arroyo and P. Kukura, "Interferometric scattering microscopy (iscat): new frontiers in ultrafast and ultrasensitive optical microscopy," *Physical Chemistry Chemical Physics*, vol. 14, no. 45, pp. 15 625–15 636, 2012.

[151] A. Dubois, L. Vabre, A.-C. Boccara, and E. Beaurepaire, "High-resolution full-field optical coherence tomography with a linnik microscope," *Applied optics*, vol. 41, no. 4, pp. 805–812, 2002.

[152] A. Dubois, K. Grieve, G. Moneron, R. Lecaque, L. Vabre, and C. Boccara, "Ultrahigh-resolution full-field optical coherence tomography," *Applied optics*, vol. 43, no. 14, pp. 2874–2883, 2004.

[153] H. Subramanian, P. Pradhan, Y. Liu, I. R. Capoglu, X. Li, J. D. Rogers, A. Heifetz, D. Kunte, H. K. Roy, A. Taflove *et al.*, "Optical methodology for detecting histologically unapparent nanoscale consequences of genetic alterations in biological cells," *Proceedings of the National Academy of Sciences*, vol. 105, no. 51, pp. 20 118–20 123, 2008.

[154] G. Daaboul, A. Yurt, X. Zhang, G. Hwang, B. Goldberg, and M. Ünlü, "High-throughput detection and sizing of individual low-index nanoparticles and viruses for pathogen identification," *Nano letters*, vol. 10, no. 11, pp. 4727–4731, 2010.

[155] G. G. Daaboul, P. Gagni, L. Benussi, P. Bettotti, M. Ciani, M. Cretich, D. S. Freedman, R. Ghidoni, A. Y. Ozkumur, C. Piotto, D. Prosperi, B. Santini, M. S. Ünlü, and M. Chiari, "Digital detection of exosomes by interferometric imaging," *Scientific Reports*, vol. 6, 2016.

[156] O. Avci, M. I. Campana, C. Yurdakul, and M. S. Ünlü, "Pupil function engineering for enhanced nanoparticle visibility in wide-field interferometric microscopy," *Optica*, vol. 4, no. 2, pp. 247–254, 2017.

[157] S. Kang, S. Jeong, W. Choi, H. Ko, T. D. Yang, J. H. Joo, J.-S. Lee, Y.-S. Lim, Q.-H. Park, and W. Choi, "Imaging deep within a scattering medium using collective accumulation of single-scattered waves," *Nature Photonics*, vol. 9, no. 4, pp. 253–258, 2015.

[158] T. E. Matthews, M. Medina, J. R. Maher, H. Levinson, W. J. Brown, and A. Wax, "Deep tissue imaging using spectroscopic analysis of multiply scattered light," *Optica*, vol. 1, no. 2, pp. 105–111, 2014.

[159] D. Huang, E. Swanson, C. Lin, J. Schuman, W. Stinson, W. Chang, M. Hee, T. Flotte, K. Gregory, C. Puliafito, and J. Fujimoto, "Optical coherence tomography," *Science*, vol. 254, no. 5035, pp. 1178–1181, 1991.

[160] T. N. Ford, K. K. Chu, and J. Mertz, "Phase-gradient microscopy in thick tissue with oblique back-illumination," *Nature Methods*, vol. 9, no. 12, pp. 1195–1197, 2012.

[161] M. E. Kandel, C. Hu, G. N. Kouzehgarani, E. Min, K. M. Sullivan, H. Kong, J. M. Li, D. N. Robson, M. U. Gillette, C. Best-Popescu *et al.*, "Epi-illumination gradient light interference microscopy for imaging opaque structures," *Nature communications*, vol. 10, no. 1, pp. 1–9, 2019.

[162] M. A. Choma, A. K. Ellerbee, C. Yang, T. L. Creazzo, and J. A. Izatt, "Spectral-domain phase microscopy," *Optics letters*, vol. 30, no. 10, pp. 1162–1164, 2005.

[163] M. V. Sarunic, S. Weinberg, and J. A. Izatt, "Full-field swept-source phase microscopy," *Optics Letters*, vol. 31, no. 10, pp. 1462–1464, 2006.

[164] T. Yamauchi, H. Iwai, M. Miwa, and Y. Yamashita, "Low-coherent quantitative phase microscope for nanometer-scale measurement of living cells morphology," *Optics express*, vol. 16, no. 16, pp. 12 227–12 238, 2008.

[165] C. Edwards, B. Bhaduri, B. Griffin, L. Goddard, and G. Popescu, "Epi-illumination diffraction phase microscopy with white light," *Optics letters*, vol. 39, no. 21, pp. 6162–6165, 2014.

[166] Z. Yaqoob, T. Yamauchi, W. Choi, D. Fu, R. R. Dasari, and M. S. Feld, "Single-shot full-field reflection phase microscopy," *Optics express*, vol. 19, no. 8, pp. 7587–7595, 2011.

[167] T. Zhang, C. Godavarthi, P. C. Chaumet, G. Maire, H. Giovannini, A. Talneau, M. Allain, K. Belkebir, and A. Sentenac, "Far-field diffraction microscopy at $\lambda/10$ resolution," *Optica*, vol. 3, no. 6, pp. 609–612, 2016.

[168] Y. Choi, P. Hosseini, W. Choi, R. R. Dasari, P. T. So, and Z. Yaqoob, "Dynamic speckle illumination wide-field reflection phase microscopy," *Optics letters*, vol. 39, no. 20, pp. 6062–6065, 2014.

[169] Y. Choi, P. Hosseini, J. W. Kang, S. Kang, T. D. Yang, M. G. Hyeon, B.-M. Kim, P. T. So, and Z. Yaqoob, "Reflection phase microscopy using spatio-temporal coherence of light," *Optica*, vol. 5, no. 11, pp. 1468–1473, 2018.

[170] T. S. Ralston, D. L. Marks, P. S. Carney, and S. A. Boppart, "Inverse scattering for optical coherence tomography," *Journal of the Optical Society of America A*, vol. 23, no. 5, pp. 1027–1037, May 2006.

[171] D. L. Marks, T. S. Ralston, S. A. Boppart, and P. S. Carney, "Inverse scattering for frequency-scanned full-field optical coherence tomography," *Journal of the Optical Society of America A*, vol. 24, no. 4, pp. 1034–1041, 2007.

[172] A. Federici, H. S. G. da Costa, J. Ogien, A. K. Ellerbee, and A. Dubois, "Wide-field, full-field optical coherence microscopy for high-axial-resolution phase and amplitude imaging," *Applied optics*, vol. 54, no. 27, pp. 8212–8220, 2015.

[173] S. Uttam and Y. Liu, "Fourier phase in fourier-domain optical coherence tomography," *Journal of the Optical Society of America A*, vol. 32, no. 12, pp. 2286–2306, 2015.

[174] T. Yamauchi, H. Iwai, and Y. Yamashita, "Label-free imaging of intracellular motility by low-coherent quantitative phase microscopy," *Optics express*, vol. 19, no. 6, pp. 5536–5550, 2011.

[175] T. M. Elfouhaily, C.-A. Guérin *et al.*, "A critical survey of approximate scattering wave theories from random rough surfaces," *Waves in Random Media*, vol. 14, no. 4, pp. R1–R40, 2004.

[176] T. Kim, R. Zhou, L. Goddard, and G. Popescu, "Solving inverse scattering problems in biological samples by quantitative phase imaging," *Laser & Photonics Reviews*, vol. 10, no. 1, pp. 13–39, January 2015.

[177] R. Zhou, D. Jin, P. Hosseini, V. R. Singh, Y.-h. Kim, C. Kuang, R. R. Dasari, Z. Yaqoob, and P. T. So, "Modeling the depth-sectioning effect in reflection-mode dynamic speckle-field interferometric microscopy," *Optics express*, vol. 25, no. 1, pp. 130–143, 2017.

[178] C. Hu and G. Popescu, "Physical significance of backscattering phase measurements," *Optics letters*, vol. 42, no. 22, pp. 4643–4646, 2017.

[179] O. Avci, R. Adato, A. Y. Ozkumur, and M. S. Ünlü, "Physical modeling of interference enhanced imaging and characterization of single nanoparticles," *Optics express*, vol. 24, no. 6, pp. 6094–6114, 2016.

[180] C.-A. Guérin and A. Sentenac, "Second-order perturbation theory for scattering from heterogeneous rough surfaces," *Journal of the Optical Society of America A*, vol. 21, no. 7, pp. 1251–1260, 2004.

[181] C. Sheppard, "Imaging of random surfaces and inverse scattering in the kirchoff approximation," *Waves in random media*, vol. 8, no. 1, pp. 53–66, 1998.

[182] E. Mudry, P. Chaumet, K. Belkebir, G. Maire, and A. Sentenac, "Mirror-assisted tomographic diffractive microscopy with isotropic resolution," *Optics letters*, vol. 35, no. 11, pp. 1857–1859, 2010.

[183] B. Simon, L. Vonna, and O. Haeberlé, "A versatile transmission/reflection tomographic diffractive microscopy approach," *Journal of the Optical Society of America A*, vol. 36, no. 11, pp. C18–C27, 2019.

[184] P. Ledwig, M. Sghayyer, J. Kurtzberg, and F. E. Robles, "Dual-wavelength oblique back-illumination microscopy for the non-invasive imaging and quantification of blood in collection and storage bags," *Biomedical Optics Express*, vol. 9, no. 6, pp. 2743–2754, 2018.

[185] P. Ledwig and F. E. Robles, "Epi-mode tomographic quantitative phase imaging in thick scattering samples," *Biomedical Optics Express*, vol. 10, no. 7, pp. 3605–3621, 2019.

[186] T. Laforest, M. Künzi, L. Kowalczuk, D. Carpentras, F. Behar-Cohen, and C. Moser, "Transscleral optical phase imaging of the human retina-topi," *arXiv preprint arXiv:1905.06877*, 2019.

[187] R. Horstmeyer, J. Chung, X. Ou, G. Zheng, and C. Yang, "Diffraction tomography with fourier ptychography," *Optica*, vol. 3, no. 8, pp. 827–835, 2016.

[188] R. J. Wombell and J. A. DeSanto, "Reconstruction of rough-surface profiles with the kirchhoff approximation," *Journal of the Optical Society of America A*, vol. 8, no. 12, pp. 1892–1897, 1991.

[189] J. A. DeSanto, "Exact spectral formalism for rough-surface scattering," *Journal of the Optical Society of America A*, vol. 2, no. 12, pp. 2202–2207, 1985.

[190] P. Beckmann and A. Spizzichino, *The scattering of electromagnetic waves from rough surfaces*. Norwood, MA, Artech House, Inc., 1987.

[191] C. Sheppard, T. Connolly, and M. Gu, "Imaging and reconstruction for rough surface scattering in the kirchhoff approximation by confocal microscopy," *Journal of Modern Optics*, vol. 40, no. 12, pp. 2407–2421, 1993.

[192] K. D. Unger, P. C. Chaumet, G. Maire, A. Sentenac, and K. Belkebir, "Versatile inversion tool for phaseless optical diffraction: tomography," *Journal of the Optical Society of America A*, vol. 36, no. 11, pp. C1–C8, 2019.

[193] A. Matlock, A. Sentenac, P. C. Chaumet, J. Yi, and L. Tian, "Inverse scattering for reflection intensity phase microscopy," *Biomedical optics express*, vol. 11, no. 2, pp. 911–926, 2020.

[194] C. J. R. Sheppard and F. Aguilar, "Fresnel coefficients for weak reflection, and the scattering potential for three-dimensional imaging," *Optics Communications*, vol. 162, no. 4-6, pp. 182–186, 1999.

[195] B. T. Draine and P. J. Flatau, "Discrete-dipole approximation for scattering calculations," *Journal of the Optical Society of America A*, vol. 11, no. 4, pp. 1491–1499, 1994.

[196] S. Khadir, P. C. Chaumet, G. Baffou, and A. Sentenac, "Quantitative model of the image of a radiating dipole through a microscope," *Journal of the Optical Society of America A*, vol. 36, no. 4, pp. 478–484, 2019.

[197] P. C. Chaumet, A. Sentenac, and D. Sentenac, "Idiot friendly discrete dipole approximation Repository," https://github.com/pchaumet/IF-DDA, 2019.

[198] K. R. Porter, V. Fonte, and G. Weiss, "A scanning microscope study of the topography of hela cells," *Cancer research*, vol. 34, no. 6, pp. 1385–1394, 1974.

[199] H.-Y. Liu, D. Liu, H. Mansour, P. T. Boufounos, L. Waller, and U. S. Kamilov, "SEAGLE: Sparsity-driven image reconstruction under multiple scattering," *IEEE Transactions on Computational Imaging*, vol. 4, no. 1, pp. 73–86, 2018.

[200] Y. Xue, S. Cheng, Y. Li, and L. Tian, "Reliable deep-learning-based phase imaging with uncertainty quantification," *Optica*, vol. 6, no. 5, p. 618, May 2019. [Online]. Available: http://dx.doi.org/10.1364/OPTICA.6.000618

[201] F. Ströhl, S. Jadhav, B. S. Ahluwalia, K. Agarwal, and D. K. Prasad, "Object detection neural network improves fourier ptychography reconstruction," *Optics Express*, vol. 28, no. 25, pp. 37 199–37 208, 2020.

[202] H. Pinkard, Z. Phillips, A. Babakhani, D. A. Fletcher, and L. Waller, "Deep learning for single-shot autofocus microscopy," *Optica*, vol. 6, no. 6, pp. 794–797, 2019.

[203] L. Shen, W. Zhao, and L. Xing, "Patient-specific reconstruction of volumetric computed tomography images from a single projection view via deep learning," *Nature biomedical engineering*, vol. 3, no. 11, pp. 880–888, 2019.

[204] G. Ongie, A. Jalal, C. A. Metzler, R. G. Baraniuk, A. G. Dimakis, and R. Willett, "Deep learning techniques for inverse problems in imaging," *IEEE Journal on Selected Areas in Information Theory*, vol. 1, no. 1, pp. 39–56, 2020.

[205] P. Ledwig and F. E. Robles, "Quantitative 3d refractive index tomography of opaque samples in epi-mode," *Optica*, vol. 8, no. 1, pp. 6–14, 2021.

[206] M. G. Gustafsson, D. Agard, J. Sedat *et al.*, "I5m: 3d widefield light microscopy with better than 100nm axial resolution," *Journal of microscopy*, vol. 195, no. 1, pp. 10–16, 1999.

[207] S. Hell and E. H. Stelzer, "Properties of a 4pi confocal fluorescence microscope," *Journal of the Optical Society of America A*, vol. 9, no. 12, pp. 2159–2166, 1992.